SYNTHESIS, CHARACTERIZATION, AND ELECTROCHEMICAL PROPERTIES OF MESOPOROUS SPINEL $LiMn_{2-x}M_xO_4$ (M = Mn, Fe, Co, Ni, AND Cu) THIN FILMS

A DISSERTATION SUBMITTED TO
THE GRADUATE SCHOOL OF ENGINEERING AND SCIENCE
OF BILKENT UNIVERSITY
IN PARTIAL FULFILLMENT OF THE REQUIREMENTS FOR
THE DEGREE OF
DOCTOR OF PHILOSOPHY
IN
CHEMISTRY

By
Irmak Karakaya Durukan
May 2024

SYNTHESIS, CHARACTERIZATION, AND ELECTROCHEMICAL PROPERTIES OF MESOPOROUS SPINEL $LiMn_{2-x}M_xO4$ (M = Mn, Fe, Co, Ni, AND Cu) THIN FILMS

By Irmak Karakaya Durukan
May 2024

We certify that we have read this dissertation and that, in our opinion, it is fully adequate, in scope and quality, as a dissertation for the degree of Doctor of Philosophy.

_____
Ömer Dağ
Advisor

_____
Ferdi Karadaş

_____
Atilla Cihaner

_____
Emren Nalbant

_____
Halil İbrahim Okur

Approved for the Graduate School of Engineering and Science:

_____
Orhan Arıkan
Director of the Graduate School

ABSTRACT

SYNTHESIS, CHARACTERIZATION, AND ELECTROCHEMICAL PROPERTIES OF MESOPOROUS SPINEL $LiMn_{2-x}M_xO4$ (M = Mn, Fe, Co, Ni, AND Cu) THIN FILMS

Irmak Karakaya Durukan
Ph.D. in Chemistry
Advisor: Ömer Dağ
May 2024

Mesoporous $LiMn_{2-x}M_xO_4$ electrodes are promising candidates for efficient oxygen evolution (OER) electrocatalysis. In this study, mesoporous $LiMn_{2-x}M_xO_4$ (where M is Mn, Fe, Co, Ni, and Cu) thin films have been fabricated by employing molten-salt assisted self-assembly (MASA) method on fluorine doped tin oxide (FTO) surface. The electrodes are characterized according to their structure, morphology, and thicknesses using various characterization techniques. The electrochemical properties of the films are comprehensively investigated under acidic, alkaline, neutral, and non-aqueous solutions.

The manganese oxide-based electrodes undergo Mn(III) and Mn(VI) disproportionation reactions. Here, we have extensively investigated these disproportionation reactions by post-characterization techniques after electrochemical experiments using $LiMn_{2-x}M_xO_4$ (M is Fe, Co, Ni, and Cu and x is 0, 0.1, 0.3, 0.4, and 0.67) and Mn_3O_4 electrodes. The $LiMn_2O_4$ thin films are found to be more stable in OER compared to Mn_3O_4. Lithium de-intercalation of the $LiMn_2O_4$ films produces a λ-MnO_2 phase robust against Mn(VI) disproportionation. The electrochemical degradation rates are investigated using the $LiMn_2O_4$ electrodes, fabricated at various spin rates (from 2000 and 10000 rpm). The film thicknesses are between 150 and 500 nm. The $LiMn_2O_4$ electrode at 5000 rpm is more resistant to physical degradation during electrochemical tests. Charge capacity values of the thin films are determined by electrochemical experiments in $LiNO_3$ electrolyte and found to be between 136 and 273 mC/cm^2 for the films, then these values are used to calculate their approximate weights (between 30 and 60 $\mu g/cm^2$). The annealing temperature for the $LiMn_2O_4$ thin films is also optimized for a stable OER. The $LiMn_2O_4$ film,

fabricated at 5000 rpm spin rate and annealed at 300 ^{o}C, is found to be a more robust and efficient electrode with a 60 mV/dec Tafel slope and 812 mV overpotential at 10 mA/cm^2 current density. The same fabrication parameters are used for the other mesoporous $LiMn_{2-x}M_xO_4$ thin films.

The $LiMn_{2-x}M_xO_4$ thin films are used to collect their N_2-adsorption-desorption isotherms. The isotherms display type IV hysteresis, characteristic of mesoporous materials. BET surface areas are estimated as 98, 99, 116, 112, and 75 m^2/g for the $LiMn_2O_4$, $LiMn_{1.7}Fe_{0.3}O_4$, $LiMn_{1.7}Co_{0.3}O_4$, $LiMn_{1.7}Ni_{0.3}O_4$ and $LiMn_{1.7}Cu_{0.3}O_4$, films, respectively. Moreover, the $LiMn_{2-x}M_xO_4$ electrodes (fabricated at 5000 rpm spin rate and 300 ^{o}C annealing temperature) are investigated for lithium de-intercalation/intercalation behavior in 1 M $LiNO_3$ solution. Then, the same electrodes are used to collect 300 CVs, CAs, and CPs in 1 M KOH solution to evaluate electrochemical behaviors. From these measurements, the origin of phase separation and bearing lower oxidation states of the nickel and copper at higher x values are identified in the spinel structure. The Mn(VI) disproportionation reaction on the $LiMn_{2-x}M_xO_4$ electrodes is investigated by CV cycling experiments in 1 M KOH. The $LiMn_2O_4$, $LiMn_{2-x}Fe_xO_4$, and $LiMn_{2-x}Cu_xO_4$ electrodes undergo fast degradation compared to $LiMn_{2-x}Co_xO_4$ and $LiMn_{2-x}Ni_xO_4$ through the dispersion of $[MnO_4]^-$ and $[FeO_4]^{2-}$ ions and dissolution of the CuO phase formed in the electrodes during OER. The $LiMn_{1.7}M_{0.3}O_4$ thin films on FTO are used in OER electrocatalysis and the overpotential values at 10 mA/cm^2 are evaluated as 645, 686, and 657 mV for the $LiMn_{1.7}Fe_{0.3}O_4$, $LiMn_{1.7}Co_{0.3}O_4$, $LiMn_{1.7}Ni_{0.3}O_4$ electrodes, respectively. The exact compositions are also coated on graphite substrates and their overpotential values are also evaluated as 629, 462, 440, and 532 mV at 10 mA/cm^2 for the $LiMn_2O_4$, $LiMn_{1.7}Fe_{0.3}O_4$, $LiMn_{1.7}Co_{0.3}O_4$, $LiMn_{1.7}Ni_{0.3}O_4$ electrodes, respectively. The $LiMn_{1.7}Co_{0.3}O_4$ on graphite and $LiMn_{1.7}Ni_{0.3}O_4$ on FTO electrodes are found to be the most robust and efficient electrodes at a 50 mA/cm^2 current density.

Keywords: lyotropic liquid crystalline mesophase, molten-salt assisted self-assembly, mesoporous materials, thin films, lithiated manganese oxide, bimetallic oxide, lithiation-delithiation, electrocatalysis, oxygen evolution reaction, manganese disproportionation reaction

ÖZET

MEZOGÖZENEKLİ SPİNEL $LiMn_{2-x}M_xO_4$ (M = Mn, Fe, Co, Ni VE Cu) İNCE FİLMLERİN SENTEZİ, KARAKTERİZASYONU VE ELEKTROKİMYASAL ÖZELLİKLERİ

Irmak Karakaya Durukan
Kimya, Doktora
Tez Danışmanı: Ömer Dağ
Mayıs 2024

Mezogözenekli $LiMn_{2-x}M_xO_4$ elektrotlar, suyun elektrokimyasal oksidasyonu (SEO) için umut verici adaylardır. Bu çalışmada, flor katkılı kalay oksit (FTO) yüzeyi üzerinde eriyik tuz destekli kendiliğinden oluşma (EDKO) yöntemi kullanılarak mezo gözenekli $LiMn_{2-x}M_xO_4$ (M= Mn, Fe, Co, Ni ve Cu) ince filmler üretilmiştir. Elektrotlar kristal yapılarına, film morfolojilerine ve kalınlıklarına göre birçok yöntem ile karakterize edilmiştir. Filmlerin elektrokimyasal özellikleri asidik, alkali, nötr ve sulu olmayan koşullar altında kapsamlı bir şekilde araştırılmıştır.

Yüzey Mn(III) ve Mn(VI) türlerinin elektrokimyasal bozulumları, elektrokimyasal deneylerden sonraki karakterizasyon teknikleri ile gösterilmiştir. $LiMn_2O_4$ ince filmleri, MASA yöntemi kullanılarak üretilen Mn_3O_4 elektrotlara kıyasla suyun elektrokimyasal oksidasyonunda daha kararlı bulunmuştur. $LiMn_2O_4$ filmlerinde lityum deinterkalasyonunun, Mn(VI) bozulumuna karşı dayanıklı λ-MnO_2 yapısını oluşturduğu gösterilmiştir. $LiMn_2O_4$ filmlerin 2000 rpm ve 10000 rpm arasında çeşitli dönüş hızlarında üretilmesinden sonra elektrotlarının elektrokimyasal bozunma hızları araştırılmıştır. Bu film kalınlıkları 150 ila 500 nm arasında elde edilmiştir ve 5000 rpm dönüş hızıyla elde edilen $LiMn_2O_4$ elektrotunun fiziksel bozunmaya karşı daha dirençli olduğu gözlenmiştir. İnce filmlerin kapasite değerleri $LiNO_3$ elektrolitinde yapılan elektrokimyasal deneylerle, bu filmler için 136 ile 273 mC arasında belirlenmiş, bu değerler FTO üzerindeki 30 ile 60 μg/cm^2 arasında çeşitlilik gösteren film ağırlıklarına çevrilmiştir. $LiMn_2O_4$ ince filmlerinin tavlama sıcaklığı, daha kararlı bir elektrokimyasal oksidasyon için optimize edilmiştir.

5000 rpm dönüş hızında üretilen ve 300 ^{o}C'de tavlanan $LiMn_2O_4$ filmi 60mV/dec Tafel eğrisi ve 10mA/cm^2 akımda 812 mV ek potansiyel değeri vermiştir. FTO yüzeyinde, mezo gözenekli $LiMn_{2-x}M_xO_4$ ince filmlerin de üretimi için aynı üretim parametreleri uygulanmıştır.

Ek olarak, $LiMn_{2-x}M_xO_4$ elektrotlarının 5000 rpm dönüş hızında ve 300 ^{o}C tavlama sıcaklığında lityumun deinterkalasyon davranışı araştırılmıştır. BET yüzey alanları $LiMn_2O_4$, $LiMn_{1.7}Fe_{0.3}O_4$, $LiMn_{1.7}Co_{0.3}O_4$, $LiMn_{1.7}Ni_{0.3}O_4$ ve $LiMn_{1.7}Cu_{0.3}O_4$ için sırasıyla 98, 99, 116, 112 ve 75 m^2/g olarak rapor edilmiştir. $LiNO_3$ ortamında $LiMn_2O_4$, $LiMn_{2-x}Fe_xO_4$, $LiMn_{2-x}Co_xO_4$, $LiMn_{2-x}Ni_xO_4$ ve $LiMn_{2-x}Cu_xO_4$ elektrotları için lityum iyon interkalasyon ve de-interkalasyon süreçleri araştırılmıştır. Yüksek x değerlerinde nikel ve bakırın daha düşük oksidasyon durumlarına sahip olduğu ve spinel kristal yapısında faz ayrımının oluştuğu belirlenmiştir. $LiMn_{2-x}M_xO4$ elektrotları üzerindeki Mn(VI) bozulum tepkimesi, 1 M KOH'da elektrokimyasal döngü deneyleri ile araştırılmıştır. $LiMn_2O_4$, $LiMn_{2-x}Fe_xO_4$ ve $LiMn_{2-x}Cu_xO_4$ elektrotları, MnO_4^- ve FeO_4^{2-}'nin elektrolite dağılması ve elektrotlarda CuO fazının oluşması nedeniyle $LiMn_{2-x}Co_xO_4$ ve $LiMn_{2-x}Ni_xO_4$ elektrotlarına kıyasla hızlı bir bozulmaya uğramıştır. FTO üzerindeki $LiMn_{1.7}M_{0.3}O_4$ ince filmleri SEO elektrokatalizinde test edilmiş ve 10 mA/cm^2 akım değerindeki ek potansiyel değerleri $LiMn_{1.7}Fe_{0.3}O_4$, $LiMn_{1.7}Co_{0.3}O_4$, $LiMn_{1.7}Ni_{0.3}O_4$ için sırasıyla 645, 686 ve 657 mV olarak elde edilmiştir. Aynı kompozisyonlar grafit substratlar üzerine de kaplanmıştır ve $LiMn_2O_4$, $LiMn_{1.7}Fe_{0.3}O_4$, $LiMn_{1.7}Co_{0.3}O_4$, $LiMn_{1.7}Ni_{0.3}O_4$ için 10 mA/cm^2 akım değerinde sırasıyla 629, 462, 440 ve 532 mV ek potansiyel değerleri elde edilmiştir. Grafit üzerindeki $LiMn_{1.7}Co_{0.3}O_4$ filmi ve FTO üzerindeki $LiMn_{1.7}Ni_{0.3}O_4$'ün, 50 mA/cm^2 akım değerinde bile kararlı ek potansiyel sonuçları göstermiş ve bu elektrotların sağlam ve verimli elektrotlar olduğu kanıtlanmıştır.

Anahtar kelimeler: liyotropik sıvı kristal, eriyik tuz destekli kendiliğinden oluşma, mezogözenekli malzeme, ince film, lityum mangan oksit, iki metalli oksit, lityum interkalasyonu-deinterkalasyonu, elektro-kataliz, su oksidasyonu, mangan bozulumu

ACKNOWLEDGEMENTS

Foremost, I would like to express my most considerable appreciation to my supervisor, Prof. Ömer Dağ, for his boundless support, patience, and assistance over the last eight years. You are the best scientist that I know so far. Your creative perspective on the experimental designs, approach to the methodologies, and proficiency in inorganic chemistry were perfect. I am always pleased to learn from you and discuss all kinds of subjects with you. I was able to complete this thesis and took my Ph.D. thanks to your excellent guidance, practical and theoretical feedback, and invaluable contributions. It was an honor to work under your supervision. Thank you Ömer Hocam! Forever, you will be my role model as a scientist!

I specifically would like to thank professors Ferdi Karadaş and Burak Ülgüt for their enlightening feedback about electrocatalysis and electrochemistry. Your contributions were significant to this work. Thanks to you, I learned the theory behind electrochemistry. Also, I would like to thank Prof. Atilla Cihaner for his helpful comments and for spending his valuable time on my thesis progress. I want to thank all the professors in the Bilkent University Chemistry Department. I always felt lucky to take the courses from the instructors who were experts in their fields. I learned many valuable things due to these courses. They all made me a qualified student in all fields of chemistry.

Thanks to each former and recent member of Dag Research Group for everything. This group became my second family. Each member has contributed to my learning, succeeding, and overcoming technical issues while making the lab environment enjoyable and calm. Special thanks to my beloved best friend and lab mate, Assel Amirzhanova. You were always with me whenever I needed technical help and support for life issues. You led me to be energetic, well-cared, and to be a pop culture slave… Also, thanks to my sister and ex-life mate, Işıl Ulu. You occupied twelve years of my life and will go on forever. You were always with me in this challenging way. Your support, motivation, and encouragement were very precious to me. Thanks for sharing these joyful years with me and making each of them memorable.

I would like to express my most profound appreciation to my mother and father, Tenzile and Fehmi Karakaya. Thanks for your endless support, patience, sacrifices, and belief in me. I am always proud of being your child. Now, I come to these days thanks to you. I could not succeed if you did not stand behind me in this life. Thank you for all! Special thanks to my beloved brother, Kaan Karakaya, for always being here whenever I needed it. Your star also rises in chemistry. We will always be remembered as chemist siblings! Also, I would like to thank Yasemin and Mustafa Durukan. Your contributions have been undeniable in recent years.

Lastly, I would like to express my most incredible gratitude to the other half of my life, Mete Batuhan Durukan. Thank you for your encouragement on this journey. You always motivated me even when I doubted myself. You provided practical and technical feedback for my research. Thank you for all the conversations and emotional support! I hope we will work together one day and our dreams will come true. Also, I would like to thank my lovely cats, Mayıs, Benek, and Korsan. Your existence is the most significant source of my inspiration. You always made me happy and full of spirit. You are the meaning of my life.

To my cats, Mayıs, Benek, and Korsan…

Contents

List of Figures

List of Tables

List of Abbreviations

LC : Liquid Crystal
LLC : Lyotropic Liquid Crystal
LMO : Lithium Transition Metal Oxide
MASA : Molten salt Assisted Self Assembly
SILAR : Successive Ionic Layer Adsorption and Reaction
XRD : X-ray Diffraction
POM : Polarized Optical Microscopy
SEM : Scanning Electron Microscopy
TEM : Transmission Electron Microscopy
EDX : Energy Dispersive X-ray Spectroscopy
XPS : X-ray Photoelectron Spectroscopy
ATR-FTIR : Attenuated Total Reflection Fourier-Transform Infrared
BET : Brunauer, Emmett, and Teller
PDF : Powder Diffraction File
OER : Oxygen Evolution Reaction
ORR : Oxygen Reduction Reaction
HER : Hydrogen Evolution Reaction
WE : Working Electrode
RE : Reference Electrode
CE : Counter Electrode
FTO : Fluorine doped Tin Oxide
NHE : Normal Hydrogen Electrode
CV : Cyclic Voltammetry
LSV : Linear Sweep Voltammetry
CA : Chronoamperometry
CP : Chronopotentiometry
GCD : Galvanostatic Charge Discharge
RDS : Rate Determining Step

Chapter 1

1. Introduction

1.1 Mesoporous Materials

Mesoporous materials are classified as materials with a porosity between microporous and macroporous materials and have a pore size between 2 and 50 nm. By controlling the pore sizes in mesoscale, several electronic and chemical properties of the materials could be modified that make them suitable for specific applications. Hence, mesoporous materials have significant roles in energy applications such as energy storage, battery, and catalytic reactions due to their high surface area and providing more active sites by contrast with bulk materials.[1], [2] Regarding the functional and novel behavior of transition metals, their mesoporous oxides are as important and have been investigated in terms of synthesis methods, nanocrystallite size, morphology, pore size, and pore-volume distributions, and surface area to correlate the properties with their material behaviors under various experimental conditions and applications. [3]–[5]

1.1.1 Synthesis of Mesoporous Metal Oxides

There are two common methods for the synthesis of mesoporous metal oxides, known as hard templating and soft templating. Hard templating is based on using a rigid and porous template like porous carbon or silica that is mixed with an inorganic precursor. The aim of the process is that the precursor fills the pores of the template and mimics the shape of the rigid structure. The path is followed by a treatment such as calcination that provides a mixed solid including both metal oxide and hard template. Then, the hard template is removed by a

strong acid or base depending on the template feature, and pure mesoporous metal oxide is obtained.[6]–[8]

In the soft templating method, the template is defined as soft because it is based on a surfactant that is in a micelle and/or liquid crystalline mesophase. Inorganic precursor surrounds ionic or non-ionic surfactant head groups and assembles on the surface of micellar structures to form a mesostructured semisolid or gel phase. After solidification of the precursor, the soft template is removed by chemical or heat treatment. In contrast to hard templating, these treatments are milder compared to using strong acids or bases.[9] Schematic representations of hard and soft templating methods are shown in Figure 1.1.

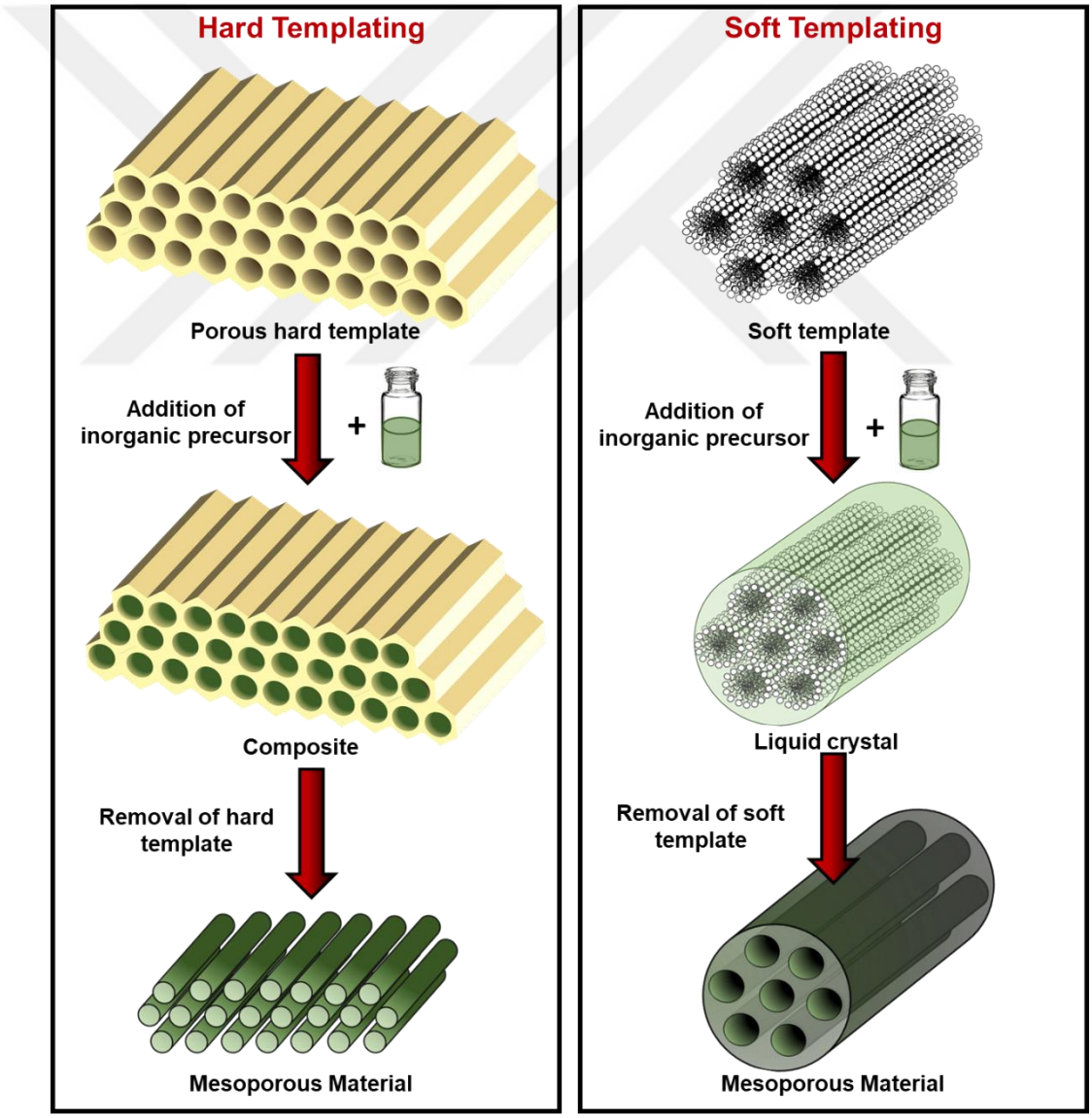

Figure 1.1 Schematic representations of hard and soft templating methods.

There are many studies on the synthesis of mesoporous materials by employing hard and soft templating methods. These materials have been used in many applications using their porous properties. Schüth *et al.* synthesized an ordered mesoporous carbon using a porous SBA-15 silica as a hard template. The mesoporous carbon has an around 2000 m^2/g BET surface area with a 10 nm pore size distribution.[10] The same research group also focused on the synthesis of mesoporous MgO using carbon aerogel as a hard template and obtained mesoporous MgO product with a 154 m^2/g BET surface area and 12.6 nm average pore size.[11] Mesoporous SnO_2 and TiO_2 have also been synthesized using porous KIT-6 and SBA-15 as hard templates.[12], [13] These materials have 160 to 200 m^2/g BET surface area with around 3.5 nm pore size and have been employed for battery and catalytic reactions with better activity (compared to their bulks).[12], [13] Wang *et al.* synthesized mesoporous $NiFe_2O_4$ using a porous KIT-6 silica as a hard template. They obtained mesoporous $NiFe_2O_4$ with a 121 m^2/g BET surface area and 3-4 nm pore size diameters.[14] Bruce *et al.* fabricated mesoporous ternary mixed metal oxide ($NiCoMnO_4$) by utilizing KIT-6 as a hard template. They reported the material's BET surface area as 154 m^2/g with a pore-size distribution between 3.7 and 11.5 nm.[15] On the other hand, several soft templating methods have also been employed for the synthesis of mesoporous materials. Zhao *et al.* synthesized mesoporous carbon using a soft template by incorporation of F127 triblock copolymer and polyurethane that has a 660 m^2/g BET surface with 10.2 nm pore size.[16] Humphrey *et al*. fabricated mesoporous Co_3O_4 by utilizing a direct soft templating route. They have obtained a 367 m^2/g BET surface area and a 10 nm pore size diameter.[17] Kim *et al.* have synthesized mesoporous NiO using a unique soft templating method that involves poly(styrene block-acrylic acid-block-ethylene glycol) block copolymer and nickel nitrate precursor. They obtained a mesoporous NiO having 97 m^2/g BET surface area.[18] Dag *et al.* also worked on a unique soft-templating synthesis route for the fabrication of mesoporous transition metal oxide, sulfide, and phosphate thin films.[19]–[28] The films have various BET surface areas and pore size distributions, depending on the type of transition metal salts, triblock copolymer, and solvents. This synthesis method is based on lyotropic liquid

crystalline mesophases and provides homogeneity and high yield of desired products; see later.[19]–[28]

1.1.2 Lyotropic Liquid Crystals (LLC)

Liquid crystal (LC) is defined as a meso-phase in between solid and liquid phases. Thus, they show ordered structures like solids and concurrently, they are fluidic like liquids. They are classified as thermotropic and lyotropic liquid crystals. Thermotropic ones show liquid crystal properties in exact temperature ranges.[29] Lyotropic liquid crystals (LLC) are formed by surfactants that have hydrophilic heads and hydrophobic tails and a solvent. Depending on the solvent hydrophilicity, surfactant chains are aligned and aggregated in the solvent to form micellar structures. When the solvent reaches the exact concentration, micelles assemble to form an ordered structure called LLC or meso-phase. [30] LLCs have larger unit cells because they are formed by large micellar units and could be investigated by X-ray diffraction technique (XRD) at small angles. For their d-spacing, Bragg's equation could be used, see Equation 1.1.

$$n\lambda = 2d \sin\theta \qquad \textbf{Equation 1.1}$$

Where θ is half of the measured angle (°), d is d-spacing (Å), λ is the X-ray wavelength (1.5405 Å) and n is an integer, 1.

Due to the large d-spacing of LLCs, diffractions of mesophase are observed in small theta regions. Thus, small angle XRD analysis is commonly used for the examination of liquid crystal mesophases. In addition to XRD, LLCs could be also investigated under a polarized optical microscope (POM). The hexagonal structure of LLCs could be observed as a texture under POM because they are anisotropic and display focal conic fan texture under POM.[31] In contrast to the hexagonal phase, the cubic phase is dark under POM, because it forms an isotropic structure.[32] The solvent in the LLC mesophase is important and could be water[32], organic solvents[17], [18], ionic liquids[33], and even salts[22] in their molten phases. The molten salts and surfactants assemble into LLC mesophases, depending on the amount of salts, water, and type of counter anions

of the salts.[31], [32] For instance, it was previously demonstrated that an increase in the mole ratio of transition metal salt and surfactant might cause a transformation of LLC mesophase from hexagonal to cubic.[31] In another case, surfactant type might affect LLC mesophase stability.[32]

1.1.3 Molten Salt Assisted Self Assembly Method (MASA)

Dag et al. in 2011, showed a new soft templating method to synthesize mesoporous materials having uniform pore size distribution and high surface area.[27] Soft template in this method includes two types of surfactants that are non-ionic (such as pluronics, P123) and charged (such as cetyltrimethylammonium bromide, CTAB) surfactants. Non-ionic surfactants form micellar structures and charged surfactants also participate in the micelles in the solvent. After the addition of transition metal salt precursor and reaching the exact concentration of the water, the LLC mesophase formation occurs. Hydrophilic parts of charged surfactant cause a charge balance between the micelle interface and salt species in mesophase and it amplifies the stability of the LLCs. MASA method also provides columbic attraction between adjacent micelles and creates confined domains among them. As a result of this assembly process, the salt species reside in molten form among the micelle domains in the mesophase. The molten phase provides high ratios of salt/surfactant systems in LLC mesophases without any salt crystal formation.[27] A Schematic representation of LLC formation using two surfactants is represented in Figure 1.2.

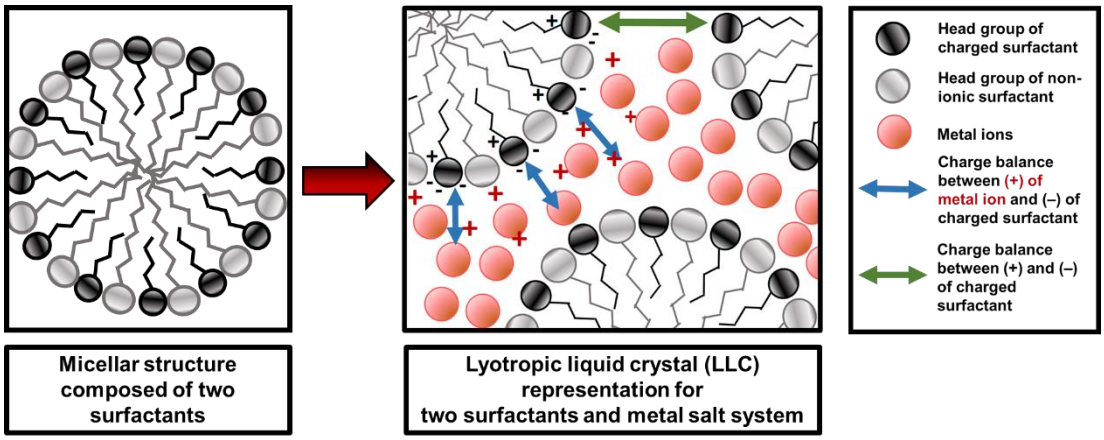

Figure 1.2 Schematic representation of LLC by two surfactants and transition metal salts. (MASA method)

The LLCs obtained by the MASA method could be considered as uniform and homogenous systems to get a high yield of pure mesoporous transition metal oxides.[26] The mesophase is also appropriate for more than one type of salt. This provides flexibility and also opportunities to produce mesoporous mixed metal oxide thin films.[24], [25], [34] The mesoporous films were produced by calcination of these LLC films through effective burning of the surfactant molecules. It yields solid materials containing mesopores surrounded by thin metal oxide walls. Schematic representations of the LLC and mesoporous films are shown in Figure 1.3.

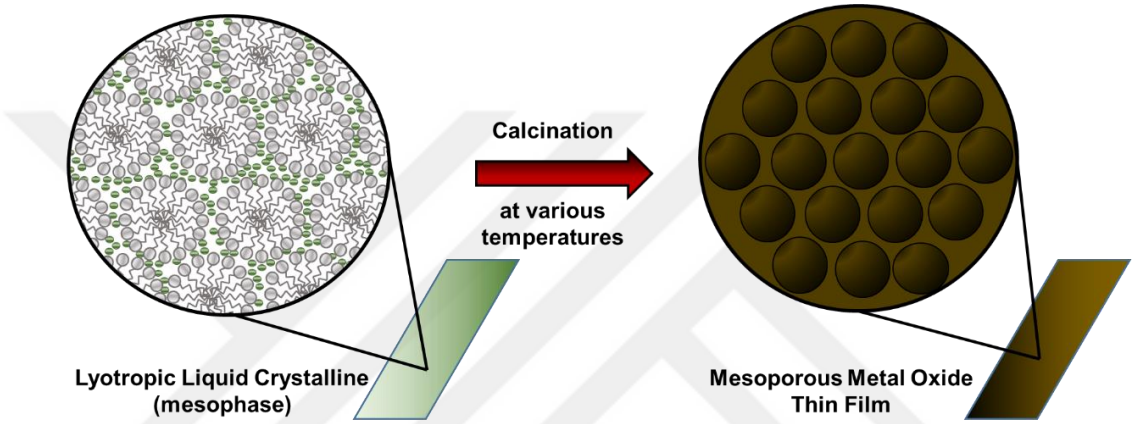

Figure 1.3 Schematic representation of mesoporous metal oxide thin films after calcination of LLC thin film.

Dag research group has synthesized various types of mesoporous transition metal oxides, sulfides, selenides, phosphates, and pyrophosphates by employing the MASA method. In 2011, the first mesoporous ZnO-SiO_2 and CdO-SiO_2 thin films were fabricated using CTAB and 10-lauryl ether surfactants with an 85 and 430 m^2/g BET surface area, respectively.[27] In 2013, they synthesized mesoporous Zn_2TiO_4 and $CdTiO_3$ with around 230 m^2/g surface area. $CdTiO_3$ films can also be reacted with H_2S to produce mesoporous CdS films. Thus, they showed that films fabricated by MASA provide a convenient film interface for an efficient sulfurization reaction.[22] In 2014, mesoporous $MnTiO_3$ and $CoTiO_3$ thin films were fabricated with very high surface areas, such as 445 and 316 m^2/g using transition metal precursors, CTAB and 10-lauryl ether.[35] Lithiated manganese and cobalt oxides have also been fabricated as mesoporous thin films with a BET surface area varying from 50 to 150 m^2/g. Furthermore, these films have also been tested for electrocatalytic oxygen evolution reaction (OER) and

displayed better catalytic performances, compared to their bulk forms. Thus, these investigations show the advantage of mesoporosity of these materials.[25], [28] Mesoporous NiO, $MnCo_2O_4$, $NiCo_2O_4$, and $ZnCo_2O_4$ thin films have been effectively fabricated by the MASA method. Mesoporous binary metal oxides have a higher BET surface area of up to 250 m^2/g. These films have been mainly employed as OER catalysts. Mechanistic and electrocatalytic information could be extracted from these electrochemical investigations since the thin films allow easy, fast, and simple characterization during and after the electrochemical process.[23], [24], [26] Also mesoporous transition metal pyrophosphates have been synthesized by employing the MASA approach. Characterization of these films provided strong evidence for the transformation of phosphate or pyrophosphates into metal hydroxides in alkaline media that has been used in electrochemical measurements.[20]

In conclusion, mesoporous thin films provide many advantages for electrochemical characterization and catalysis due to having high surface area and more active sites. These thin films are commonly fabricated on a conductive substrate and they can be directly used in various applications without any additives. This makes the films easy for simple characterization during and after electrochemical tests.

1.2 Fundamentals of Electrochemical Characterization

1.2.1 Electrochemical Quantitative Analysis of Metal Sites

Cyclic voltammetry (CV) method is used to determine the concentration of redox-active species on the electrode surface. Mostly, species such as H^+, OH^-, and H_2O in electrolytes are adsorbed on the electrode surface and consumed by the redox reaction. In the voltammogram, this is observed as redox peaks. So, the current density of these peaks, from the adsorbed species, is directly dependent on the scan rate and the surface coverage.[36], [37] The relation among the current density of peak (i_p), scan rate (ν), and surface coverage (Γ) is given in equation 1.2.

$$i_p = \frac{n^2 F^2}{4RT} \nu A \Gamma$$ **Equation 1.2**

Where i_p is the current of the peak maxima, n is the number of electron transfer, F is the Faraday constant, 96485 (C mol^{-1}), R is the gas constant, 8.314 J K^{-1} mol^{-1}, T is the temperature (K), ν is the scan rate (V s^{-1}), A is the electrode area (cm^2), Γ is the surface coverage (mol cm^{-2}).

For freely diffusive redox species, the current density is directly dependent on the square root of the scan rate ($\nu^{1/2}$).[37] This behavior could be explained by the Randles-Sevcik equation, shown in equation 1.3.

$$i_p = 0.446\, n\, F\, A\, C^0 \left(\frac{n\, F\, \nu\, D_0}{R\, T}\right)^{1/2}$$ **Equation 1.3**

Where i_p is the current of the peak maxima, n is the number of electron transfer, F is the Faraday constant, 96485 (C mol^{-1}), R is the gas constant, 8.314 J K^{-1} mol^{-1}, T is the temperature (K), ν is the scan rate (V s^{-1}), A is the electrode area (cm^2), D_0 is diffusion coefficient of redox species ($cm^2 s^{-1}$), C_0 is bulk concentration of the electrolyte (mol cm^{-3})

The concept of adsorbed and diffusive species is about surface or bulk electrochemical processes during redox reactions. Notice that, the redox process based on adsorbed species is responsible for only the surface of the active material. This concept is generally valid for double-layer capacitors due to being only surface relation. The quantity extracted from equation 1.2 might be also correlated to catalytically active metal sites since ions to be oxidized or reduced in the electrolyte mostly interact with these active metal sites on the surface. Metal sites are occupied in the bulk of the material and do not interact with electrolyte in this type of redox process. On the other hand, diffusive redox species are based on bulk material. Active metal sites in the bulk material are also reduced or oxidized at exact potential ranges. Ions in the electrolyte could diffuse in the bulk material to compensate the charge (the charge balance in the bulk part) since the interior metal sites are also oxidized or reduced. This redox process is generally valid for battery-type electrochemical reactions.

Quantitative analysis of active species on the electrode's internal and external surface and charge capacity could be obtained from the redox peaks. The amount of charge is directly proportional to the amount of oxidized or reduced species on the electrode.[38], [39] Cyclic voltammetry can be utilized for the calculation of the charge capacity (Q) of an electrode using equation 1.4.

$$Q = \frac{1}{\nu} \int i \, dV \qquad \textbf{Equation 1.4}$$

Where capacity is electrical charge (Coulomb), ν is the scan rate (V s^{-1})

In Equation 1.4, the calculation method for the electrical charge of a faradaic process was demonstrated. The integral of current versus voltage refers to the area under a certain oxidation or reduction peak in the equation. Then, this integration value is divided into scan rate to obtain electrical charge in units of A.s (Coulomb). The charge could be converted into the total electron number involved in the faradaic process. In addition to the CV technique, galvanostatic charge-discharge (GCD) is an alternative method to obtain charge capacity for a faradaic process. In this process, the electrode is charged or discharged with an exact current value. Thus, both faradaic and non-faradaic processes are driven by a constant current at a certain potential range. Charge or discharge time is the experimental result that gives information about the capacity of the active material. The charge of the faradaic process could be easily extracted by multiplying GCD current (A) and time (s) in the Coulomb unit.[40]

Therefore, quantitative analysis of the active sites would provide information about the electrocatalytic reaction efficiency. More active sites on an electrode surface mean more interaction between ionic species in the electrolyte and active metal sites. It implicitly enhances the electrocatalytic reaction rates. Oxygen evolution reaction is one of the important electrocatalytic reactions, which has a strong dependency on the number of active sites on the electrode surface.

1.2.2 Theoretical Aspect of Oxygen Evolution Reaction (OER)

The clean energy demand has increased in recent years because fossil fuel usage has harmful environmental impacts. Hydrogen is one of the clean energy sources and it could be extracted by water reduction. The hydrogen required for the energy could be obtained by using proper electrocatalysts like metal oxides used in water splitting.[41] However, this process requires two electrodes, where both cathodic (water reduction) and anodic (oxygen evolution reaction (OER) or water oxidation reaction) processes take place. It is well-established that the O_2 evolution side of water splitting is found to be kinetically limiting, compared to water reduction, because OER requires multistep electron transfer (4 electrons) besides the 2 electron process of hydrogen evolution reaction (HER). Thus, between these two half reactions, water oxidation is the limitation for hydrogen production.[42]

For a good electrode performance, the following parameters need to be evaluated from the electrochemical data. Equation 1.5 is the Tafel equation, used to evaluate the electrocatalytic activities of electrocatalysts in water splitting and also other catalytic processes. The equation provides information on the kinetics of the catalytic reactions.[36] The logarithm of current (log *i*) is linearly dependent on the overpotential (η), see Equation 1.5.

$$\eta = a + b\,log(i) \qquad \textbf{Equation 1.5}$$

Where η is the overpotential (V), i is the current (A), (alternatively current density, j could be used (A cm^{-2})), b is the Tafel slope (V dec^{-1} or mV dec^{-1}), a is an empirical value.[43]

According to the Tafel equation, in an electrochemical reaction, the logarithm of current density is linearly dependent on overpotential but this linearity depends on a parameter "b" in the equation, known as "Tafel slope". For a good activity of a catalyst, smaller values of the Tafel slope are in demand because a lower overpotential should result in a higher current density. Therefore, a lower Tafel slope is a good indicator of the good activity and efficiency of a catalyst in a reaction.[43]

In the analysis of electro-catalysts, the performance of a material could be also reported as an overpotential during the OER. The required potential is extracted from the Nernst equation directly. The water oxidation reaction is given below [36]:

$$2\,H_2O_{(l)} \rightarrow O_{2_{(g)}} + 4H^+ + 4e^- \qquad E^o = 1.229\,V\ vs\ NHE$$

The Nernst Equation is given in Equation 1.6:

$$E = E^o + \frac{RT}{nF} ln\, P_{O_2} [H^+]^4 \qquad \textbf{Equation 1.6}$$

Where E is the potential (V), E^o is the standard potential (for OER: 1.229 V), R is the gas constant, 8.314 J K^{-1} mol^{-1}, T is the temperature (^oK), n is the number of electrons, F is the Faraday constant, 96485 (C mol^{-1}) , P_{02} is 1 atm.[36]

The theoretical required potential ($E^{theoretical}$) could be found using Equation 1.6. Because of the H^+ ion component, the potential is dependent on the pH of the solution. So, Equation 1.6 can be rewritten as in Equation 1.7.

$$E = 1.229V - 0.059\,pH\ (V\ vs\ NHE) \qquad \textbf{Equation 1.7}$$

The theoretical potential or required energy for OER decreases with increasing pH of the solution. Many metal oxides are used in an alkaline medium with a pH 14 because this pH value brings a potential of 0.404 V vs NHE and also the catalytic reaction involves an OH^- attacking on the surface of metal oxide sides to form O-O bond on the active sides. The extracted potential from Equation 1.7, is the required potential for a perfect catalyst and the system without any resistance, having only a slight diffusion problem. Otherwise, an additional potential, which is called overpotential "η" is required to drive the reaction. The

efficiency of a catalyst in OER is reported in terms of η in the voltage unit at a defined current density. Small overpotential represents a better catalytic performance in electrochemical reactions. The overpotential is obtained from Equation 1.8.

$$\eta = E^{exp} - E^{theoretical} \qquad \textbf{Equation 1.8}$$

Where E^{exp} is experimental potential (V)

1.2.3 Thermodynamic and Electrochemical Diagrams based on Transition Metal Oxidation States and Phases

1.2.3.1 Frost-Ebsworth Diagram

Frost diagram is a plot showing the relation between Gibb's free energy and oxidation states of the electrochemical species. Thus, free energy could be converted to electrochemical potential values.[44] These potential values are attributed to redox voltages for transition from one oxidation state to another. Stabilities and transition potentials of the species are also affected by the pH of the environment. For instance, the specific oxidation state of a chemical specie might be stable in acidic media but doesn't show stability in basic media. Frost diagram of manganese is shown in Figure 1.4.

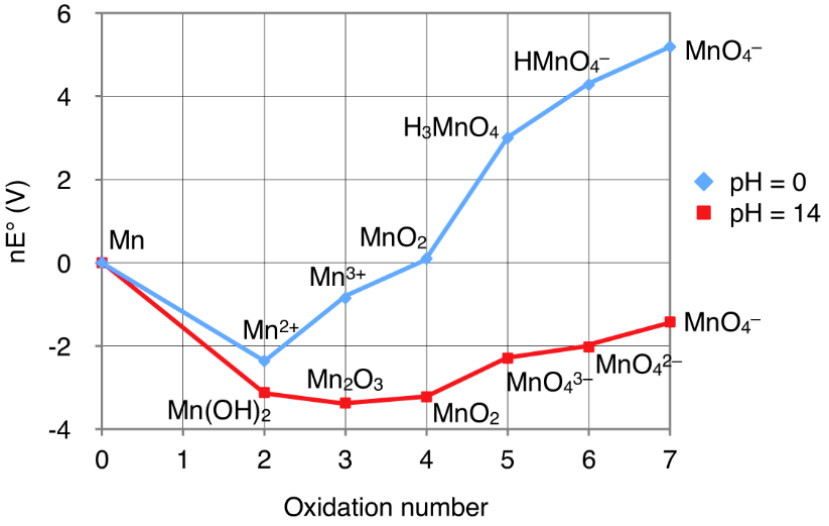

Figure 1.4 Frost-Ebsworth diagram of manganese. *Retrieved from D. Shriver and P. Atkins, Inorganic Chemistry, 5th ed. Oxford University Press, 2010.*

According to the diagram in Figure 1.4, various oxidation states of manganese are shown according to potential values at pH = 0 and pH = 14. The type of manganese species depends on the acidity and basicity of the media. The Frost diagram is used to determine comproportionation and disproportionation reactions of the chemical species. These reactions are identified by hills and valleys on the plot. A hill is obtained when the left slope is steeper than the right slope, and a valley is formed when the right slope is steeper than the left slope. If an oxidation specie is on top of the hill, it favors a disproportionation reaction into the adjacent oxidation states. For instance, in an acidic environment, Mn^{3+} is on the top of the hill and it disproportionates to Mn^{2+} and MnO_2. Two adjacent oxidation states on the edge of the valley favor comproportionation when the middle oxidation state is at the bottom of a valley. For instance, $Mn(OH)_2$ and MnO_2 go through a comproportionation reaction to form Mn_2O_3. By using the Frost diagram one can predict any oxidation state of species whether it goes to disproportionation or comproportionation reaction.

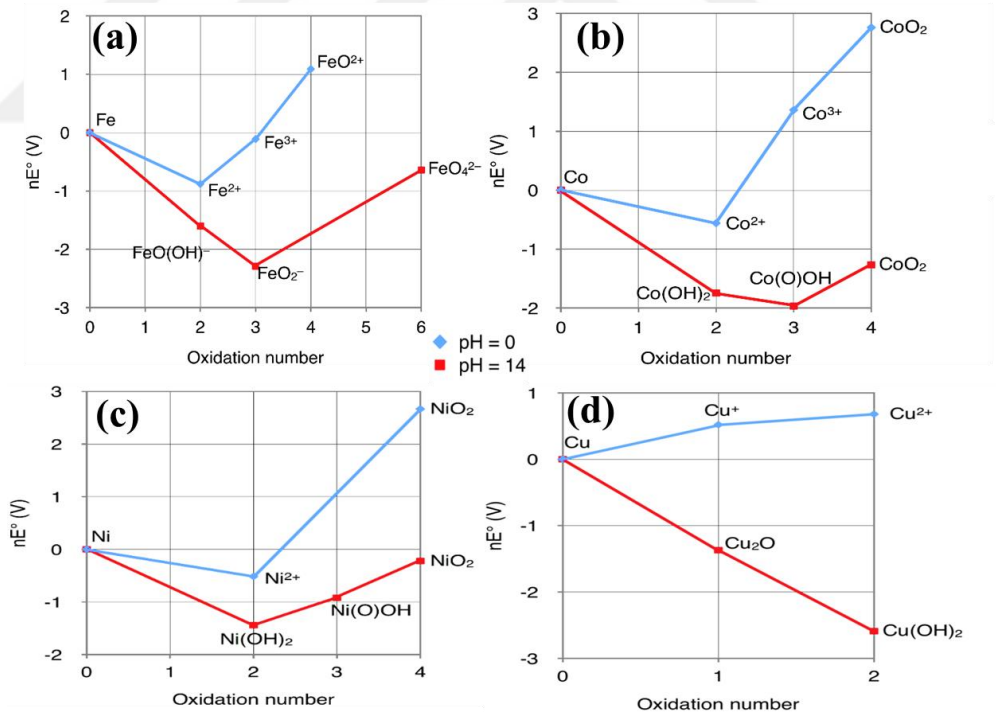

Figure 1.5 Frost-Ebsworth diagram of (a) iron, (b) cobalt, (c) nickel, (d) copper. *Retrieved from D. Shriver and P. Atkins, Inorganic Chemistry, 5th ed. Oxford University Press, 2010.*

According to the Frost diagram of iron in Figure 1.5 (a), Fe^{2+} and FeO^{2+} species undergo comproportionating reaction to form Fe^{3+} species at pH = 0. In

the basic side, one significant comproportionating reaction takes place by $FeO(OH)^-$ and FeO_4^{2-} to FeO_2^- and no disproportionation reaction takes place for iron species. In the Frost diagram of cobalt, see Figure 1.5 (b), the disproportionation reaction between Co^{2+} and CoO_2 into Co^{3+} at pH = 0 and $Co(OH)_2$ and CoO_2 into CoOOH at pH = 14. The nickel Frost diagram is shown in Figure 1.5 (c).

In Frost diagram of nickel, there are two comproportionating reactions. At pH = 0, Ni metal and NiO_2 undergo to Ni^{2+}species. On the alkaline side, $Ni(OH)_2$ and NiO_2 undergo comproportionating into NiOOH. Frost diagram of copper has been shown in Figure 1.5 (d). It is clear that Cu^+ disproportionates into Cu metal and Cu^{2+} at pH = 0 according to the diagram. At pH = 14, there are no explicit comproportionation or disproportionation reactions of copper species.

1.2.3.2 Pourbaix Diagram

The Pourbaix diagram is a plot to show the thermodynamic stability of phases at an exact potential range and pH value in an electrochemical system. The Pourbaix diagram of manganese is shown in Figure 1.6.

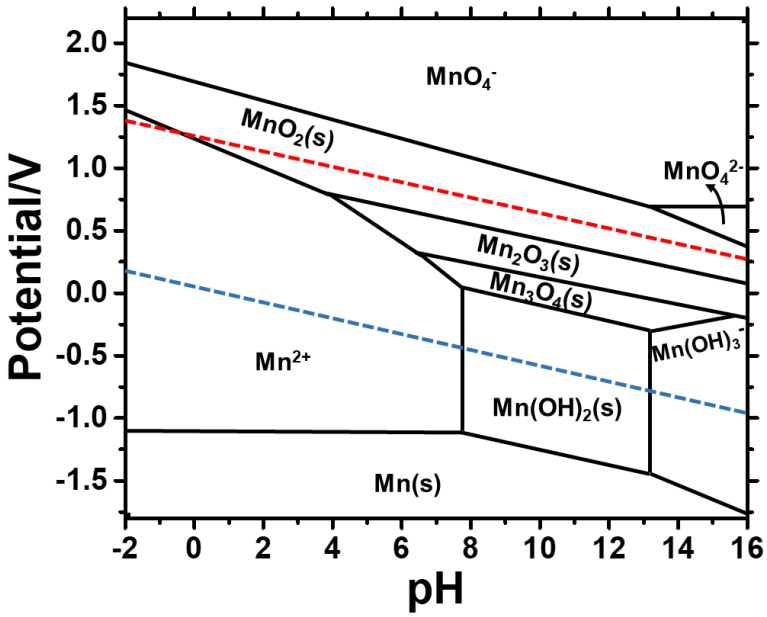

Figure 1.6 Pourbaix diagram of manganese.

Manganese is one of the unique transition metals that has many oxidation states and phases and is also one of the most abundant elements in the earth

crust. Figure 1.6 shows these diversities of the manganese oxidation states and phases in terms of pH and potential values. At higher potential values, manganese prefers the formation of permanganate ions. The formation mechanism will be explained by a disproportionation reaction of the manganate ion, in the next sessions. Furthermore, the phase conversions follow different paths in acidic and basic environments. Notice that on the basic side, $Mn(OH)_2$ formation is favored and it is gradually oxidized to Mn_3O_4, Mn_2O_3, and MnO_2. On the acidic side, manganese prefers to be Mn^{2+} in a very wide potential window.

According to the Pourbaix diagram shown in Figure 1.7 (a), iron also forms $[FeO_4]^{2-}$ anion at higher potentials. There is a significant difference compared to the manganese case. The $[MnO_4]^{2-}$ ion undergoes a disproportionation reaction to form MnO_2 and $[MnO_4]^-$ ion. However, Fe^{3+} or Fe_2O_3 directly goes to $[FeO_4]^{2-}$ ion by an oxidation process. As a result, iron content on the electrode surface might be lost by the formation of this ion at higher potentials.

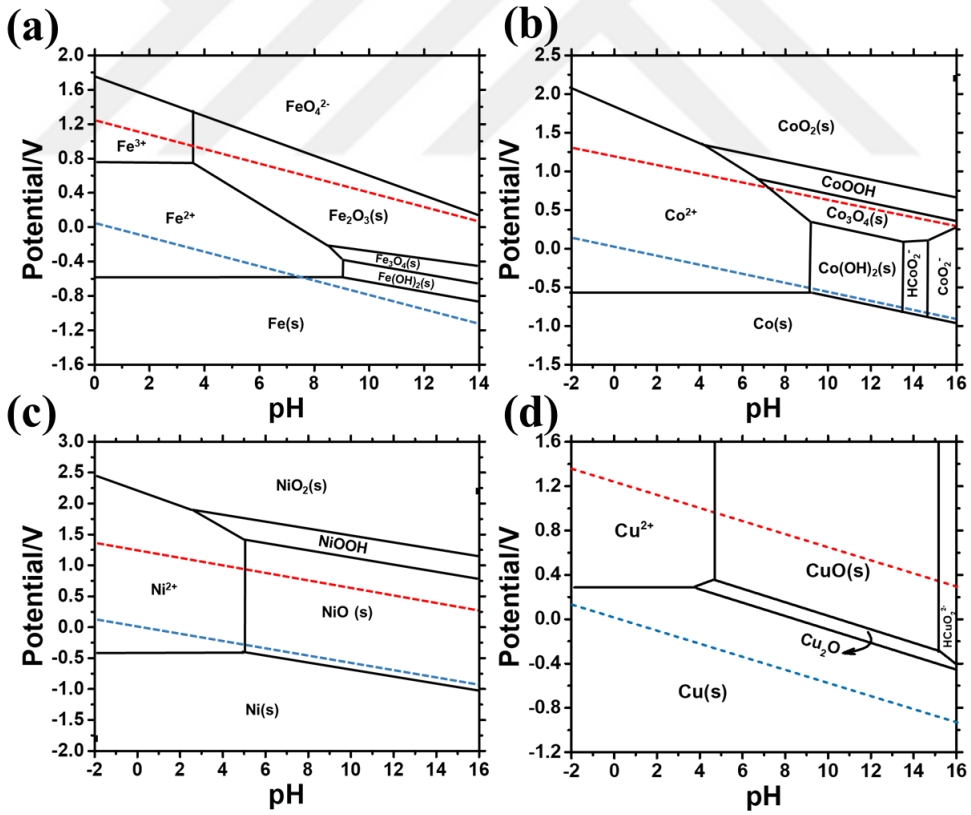

Figure 1.7 Pourbaix diagrams of (a) iron, (b) cobalt, (c) nickel, and (d) copper.

According to the Pourbaix diagram of cobalt shown in Figure 1.7 (b), $Co(OH)_2$ and Co_3O_4 species are favored at high pH values and lower

potentials.[45] At higher voltages, these species theoretically are converted to CoOOH in an alkaline environment. Notice that manganese and iron showed disproportionation at very high potentials and showed ionic features such as $[MnO_4]^-$ and $[FeO_4]^{2-}$. However, cobalt doesn't show any disproportionation due to Co(IV) in CoO_2 form.

According to the Pourbaix diagram of nickel in Figure 1.7 (c), NiOOH formation is favored at high potentials.[46] Similar to cobalt, nickel has no disproportionation behavior due to NiO_2 formation. However, nickel Pourbaix diagrams in literature are still inconsistent with each other. This is expected because NiOOH is favorably reduced to $Ni(OH)_2$ demonstrated in many works. Most of the Pourbaix diagram shows NiO is the main phase rather than $Ni(OH)_2$. Notice that copper has no disproportionation reaction at high potentials, see Figure 1.7 (d). CuO formation is favored at high potentials showing that copper could reach Cu(II) as the highest oxidation state.[47]

1.2.4 Electrochemical Disproportionation Mechanisms of Manganese

According to the Frost and Pourbaix diagrams of manganese, there are two disproportionation reactions that have a significant effect on the degradation of manganese species on the electrode surface. The first one is the Mn(III) disproportionation reaction into Mn(II) and MnO_2. The complete disproportionation reaction of Mn(III) is given in equation 1.9.

$$2Mn^{3+} + 2H_2O \rightarrow Mn^{2+} + MnO_2 + 4H^+ \qquad \textbf{Equation 1.9}$$

Mn(III) disproportionation reaction explains the degradation mechanism of the manganese-based electrodes. Two Mn(III) species undergo disproportionation into Mn(II) and Mn(IV) as MnO_2. In this process water is consumed and hydronium concentration on the electrode surface amplifies.[48], [49] Thus, half of the manganese content on the surface is dissolved as ionic Mn(II), and half of it is re-deposited on the surface as MnO_2.

Secondly, manganese also has a disproportionation reaction at higher potentials, these voltage range is generally overlapped with catalytic water oxidation reaction. Therefore, observation of faradaic peaks of manganese oxidation and reduction reactions to Mn(V), Mn(VI), and Mn(VII) is impossible since high OER faradaic current masks the oxidation peaks of manganese species. The second disproportionation reaction of manganese is given in equation 1.10.

$$3MnO_4^{2-} + 4H^+ \rightarrow 2MnO_4^- + MnO_2 + 2H_2O \qquad \textbf{Equation 1.10}$$

In the disproportionation reaction mechanism, three manganates (MnO_4^{2-}) are converted into two permanganates (MnO_4^-) and a MnO_2. [50], [51] Thus MnO_2 might be deposited on the electrode surface besides permanganate ion formation causing a decay of the manganese content by dissociation into the electrolyte. In 2024, we comprehensively investigated Mn(VI) disproportionation mechanisms with various polymorphs of manganese oxides in different electrolytes (see later). The type of manganese oxide affects the Mn(VI) disproportionation rate and degradation could be diminished by using the proper polymorph of Mn_xO_y. They also showed that cation type in the electrolyte plays a role in disproportionation reaction by utilizing some quantitative analysis.[52]

1.2.5 Mechanistic Insight of Oxygen Evolution Electrocatalysis

In the OER mechanism suggested in this work is based on the nucleophilic acid-base reaction, which includes the nucleophilic attack of OH^- to the oxygen of metal-oxo (M=O) species. The activity and electrophilicity of the M=O sites on the surface may be enhanced by incorporating more electronegative transition metals into the spinel crystal structure.[24] Thus, the formation of M=O is a critical step for the formation of required intermediates for OER mechanisms such as M-OOH, O_2^-, and O_2 desorbs from active metal sites, sequentially. The electronegativity difference between two metals enhances the formation of M=O since a metal having higher electronegativity pulls the electron density on the

neighboring metal side to itself, where the neighboring metal ion is oxidized. By hydrogen transport between the two coordinated OH species on metal sites, the M=O formation is favored on the surface, where the neighboring metal ion has a lower electronegativity.[34]

Manganese-based catalysts might be considered as alternatives for OER electrocatalysts due to the high abundance and less toxicity of manganese among other 1st row transition metals. Manganese sites on the electrode surface could bear several oxidation states and it provides unique electrocatalytic sides for likely OER mechanisms on the electrode surface. It is hard to demonstrate the certain oxidation states of manganese during OER catalysis on the electrode surface. There are investigations in the literature that show the surface Mn=O formation during the OER process.[53] In 2019, Nakamura et al. reported that MnO_2 formed in an acidic medium from MnO_4^- that is produced at high onset potentials. They have shown the formation of the permanganate ion in the electrolyte solution by observing an intense pink color and characteristic permanganate UV-Vis spectrum.[54] Sun et al. showed that the Mn(VII)=O intermediate for the catalytic OER process by FTIR spectroscopy. The electrode prepared under a neutral environment displayed a metal oxygen stretching band at around 600 cm^{-1} that shifts to a higher frequency, to around 912 cm^{-1} due to a Mn=O double bond formation. In addition to that, they also observed an amplification of the 912 cm^{-1} peak upon using the electrode at higher potentials.[55] These investigations and the Mn=O generation during the OER process on the electrode surface help suggest an OER mechanism on the electrode surface. We believe that these active manganese species are the likely species for an efficient OER electrocatalysis which was shown in the suggested OER mechanism in our previous work.[34]

1.3 Manganese-based Oxides as Energy Storage Materials and Oxygen Evolution Electrocatalysts

Transition metal oxides have been investigated in recent years for various energy storage and catalytic reactions. Catalytic properties and stabilities, under

experimental conditions, could be different for each transition metal due to distinctive features. A metal oxide having only one type of metal could work well in certain catalytic reactions and contrarily it couldn't show great efficiency for other applications. Manganese is one of the candidates to fabricate cost-effective and environmentally safe electrodes due to its higher abundance and non-toxicity.[56] It has also a significant drawback for energy applications such as Mn(III) and Mn(VI) disproportionation that leads to fast degradation of the electrodes. Thus, the addition of other transition metals such as Fe, Co, and Ni into manganese-based electrodes might provide durability to the electrodes during the OER process. Also, the synergistic electronic effect between manganese and the other metal sites might enhance the catalytic efficiencies of the electrodes.[24]

1.3.1 Manganese Oxides as Energy Storage Materials and Oxygen Evolution Reaction Electrocatalysts

Manganese oxides are preferred in several applications such as batteries, supercapacitors, and various types of catalytic oxidation and reduction reactions due to their low toxicity and higher abundance. There are numerous works on electrochemical applications of manganese oxides and these materials have been synthesized using several different methods to control surface areas and morphologies.

In 2007, Li and coworkers, synthesized mesoporous MnO_2 utilizing electrodeposition of MnO_2 in electrolytes containing triblock copolymers. Two different surfactants, namely P123 and F127, were used in the self-assembly process in the electrodeposition. The pore size between the MnO_2 particles was measured to be around 4 nm for both templates with slightly different morphologies. Calcined MnO_2 electrodes were tested in terms of charge storage in 0.5 M Na_2SO_4 electrolytes in three electrodes system and resulted in a specific capacitance of 377 F/g for P123 and 449 F/g for F127 templates.[57] Li *et al.* in 2011, synthesized α-MnO_2 bearing particles with an average size of 5 nm. They utilized the reduction of permanganate ions in an ascorbic acid (AA) rich environment to produce a mesoporous structure. At the optimized molar ratio between $KMnO_4$ and AA, they calcined the precursor and obtained α-MnO_2 with

a surface area of 284 m^2/g. Then, the electrode was tested in a 0.5 Na_2SO_4 solution using a three electrodes setup that resulted in 200 F/g specific capacitance. An actual capacitor test was also performed using activated carbon as the negative electrode and MnO_2 as the positive electrode which yielded 23 F/g specific capacitance.[58] In 2013, Wang and coworkers worked on mesoporous MnO_2 and synthesized their materials using a precursor containing P123. They desired to control morphologies of MnO_2 particles with the addition of alkali salts, Na_2CO_3, $NaHCO_3$, and NaOH into the mixture followed by precipitation and calcination processes. They reached a maximum surface area (263 m^2/g) of MnO_2 with around 4.9 nm pore size when Na_2CO_3 was utilized in the precipitation process. Then they tested these manganese dioxide types for charge storage in 1 M Na_2SO_4 solution. Material having the highest surface area gave 172 F/g specific capacitance and they also claimed that surface areas of the MnO_2 electrodes directly affected the specific capacitance values in electrochemical measurements.[59] Nandi *et al.* in 2020, fabricated MnO_2 electrodes using mesoporous silica hard template and they could synthesize mesoporous MnO_2 with a surface area of 453 m^2/g and pore size of 3.6 nm. They found its specific capacitance as 1158 F/g in 1 M Na_2SO_4 electrolyte.[60]

Mesoporous MnO_x electrodes have also been investigated for battery applications. In 2018, Ramesha and coworkers worked on hard-templated mesoporous β-MnO_2 as an anode material for Li-ion battery application. For both SBA-15 and MCM-48 templates, they obtained 28 m^2/g surface areas with pore diameters of 8.9 and 6.2 nm, respectively. Discharge capacity values were reported as 1291 mAh/g for SBA-15 and 1450 mAh/g for MCM-48 templates in the 1st GCD cycle. After several GCD cycles, they observed discharge capacity sequentially diminished to 245 mAh/g and 345 mAh/g, respectively. [61] Yoon *et al.* in 2021, synthesized mesoporous MnO_2 as anode material for Li-ion batteries. They utilized a hard templating method and focused on mesoporous silica named KIT-6. After BET estimation, they found 111 m^2/g surface area and approximately 3 nm particle size. According to Li-ion battery tests, 1361 mAh/g capacity could be obtained when the electrode was used as anode material.[62]

In addition to energy storage applications, manganese oxides have also been used in electrocatalytic reactions mainly for oxygen evolution reaction (OER). Suib and coworkers, synthesized mesoporous Mn_2O_3 electrodes using the Pluronic P123 containing sol-gel method. Then, surface area alterations on electrodes were investigated according to the annealing temperatures of the materials. At 450 ^oC, the surface area of the crystalline material was found 150 m^2/g with a 4.3 nm pore diameter. Then the electrode was tested in robust OER electrocatalysis in 0.1M KOH and it gave 507 mV overpotential at 10 mA/cm^2.[63] Colavita *et al.* also worked on mesoporous manganese oxides and utilized a template-free synthesis method using acetate salt of manganese followed by solvothermal synthesis. After annealing the material, mesoporous Mn_2O_3 electrodes were obtained with a 109 m^2/g surface area and 10 nm pore sizes. After testing the electrode in the electrocatalytic OER process with an overpotential of 427 mV at 10 mA/cm^2 in 1M NaOH electrolyte.[64] Besides soft synthesis methods, Kumar and coworkers worked on mesoporous MnO_2 electrocatalysts synthesized by hard-templating method. They used four types of mesoporous silica templates namely SBA-15, KIT-6, MCM-41, and MCM-48, and compared the surface areas of the manganese oxides produced by these templates. They found that KIT-6 resulted in a higher surface area of 50 m^2/g with 6.2 nm pores diameter. The electrode was tested in 0.1M KOH electrolyte for OER and it yielded a 60 mV/dec Tafel slope. In the linear sweep voltammogram of the electrode, 10 mA/cm^2 current density was reached at 1.84 V vs RHE which approximately corresponds to 450 mV overpotential at 10 mA.[65]

Spinel lithiated manganese oxides are also considered one of the promising candidates for energy storage applications due to the easy oxidation and reduction process of Mn(III) and Mn(IV) species that provide reversible lithiation and delithiation. This redox process takes place in bulk materials. Thus, high charge densities could be reached and these are mostly used as cathode materials in lithium-ion batteries. There are numerous works on bulk $LiMn_2O_4$ cathodes. However, reducing the size of the particles in these types of materials shortens the diffusion path of the lithium, and the power densities of the materials become more efficient compared to bulk versions.[66] In 2007, Xia *et al*. synthesized mesoporous $LiMn_2O_4$ by hard-templating technique. Mesoporous

silica KIT-6 had been employed and it yielded a mesoporous $LiMn_2O_4$ with 55 m^2/g surface area with pore size distributions centered at both 5 and 18 nm. Then, the mesoporous material was used as a cathode in battery application in a non-aqueous $LiPF_6$ solution which yielded 70 mAh/g. When the mesoporous $LiMn_2O_4$ was compared with the commercial one, capacity retention of the mesoporous type was found to be less and the electrode could still maintain 94% of the initial capacity even when the electrode was cycled 500 times.[67] Bruce *et al.* also worked on the mesoporous $LiMn_2O_4$ employing the hard templating method. KIT-6 template was used and 90 m^2/g surface area was obtained with 7 nm wall thickness of the particles. After GCD curves, the discharge capacity of the mesoporous $LiMn_2O_4$ was determined to be around 70 mAh/g. Slower degradation in capacity during cycling was also demonstrated in the study.[68] In 2016, Chen and coworkers studied mesoporous lithiated manganese oxides synthesized by soft-template containing Pluronic 123. The surface area of mesoporous $LiMn_2O_4$ was found to be 44 m^2/g with around 5 nm pore size. Then, the electrode was used in the GCD experiment and 118.8 mAh/g capacity was obtained at slow charging experiments in $LiPF_6$ electrolyte. The work also showed that the mesoporous cathode materials could bear higher capacities compared to bulk materials.[66].

In addition to the charge storage feature, the electrocatalytic OER performance of $LiMn_2O_4$ was also investigated. Commonly, bulkier types of $LiMn_2O_4$ were studied in the catalytic reactions. It is commonly known that lithium could be extracted from the $LiMn_2O_4$ matrix electrochemically or chemically. In an alkaline environment, $LiMn_2O_4$ is converted into λ-MnO_2 at OER potential ranges.[52] Thus, λ-MnO_2 structure is critical for efficient OER. In 2013, Dismukes *et al.* worked on various polymorphs of manganese oxides and they found that λ-MnO_2 was one of the promising polymorphs for OER electrocatalysis.[69] There are a couple of works based on $LiMn_2O_4$ electrodes tested in the OER process. However, materials were synthesized in macro sizes that yielded lower surface areas. The $LiMn_2O_4$ electrodes resulted in a Tafel slope of between 89 and 139 mV/dec in alkaline electrolytes. [70], [71] In 2018, we synthesized mesoporous $LiMn_2O_4$ thin films by a soft-templating method. We reported the film with 98 m^2/g surface area and 11 nm average pore size. Then

the electrode was used in long-term OER electrocatalysis. The Tafel slope of mesoporous $LiMn_2O_4$ was found to be 124 mV/dec with an overpotential of 525 mV at 1 mA/cm^2 current density.[25]

For manganese-based electrodes, degradation of the active material is commonly inevitable due to manganese nature. In energy storage and battery tests, manganese species undergo Mn(III) disproportionation. Two Mn(III) species disproportionate into Mn(II) and Mn(IV) causing loss of ionic Mn(II) content where Mn(IV) is re-deposited on electrode surface as MnO_2.[72]–[75] In addition to Mn (III) disproportionation, there are indirect problems such as structural destruction due to Jahn Teller distortion, deposition of Mn(II) on the anode surface, and, inactive Mn_3O_4 formation on the cathode surface that brings capacity fading for both battery and energy storage applications.[76]–[78] To overcome the degradation issue of manganese, many works have been devoted. Song and coworkers focused on electrolytes used in the electrochemical cells. They used metal-ion-chelating organogel electrolytes and suppressed the Mn(III) disproportionation by chelating Mn (II) ions on the cathode surface. By enriching Mn(II) species on the cathode surface, much Mn (II) dispersion is prevented supported by the Le Chatelier principle.[79] Liu *et al.* worked on the "mild electrolyte" field by pre-addition of Mn^{2+} into the electrolyte. Thus, they provided reversible Mn(II)/MnO_2 by this addition and showed that specific capacity was almost the same even after 5000 cycles.[80] Liu and coworkers focused on anionic substitution into manganese dioxide electrodes to adjust the electronic affinity of the electrode. They suggested that manganese sites by much electronegative F^- adjacent sites and claimed suppression of Mn(III) formation. They also showed that the capacity retention of the substituted electrode was quite small by cycling the electrode up to 100000 times.[81] Wang *et al.* showed cobalt substitution into a manganese oxide matrix to prevent degradation of the electrodes. They found that capacity retention was 80% after 1000 cycles for cobalt-doped electrodes and compared the electrode with non-doped manganese oxides. The capacity of the doped manganese oxide was found to be more compared to a typical manganese oxide.[82] Niu *et al.* worked on morphological features of the electrodes to diminish capacity retention during electrochemical cycling. They synthesized their oxides as quantum dots on a porous carbon

framework and claimed that the Mn-O-C bond on the interface might diminish the Jahn Teller effect and disproportionation. After electrochemical cycling experiments, they found that capacity retention is almost 86% after 1500 cycles.[83]

For OER, Mn(VI) disproportionation reaction takes place where three Mn(VI) undergo one Mn(IV) and two Mn(VII) species. Mn(VII) is responsible for the degradation of active metal sites by the generation of permanganate (MnO_4^-) ions. There are a couple of studies demonstrating the dispersion of permanganate into the electrolyte that causes catalytic instabilities of the electrodes. They only highlighted permanganate formation at certain potential values and degradations of manganese sites on the electrode surfaces.[71], [84], [85]

1.3.2 Manganese-based Bimetallic Oxides as Energy Storage and Oxygen Evolution Reaction Electrocatalysts

Many recent works focus on catalytic reactions based on mixed transition metal oxides in the literature. These metal oxides could include two or more transition metals to enhance the catalytic efficiencies compared to mono-metallic oxides. The reason of the catalytic enhancement is considered as a synergistic effect between two or multiple transition metal species. This synergistic effect could be thought of as an electronic interaction due to the electronegativity difference between transition metals. There are many works on mixing transition metals in one system and they reported the enhancement of catalytic activities for mixed oxides by comparing single transition metal oxide materials. [24], [86]

Several types of manganese-based bimetallic oxides have been synthesized for various applications such as energy storage and electrocatalysis of various compounds. Water oxidation (OER) is one of the significant electrocatalytic reactions for these types of oxide materials. Among other transition metals, 1st row transition metal integration into a manganese oxide matrix could lead to some advantages in the OER process. They are more abundant on earth-crust compared to other transition metals which results in reasonable prices.[56] Secondly, the degradation of manganese-based oxides could be diminished with the addition of trace amounts of other 1st row transition

metals.[34] Note that the electrocatalytic OER takes place on the surface of the electrodes and only surface metal species are responsible for catalysis. It brings a fabrication approach to these materials based on a synthesis of mesoporous forms. Porosity in these oxides brings higher surface areas which may provide more interaction between active metal sites and aqueous solution for electrolysis.

Iron manganese oxides were synthesized in bulk and mesoporous forms for an efficient and stable OER process. Gao *et al.* synthesized porous $FeMn_2O_4$ particles with approximately 50 m^2/g. Then, they showed an annealing effect on the surface area of the materials by increasing the temperature which resulted in a decrease in surface area. Then these electrodes were used in OER experiments in 1 M KOH and they reported material, calcined at 500 ^oC, is better among other temperatures with a 105 mV/dec Tafel slope and 360 mV overpotential at 10 mA/cm^2 current density.[87] Gao and coworkers also did surface construction of the porous $FeMn_2O_4$ by a simple cooling procedure that provides surface distortion of $FeMn_2O_4$ particles. They demonstrated the particles with around 200 nm size and surface area was reported as 45 m^2/g. After testing electrochemical properties in 1 M KOH, the distorted structure of $FeMn_2O_4$ gave higher double-layer capacitance, 9.21 mF/cm^2 which was a comparable number concerning non-distorted $FeMn_2O_4$ (2.61 mF/g).[88] In 2023 Peng *et al.* fabricated a porous $FeMn_2O_4$ electrode on nickel foam by hydrothermal treatment of manganese and iron precursors. These electrodes were tested electrochemically under a magnetic field. They showed that the double layer capacitance of the electrode enhanced from 13.2 mF/cm^2 to 29.9 mF/cm^2 when a 105 mT magnetic field was applied. Magnetic field effect was also demonstrated in electrocatalytic OER performances in 1 M KOH. Tafel slope also decreased from 71.8 mV/dec to 50.0 mV/dec after applying a 105 mT magnetic field. This enhancement of OER efficiency was also demonstrated by decreasing overpotential value at 20 mA/cm^2. Before applying the magnetic field, 317 mV overpotential was reported. When 105 mT magnetic field, the overpotential of $FeMn_2O_4$ was reported as 274 mV at 20 mA/cm^2.[89]

Cobalt-substituted manganese oxide electrodes were also fabricated as porous to enhance catalytic OER activities. Driess and coworkers investigated

porous $CoMn_2O_4$ electrodes by synthesizing them with the calcination of precursors including acetate salts of manganese and cobalt. Oxide materials were synthesized as spheres having diameters between 2 and 4 μm and these spheres consisted of smaller particles with sizes between 70 and 120 nm. After electrochemical analysis in 0.1 M KOH electrolyte, porous $CoMn_2O_4$ yielded a Tafel slope of 64 mV/dec and 600 mV overpotential at 10 mA/cm^2 current density.[90] Chen *et al.* fabricated ultra-small and monodispersed $CoMn_2O_4$ nanodots for efficient OER electrocatalysis on reduced graphene oxide. The average pore size of the material was estimated at 3.7 nm (BJH method) with a BET surface area of 412 m^2/g. OER catalytic property of the composite was obtained in 0.1 M KOH. Tafel slope was reported as 56 mV/dec and the potential for 10 mA/cm^2 was reported as 1.5 V vs RHE from the LSV curve.[91] Du *et al.* synthesized $CoMn_2O_4$ on carbon fiber. They did a thermal treatment on the $CoMn_2O_4$ to see the effect of particle size on OER efficiencies. Inherently, an increase in annealing temperature increased the $CoMn_2O_4$ particle sizes from 20 to 60 nm. Then, electrochemical tests were performed in 1M KOH electrolyte using a three-electrode cell. Tafel slope of $CoMn_2O_4$ at 400 ^{o}C is 124 mV/dec with a 393 mV overpotential at 10 mA/cm^2. At an annealing temperature higher than 400 ^{o}C, the Tafel slope decreased to 90 mV/dec. Also, the overpotential decreased to 337 mV after heat treatment.[92] Huang and coworkers also worked on $CoMn_2O_4$ anchored on carbon nanotubes. By SEM imaging, the size of the $CoMn_2O_4$ particles was reported as around 5 nm. The overpotential was determined as 560 mV at 10 mA/cm^2 current density in a 0.1 M KOH solution for OER.[93]

Manganese and nickel-based electrodes were also electrochemically investigated in various applications mainly for energy storage. Liu *et al.* worked on mesoporous $NiMn_2O_4$ electrodes as cathode materials for capacity applications. They synthesized $NiMn_2O_4$ by sol-gel method using a mixture of metal salts, citric acid, and propylene oxide followed by annealing at various temperatures. At 300 and 400 ^{o}C, they obtained 201 and 181 m^2/g surface areas, respectively, with 8-10 nm pore diameters. They tested their charge-discharge efficiencies in 1 M Na_2SO_4 and recorded the highest capacitance value as 243 F/g for mesoporous $NiMn_2O_4$ annealed at 300^{o}C.[94] Das and coworkers also worked

on a sol-gel method to synthesize mesoporous $NiMn_2O_4$ bearing high surface area. They used acetate salts of manganese and nickel followed by mixing them with ethylene glycol and poly (vinyl pyrrolidone) (PVP). After calcination at 400°C, the BET surface area of the $NiMn_2O_4$ was estimated as 43 m^2/g with an average pore size distribution of 13 nm. They tested the electrodes in 1 M Na_2SO_4 and found the capacitance value as 875 F/g.[95] The same research group also synthesized mesoporous $NiMn_2O_4$ electrodes hydrothermally employing the sol-gel method with the addition of charge surfactants CTAB and SDS. BET surface areas were estimated at 36 and 59 m^2/g for CTAB and SDS precursors, respectively. The average pore diameter was reported as 10 nm for CTAB and 4.5 nm for SDS-based synthesis. Then, they used mesoporous $NiMn_2O_4$ fabricated by SDS surfactant in GCD measurements in 1 M Na_2SO_4 and reported 1880 F/g specific capacitance in slower charge-discharge current densities.[96] In 2019, Zignani and coworkers fabricated $NiMn_2O_4$ on carbon nanofibers by electrospinning technique. They reported the BET surface area of the composite as 193 m^2/g having an average $NiMn_2O_4$ particle size of 20 nm. They tested the electrode OER performance in 6 M KOH electrolyte and showed that a 181 mA/cm^2 current density might be reached at 1.8 V vs RHE.[97] Shim *et al.* showed OER electrocatalysis based on $NiMn_2O_4$ electrodes fabricated on nickel foam. They specifically focused on microwave synthesis at various temperatures that yielded nanosheets and nanospheres formations. The electrocatalytic properties for both OER and HER sides in 1M KOH were tested and they reported 248 mV overpotential at -10 mA/cm^2 in HER electrocatalysis and 198 mV/dec Tafel slope. For OER studies, they reached a 250 mV overpotential value at 10 mA/cm^2. Tafel slope in OER catalysis was reported as 218 mV/dec. For overall water splitting, they used their $NiMn_2O_4$ electrodes for both anode and cathode parts and constructed the cell that provides 10 mA/cm^2 current density at 1.69 V for the overall water splitting process.[98]

Copper-based manganese oxides are also promising candidates for energy applications due to their earth crust abundance, costs, and environmental safeness. There are few works on manganese-based copper oxides in energy applications. Luo *et al.* worked on $CuMn_2O_4$ anchored on graphene nanosheets as the electrode for a supercapacitor application. [99] The $CuMn_2O_4$ was

synthesized via the sol-gel method by mixing acetate salts of metals and poly (vinylpyrrolidone) followed by a thermal treatment. Anchoring of the material on graphene was done by a physical grinding method. BET surface area of the composite was found as 144 m^2/g. The charge storage capacity of the electrode was tested in 1 M Na_2SO_4. The specific capacitance of the material was reported as 342 F/g from GCD data.[99] Abruna and Fang worked on $CuMn_2O_4$ nanocatalysts to investigate oxygen reduction reaction (ORR) efficiencies in alkaline media.[100] They synthesized two morphologies of the particles: nanospheres and nano octahedrons. Thus, they showed the morphology effect of the nanoparticles on ORR. In 1 M KOH, they reported that the mass activity of octahedrons (37.6 A/g) was higher than spherical particles (23.2 A/g) at 0.85 V vs RHE.[100] Cho and coworkers worked on defect-rich $CuMn_2O_4$ nanoparticles to investigate the effect of defective surface on electrocatalytic OER properties in 1M KOH. [101] Non-defected particles resulted in 517 mV overpotential at 10 mA/cm^2 whereas the defected particles yielded 406 mV overpotential at the same current density. Tafel slopes of the electrodes also correlated with the OER behavior of the electrodes by providing an improved Tafel slope of 196 mV/dec and 135 mV/dec for the non-defected and defected nanoparticles, respectively.[101]

1.3.3 Synergistic Effect of Neighboring Metal Ion in the Surface Structure of Active Metal Side

Water splitting (OER) stands as a fundamental catalytic reaction for electrochemical energy conversion. Transition metals and their oxides are promising candidates for OER electrocatalysis due to their high earth abundance, low cost, and tunable features. Many studies have shown that bimetallic oxide catalysts are more efficient in OER electrocatalysis, compared to their monometallic oxide forms. The synergistic effect between two metal sites adjusts the electronic properties of the catalyst surface and enhances not only electrocatalytic OER performance[102]–[109], but also other electrochemical properties.[110]–[114].

In the literature, there are many investigations towards estimating the rate-determining step (RDS) of the OER in an alkaline media. Many experimental

studies and DFT calculations have demonstrated that M-OOH formation is the RDS; thus, attacking OH^- species to active oxygen sites on the electrode surfaces plays a critical role in enhancing the rate of OER.[107]–[109] There are some general suggestions on how the OER rate can be enhanced by the integration of two metals in oxides through variation in electronic structure, intermediate stabilization, and charge transfer.[102] Also, the electronegativity difference between the two metal sites on the electrode surface plays a vital role in the OER rate. We also suggested an OER mechanism based on the presence of Mn and Co sites on the oxide surface and explained using the electronegativity difference as a consequence synergistic effect.[34] A schematic representation of the mechanism is shown in Figure 1.8.

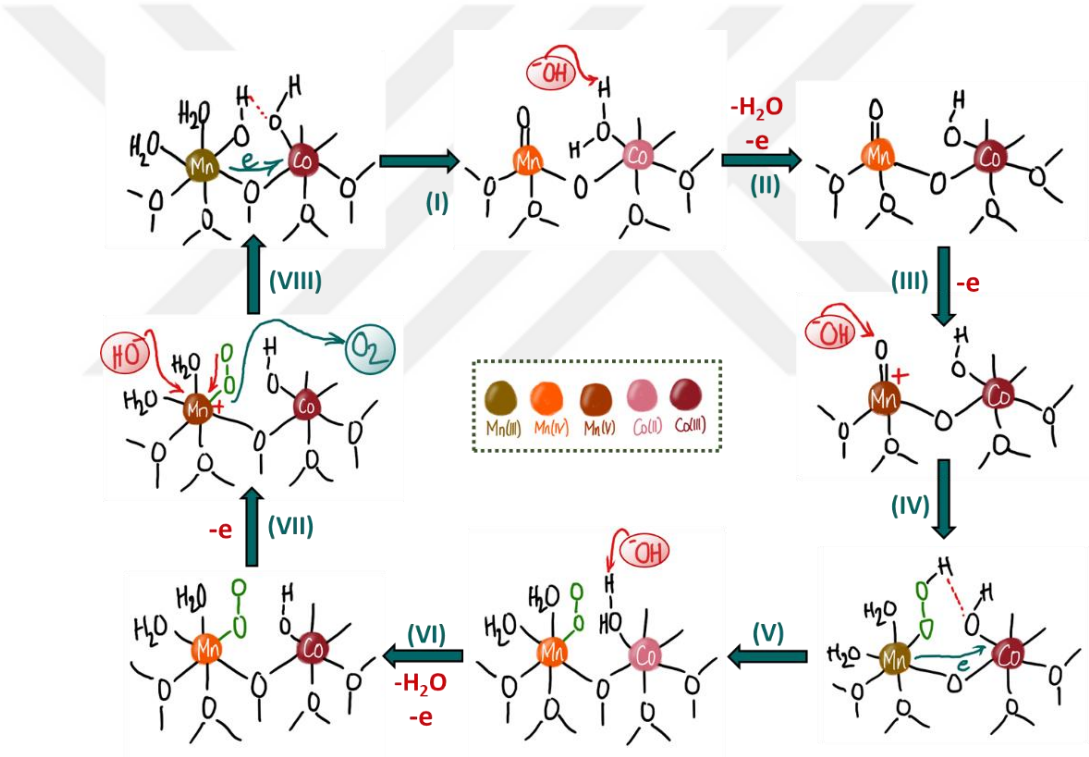

Figure 1.8 Schematic representation of oxygen evolution reaction mechanism on $LiMn_{2-x}Co_xO_4$ surface.

According to the mechanism, the reaction starts with an electron donation from a less electronegative Mn(III) site to a more electronegative Co(III) site to form Mn(IV)=O (metal-oxo bond). With further oxidation, the Mn(IV) becomes very active and thermodynamically unstable, with highly electrophilic oxo-oxygen (Mn(V)=O) on the surface. This feature is very reactive for a nucleophilic attack of OH^- to form Mn-OOH (O-O bond forms). The OH^- attack reduces the

manganese side back to Mn(III). The process continues with an electron transfer from the manganese to cobalt, attacking hydroxide species on relevant sides and oxygen gas production in further steps, see scheme in Figure 1.8. Briefly, we assume that the electronegative Co(III) pulls electrons to itself from the Mn(III) side to make the manganese side more electrophilic and also makes the formation of Mn-OOH easier. This step is believed to be the rate-determining step in the OER. In this thesis, we also tested other transition metals such as iron, nickel, and copper in $LiMn_{2-x}M_xO_4$ spinel structures to understand the effect of electronegativity difference between the manganese and other metal sides and to improve the electrode efficiency and robustness in OER.

1.4 Motivation of the Thesis

In this thesis work, mesoporous spinel lithiated bimetallic oxide thin films were synthesized for efficient OER electrocatalysis. Manganese disproportionation reactions were investigated in mesoporous spinel $LiMn_2O_4$ thin films by variation of electrochemical conditions. After optimization of the experimental conditions, $LiMn_{2-x}M_xO_4$ (where M is Mn, Fe, Co, Ni, and Cu) thin films were also fabricated, and electrochemical properties were investigated. Stabilities of the electrodes will be considered as the main issue regarding manganese disproportionation reactions and optimized quantities of transition metals in $LiMn_{2-x}M_xO_4$ were determined to eliminate the degradation caused by disproportionation reactions. 1st row transition metals are used in various compositions to benefit from the electronegativity concept in an effective OER catalytic mechanism. In the $LiMn_{2-x}M_xO_4$ system, lithium has a significant role in the structure. Firstly, lithium salt brings stability to the LLC phase even at high transition metal salt concentrations in the mesophase. Secondly, the de-intercalation of lithium ions during the catalytic process produces a unique active surface distinct from common transition metal oxides.

This work presents a new perspective on Mn(III) and Mn(VI) disproportionation reactions and flashes on fabrication and quantitative analysis of lithiated manganese-based metal oxides in order to procure efficient, robust, abundant, and environmentally safe OER electrocatalysts.

Chapter 2

2 Experimental Section

2.1 Synthesis and Characterization of LLC Thin Films

The solutions of salts and surfactants were prepared using $LiNO_3$, nitrate salts of transition metals ($Mn(NO_3)_2.4H_2O$, $Fe(NO_3)_3.9H_2O$, $Co(NO_3)_2.6H_2O$, $Ni(NO_3)_2.6H_2O$, $Cu(NO_3)_2.3H_2O$), pluronic, P123 as a non-ionic surfactant and cetyltrimethylammonium bromide (CTAB) as a charged surfactant, concentrated HNO_3 (65 %), and absolute ethanol (99.9 %).

In a general solution preparation, firstly, 0.125 mmol (0.725 g) P123 is completely dissolved in 5 g ethanol by stirring, and then 0.125 mmol (0.045 g) CTAB is added to the solution. To this clear solution, first 2.5 mmol (0.173 g) $LiNO_3$ salt at once, and after 5 min, concentrated HNO_3 (0.5 g) is added dropwise and stirred to obtain a homogenous clear solution. The transition metal salts (a total of 5 mmol) are added to the clear solution sequentially at 5-minute intervals. Then, the vial is sealed and stirred for 1 day to obtain a homogenous and clear solution. The mole ratio of each ingredient for all solutions is tabulated in Table 2.1. Notice that 1 mole ratio corresponds to 0.125 mmol for each of P123 and CTAB in the table. Thus, 2.5 mmol corresponds to a 20 mole ratio of $LiNO_3$ salt with respect to surfactant. The total transition metal salt mole ratio is 40 with respect to surfactant. For the bimetallic (for the transition metals) systems, 5 mmol (40 mol ratio) is also divided into sub-mole portions for each transition metal salt and their mole ratio notations were also tabulated in the 1st column in

the table. Notations for percent distributions of the bimetallic systems were also tabulated in the 2nd column in Table 2.1. Table 2.2 tabulate the amount (g) of the ingredients for each solution of the LiMn%-M% systems.

Mol ratios of chemicals in the solutions Li-Mn-M-CTAB-P123	**Notation of mole percentage of Mn%-M% in the solutions**
20Li-40Mn-1CTAB-1P123	LiMn100
20Li-38Mn-2M-1CTAB-1P123	LiMn95-M5
20Li-34Mn-6M-1CTAB-1P123	LiMn85-M15
20Li-30Mn-10M-1CTAB-1P123	LiMn75-M25
20Li-26.6Mn-13.3M-1CTAB-1P123	LiMn66-M33

Table 2.1 Mol ratios of chemicals in the solutions and notation of the solutions by mole percentages of manganese and metal nitrate salts.

	$LiNO_3$	$Mn(NO_3)_2$	CTAB	P123	HNO_3	EtOH
LiMn100	0.173	1.255	0.045	0.725	0.5	5

	$LiNO_3$	$Mn(NO_3)_2$	$Fe(NO_3)_3$	CTAB	P123	HNO_3	EtOH
LiMn95-Fe5	0.173	1.192	0.101	0.045	0.725	0.5	5
LiMn85-Fe15	0.173	1.066	0.303	0.045	0.725	0.5	5
LiMn75-Fe25	0.173	0.941	0.505	0.045	0.725	0.5	5
LiMn66-Fe33	0.173	0.836	0.671	0.045	0.725	0.5	5

	$LiNO_3$	$Mn(NO_3)_2$	$Co(NO_3)_2$	CTAB	P123	HNO_3	EtOH
LiMn95-Co5	0.173	1.192	0.073	0.045	0.725	0.5	5
LiMn85-Co15	0.173	1.066	0.218	0.045	0.725	0.5	5
LiMn75-Co25	0.173	0.941	0.364	0.045	0.725	0.5	5
LiMn66-Co33	0.173	0.836	0.483	0.045	0.725	0.5	5

	$LiNO_3$	$Mn(NO_3)_2$	$Ni(NO_3)_2$	CTAB	P123	HNO_3	EtOH
LiMn95-Ni5	0.173	1.192	0.073	0.045	0.725	0.5	5
LiMn85-Ni15	0.173	1.066	0.218	0.045	0.725	0.5	5
LiMn75-Ni25	0.173	0.941	0.364	0.045	0.725	0.5	5
LiMn66-Ni33	0.173	0.836	0.483	0.045	0.725	0.5	5

	$LiNO_3$	$Mn(NO_3)_2$	$Cu(NO_3)_3$	CTAB	P123	HNO_3	EtOH
LiMn95-Cu5	0.173	1.192	0.604	0.045	0.725	0.5	5
LiMn85-Cu15	0.173	1.066	0.181	0.045	0.725	0.5	5
LiMn75-Cu25	0.173	0.941	0.302	0.045	0.725	0.5	5
LiMn66-Cu33	0.173	0.836	0.401	0.045	0.725	0.5	5

Table 2.2 Amount of ingredients (in grams) in the solutions of LiMn%-M% systems.

The solutions were used by drop-cast coating for thick and spin coating for thin LLC films. The thick films were prepared on microscope slides by using 8 drops of the homogenous solutions and aged to be gel for an hour. The thick LLC films were used to synthesize lithium transition metal oxides for some analysis that requires more powder samples. In the second path, a spin coating technique was used to obtain thin films of the LLC. To prepare the thin films, a few drops of the solution were put on a glass substrate and spun at 2000 rpm for 10 seconds. The thin films were used for characterization techniques such as small angle XRD, ATR-FTIR techniques, and POM analysis. Schematic representations of both drop-cast and spin-coating methods are shown in Figure 2.1.

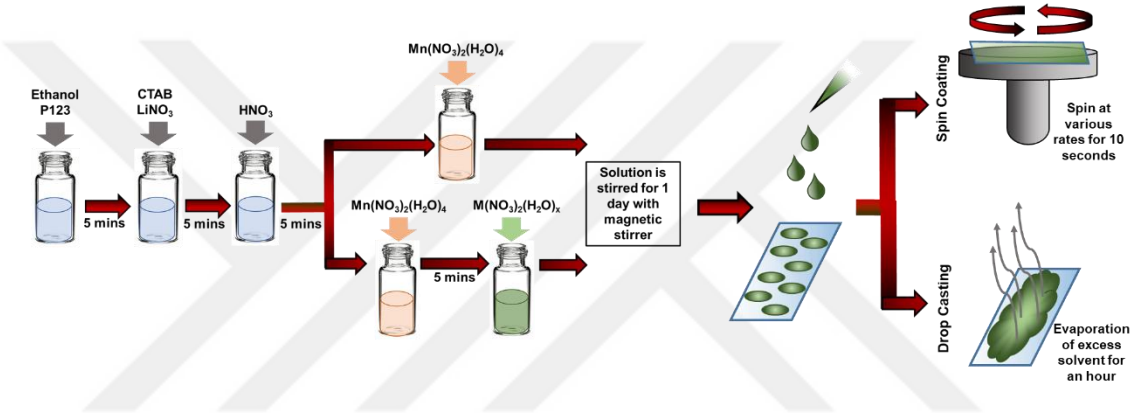

Figure 2.1 Schematic representation of the preparation of the LLC mesophases by spin coating and drop-cast coating methods.

2.2 Synthesis and Characterization of Mesoporous Spinel Lithiated Metal Oxides (LMOs)

Synthesis of mesoporous spinel LMOs has been achieved by using the MASA method. The LLC films, obtained from drop-cast or spin coating, were calcined at 300 ^{o}C. Drop-cast coated films were calcined for 3 hours because of being thick and scraped for the XRD and N_2 adsorption-desorption measurements. The spin-coated films were calcined for 2 hours. These films were also scraped from the substrate for SEM and TEM imaging, EDX, and powder XPS analysis. In Figure 2.2, real images of transparent thin and opaque thick films of LMOs on glass substrates were shown. Table 2.3 tabulates the notations and empirical formulas of the mesoporous spinel $LiMn_{2-x}M_xO_4$ that are synthesized by the MASA method.

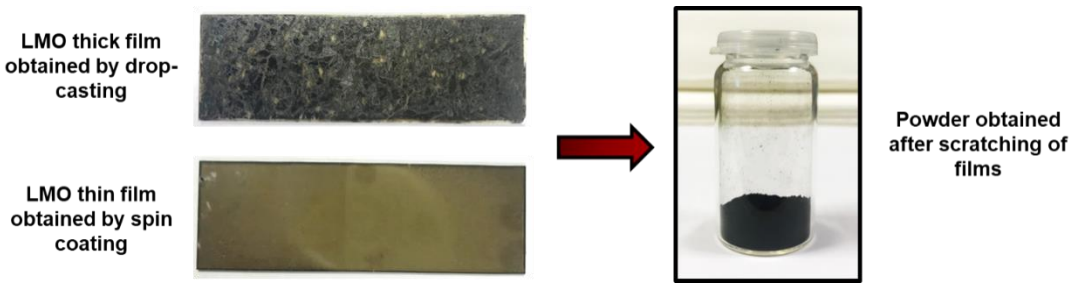

Figure 2.2 Images of LMO thick and thin films on glass substrate.

Mole percentage notation of solutions for LLCs and LMOs Mn%-M%	**LMOs are synthesized by calcination of (Mn%-M%) LLCs ($LiMn_{2-x}M_xO_4$)**
LiMn100	$LiMn_2O_4$
LiMn95-M5	$LiMn_{1.9}M_{0.1}O_4$
LiMn85-M15	$LiMn_{1.7}M_{0.3}O_4$
LiMn75-M25	$LiMn_{1.5}M_{0.5}O_4$
LiMn66-M33	$LiMn_{1.33}M_{0.66}O_4$

Table 2.3 Percentage notations (Mn%-M%) of LMOs and empirical formulas of Spinel $LiMn_{2-x}M_xO_4$.

2.3 Preparation of Working Electrodes

The LMOs, synthesized using the MASA process over a conductive substrate, fluorine-doped tin oxide (FTO), were used for water oxidation reaction as working electrodes (WEs). The WE was fabricated by spin coating (with an area of 1 cm^2) of solutions of the corresponding compositions and then calcined. The gel film covered by spin coating over the FTO was calcined at various temperatures, generally at 300 ^oC for 1h. The electrodes were used for electrochemical measurements and also for analysis like XPS, SEM, EDX, etc. Schematic representation of the preparation of WEs and the photographs of the electrodes are shown in Figure. 2.3.

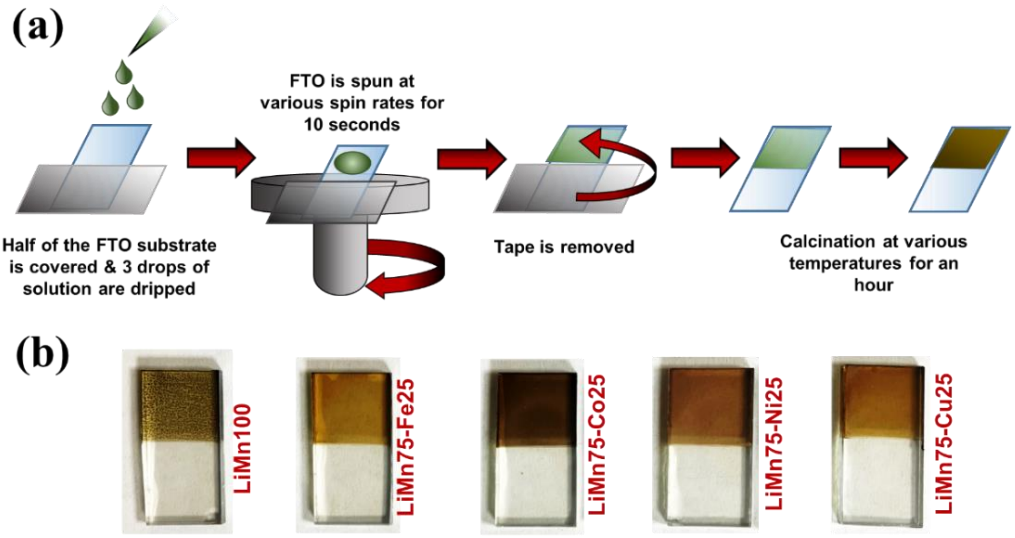

Figure 2.3 (a) Schematic representation of the preparation of WEs over FTO substrates, (b) Photographs of the LiMn100 and LiMn75-M25 (where M = Fe, Co, Ni, Cu) electrodes on FTO substrates.

Thin films were also fabricated on a much conductive substrate, such as a graphite rod to prevent resistive domination of FTO substrate on overpotential values. As a fabrication procedure, graphite rods (diameter: 3 mm, length: 30 mm) were washed with EtOH followed by a drying process at 100 ^{o}C for 30 minutes. The main solution was diluted for 5 times by volume with absolute EtOH (2 ml of precursor solution and 8 ml of pure EtOH). 20 mm of the graphite rod was covered with a non-permeable tape and 10 mm of the rod was left for the coating procedure. A dip coating instrument was set to 10 cm/min speed. The taped part of the rod was hocked to the clip of the dip coater. Then, 10 mm of the non-taped side of the rod was immersed into the solution completely via a dip coating instrument. Instantly, the rod was pulled out with the same speed and left for the evaporation of EtOH for 30 seconds. Similar calcination procedures depicted above, were applied for the calcination of the electrodes.

2.4 Instrumentation

2.4.1 X-ray Diffraction (XRD)

Small and wide-angle X-ray diffraction (XRD) patterns of the liquid crystal films on the glass substrates were recorded utilizing Rigaku Miniflex diffractometer, equipped with Cu Kα (1.54056 Å) X-ray source operated at 30 kV

and 15 mA. LLC coated glass slides were placed into the sample holder of the diffractometer and the XRD patterns were recorded between 1 and 5°, 2θ, with a scan rate of 0.5°/min. The wide-angle XRD patterns of films were recorded between 10 and 80°, 2θ, with a scan rate of 3°/min.

The wide-angle XRD patterns of powders (obtained after scratching) and mesoporous thin films were collected using Panalytical multipurpose X-ray diffractometer, equipped with a Cu Kα (1.54056 Å) X-ray source, operated at 45 kV and 40 mA. The powder materials were packed smoothly into a silicon holder. The XRD patterns were recorded between 10° and 80°, 2θ, with the 1°/min scan rate. XRD patterns of the thin films were directly recorded on FTO substrates. After recording the patterns, SnO_2 signals were utilized to calibrate the whole pattern to correct possible diffraction shifts.

PDF cards of the Joint Committee on Powder Diffraction Standards (JCPDS) were utilized for the identification and indexing of crystal structures of the metal oxides.

2.4.2 X-ray Photoelectron Spectroscopy (XPS)

XPS spectra were obtained using a Thermo Scientific K-alpha photoelectron spectrometer equipped with Al Kα monochromatic source (1486.68 eV) and a 400 μm spot size under ultra-high vacuum conditions. Spectra of the films were directly recorded on the FTO surface. The conductive FTO surface was contacted with the holder of the device with a metal ribbon to compensate charging of the material. All spectra were calibrated according to C 1s peak at 284.8 eV, and elemental percentages were analyzed using the XPS survey spectra. Mn $2p_{3/2}$ spectra were plotted after normalization of the Mn $2p_{3/2}$ region between 0 and 100 to identify shoulder peaks and compare their relative contributions.

2.4.3 Scanning Electron Microscopy (SEM) & Energy Dispersive X-ray (EDX) Spectroscopy

SEM images of the thin films were directly recorded using (FEI) Quanta 200 F scanning electron microscope at 15 keV beam energy under high vacuum

conditions. The FTO or graphite substrate (bearing sample) was placed on a conductive stub. Conductive parts of the electrodes were contacted with stubs with the help of carbon tape to allow electron flow. The thickness of the films was investigated by coating the films on a silicon wafer. After coating, the wafer was cut with a certain alignment to obtain smoother film structures. The silicon piece was attached with a 90^{o} angle over a stub. Notice that the cut part of the wafer was directly exposed to the electron beam. Elemental compositions on the samples were evaluated from the EDX detector of the device, equipped with the microscope.

2.4.4 N_2 (77.4 K) Adsorption-Desorption Isotherms

100 mg of a powder was obtained by scratching thick films. Before the measurement, the powder samples were dehydrated under vacuum conditions at 200 ^{o}C for 2 hours. The isotherms were collected by using TriStar 3000 (Micrometrics) in the relative pressure range of 0.01 to 0.99 atm. Surface areas of the materials were estimated using the Brunauer-Emmett-Teller (BET) analysis method using 5 points in the range of 0.05 to 0.3 P/P_0. Pore size distributions were also estimated using the Barrett-Joyner-Halenda (BJH) method.

2.4.5 Fourier Transform Infrared (FTIR) Spectroscopy

FTIR spectra of the films were recorded using Bruker Alpha Platinum spectrometer with 4 cm^{-1} resolutions and 64 scans. The transmission compartment was equipped with a spectrometer. Films were scraped from the FTO substrate and ground with 200 mg of KBr. Fine powders were pressed to obtain KBr pellets.

2.4.6 Inductively Coupled Plasma Mass Spectrometry (ICP-MS)

Quantitative analysis of metals was performed by Thermo Fischer Scientific XSeries II spectrometer. Argon was used as carrier gas. A calibration plot was constructed using 2% HNO_3 solutions containing 62.5, 125, 250, 500, and 1000 ppb of the analyzed metal ions. Thin films were scraped from the FTO surface (10 mm x 10 mm) and dissolved in 6.0 ml of 1.0 M HNO_3 solution. Half of the solution (3.0 ml) was taken and diluted with the addition of 6.0 ml of ultra-pure deionized

water to adjust the pH of the solution to a pH of 2% HNO_3. These solutions were directly used in the measurements. To identify metal quantities after electrochemical measurements (performed in 20 mL of 1.0 M $LiNO_3$ or 1.0 M KNO_3 electrolyte), 7.0 mL of the electrolyte was drawn in a syringe and 1.0 mL of 3.0 M HNO_3 was added to acidify the solution. In alkaline electrolytes (20 ml), 5.0 ml of the electrolyte was drawn in a syringe and acidified by 3.0 ml of 3.0 M HNO_3 solution. These solutions were directly used in ICP-MS analysis. Metal amounts were obtained as ppb experimentally and moles and µg quantities were also calculated at the end of the experiment considering the dilution factors of the electrolytes.

2.5 Electrochemical Analysis

2.5.1 Catalytic Experiments Based on Water Oxidation Reaction

Electrochemical experiments were performed via Gamry Instruments, Potentiostats PC14G750, and IFC5000-07565. The polypropylene (PP) cell was used to prevent the aging effect of the electrolyte. As reference electrode (RE), Ag/AgCl (3.5M KCl) was used and potential was converted and reported with respect to the normal hydrogen electrode (NHE). A platinum wire was used as a counter electrode (CE) and the working electrodes (WE) were used as LMOs on FTO or graphite rod substrates. A schematic representation of the electrochemical cell is shown in Figure 2.4.

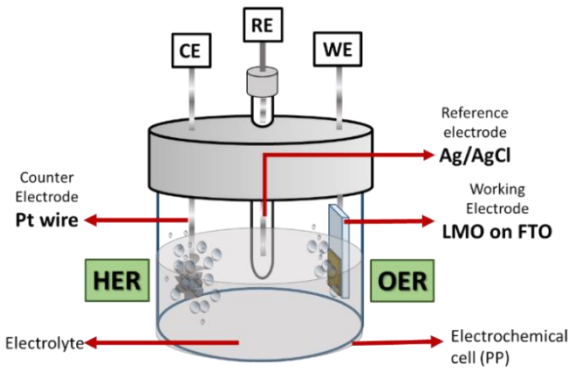

Figure 2.4 Schematic illustration of electrochemical cell and components.

The experiments were performed in an alkaline medium (pH~14), 1 M KOH or LiOH electrolyte solutions. Before all electrochemical measurements, nitrogen gas was purged into the electrolyte solution for 15 minutes to get rid of

any dissolved oxygen. Measurement was started with cyclic voltammetry (CV) for analysis of the general behavior of the electrodes. Then, multistep chronoamperometry (CA) was done by increasing potential sequentially with 0.01 V increments and Tafel slope data were extracted by plotting log(j) vs overpotential. Finally, chronopotentiometry (CP) experiments were performed for exact current densities from 1mA/cm^2 to 50 mA/cm^2 to get information about overpotential values for OER at different current densities.

2.5.2 Investigation of Active Metal Sites on Electrode Surface

Three electrodes set up, composed of LMO-coated FTO as WE, Ag/AgCl (3.5M KCl) as RE, and platinum wire as CE in aqueous electrolytes is used in the electrochemical measurements. Analysis has been carried out in several types of aqueous electrolyte solutions.

For neutral conditions, 1 M KNO_3, $NaNO_3$, and $LiNO_3$ solutions were used as electrolytes to identify metal species on the electrode surface and for the identification of potential windows for cyclic voltammetry. Highly resolved peaks are observed in the slow scan rate cycling such as 5 mV/s. Further characterization techniques such as XRD and XPS were employed for the investigation of manganese species after the electrochemical process. The electrolytes were prepared by mixing 1 M KNO_3 or 1 M $LiNO_3$ using the required amounts of 1 M HNO_3 or 1 M LiOH to adjust the pH of the solutions. pH dependence of manganese species was investigated by LSV, CV experiment in these acidic and basic electrolytes. To avoid the OER side in the cycles, non-aqueous electrolytes were also tested by using supporting electrolyte of 1 M $LiClO_4$ or 1 M $NaClO_4$ in acetonitrile (MeCN) and three electrodes set up (LMO coated FTO as WE, Ag wire as RE, platinum wire as CE).

For cycling experiments, the electrodes were cycled between -0.4 and 1 V or 0 and 1 V in 1M KOH or 1M LiOH solution. For further analysis, the electrodes were washed. ***The washing procedure follows***; washing the electrodes for 30 seconds by keeping them in ultra-pure deionized water with sonication. Then de-ionized water was renewed and the above procedure was repeated. In total, the washing step was repeated as an optimized washing procedure.

Chapter 3

3 Results & Discussion

3.1 Synthesis, Characterization, and Electrochemical Properties of Mesoporous $LiMn_2O_4$ Thin Films

3.1.1 Synthesis and Characterization of Mesoporous $LiMn_2O_4$ Thin Films

Mesoporous $LiMn_2O_4$ (LiMn100) thin films have been synthesized by molten salt-assisted self-assembly method followed by a calcination process. Before the calcination, a liquid crystalline mesophase (LLC) formation was investigated for thin and thick gel films of 20Li-40Mn-1C-1P (Li, Mn, C, and P stand for $LiNO_3$, $[Mn(OH_2)_4](NO_3)_2$, CTAB and P123, respectively, the coefficients are mole ratios of each ingredient) system. Precursor solutions were coated on glass substrates by drop-casting and spin-coating (2000 rpm) techniques and their small-angle XRD patterns were recorded, see Figure 3.1 (a). For LLC thin film spun at 2000 rpm, diffraction at 1.46 $2\theta^o$ is the indication for the oriented mesostructures that result from the LLC formation. The diffraction appears in a freshly prepared thin film. For thick gel films, the diffraction line appears in 1 hour after drop-coating. This might be due to the evaporation of excess solvent that takes a longer time for thicker gel phases. Since spin coating is an effective method for fast evaporation of the solvent. In addition to the formation of LLC, stabilities of the mesophase were also investigated. The wide-angle XRD patterns of both thick and thin films are shown in Figure 3.1 (b).

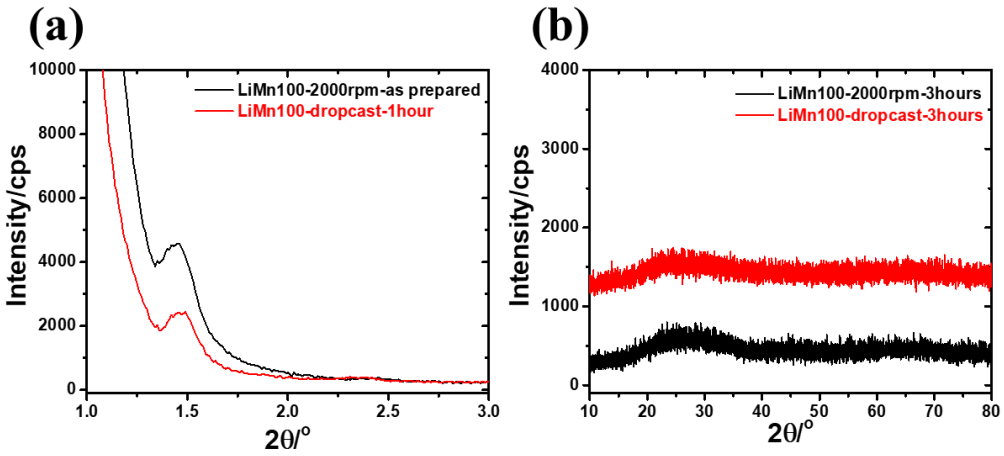

Figure 3.1 XRD patterns of spin-coated and drop-casted 20Li-40Mn-1C-1P LLC samples in the (a) small-angles and (b) wide-angles.

For the formation of the LLC phase, the coated samples were aged for 3 hours to determine if there is any salt crystallization from the mesophase by recording their XRD patterns. Luckily, there are no diffraction lines due to salt crystals meaning that there is no salt crystallization on the gel films. Gel phases are quite stable for up to 3 hours and are ready to be calcined.

After calcination of the LLC films, wide-angle diffractions of mesoporous LiMn100 were initially recorded between 10 and 80°, 2θ. Drop-casted mesophase was aged for 1 hour for complete gelation and calcined at 300 °C for 3 hours. As-prepared spin-coated thin film was instantly calcined at 300°C for 2 hours. In Figure 3.2, XRD patterns of thick and thin calcined films of LiMn100 are shown.

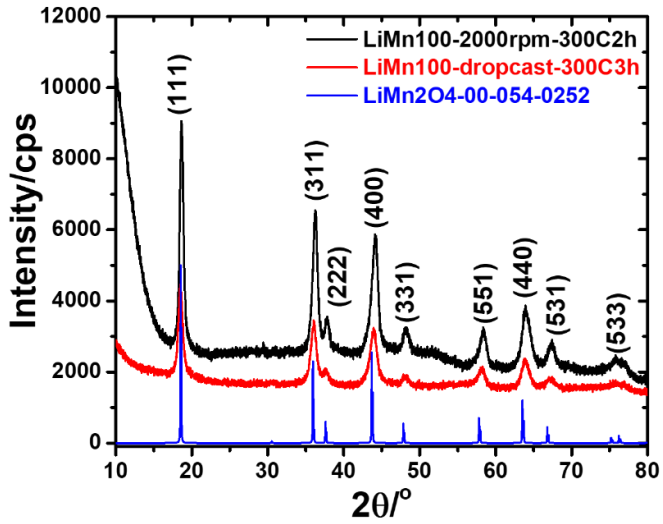

Figure 3.2 Wide-angle XRD patterns of LiMn100 powders obtained by spin-coating and drop-casting.

Notice that both diffraction patterns of the thick and thin films are quite similar to each other and correspond to the same crystal structure. Also, diffractions could also be indexed to the reference diffraction data of spinel-$LiMn_2O_4$ (ICDD card no. 00-054-0252, space-group: Fd3m). In addition to the crystal structure of the mesoporous LiMn100 thick films the drop-casted LiMn100 powder, obtained by scraping the films, was used to collect the N_2 adsorption-desorption isotherm that was used to evaluate its BET surface area and BJH pore size distribution. The N_2 adsorption-desorption isotherm of the LiMn100 sample, calcined at 300 ^oC is shown in Figure 3.3(a).

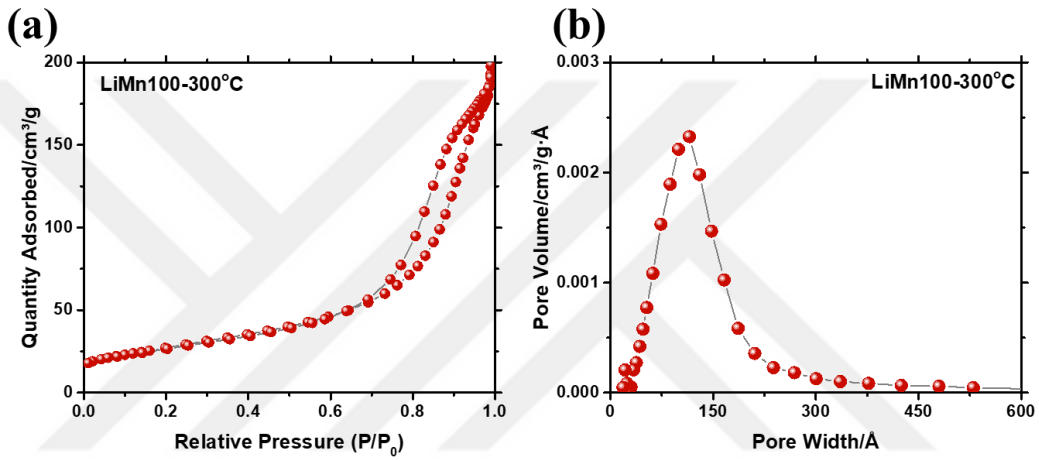

Figure 3.3 (a) N_2 adsorption-desorption isotherm of LiMn100 thick films, (b) BJH pore size distribution plot of LiMn100 thick films.

According to the BET calculation, the surface area of the powder was calculated as 98 m^2/g. BJH pore size analysis gave an 11.1 nm average pore diameter, which might be attributed to the mesopores in the film, see Figure 3.3(b).

The LiMn100 thick and thin films were mainly analyzed by using the above common characterization techniques. Several other techniques were also employed for the comprehensive characterization of the mesoporous LiMn100 thin films. Further characterizations of $LiMn_2O_4$ will be represented and discussed in parallel with electrochemical discussions in the next sections.

3.1.2 Electrochemical Characterization of Mesoporous $LiMn_2O_4$ Electrodes in Aqueous Electrolytes

Electrochemical measurements using spinel $LiMn_2O_4$ as working electrodes were generally carried by cyclic voltammetry (CV) or linear sweep voltammetry (LSV) followed by chronoamperometry (CA), chronopotentiometry (CP) experiments. Manganese sites on electrode surfaces were comprehensively analyzed by cycling the electrodes in various potential windows, and different types of electrolytes at various pH values. Further characterization techniques (such as XPS, XRD, and FTIR) were used after electrochemical processes to comprehend the electrode behaviors considering the change in the manganese oxidation states and its different oxide forms. The LiMn100 electrodes were fabricated by spin-coating at 2000 rpm followed by calcination at 300 ^oC.

The first analysis of $LiMn_2O_4$ (LiMn100) was started by the cycling of the electrodes in neutral aqueous electrolytes between -0.5 and 1.5 V with a sweep rate of 5 mV/s. CV curves of the LiMn100 electrode in 1 M $LiNO_3$, $NaNO_3$, and KNO_3 solutions are shown in Figure 3.4.

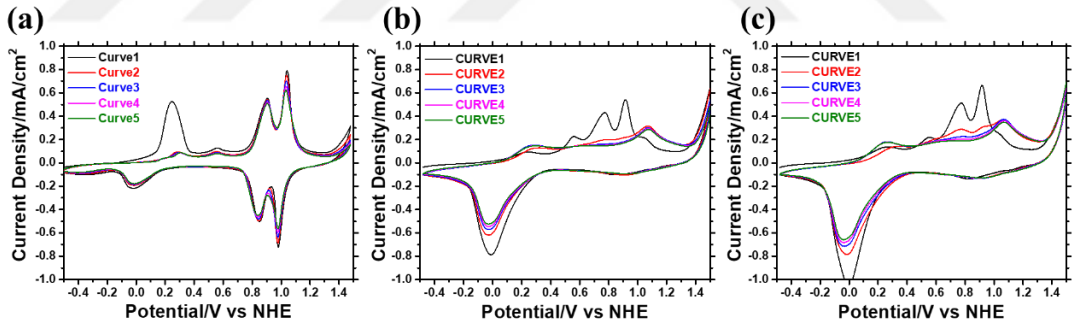

Figure 3.4 Cyclic voltammograms of LiMn100 in various neutral aqueous electrolytes with a sweep rate of 5 mV/s: (a) 1M $LiNO_3$, (b) 1M $NaNO_3$, (c) 1M KNO_3.

Cycling of the LiMn100 electrode in 1 M $LiNO_3$ provides many redox peaks in the voltammograms, see Figure 3.4 (a). In the 1st CV curve, a huge oxidation peak appears at 0.25 V and further cycling process causes the replacement of the main peak with two small overlapped peaks. There are many studies, showing a Li^+ intercalation into $LiMn_2O_4$ at 3 V vs Li/Li^+ to form $Li_2Mn_2O_4$.[115] Thus, the reduction potential for the Li^+ insertion in an aqueous media is approximately 0.05 V vs NHE, where the Li^+ ion is intercalated into the LiMn100 electrode to

form $Li_2Mn_2O_4$. Then, the oxidation peak of this process at 0.25 V might be due to the oxidation of $Li_2Mn_2O_4$ back to $LiMn_2O_4$. Additionally, having a huge faradaic current and charge under the peak also supports that the lithium intercalation/deintercalation is not only a surface process but also involves the bulk of the electrode. The decay of the peak current after 1st cycle shows that Li^+ insertion might be hindered/prevented by the formation of another manganese species on the electrode surface by sweeping to the negative potential side. These formations might be also seen by other small redox peaks between -0.2 and 0.4 V in 2nd and later CV cycles. The likely reasons for these will be discussed in later sections. Two redox peaks are observed clearly at 0.85 and 1 V vs NHE (corresponds to approximately 3.9 and 4.1V vs Li/Li^+) and belong to Li-intercalation and deintercalation process in $LiMn_2O_4$ cathode materials.[116] Note also that the lithium intercalation and de-intercalation into the LiMn100 process are reversible in lithium-rich electrolyte.

When the LiMn100 electrode was cycled in 1 M $NaNO_3$ and 1 M KNO_3 electrolytes, no lithium insertion into $LiMn_2O_4$ was observed, because the peak at 0.25 V did not appear as expected, see Figure 3.4 (a) and (b). Also, lithium deintercalation from $LiMn_2O_4$ was clearly observed in the 1st cycle, but there was no deintercalation while sweeping the electrode to the reverse side, due to the poor Li^+ ion environment. Thus, the lithium insertion process is not reversible in the $NaNO_3$ and KNO_3 electrolytes. However, new redox peaks are observed at a formal potential of 1 V vs NHE by further cycling of the electrode. The new peaks might be due to the formation of a new surface or phase transformation on the electrode surface, which will be discussed in later sections.

3.1.2.1 XPS Analysis of Manganese Sites on mesoporous $LiMn_2O_4$ Electrodes in $LiNO_3$ Electrolyte

The LiMn100 electrode was first cycled in 1 M $LiNO_3$ electrolyte in a potential range of -0.5 and 1.5 V with a 5 mV/s sweep rate. The potential window is limited to intentionally exclude the OER to determine the change on the electrode surface before the electrocatalytic process. CV of the LiMn100 electrode in 1 M $LiNO_3$ electrode is shown in Figure 3.5(a).

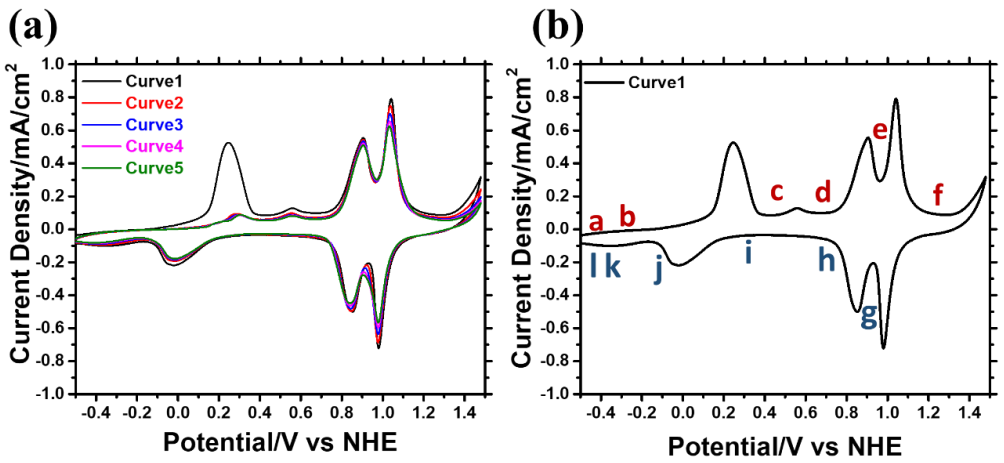

Figure 3.5 Cyclic voltammogram of LiMn100 in 1M $LiNO_3$ cycles between -0.5 and 1.5V with a scan rate of 5 mV/s: (a) 5 cycles, (b) 1st cycle with labeled potentials.

According to the voltammograms, 5 cycles, there are several oxidation and reduction peaks due to different forms of manganese on the electrode surface. To better determine the chemical species, XPS spectra were collected at labeled potentials in 1st cycle of the electrode, see Figure 3.5(b). Red small case letters correspond to potentials chosen for the end of each linear sweep voltammetry. At each potential, the fresh electrode was used and LSV was always started from -0.5 V then, sweeping was stopped at an exact potential (labeled with letters in Figure 3.5(b)). The working electrode was removed from the cell and the XPS spectrum of the electrode was recorded directly from the FTO surface as an ex-situ process after the washing and drying procedure of the electrode. For negative sweep or reduction of the manganese species, another set of CVs was recorded. The CV cycling was initiated at -0.5 V, followed by positive scanning up to 1.5 V. In the reverse cycle, from 1.5 V to -0.5 V, the experiment was stopped at a chosen potential by passing the reduction peak of manganese species. These labeled potentials are shown in Figure 3.5 (b) with blue letters. The same washing and drying procedure was employed for the WE before the XPS analysis.

Firstly, manganese species on the electrode surface at -0.5 V were analyzed by XPS spectra. The electrode was exposed to a constant -0.5 V for 30 seconds by conditioning method and this potential refers to label "a" in Figure 3.5 (b). Then, the electrode was used to record the XPS spectra in the O 1s, Mn 2p, and Mn 3s regions and these spectra were compared with the spectra of the non-

used LiMn100 electrode. The O 1s, Mn 2p, and Mn 3s XPS spectra of used and un-used LiMn100 are shown in Figure 3.6.

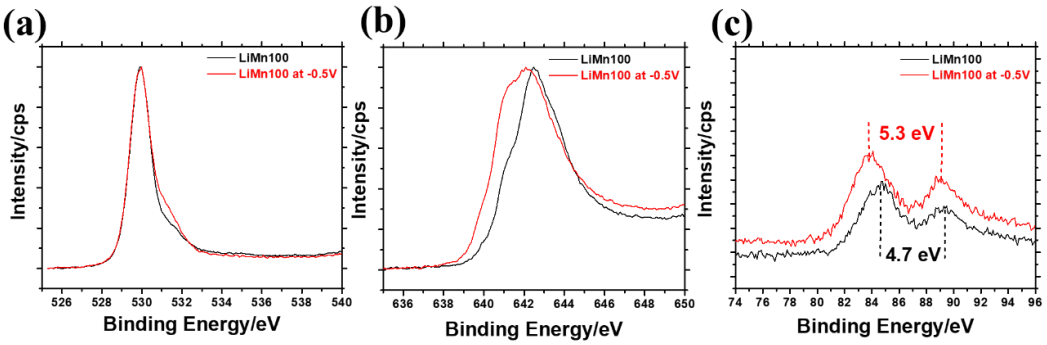

Figure 3.6 XPS spectra of LiMn100 and $LiMn_2O_4$ at -0.5 V: (a) O 1s, (b) Mn 2p ($^2P_{3/2}$) and (c) Mn 3s.

According to the O 1s spectra, the peak shape shows two types of oxygens on the electrode surface. The major peak (due to lattice oxygens) appears at 529.9 eV in the spectra. The shoulder at 531.2 eV is due to the hydroxyl oxygens and it is amplified by applying -0.5 V to the electrode. Thus, hydroxide formation on the surface may be triggered at that negative potential due to water reduction or oxygen reduction reactions or just by dipping it into the electrolyte solution. In addition to that, reduction of surface Mn (III) and Mn(IV) species to lower oxidation states such as metallic manganese or Mn(II) may occur. In the Pourbaix diagram of manganese, Mn^{2+} species is also observed as a thermodynamically stable phase at -0.5 V and pH 6.6, see Figure 1.6. As a result, the formation of both Mn^{2+} and OH^- on the electrode surface might cause the formation of $Mn(OH)_2$ on the electrode surface, since K_{sp} of $Mn(OH)_2$ is $2x10^{-13}$ and it is quite high for an immediate precipitation of manganese (II) as $Mn(OH)_2$.[117] The Mn 2p($^2P_{3/2}$) XPS spectrum of the LiMn100 electrode at -0.5 V displays an amplified peak at 641 eV, referring to a formation of Mn(II) on the electrode surface. Following the Mn 2p XPS measurement, the Mn 3s spectra of LiMn100 and LiMn100 at -0.5 eV were also recorded. There were two peaks in Mn 3s spectra due to the coupling of 3s electron with the 3d valance electrons, one is observed at around 89 eV and the other is located between 81 and 87 eV. Thus, the binding energy difference between these two peaks provides information about the oxidation state of manganese.[118] The LiMn100 electrode displays a 4.7 eV and this difference is attributed to a mixture of Mn(III) and Mn(IV) features.[118]

By applying a voltage on the electrode (used $LiMn_2O_4$ electrodes), the separation between these two peaks gets wider. It means the manganese oxidation state decreases from Mn(III) and Mn(IV) to Mn(II). In addition to Mn(II) formation, OH^- concentration is also enhanced on the electrode surface and causes the $Mn(OH)_2$ formation. When the electrode was used by LSV from -0.5 to -0.3 V (labeled with "b" in Figure 3.5 (b)), O 1s, Mn 2p ($^2P_{3/2}$) and Mn 3s spectra were recorded and compared with the spectra at -0.5 V. No significant change was observed in the XPS spectra of LiMn100 at -0.5 and -0.3 V, see Figure 3.7.

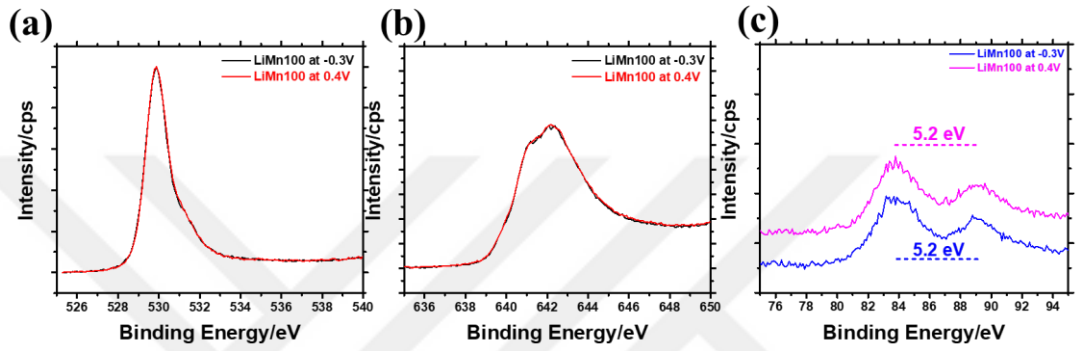

Figure 3.7 XPS spectra of LiMn100 at -0.3 V and $LiMn_2O_4$ at 0.4 V: (a) O 1s, (b) Mn 2p ($^2P_{3/2}$) and (c) Mn 3s.

The first oxidation peak of LiMn100 is observed at 0.25 V by the linear sweep and the XPS spectra of the electrodes at -0.3 and 0.4 V (labeled with "c" in Figure 3.5 (b)) were compared to show change on the electrode surface by this oxidation peak. The O 1s, Mn 2p, and Mn 3s XPS spectra of LiMn100 at -0.3 V and LiMn100 at 0.4 V are shown in Figure 3.8.

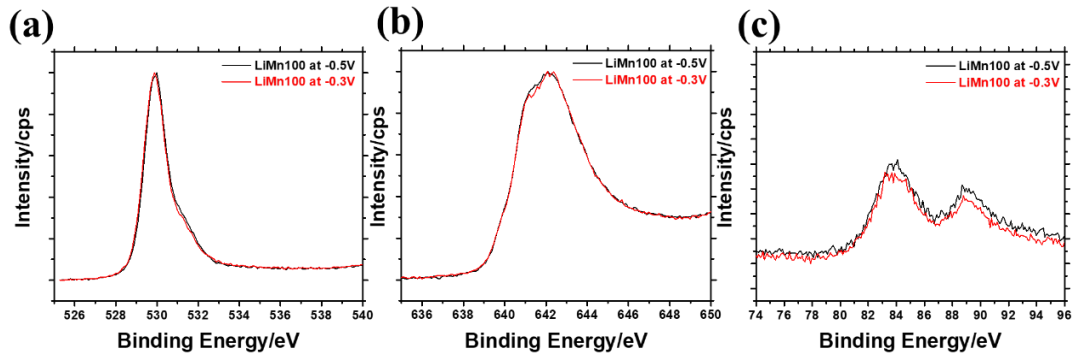

Figure 3.8 XPS spectra of LiMn100 at -0.5 V and $LiMn_2O_4$ at -0.3 V: (a) O 1s, (b) Mn 2p ($^2P_{3/2}$) and (c) Mn 3s.

According to O 1s, Mn 2p($^2P_{3/2}$), and Mn 3s XPS spectra, represented in Figure 3.8, there are no significant changes observed at 0.4 V (after oxidation

peak at 0.25 V) compared to XPS spectra of LiMn100 at -0.3 V. This shows that the pre-formed Mn(II) species, accordingly $Mn(OH)_2$, on the electrode surface, is preserved. However, the peak at 0.25 V might be correlated to structural change in spinel $LiMn_2O_4$. Most of the previous studies show that the Li^+ ions of electrolyte are inserted into $LiMn_2O_4$ and Mn(IV) is converted to Mn(III) to form $Li_2Mn_2O_4$ at 3 V vs Li/Li^+ by XRD technique. [115], [119], [120] Thus, the peak at 0.25 V might be attributed to Mn^{+3}/Mn^{+4} redox couple. This process modifies the LMOs but no specific change occurs on the electrode surface and there is still $Mn(OH)_2$ species on the electrode surface. Therefore, observing the same spectra from LiMn100 at -0.3 and 0.4 V is not extraordinary. From another perspective, the surface Mn(II) species might be oxidized at 0.25 V, current density of this redox process might be lower and masked by the Li-insertion peak. Notice that the intense peak at 0.25 V is altered by two small oxidation peaks in 2nd cycle, see Figure 3.5(a). This shows that the lithium insertion takes place in the 1st CV only and $Mn(OH)_2$ on the electrode surface might be oxidized to Mn_3O_4 and Mn_2O_3 sequentially.

The XPS analysis was continued by comparing the LiMn100 electrode surface at 0.4 and 0.7 V labeled with “c” and “d” in Figure 3.5 (b), respectively. XPS spectra of O 1s, Mn 2p, and Mn 3s regions of LiMn100, at these potentials, are shown in Figure 3.9.

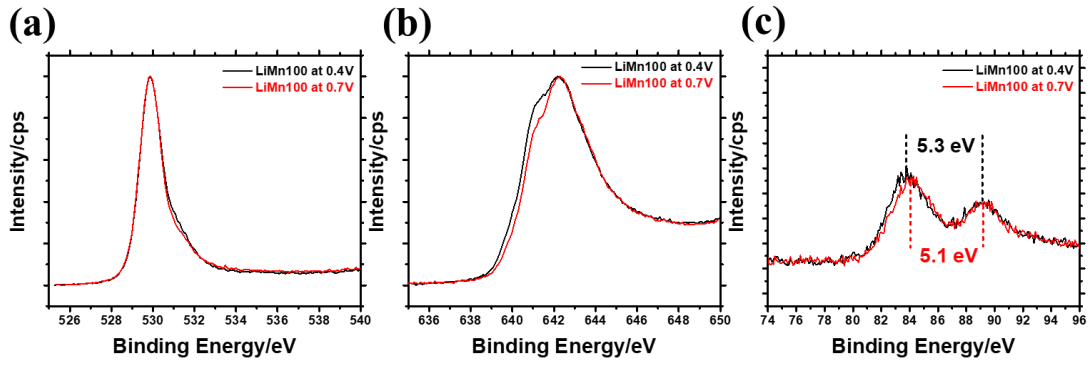

Figure 3.9 XPS spectra of LiMn100 at 0.4 V and $LiMn_2O_4$ at 0.7 V: (a) O 1s, (b) Mn 2p ($^2P_{3/2}$) and (c) Mn 3s.

The spectra show that oxygen species on the electrode surface are very similar since spectra of LiMn100 at 0.4 and 0.7 V are overlapping to a huge extent, compare the O 1s XPS spectra in Figure 3.9 (a). However, the Mn 2p region shows a decrease in peak intensity in the Mn(II) region referring that Mn(II) features are

oxidized to Mn(III) or Mn(IV). The Mn 3s XPS spectra also correlate with the increase of the oxidation state of manganese from 0.4 to 0.7 V, see Figure 3.9 (c). Combining the information gathered from the manganese and oxygen spectra at 0.7 V shows the presence of Mn(III), Mn(IV), and Mn(II) hydroxide features. Therefore, the oxidation peak at 0.55 V might be due to MnO_2 formation by the oxidation of Mn_2O_3 species on the surface and related to stepwise oxidation of $Mn(OH)_2$ or Mn_3O_4. Notice that, MnO_2 formal potential by oxidation of Mn_2O_3 is approximately equal to 0.6 V at neutral conditions and it could be correlated with the formation surface MnO_2 on the electrode.

The LSV measurement was followed by XPS analysis of LiMn100 at 0.95 V. Oxidation peaks at 0.9 and 1.0 V were attributed to two steps Li^+ de-intercalation process from the $LiMn_2O_4$ electrode in the acidic $LiNO_3$ electrolyte experiments in the previous section. The first evidence is the invariant potential values of the peaks in the case of altering the pH of the environment. Secondly, XPS analysis was performed to identify the complete oxidation state in the enhancement of manganese species for both surface and bulk phases. The XPS spectra of the Li Mn100 at 0.7 V and 0.95 V are shown in Figure 3.10.

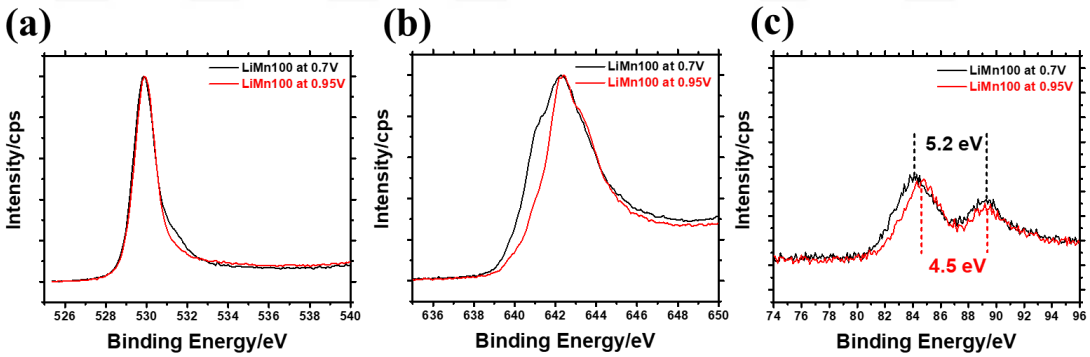

Figure 3.10 XPS spectra of LiMn100 at 0.7 V and $LiMn_2O_4$ at 0.95 V: (a) O 1s, (b) Mn 2p ($^2P_{3/2}$) and (c) Mn 3s.

According to the O 1s XPS spectrum of LiMn100 electrode at 0.95 V in Figure 3.10 (a), the peak intensity at 531.2 eV decreases, and only the lattice oxygen peak at 529.9 eV was observed. It shows that the surface has only Mn_xO_y features without any formation such as metal hydroxide or metal oxyhydroxide. Also, the Mn 2p region shows peak intensity in the Mn(II) region diminishes when the potential reaches 0.95V. The peak separation in the Mn 3s region, binding energy difference, becomes 4.5 eV and is clearly attributed to the MnO_2

formation.[118] When the LiMn100 electrode was swept to 1.2 V, the O 1s, Mn 2p and Mn 3s XPS spectra showed almost the same peak shapes and peak separations corresponding to complete MnO_2 formation, which is produced by complete lithium de-intercalation process in the $LiMn_2O_4$ electrode, see Figure 3.11.

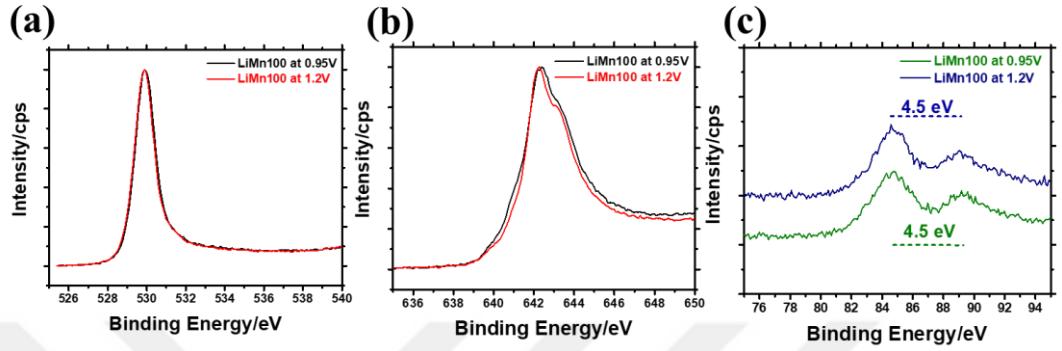

Figure 3.11 XPS spectra of $LiMn_2O_4$ at 0.95 V and LiMn100 at 1.2 V: (a) O 1s, (b) Mn 2p ($^2P_{3/2}$) and (c) Mn 3s.

XPS spectra, after reverse sweeping from 1.5 to -0.5 V were also recorded by stopping at potentials over the reduction peaks of the manganese species. These labeled potentials are shown in Figure 3.5 (b) with blue letters. The XPS spectra, obtained from negative sweep were compared with the XPS spectra of positive sweep potentials in the same potential regions to elucidate whether the manganese species are in the same forms or not. In spectra, potentials cut by positive sweep were labeled by "LiMn100 #V", and potentials reached by negative sweep were labeled by "Rev #V". The XPS spectra, recorded from LiMn100 at 0.95 V and Rev. 0.9 V labeled as "e" and "g" in Figure 3.5(b), respectively, are shown in Figure 3.12.

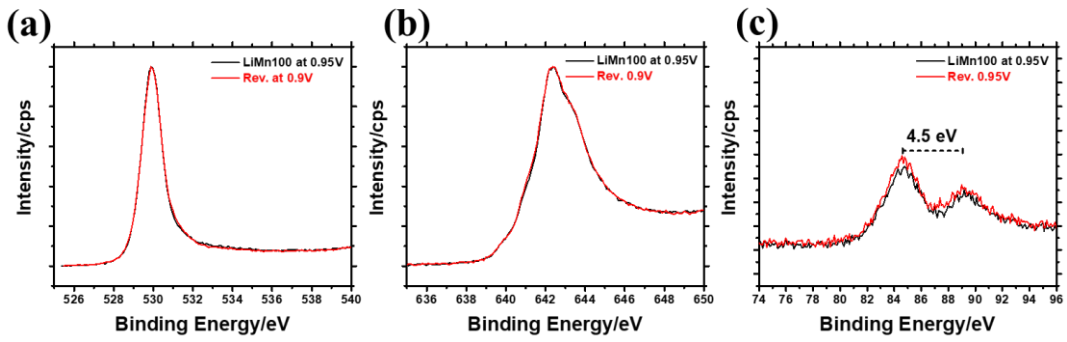

Figure 3.12 XPS spectra of LiMn100 at 0.95 V and LiMn100 at rev 0.9 V: (a) O 1s, (b) Mn 2p ($^2P_{3/2}$) and (c) Mn 3s.

When the XPS spectra of LiMn100 at 0.95 and rev 0.9V are compared, the same peak shapes and oxidation states are observed in the O 1s, Mn 2p, and Mn 3s regions. Thus, the electrode displays a reversible behavior at these potentials. LiMn100 electrode is swept to 0.75 V from 0.9 V to keep all the Li^+ content in the electrode and the XPS spectrum was compared with the XPS spectrum of LiMn100 at 0.7 V by a positive sweep. The XPS spectra of LiMn100 at 0.7 V (labeled "d" in Figure 3.5(b)) and LiMn100 at 0.75V by reverse sweep (labeled "h" in Figure 3.5(b)) are shown in Figure 3.13.

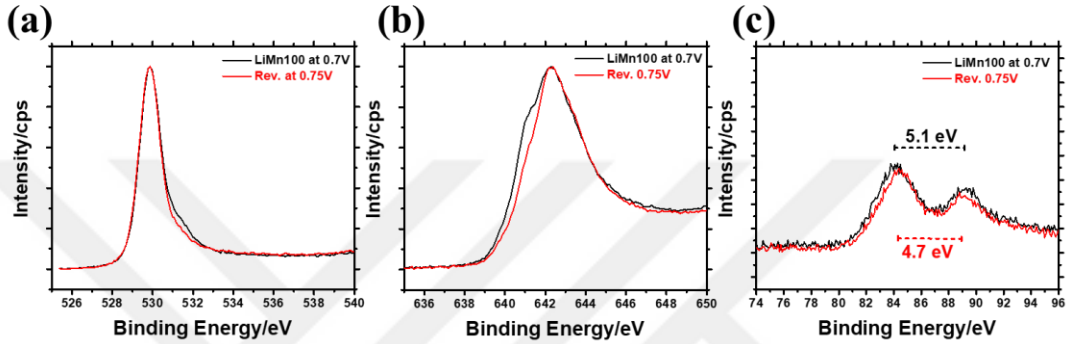

Figure 3.13 XPS spectra of LiMn100 at 0.7 V and LiMn100 at rev 0.75 V: (a) O 1s, (b) Mn 2p ($^2P_{3/2}$) and (c) Mn 3s.

The O 1s XPS spectrum of LiMn100 at rev 0.75V doesn't show any hydroxyl feature after the lithium intercalation process and dominantly displays a peak due to lattice oxygen at 529.9 eV, see Figure 3.13(a). Also, the shoulder in lower binding energy in the Mn 2p region shown in Figure 3.13(b) didn't amplify much by reverse sweeping to 0.75 V compared to LiMn100 at 0.7 V. It means that the manganese species are not completely converting to the same form of LiMn100 at 0.7 V. In the LiMn100 Mn 3s spectra, it is also shown that the peak separation is smaller in the reverse sweeping case. It means that the oxidation state of the manganese species at rev 0.75 V is higher than at 0.7 V. Notice that all O 1s, Mn 2p, and Mn 3s spectra of LiMn100 at rev 0.75 V are quite similar to the XPS spectra of $LiMn_2O_4$ electrode without electrochemical treatment. Thus, this might be attributed to the recovery of our starting material after the complete lithium insertion process.

After XPS analysis at 0.75 V by reversed sweep, the non-faradaic region swept from 0.75 to 0.3 V was also analyzed, and the XPS spectra of LiMn100 at

0.75 V (labeled with “h” in Figure 3.5(b)) and 0.3 V (labeled with “i” in Figure 3.5(b)) reached by sweeping on the reverse side are shown in Figure 3.14.

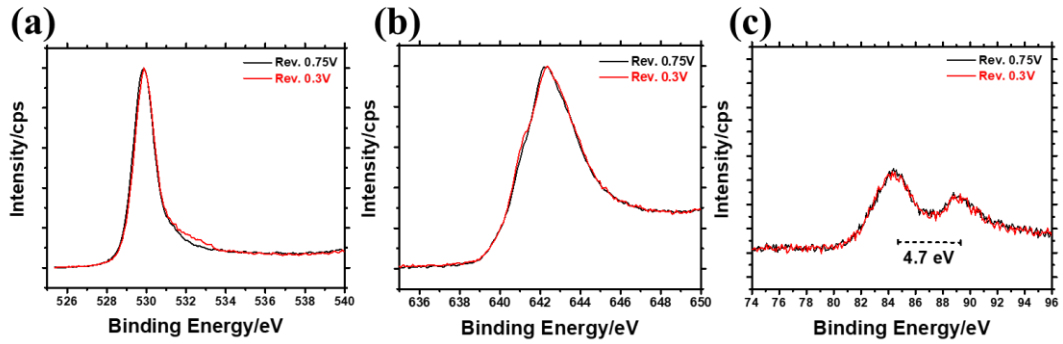

Figure 3.14 XPS spectra of LiMn100 at rev 0.75 V and LiMn100 at rev 0.3 V: (a) O 1s, (b) Mn 2p ($^2P_{3/2}$) and (c) Mn 3s.

According to the XPS spectra of LiMn100 at 0.75 V and 0.3 V by reverse sweeping, no significant change is observed in the manganese species. Peak shapes and separations are almost the same at two potential values of the electrode, see Figure 3.14 (b) and (c). However, O 1s spectra display a shoulder at 532 eV, likely due to oxo-species or surface peroxide formations, see Figure 3.14 (a). Thus, this might provide information about the formation of MnOOH on the electrode surface by reduction of surface MnO_2.

In addition to that, the XPS results of LiMn100 at 0.3 V by reversed sweeping (labeled with “i” in Figure 3.5(b)) were also compared with LiMn100 at 0.4 V by a positive sweep (labeled with “c” in Figure 3.5(b)). Their spectra are shown in Figure 3.15.

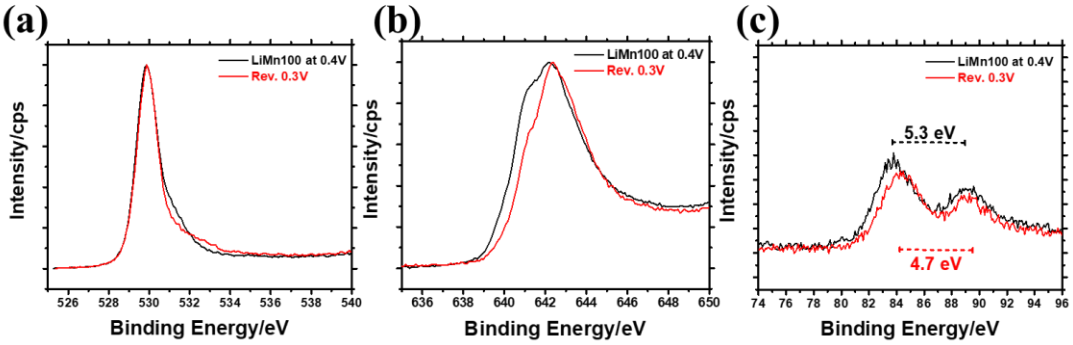

Figure 3.15 XPS spectra of LiMn100 at 0.4 V and LiMn100 at rev 0.3 V: (a) O 1s, (b) Mn 2p ($^2P_{3/2}$) and (c) Mn 3s.

When the spectra at two potentials are compared in the O 1s region, the electrode surface displays a hydroxide feature at 0.4 V by the positive side

sweeping. However, the LiMn100 electrode at 0.3 V by reverse sweep shows manganese peroxide species, see Figure 3.15 (a). On the other hand, both Mn 2p and Mn 3s spectra show that the LiMn100 at 0.3 V by reverse sweep has manganese species on the surface at higher oxidation states. In the Mn 2p, there is a distinct shoulder, amplified at a lower binding energy in the LiMn100 at 0.4 V by a positive sweeping but this shoulder didn't appear in the LiMn100 rev. 0.3 V sample. Thus, by a reverse sweeping of LiMn100 oxidation state of manganese is still higher, see Figure 3.15 (b).

This information might also be obtained from the peak separation in the Mn 3s spectra at those two potentials in Figure 3.15 (c). For this purpose, the XPS spectra of LiMn100 at 0.3 V by reverse sweep and spectrum after the reduction peak of LiMn100 at -0.15 V can be compared. When the electrode was swept from 0.3 V to -0.15 V (labeled with "i" and "j" respectively in Figure 3.5), a reduction process took place at 0 V. Thus, XPS spectra were collected at the potentials before and after this peak. The XPS spectra of LiMn100 at 0.3 V and -0.15 V by reverse sweep are shown in Figure 3.16.

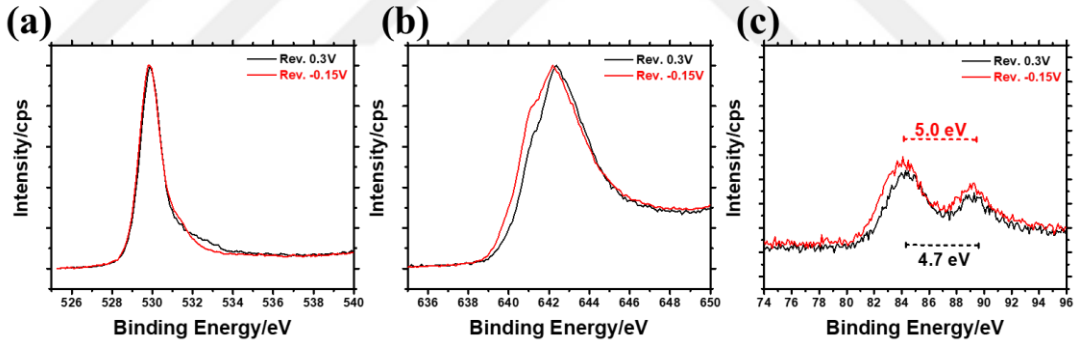

Figure 3.16 XPS spectra of LiMn100 at rev 0.3 V and LiMn100 at rev -0.15 V: (a) O 1s, (b) Mn 2p ($^2P_{3/2}$) and (c) Mn 3s.

In the O 1s region, it was already indicated the peroxide formation on the electrode surface at 0.3 V by a shoulder at 532 eV. After the reduction process at 0 V, the electrode surface displays hydroxide species at -0.15 V, as indicated by a shoulder at 531.2 eV, see Figure 3.16 (a). Also, an enhanced shoulder in the lower binding energy side of Mn 2p spectra, in Figure 3.16 (b), shows that the manganese oxidation state at -0.15 V is lower than the oxidation state of manganese at 0.3 V. This might be due to MnOOH reduction to $Mn(OH)_2$ on the electrode surface.

Finally, XPS analysis was concluded with a comparison between -0.5 V, which is the starting potential of a positive sweep, and -0.5 V, which is the ending of a complete cycle by a reverse sweeping. XPS spectra of both are shown in Figure 3.17.

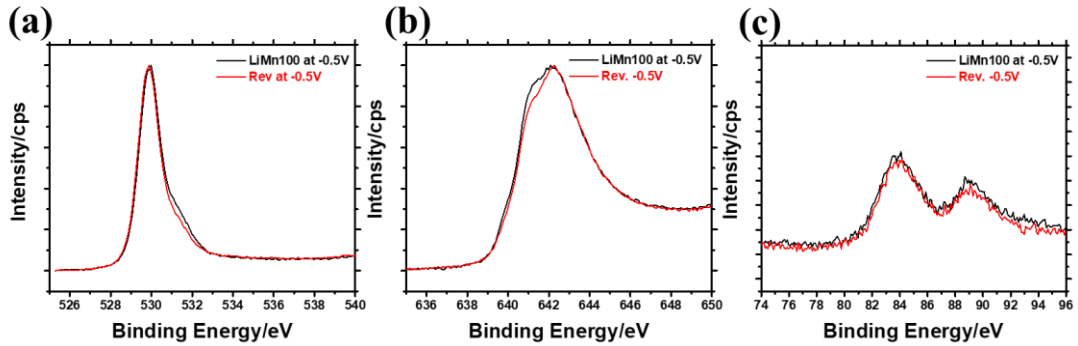

Figure 3.17 XPS spectra of LiMn100 at -0.5 V and LiMn100 at rev -0.5 V: (a) O 1s, (b) Mn 2p ($^2P_{3/2}$) and (c) Mn 3s.

The XPS spectra of LiMn100 in all O 1s, Mn 2p, and Mn 3s regions show approximately the same peak shape and binding energies. It means that a $Mn(OH)_2$ rich surface is obtained as of the starting potential after completing the whole cycle. After completing the whole cycle and $Mn(OH)_2$ formation on the electrode surface, the electrode was swept to 0.4 V in the 2nd cycle. Notice that there is no lithium insertion peak observed into bulk $LiMn_2O_4$ at 0.2 V and there are two small surface oxidation peaks observed in the 2nd cycle at 0.2 V, see Figure 3.5 (a). XPS spectra of the electrode were recorded after sweeping the electrode to 0.4 V in 2nd cycle and compared with XPS spectra at 0.4 V in 1st cycle. XPS spectra of O 1s, $Mn2p_{3/2,}$ and Mn3s regions are shown in Figure 3.18.

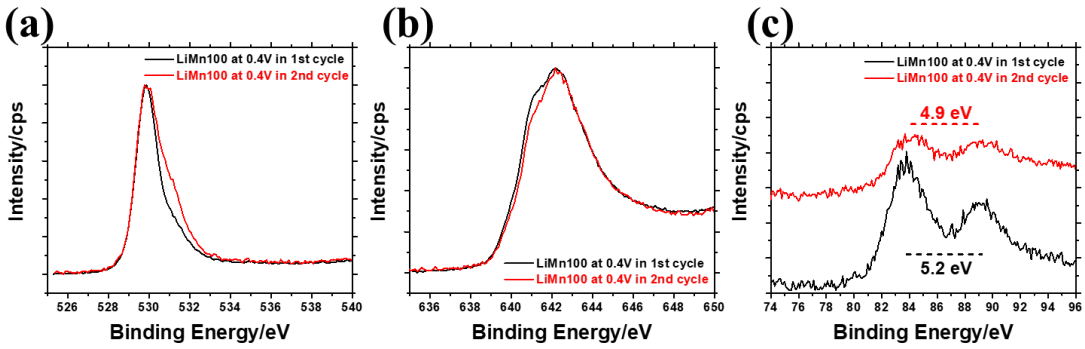

Figure 3.18 XPS spectra of $LiMn100_4$ at 0.4 V in 1st cycle and $LiMn100_4$ at 0.4 V in 2nd cycle: (a) O 1s, (b) Mn 2p ($^2P_{3/2}$) and (c) Mn 3s.

According to XPS O 1s spectra in Figure 3.18 (a), the hydroxyl region in the spectrum is amplified in the 2nd cycle when it is compared to that of the 1st cycle. This might be attributed to the oxidation of mostly surface species in the 2nd cycle rate than bulk species in the 1st cycle and oxygen species show intense hydroxyl as a shoulder because $Mn(OH)_2$ is already formed at -0.5 V.

Also, $Mn(OH)_2$ residual on the electrode surface at 0.4 V in the 2nd cycle could be proven by XPS Mn 2p spectra, see Figure 3.18(b). The shoulder peak of Mn(II) raised at 641 eV is strong evidence of the $Mn(OH)_2$ residuals when it is construed with O 1s spectra. On the other hand, the manganese oxidation state increase on the electrode surface was clearly shown in Mn 3s XPS spectra, as shown in Figure 3.18(c). The binding energy difference between the two peaks is 4.9 eV at 0.4 V in the 2nd cycle, corresponding to an increase in the oxidation state of surface manganese species to Mn(III). This might be attributed to the composition of $Mn(OH)_2$, Mn_3O_4, and Mn_2O_3 on the electrode surface.

To conclude the XPS analysis, the formation and reduction steps of MnO_2 on the surface follow two distinct paths for both positive and reverse sweepings. In the positive sweeping side from -0.5 to 1.5 V in 1 M $LiNO_3$, the $Mn(OH)_2$ formation is firstly initiated at negative potentials and it is followed by an oxidation process to form surface Mn_3O_4 and Mn_2O_3 species. After that, these species are further oxidized to MnO_2 on the electrode surface. For the reverse sweeping side from 1.5 to -0.5 V, the preformed MnO_2 is first reduced to MnOOH and followed by a reduction of MnOOH to $Mn(OH)_2$. Along with the surface change on the LiMn100 electrode, a phase change in the bulk material also takes place during the cycling LiMn100 electrode between -0.5 and 1.5 V in 1 M $LiNO_3$ electrolyte. Both surface and bulk changes in the electrode provide some information about the oxidation states and oxide forms of the manganese species.

At higher potentials (over 1.2 V), further oxidation of Mn(IV) and OER catalytic processes take place, as observed, and current density continuously increases over this potential. The LSV of the LiMn100 electrode is shown between -0.5 and 3 V with a scan rate of 5 mV/s in Figure 3.19.

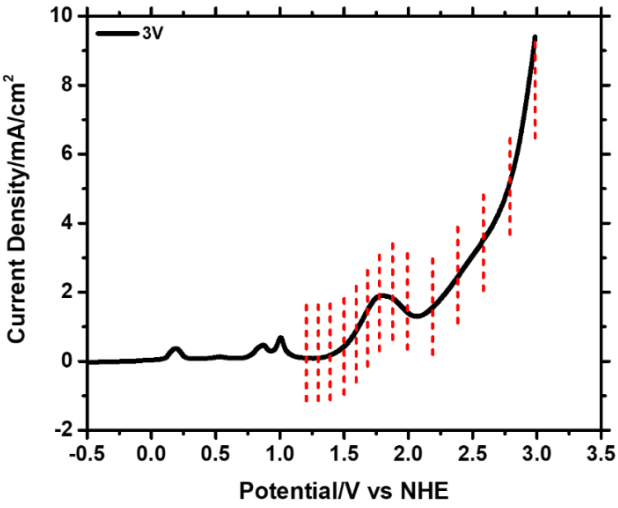

Figure 3.19 LSV of LiMn100 in 1 M $LiNO_3$ between -0.5 and 3 V with a scan rate of 5 mV/s - critical potentials assigned with red dashed lines.

XPS analysis in post catalytic process was also performed to understand the manganese behavior in the OER potentials. To do that, some final potentials in the LSV were chosen for an ex-situ XPS analysis of the LiMn100. Designated final potentials are indicated in Figure 3.19 with red dashed lines. The XPS analysis was firstly carried out using LiMn100 at 1.2, 1.3, and to 1.4 V, sequentially after performing LSV between -0.5 V and these final potentials, see Figure 3.20.

According to XPS, the O 1s spectrum of the LiMn100 electrode at 1.2 V does not show any kind of features except lattice oxygen. Increasing the final potential in the LSV to 1.3 and 1.4 V causes the enhancement in peak current density at 532 eV that might be due to an oxygen feature, which is related to manganese-oxo (Mn=O) bond formation, see Figure 3.20 (a).

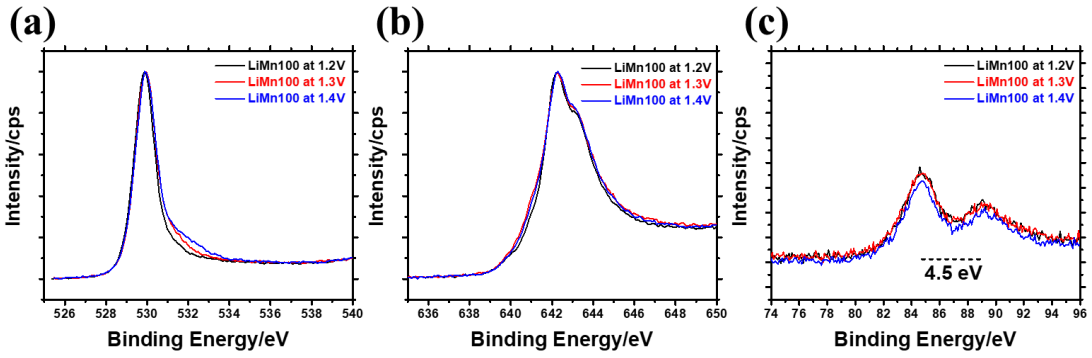

Figure 3.20 XPS spectra of LiMn100 at 1.2 V, 1.3 V and 1.4 V: (a) O 1s, (b) Mn 2p ($^2P_{3/2}$) and (c) Mn 3s.

The oxo-bond could form in the catalytic OER process as a more electrophilic oxygen side. As shown in the OER mechanism, water auto-dissociates into H_3O^+ and OH^- ions and the OH^- attacks the electrode surface (Mn=O sides) to get oxidized and form O_2 molecule. Thus, after the formation of the Mn=O bond and further oxidation of manganese makes this oxygen more electropositive/electrophilic. It means that the oxo-oxygen is ready for a nucleophilic OH^- attack.[34] When the OER starts at 1.3 V, the Mn=O formation is favored according to XPS O 1s spectra and amplified by further increments in final potentials. There are no significant changes in the manganese sides at further potential increase. It shows that the manganese is still Mn(IV). This might be raised from further oxidation of manganese to Mn(V) having quite low stability and Mn(VI) that disproportionate to Mn(IV), and Mn(VII). The manganese species with the last two oxidation states are mostly in ionic form and dissolve into electrolyte solution but the Mn(IV) might be redeposited on the electrode surface as MnO_2. Thus, Mn(IV) content on the electrode surface is preserved.

This analysis was followed by increasing the final potential of LSVs to 1.4, to 1.5, and to 1.6 V. XPS spectra of the LiMn100 after LSVs were recorded, see Figure 3.21.

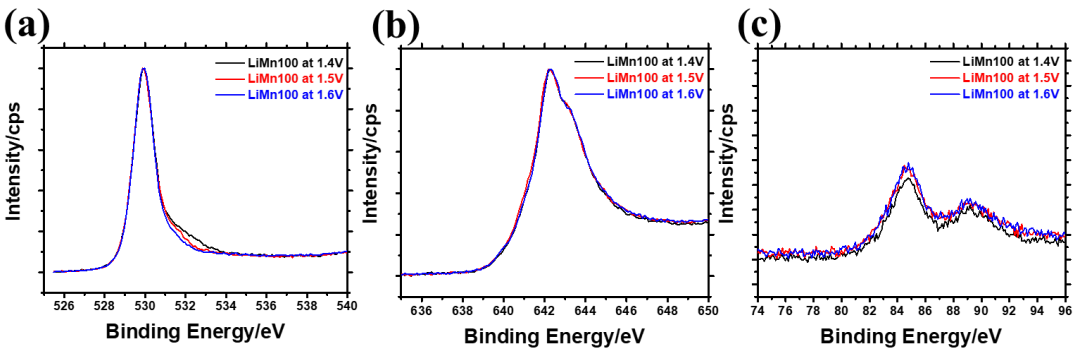

Figure 3.21 XPS spectra of LiMn100 at 1.4 V, 1.5 V and 1.6 V: (a) O 1s, (b) Mn 2p ($^2P_{3/2}$) and (c) Mn 3s.

When the final potential of LSV is set to 1.5 and to 1.6 V, a decrease in the peak intensity at 532 eV is observed, see Figure 3.21(a). The Mn=O side is reduced in amount since the water oxidation reaction is taking place more on the electrode surface at these potentials, see Figure 3.21. This might be related to the formation and simultaneous consumption of these active species on the electrode surface by the catalytic process. Also, it might be attributed to higher oxidation

states of manganese, Mn(VI), or Mn(VII) rather than Mn(V). Therefore, the dissociation mechanism of Mn(VI) or consumption of active Mn(VII) in the OER process leads to the formation of Mn(IV) on the electrode surface as MnO_2. With the further increase of final potentials to 1.8 V, there is no change observed in the peak shapes and binding energies in the O 1s, Mn 2p, and Mn 3s XPS spectra. However, over 1.9 V, the peak intensity at 532 eV increases slightly in the O 1s XPS spectrum. Notice that, this potential results in an ionic permanganate formation on the electrode surface resulting in the dispersion of permanganate ions with a unique pink color into the electrolyte. This behavior could be easily observed by the naked eye. When the potential is set to 2 V, there is no intensity increase in the peak observed at 532 eV and the formation of pink color stops on the electrode surface. XPS analysis after LSV at various final potentials was performed by sequentially increasing final potentials with an increment of 0.2 V. Up to 3 V, there is no specific change observed in the XPS spectra and all of the LiMn100 electrodes showed the same spectra, like the spectrum of LiMn100 at 1.2 V, see Figure 3.20. All of the O 1s, Mn 2p, and Mn 3s XPS spectra at further potentials are shown in Figure 3.22.

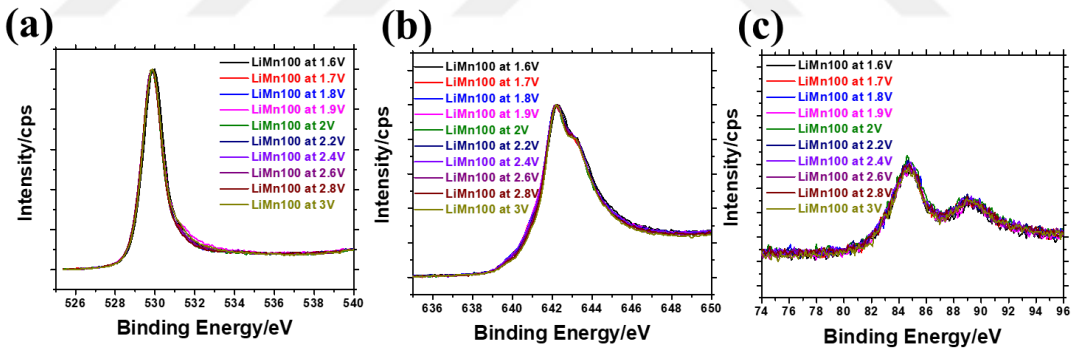

Figure 3.22 XPS spectra of LiMn100 at 1.6 V to 3 V: (a) O 1s, (b) Mn 2p ($^2P_{3/2}$)and (c) Mn 3s.

Furthermore, the LiMn100 electrode was further tested by LSV up to 3 V, followed by a chronoamperometry experiment at 3 V for 5 minutes to expose the electrode OER catalytic process at high voltages for a long time. The main aim of the experiment was to identify permanganate formation on the electrode surface and find the relation between higher oxidation states of manganese and catalytic active manganese species during water oxidation. The spectrum of the electrode was also compared with the spectrum of powder $KMnO_4$ to compare the peak

positions. XPS spectra of $KMnO_4$ and LiMn100 electrode at 3 V (after the CA experiment) are shown in Figure 3.23.

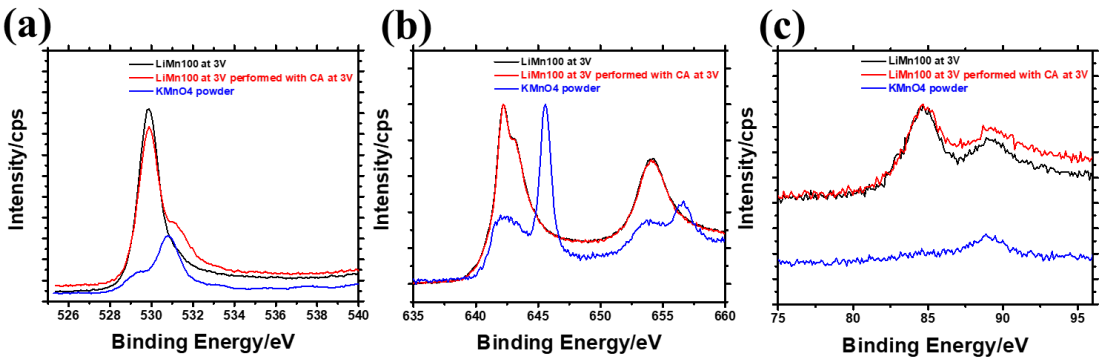

Figure 3.23 XPS spectra of LiMn100 at 3V followed by CA and $KMnO_4$ powder : (a) O 1s, (b) Mn 2p ($^2P_{3/2}$) and (c) Mn 3s.

According to the XPS spectra of LiMn100 after the CA experiment at 3 V for 5 minutes, the shoulder peak at around 531.5 eV in the O 1s region might be attributed to manganese-oxo (M=O) species since the main O 1s peak of permanganate shows same binding energy, see Figure 3.23 (a). Thus, Mn=O sites on the electrode surface are most likely involved in the OER catalytic process. On the other hand, in Figure 3.23(b), the Mn 2p spectra show no Mn(VII) formation on the electrode surface since permanganate ions are dispersed into the electrolyte solution. Thus, the electrochemically active species could be Mn(V)=O and Mn(VI)=O surface species, but the Mn(VI) species also undergo a disproportionation reaction to form Mn(IV) as MnO_2 and Mn(VII) as a permanganate ion. Observation of the Mn 2p peak shape (similar to MnO_2) could be due to consumption and fast reduction of very active Mn(V) sites. Notice that the peak intensities of Mn 3s peaks show some trend. The main peak of Mn 3s is at 89.2 eV and peaks resulting from valance electron multiplet-coupling are at lower binding energies. Permanganate powder only gives its main peak because there are no electrons in d orbitals. No peak is observed due to the multiplet-coupling of the electron in 3s. When the LiMn100 at 3 V and LiMn100 at 3 V by chronoamperometry are compared, the relative intensities of the main peak and peak resulting from multiplet-coupling are different. When the main peak at 89.2 eV is normalized in intensity for both cases, the peak at 84.8 eV of LiMn100 by CA shows lower peak intensity than LiMn100 by LSV. This might be an indication of

the formation of surface Mn(VII) species on the LiMn100 electrode surface by OER.

In the XPS analysis, all oxidation states of manganese by cycling between -0.5 and 1.5 V in 1 M $LiNO_3$ were identified to understand the change in electrode surface in the electrochemical process. This analysis provided new insights into design experiments by altering the other parameters for detailed manganese analysis. Disproportionation mechanisms of the specific manganese species and lithium intercalation and de-intercalation process will be discussed in the next sections using these XPS analysis and further characterization data.

3.1.2.2 pH Dependent Analysis of Manganese Sites on Mesoporous $LiMn_2O_4$ Electrodes

Firstly, the LiMn100 electrode (coated at 2000 rpm) was electrochemically characterized in acidic electrolytes to determine catalytic manganese species on the electrode surface. Cyclic voltammograms of LiMn100 were recorded in acidic solutions at pH 2, 3, and 4. Notice that, acidic solutions were prepared by mixing calculated volumes of 1 M HNO_3, 1M $LiNO_3$, and 1M KNO_3 solutions to obtain solutions with desired pHs. Solution molarities were kept constant at 1 M which included 1 M total cations (H^+ and either K^+ or Li^+) and 1 M total anions (NO_3^-). Upon preparation of the electrolyte solutions, their pHs were also measured to make a correct analysis of manganese phases or species at exact pHs. Electrodes were cycled at a 5 mV/s scan rate in various potential windows. These potentials were chosen according to RHE potential to provide compatibilities with water oxidation and reduction potentials in other types of electrolytes with different pHs. The CVs of LiMn100 in wide and narrow potential ranges at 5 mV/s weep rate are shown in Figure 3.24. The electrolyte was composed of HNO_3 and $LiNO_3$ and the pH of this electrolyte was recorded to be 1.93.

The electrode was swept between -0.2 and 1.8 V in the first CV, see Figure 3.24 (a). 1st curve of the voltammogram started with a current density of -0.15 mA/cm^2 at -0.2 V and became a positive non-faradaic current at 0.5 V. Thus, there was a reduction process of manganese until reaching 0.5 V. $LiMn_2O_4$ is composed

of Mn(III), Mn(IV) and surface Mn(II) species and this reduction might be caused by reduction of Mn(III) and Mn(IV) species at the electrode surface to Mn(II) at lower potentials. According to the Pourbaix diagram of manganese, Mn^{2+} formation is favored at negative and low positive potentials and it may show the dissolution of manganese from the electrode surface, see Figure 1.6. In Figure 3.24 (a), a peak at 1.2 V appears by further sweeping and this might be referred to the oxidation of Mn^{2+} species to MnO_2 and its deposition to the electrode surface. This is because the reverse side (reduction) of this oxidation peak is observed at 1.0 V and E^{θ} of this reaction at pH 1.93 is at about 1.1 V.

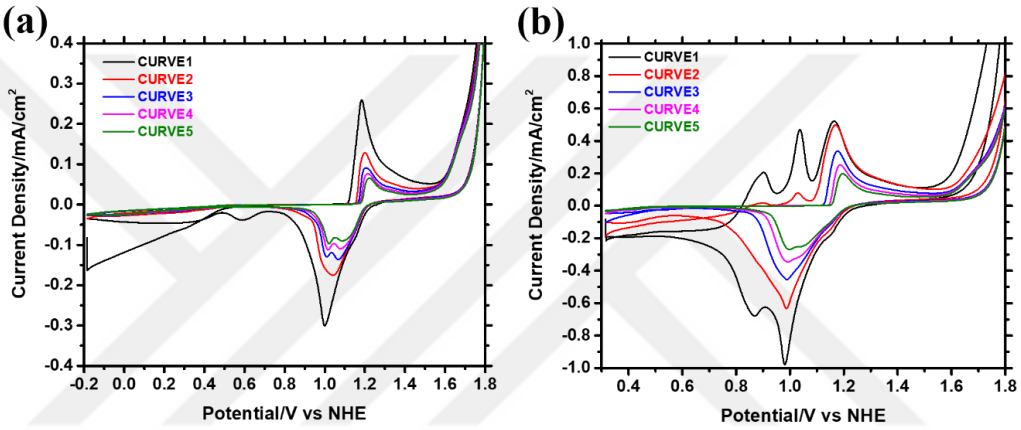

Figure 3.24 Cyclic Voltammogram of LiMn100 in electrolyte composed of HNO_3 and $LiNO_3$ (pH 1.93) with a scan rate of 5 mV/s: (a) potential range between -0.2 and 1.8 V, (b) potential range between 0.3 and 1.8 V.

According to the Pourbaix diagram, the Mn^{2+} ion to MnO_2 oxidation also occurs at about 1.1 V, see Figure 1.6. The actual deposition mechanism of Mn^{2+} might be through Mn^{3+} formation. Mn(II) oxidizes to Mn(III) in an acidic environment quickly and disproportionate to Mn^{2+} (in the electrolyte solution) and MnO_2[48], see equation 1.9. This behavior of the Mn(III) is also demonstrated by Frost diagram of manganese, see Figure 1.4.[121] A shoulder peak is observed at 1.7 V and likely corresponds to further oxidation of MnO_2 to permanganate $[MnO_4]^-$ ion. In this process oxidation MnO_2 might take place to form the first unstable manganate $[MnO_4]^{2-}$, followed by a fast disproportionation to MnO_2 (Mn(VI)) and $[MnO_4]^-$ (Mn(VII)) ion, see equation 1.10.[51]

In the 2nd cycle of CV, the current density of the oxidation peak at 1.2 V decreases since consumption of manganese in the electrode is triggered by

disproportionation of both Mn(III) and Mn(VI) species resulting in the formation of soluble Mn^{2+} and MnO_4^- ions. These ions probably disperse into the electrolyte solution in the cycling process and leach out from the electrode surface. Therefore, these free manganese species couldn't be redeposited to the electrode surface. To sign some light on these processes, further experiments were carried out by CV cycling in a narrow potential range, see Figure 3.24 (b).

When the voltammogram was inspected, the oxidation peak at 1.2 V, which belongs to the formation of MnO_2 from Mn^{2+} deposition was still observable. The reduction peak of this oxidation process overlaps with another reduction feature of the LiMn100 electrode. Like CV in a wide potential range, the Mn^{2+} and MnO_4^- formations are observed and the current density of the redox peaks decreases by further cycling due to disproportionation reactions. However, there is a significant difference between the voltammograms of LiMn100 electrodes, compare CVs in Figures 3.24(a) and 3.24(b). Two characteristic reversible peaks are observed, oxidation peaks at 0.90 and 1.05 V and reduction peaks at 0.85 and 1.00 V. Notice that, these two features are very similar to intercalation and de-intercalation of the lithium-ion in spinel $LiMn_2O_4$ cathode materials in Li-ion batteries (the calculated potentials, from NHE to Li/Li^+, correspond to 3.945 V and 4.085 vs Li/Li^+). Therefore these two peaks are assigned to de-intercalation of the Li^+ from spinel $LiMn_2O_4$ electrode.[116]

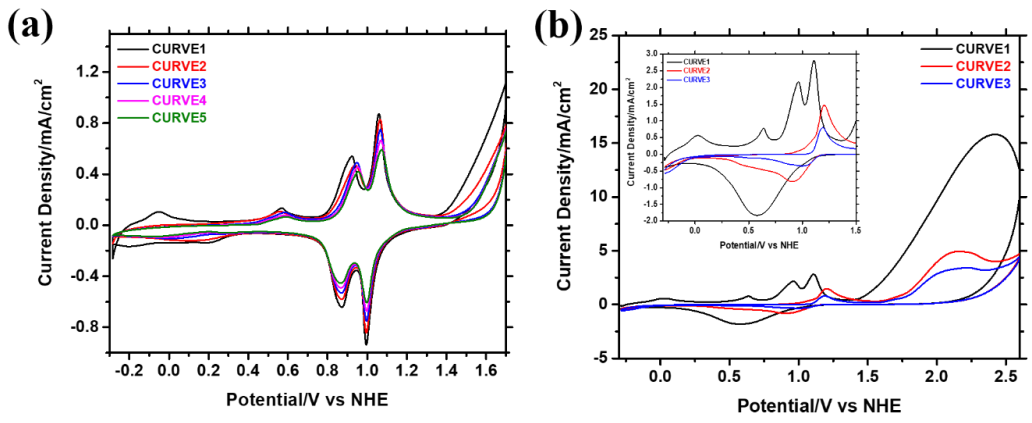

Figure 3.25 Cyclic voltammogram of LiMn100 in electrolyte composed of HNO_3 and $LiNO_3$ (pH 2.93): (a) potential range between -0.3 and 1.7 V with a scan rate of 5 mV/s, (b) potential range between -0.3 and 2.6 V with a scan rate of 20 mV/s inset graph: magnified version of cyclic voltammogram between -0.3 V and 1.5 V.

Another electrolyte solution was prepared by mixing 1 M HNO_3 and 1 M $LiNO_3$ solutions to obtain a solution with a pH 3. The prepared solution had a measured pH of 2.93. Another LiMn100 electrode was also cycled in a wide potential range between -0.3 and 2.6 V with a 20 mV/s scan rate to involve a water oxidation catalytic process, see Figure 3.25(b).

The LiMn100 electrode was cycled in the potential range of -0.3 and 1.7 V with a 5 mV/s scan rate, see Figure 3.25 (a). Lithium intercalation and deintercalation peaks are observed between 0.7 and 1.2 V. There is no potential difference for these peaks when the pH of solutions was increased from 1.93 to 2.93. It is proven that Li^+ deintercalation and intercalation reactions are pH independent. However, there is no additional peak is observed at 1.2 V since Mn^{2+} formation might take place but it is likely that it is re-deposited to the electrode surface without dispersing into the electrolyte. This behavior of Mn(II) might be explained by a small peak observed at -0.1 V. In this oxidation reaction, Mn^{2+} ions may immediately form $Mn(OH)_2$ on the electrode surface. A negative current density is observed at the low potentials in the first CV curve. This negative current density may be referred to as a reduction of oxygen species to OH^- that amplifies the hydroxide concentration on the surface. Thus, the Mn^{2+} ions may immediately react with hydroxide to form manganese hydroxide. The following oxidation peak at 0.55 V may be attributed to the oxidation of Mn(II) to Mn(III) or Mn(IV) species. From the Frost diagram, two Mn(III) undergo a disproportionation reaction to form Mn(II) and MnO_2.[121] Thus, this oxidation peak at 0.55 V might be indirectly due to the formation of MnO_2 on the electrode surface. Also in XPS analysis, we already discussed the formation of MnO_2 by the oxidation of Mn_2O_3 species on the surface and stepwise oxidation of $Mn(OH)_2$ or Mn_3O_4. Fortunately, there are many previous studies based on this peak but there is no consensus on the answer for this electrochemical feature of manganese.

The LiMn100 electrode was also used in a wide potential range CV experiment by increasing the potential window to 2.6 V with a 20 mV/s sweep rate, see Figure 3.25 (b). This voltammogram displays the same oxidation peaks as in the previous voltammogram in Figure 3.25 (a), compare 1st CV curves. When the potential window is expanded to 2.6 V, a huge peak appears in the water

oxidation region. This peak may correspond to the formation of MnO_4^- ions. As a result, the soluble Mn(VII) species are dispersed into the electrolyte and cause leaching of the manganese species from the electrode surface. The loss of manganese could be easily observed in the further CVs, 2nd and 3rd cycles, which display a decreasing oxidation and reduction peak current density of the manganese features. Furthermore, a broad and huge peak is observed at 0.55 V with a current density of -1.8 mA/cm^2, when the cycle was swept in the negative direction. The current densities of the peak at 0.55 V correlates to the current density of the oxidation peak at 2.4 V. Average potential value, according to the standard potential of these two redox peaks, is about 1.5 V and corresponds to the standard redox potential of MnO_2/MnO_4^- couple in Pourbaix diagram, see Figure 1.6. Thus, it is strong evidence for the formation of MnO_2 on the electrode surface at 0.55 V.

In $LiNO_3$ electrolytes, the LiMn100 electrode behaviors were compared by increasing the pH of the electrolytes (at pH of 2.9, 4.1, and 6.6) in Figure 3.26 (a), (b), and (c), respectively.

According to the CV curves in acidic electrolytes, the $Mn(OH)_2$ oxidation is observed at -0.1 V in Figure 3.26 (a). When the pH of the electrolyte is increased to 4.0, this small peak disappears. This is because OH^- concentration is increased in the electrolyte by increasing pH to 4.0 and oxidation potential for the Mn(II) oxidation into manganese hydroxide presumably shifts to much negative potentials. Thus, this oxidation process is not observed in this potential window.

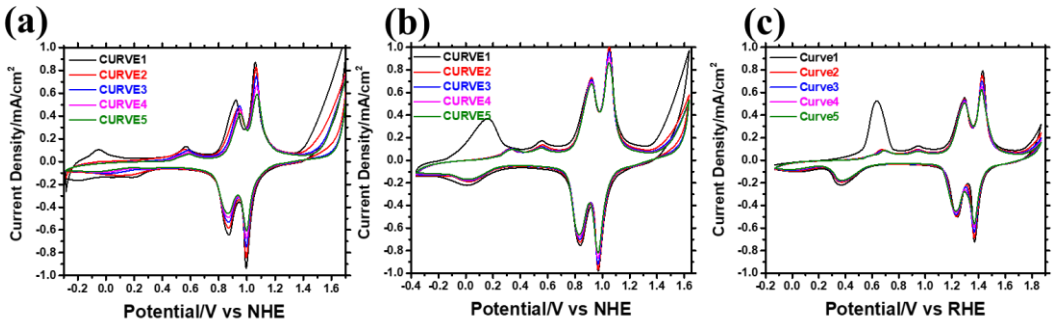

Figure 3.26 Cyclic voltammograms of LiMn100 in various acidic $LiNO_3$ electrolytes with a sweep rate of 5 mV/s with varying pH of: (a) 2.9, (b) 4.1, and (c) 6.6.

A dominant oxidation peak at 0.15 V appears, see Figure 3.26(b). Having high charge density under the peak might be explained by lithium insertion into $LiMn_2O_4$. When the LiMn100 electrode was used at a pH of 6.6, the lithium insertion peak shifted to 0.25 V, see Figure 3.26 (c).

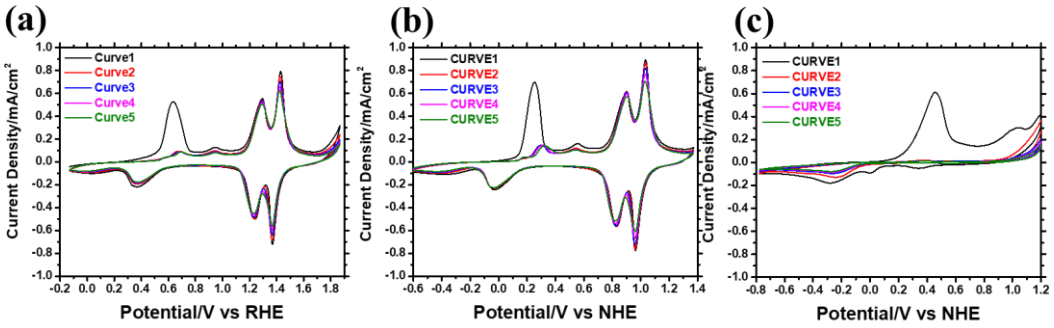

Figure 3.27 Cyclic voltammograms of LiMn100 in various basic $LiNO_3$ electrolytes with a sweep rate of 5 mV/s: (a) pH 6.6, (b) pH 9.7, and (c) pH 11.5

Increasing the pH of the $LiNO_3$ electrolyte to 9.7, no significant change was observed in the CVs, compare the CV at pH = 6.6 in Figure 3.27(b). However, there is a potential shift for the peak due to lithium insertion to $LiMn_2O_4$ from 0.25 to 0.45 V, see Figure 3.27(c). This might be a result of decreasing diffusion coefficient of lithium-ion by increasing concentration of OH^- in the environment. Thus, the insertion of lithium requires more energy in this environment.[122] The experiment was followed by cycling the LiMn100 electrode in a wide potential window at pH of 11.5 and 12.7 (refers to 1 M LiOH). The CV curves of LiMn100 at pH of 11.5 and 12.7 are shown in Figure 3.28.

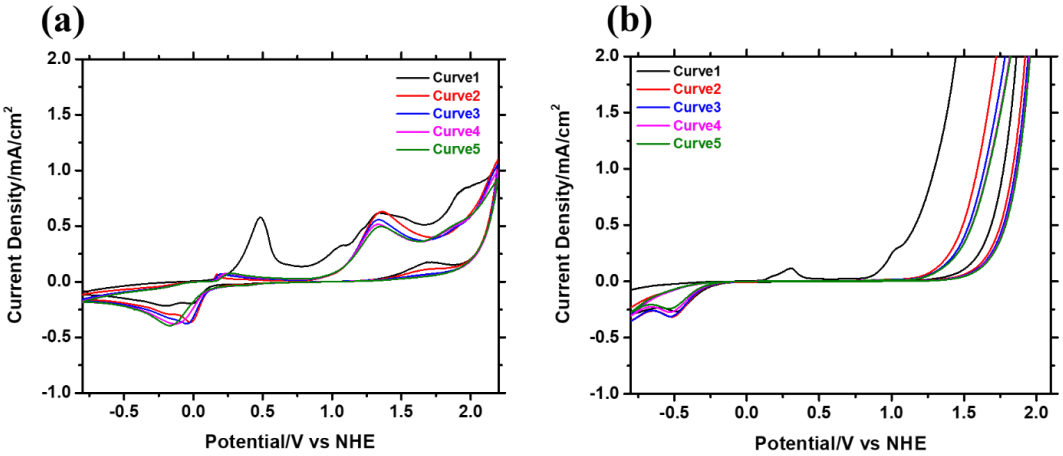

Figure 3.28 Cyclic voltammograms of LiMn100 in various basic $LiNO_3$ electrolytes with wide potential window with a sweep rate of 5 mV/s with varying pH of: (a) 11.5 and (b) 12.7.

According to CV curves in Figure 3.28(a), the electrode displays quite different CVs compared to CVs recorded in neutral 1 M $LiNO_3$ electrolyte. Notice that all oxidation peaks shifted to a higher potential due to the alkaline environment and peaks at 0.55, 0.85, and 1 V in $LiNO_3$ are also observable with shifted potentials in the CV curves. However, they are not well-resolved even if the scan rate is the same as the 1 M $LiNO_3$ case. Most likely, this effect is due to hydroxide rich environment. Additionally, cycling was also performed in a 1 M LiOH electrolyte refers to pH of 12.7, see Figure 3.28 (b). All peaks due to manganese species on the electrode surface and lithium intercalation-deintercalation disappear by further cycles. Only current increase is observed over 1.3 V.

3.1.2.3 Potential Window Dependent Analysis of Manganese Sites on Mesoporous $LiMn_2O_4$ Electrodes

To understand the disproportionation mechanism of manganese, cycling experiments with a various potential window were performed. The analysis is firstly started with the determination of potential ranges by reducing the initial potentials of the cycles. In this process, the OER part was not included, initial potentials of CV were reduced until the water reduction reaction (HER) took place. All experiments were performed at a 5 mV/s scan rate and for each CV, fresh LiMn100 electrodes were used in 1 M $LiNO_3$ electrolyte. Figure 3.29 shows the CV curves of LiMn100 in 1M $LiNO_3$ using various potential windows.

5 CV cycles were collected at each potential window. Firstly, the LiMn100 electrode was cycled in narrow potential windows. In Figure 3.29 (a), lithium de-intercalation process was only included in the CV cycles. Thus, it shows a reversible behavior without losing any manganese species in the electrode, because the current densities of both lithium deintercalation and intercalation are quite stable by further cycling. When the initial potentials of the cycles are decreased to 0.1 and -0.1 V, the peak currents still show no change even if there are surface redox processes at 0.55 V and 0.1 V, see Figure 3.29 (b) and (c).

When an ORR reaction is triggered by drawing the initial potential of the CV to -0.3 V, see Figure 3.29 (d), it is clearly observed that the ORR process and the $Mn(OH)_2$ formation are enhanced. As a result of this, an extra oxidation peak appears at -0.1 V that might be correlated to oxidation of $Mn(OH)_2$. Excess Mn(II) is oxidized to Mn(III) specie that is known as an unstable and undergoes to a disproportionation reaction to form Mn(II) and Mn(IV) as Mn^{2+} ($Mn(OH)_2$ in alkali media) and MnO_2. The Mn^{2+} species dissolve in the electrolyte. Inevitably, the manganese peaks current density in the region of 0.7 and 1.2 V decreases due to the loss of manganese content and this disproportionation reaction, see equation 1.9.

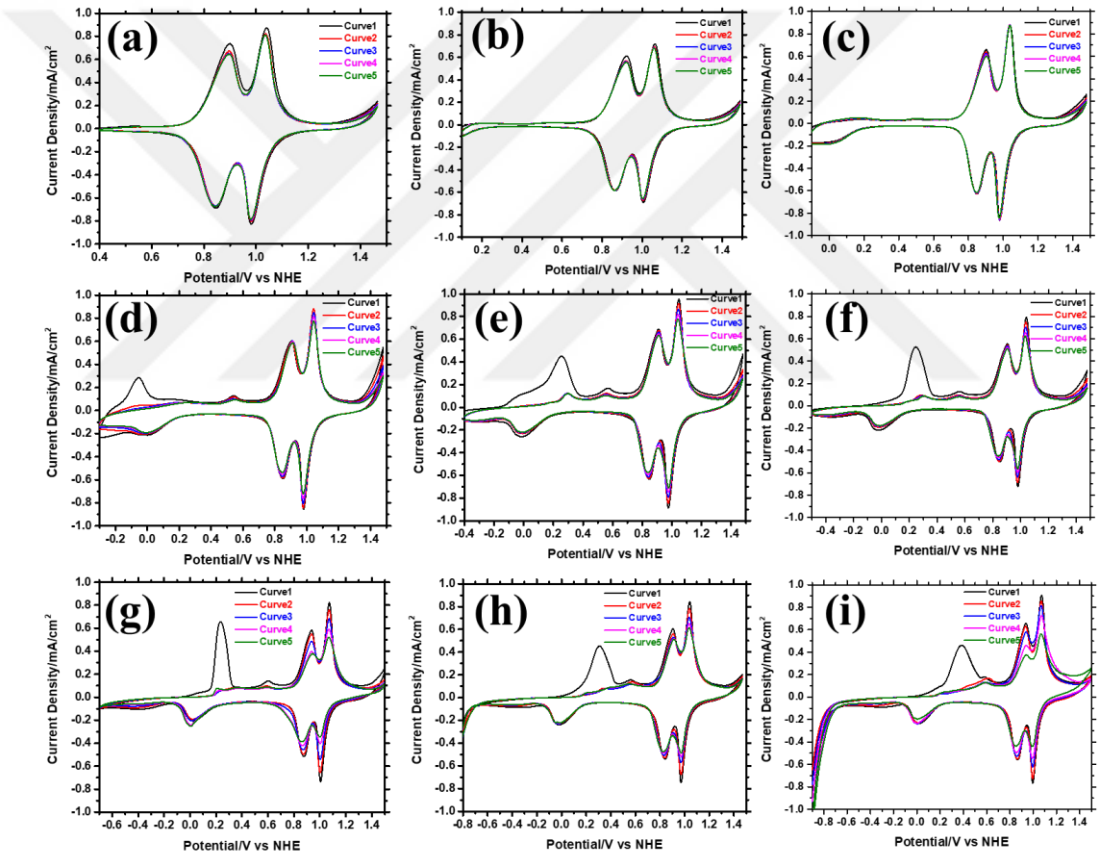

Figure 3.29 Cyclic voltammograms of LiMn100 in 1M $LiNO_3$ electrolyte with a sweep rate of 5 mV/s between # V and 1.5 V where # is: (a) 0.4, (b) 0.1, (c) -0.1, (d) -0.3,(e) -0.4, (f) -0.5, (g) -0.7, (h) -0.8, and (i) -0.9.

Furthermore, the lithium insertion process into $LiMn_2O_4$ was analyzed by initiating the CV from more negative potentials. The CV initiated at -0.4 V is shown in Figure 3.29(e). When the starting voltage is shifted to -0.4 V from -0.3 V, the peak current at -0.1 V becomes smaller, because the ORR process is triggered

more at more negative potentials. Thus, most of the Mn(II) species more readily form $Mn(OH)_2$ on the electrode surface in the alkali media. The amount of free Mn^{2+} remains is low as observed in the peak current, see oxidation peak at -0.1 V in Figure 3.29 (e). Other peak at 0.25 V is amplified because the lithium insertion process takes place as discussed in the XPS analysis section.

When the CV measurement is started from -0.5 V, the $Mn(OH)_2$ formation on the surface caused by ORR occurs readily at -0.5 V and no peak is observed at -0.1 V due to electrochemical oxidation of Mn(II), see Figure 3.29 (f). The lithium insertion takes place only between -0.5 and 0.4 V in the 1st cycle. Notice the changes in the 2nd and further cycles in the voltammograms, shown in Figure 3.29 (e), (d) and (f), these changes are due to the oxidation of surface $Mn(OH)_2$, Mn_3O_4 and Mn_2O_3 species to form surface MnO_2 at the end, as mentioned in XPS section. Lithium intercalation and deintercalation process also occur at the same voltage range but decreasing of the manganese content due to disproportionation of Mn^{3+} affects the process. The Mn(III) is formed for both $Li_2Mn_2O_4$ and Mn(II)/Mn(III) formation on the surface in Figure 3.29 (f).

In Figure 3.29 (g), when the starting potential of the CV is drawn back to -0.7 V, no significant change was observed in voltammograms when it is compared with the previous voltammogram, compare CVs in Figures 3.29 (g) and (f). In the CV, between -0.8 and 1.5 V, the water reduction/hydrogen evolution reaction (HER) process is initiated at -0.8 V by observing a significant current density decrease between -0.7 and -0.8 V, see Figure 3.29 (h). This is a catalytic reaction that produces a large amount of OH^- on the electrode surface. Thus, it reacts with the Mn(II) species to form $Mn(OH)_2$. The enhanced hydroxide formation on the electrode surface might cause covering the electrode surface with $Mn(OH)_2$ and affects the lithium insertion into $LiMn_2O_4$. Free lithium ions couldn't be inserted efficiently into the material because of the sealed surface of $LiMn_2O_4$ by $Mn(OH)_2$. It results in a shift in lithium insertion peak to 0.3 V from 0.25 V, see Figure 3.29 (h). If the CV measurement is started at -0.9 V, which includes HER reaction more dominantly. It produces a thicker $Mn(OH)_2$ layer on the $LiMn_2O_4$ electrode surface and makes the lithium insertion peak to a further shift to 0.4 V, since the lithium insertion becomes harder by thicker $Mn(OH)_2$ formation, see Figure

3.29(i). Notice that no potential shift for the peak at 0.55 V at all and it is not affected by potential window in the cycles. Thus it might be attributed to oxidation of surface Mn_xO_y species to MnO_2. Also, when the $Mn(OH)_2$ formation is further enhanced, the manganese content shows a significant decrease by further cycling, as shown between 0.7 and 1.0 V in Figure 3.29 (h) and (i).

The LiMn100 electrode was further investigated during OER catalytic process by increasing the potential window to more positive potentials towards elucidating Mn(VI) disproportionation. The CV curves of LiMn100 electrode at various potentials are shown in Figure 3.30.

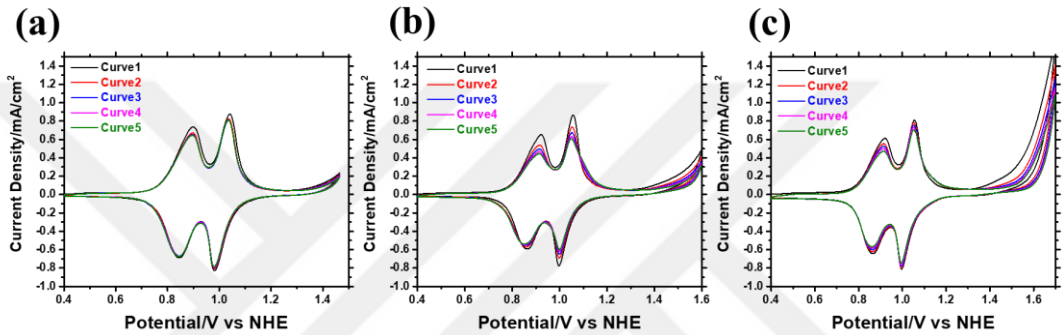

Figure 3.30 CV curves of LiMn100 between 0.4 V and # V in 1M $LiNO_3$ with a scan rate of 5 mV/s where # is: (a) 1.5, (b) 1.6, and (c) 1.7 V.

According to CV curves, the manganese content in the electrode doesn't decrease by cycling between 0.4 and 1.5 V. Thus, there is no disproportionation reaction in this potential window. However, if the CV cycling is performed between 0.4 and 1.6 V, the peak current densities of lithium intercalation and deintercalation decrease, see Figure 3.30 (b). It shows that Mn(VI) disproportionation reaction starts over 1.6 V. In this process, manganate $[MnO_4]^{2-}$ disproportionates into MnO_2 and $[MnO_4]^-$. Permanganate, Mn(VII), is in a soluble ionic form and these ions are dispersed into the electrolyte and cause a loss in the manganese content of the electrode. More positive potentials also cause the same disproportionation reaction.

3.1.2.4 Electrochemical MnO_2 Formation of Mesoporous Spinel $LiMn_2O_4$ Electrodes

For the characterization of the LiMn100 electrode after electrochemical measurements in 1 M $LiNO_3$ and 1 M KNO_3, XRD technique was employed. 1st

electrode was swept by LSV from -0.5 to 1.3 V to have complete lithium deintercalation in 1 M $LiNO_3$ electrolyte. 2nd electrode was cycled two times between -0.5 and 1.3 V until lithium deintercalation peaks disappeared completely. In the 3rd cycle, the CV measurement was stopped at 1.3 V. After that XRD patterns were recorded directly from the FTO surface. The XRD patterns of the LiMn100 electrode after electrochemical measurement in 1 M $LiNO_3$ were shown in Figure 3.31.

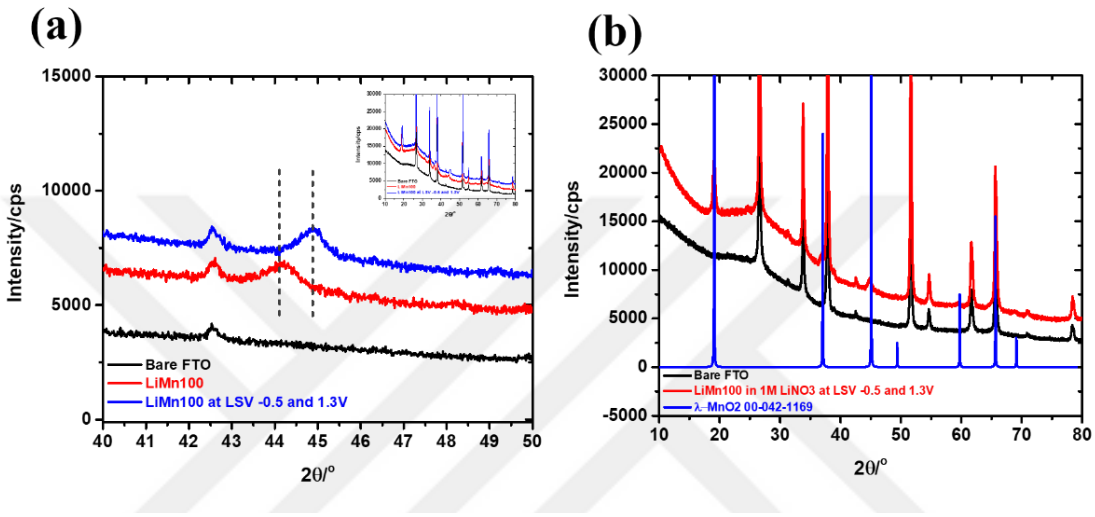

Figure 3.31 XRD patterns of LiMn100 and LiMn100 after LSV between -0.5 and 1.3 V in 1M $LiNO_3$: (a) magnified pattern and (b) full pattern with reference pattern of λ-MnO_2.

According to the XRD patterns of the LiMn100 electrodes before and after the electrochemical process, lithium ions are deintercalated from the $LiMn_2O_4$ electrode, and all the diffraction lines of LiMn100 belonging to spinel structure are shifted to higher 2θ values, see Figure 3.31(a). It means that the spinel crystal structure is preserved but the lattice parameters of the deintercalated crystals are decreased. The pattern can be indexed to the λ-MnO_2 phase upon deintercalation, see Figure 3.31(a). All the diffractions line alliance with the reference PDF card of λ-MnO_2 (ICDD card no. 00-042-1169). Many studies show that after lithium deintercalation, $LiMn_2O_4$ converts to the λ-MnO_2 phase. [115], [119]

To prove the reversibility of the LiMn100 electrode in terms of lithium intercalation and deintercalation process in our system, multiple LSV experiments were performed using the same electrode. First LSV measurement was performed on the LiMn100 electrode by starting from 0.6 V up to 1.2 V. After

proper washing and drying process, a diffraction pattern of the electrode was recorded. Same electrode was reused for a second LSV by reverse sweeping from 1.2 V to 0.6 V and another XRD pattern was recorded. This procedure is repeated 3 times to show the efficiency of lithium intercalation and de-intercalation on the same LiMn100 electrode. The LSV curves and XRD patterns after referred LSV curves are given in Figure 3.32.

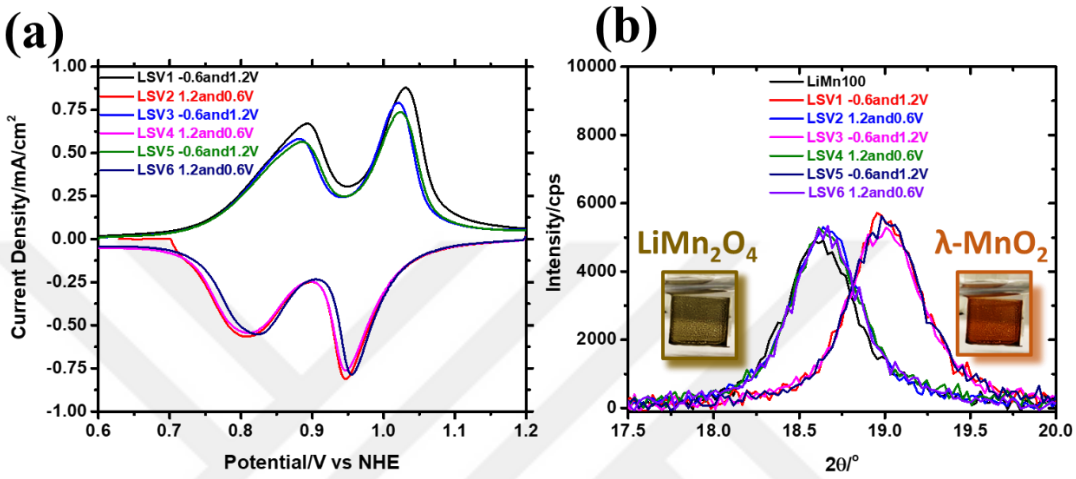

Figure 3.32 (a) Repeating LSV curves of LiMn100 between 0.6 and 1.2 V with a sweep rate of 5 mV/s, (b) XRD patterns of LiMn100 after repeating LSVs.

It is clear from the patterns (shown in Figure 3.32(b)) that the lithium deintercalation takes place and bulk $LiMn_2O_4$ is fully converted into λ-MnO_2 in the forward scan. Then, same electrode is swept back to 0.6 V from 1.2 V for the lithium intercalation back into the electrode. The diffraction line at 19.00°, 2θ, is shifted back to 18.64° and proves the conversion of the λ-MnO_2 back into $LiMn_2O_4$ without losing intensity, see Figure 3.32(b). When the LSV procedure is repeated several times, the diffraction lines are preserved the position and intensity and switches back and forth between $LiMn_2O_4$ and λ-MnO_2 line positions with respect to LSV direction. This is strong evidence that the lithium intercalation and deintercalation process is electrochemically reversible in our mesoporous LiMn100 electrodes. Brownish green color of $LiMn_2O_4$ and orange color of λ-MnO_2 were clearly observed during LSV experiments, see inset images in Figure 3.32 (b).

3.1.2.5 Quantitative Analysis of the Mesoporous $LiMn_2O_4$ Electrodes

Upon investigation of the manganese disproportionation reaction, lithium intercalation and deintercalation process were further analyzed by using the LiMn100 electrode in narrow potential windows. In this experiment, scan rate dependent measurements were carried out between 0.65 and 1.25 V, considering no disproportionation reaction occurs in this potential range. The CV curves of LiMn100 electrode are shown with scan rates varying from 2 to 20 mV/s with 2 mV/s increments in Figure 3.33.

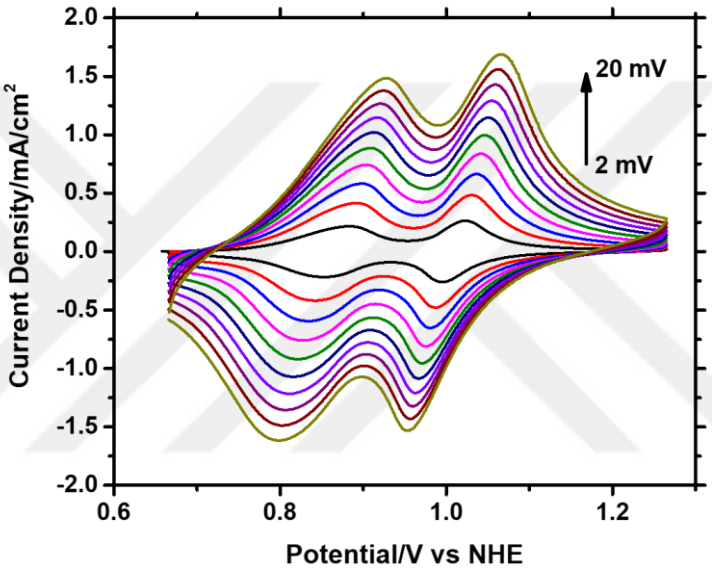

Figure 3.33 CV curves of LiMn100 electrode between 0.65 V and 1.25 V with scan rates from 2 mV/s to 20 mV/s with 2 mV/s increments.

The current density vs scan rate graphs were extracted from these CVs for each oxidation and reduction peak to quantify the lithium intercalation and deintercalation process using Equation 1.2. With respect to this equation, freely diffusing redox species show a direct relationship between the square root of scan rate versus current density. If the redox process is from the surface adsorbed species, then the scan rate is directly proportional to the current density and x = 1.[37] By using this information, the plots of both $\nu^{1/2}$ vs i_p and ν vs i_p are obtained for each peak. However, both plots failed to be linear. To eliminate this deviation, various values of x between 0.5 and 1 as the exponential of ν, were tested to obtain a perfect fit. The fitted graphs with suitable exponentials are shown in Figure 3.34 for all peaks.

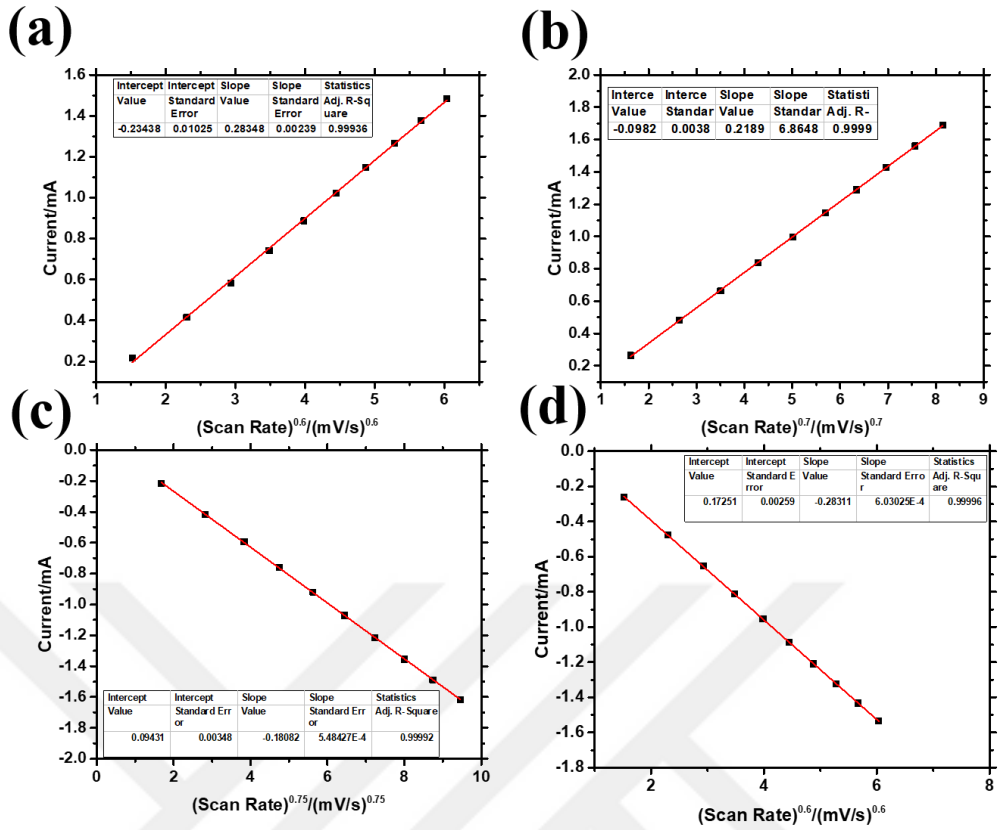

Figure 3.34 Graphs of ν^x vs i_p of LiMn100 electrode: (a) oxidation peak at 0.9 V where x: 0.6, (b) oxidation peak at 1.1 V where x: 0.7, (c) reduction peak at 0.8 V where x: 0.75, (d) reduction peak at 0.95 where x: 0.6.

All the graphs in the figure showed that the current density versus ν^x fits the best with x being 0.6 or 0.7. These values are almost in the middle of 0.5 and 1. Thus, lithium intercalation deintercalation processes show both freely diffusive (x = ½) redox property (the bulk of the material) and adsorptive (x = 1) redox property (surface of the electrode, maybe including pore surfaces) by these values.

For the quantitative analysis of the LiMn100 electrode, two experiments were performed to extract information about the catalytic load in the LiMn100 electrode. Determination of the weight of the mesoporous $LiMn_2O_4$ films is hard because of film thickness on the FTO surface. Weight measurements of the FTO coated electrode material using a 4-digit laboratory balance is not reliable, because even the weight of the thickest electrode is as big as the last digit of the balance and not reliable. A more sensitive (5 or 6 digit) balance is required to accurately determine the weight of the electrodes. Thus, it cannot be accurately

determined by using even a good laboratory balance. However, the electrochemical measurements can be very sensitive to determine the weight of the electrode by determining the total change of the non-faradaic and faradaic processes to quantify the active surface, catalytic sites, and directly intercalation and de-intercalation and weight of the sample. Firstly, the LiMn100 electrode was swept at a 5 mV/s scan rate from 0.65 to 1.2 V by a linear sweep voltammetry in 1 M $LiNO_3$. The main doubt in the experiment is whether all lithium content was deintercalated or trace amounts of lithium are still preserved in the structure. Remember that the 300 ^oC calcined sample showed only the λ-MnO_2 phase after the de-lithiation process. However, it is still possible to have a small amount of $LiMn_2O_4$ that may not be observed by XRD. Thus, this invisible $LiMn_2O_4$ diffraction might be amplified by annealing of the de-lithiated electrode at higher temperatures. For this reason, the diffraction line at 18.5^o, 2θ, of $LiMn_2O_4$ had been analyzed on the XRD patterns. In addition to the calcined and de-lithiated electrode, freshly prepared $LiMn_2O_4$ electrode at 2000 rpm was also annealed at the same temperature. Thus, areas of the diffractions were compared to make an assumption for the lithium content bearing in the structure. In Figure 3.35, diffraction patterns between 17.5^o and 20.0^o of LiMn100 electrodes annealed at 600 ^oC and annealed electrode at 600 ^oC after de-lithiation are shown.

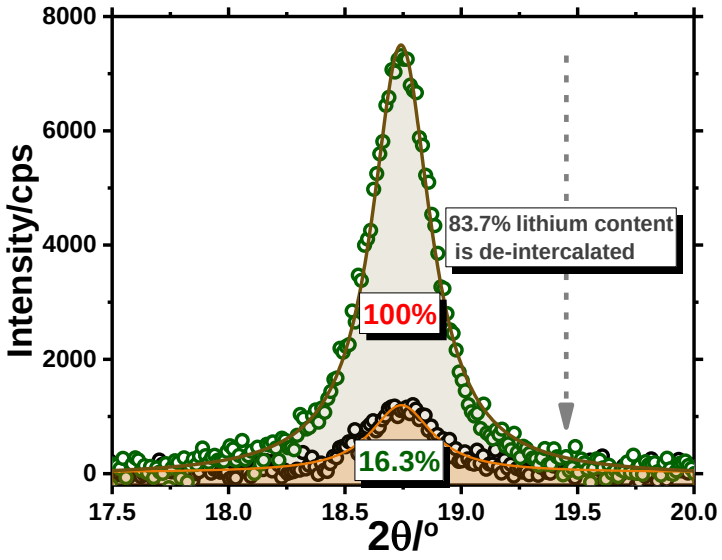

Figure 3.35 XRD patterns of LiMn100 electrodes: annealed at 600 ^oC for 1 hour (green), annealed at 600 ^oC for 1hour after de-lithiation by LSV between 0.65 and 1.2 V.

In our assumption, LiMn100 at 600 °C bears 100% of lithium content which is attributed to the diffraction area of $LiMn_2O_4$. After de-lithiation and annealing $LiMn_2O_4$, the diffraction area decreased to 16.3%. This means 83.7% of lithium leaves the structure during the LSV process. This assumption provides a much more accurate catalytic mass on the FTO surface after obtaining charge density information by LSV measurements. The LSV of the LiMn100 electrode between 0.65 and 1.2V is shown in Figure 3.36(a).

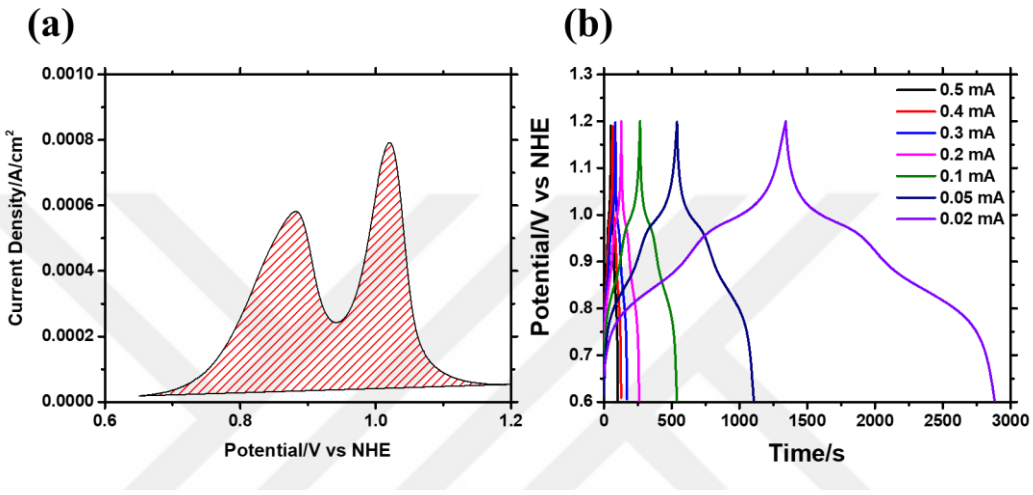

Figure 3.36 (a) LSV curve of LiMn100 between 0.65 and 1.25 V with a scan rate of 5 mV/s in 1 M $LiNO_3$ and (b) Galvanostatic charge-discharge (GCD) curves of LiMn100 between 0.6 and 1.2 V by various current densities.

To get an efficient lithium de-intercalation from $LiMn_2O_4$, the LSV experiment was performed at a 5 mV/s scan rate. Charge by the lithium de-intercalation process was calculated by integrating the area under the LSV curve (see Figure 3.36(a)), under two faradaic peaks, and dividing the area value into scan rate values, see Equation 1.4. Thus, the charge is calculated to be 24.2 mC for the LiMn100 electrode at 2000 rpm (Figure 3.36(a)), corresponding to 1.51×10^{17} electrons, where the charge of an electron is 1.62×10^{-19} C. This corresponds to Mn (III) oxidation to Mn (IV) to form MnO_2 and the amount of lithium-ion eliminated from the electrode. Dividing the number of electrons (1.51×10^{17}) to Avogadro's number gives mol of $LiMn_2O_4$ (2.507×10^{-7} mol) and multiplying by the molecular weight of $LiMn_2O_4$ (180.8 g/mol) gives the mass of the electrode. Finally, the delithiation percentage (83.7%), obtained previously from the XRD analysis is also considered. Thus, 24.2 mC corresponds to 54.3 µg of a catalytic load. The formula is given in Equation 3.1. Notice that this mass cannot be accurately measured using a 4-digit sensitive balance.

$$\text{Catalytic load } \left(\frac{\mu g}{cm^2}\right) = \frac{\text{q } \left(\frac{A \cdot s}{cm^2}\right) \times 180.8 \left(\frac{g}{mol}\right) \times 10^6 \left(\frac{\mu g}{g}\right) \times 100}{1.6 \times 10^{-19} \left(\frac{A \cdot s}{e}\right) \times 6.022 \times 10^{23} \left(\frac{e}{mol}\right) \times 83.7} \qquad \textbf{Equation 3. 1}$$

Galvanostatic charge-discharge (GCD) experiments were also performed using the LiMn100 electrode at various current densities, see Figure 3.36(b). The charge capacities (lithium deintercalation) of LiMn100 electrode are tabulated at corresponding current densities in Table 3.1.

GCD current density/mA/cm^2	Charge capacity/A.s
0.5	0.0256
0.4	0.0253
0.3	0.0255
0.2	0.0259
0.1	0.0266
0.05	0.0269
0.02	0.0268

Table 3.1 Capacity values by GCD of LiMn100 electrode at various current densities.

According to the results of the GCD curves of the LiMn100 electrode, the charge capacities increase by decreasing the GCD current density, see Table 3.1. This is expected because slower scanning by decreasing current density in the charge-discharge process ensures a more efficient de-lithiation than a fast one. Thus, the GCD experiments that are carried out at 0.05 mA/cm^2 and 0.02 mA/cm^2 are more effective for determining catalyst load since the lithium de-intercalation process provides a better result in terms of evaluating charge capacities and evaluating the catalytic load of the electrodes. A charge capacity of 26.9 mC corresponds to 1.68x10^{17} electrons and 59.7 µg catalytic load on the FTO surface. The GCD analysis is a convenient method for the determination of the weight of battery-type electrodes. Therefore, this electrochemical technique might be used for further catalytic load analysis related to $LiMn_{2-x}M_xO_4$ in 1 M $LiNO_3$ electrolyte. Also note that from our previous studies, we have determined the amount of coated material is about 0.1 mg from a large area coating weight measurement using a 4-digit balance. Therefore, it is clear that balance experiments do not provide reliable results for these types of thin film electrodes; the electrochemical measurement is a better and more reliable method.

3.1.2.6 Electrochemical Analysis of $LiMn_2O_4$ Electrodes in KNO_3

The LiMn100 electrode was also tested in a 1 M KNO_3 electrolyte. The electrode was cycled two times between -0.5 and 1.3 V until lithium deintercalation peaks completely disappeared, see Figure 3.4(c). In the 3rd cycle, the CV measurement was stopped at 1.3 V, and an XRD pattern was recorded. Figure 3.37 shows the XRD patterns of the LiMn100 electrode after CV and LSV between -0.5 and 1.3 V.

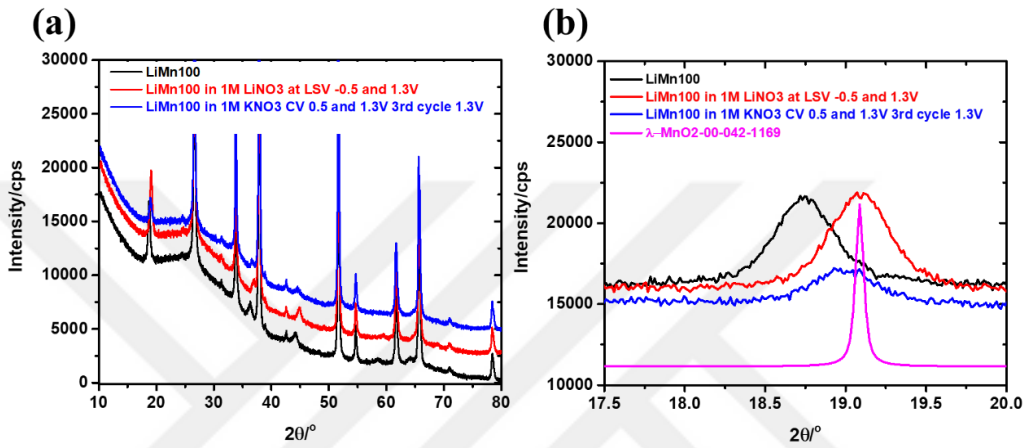

Figure 3.37 XRD patterns of LiMn100 and LiMn100 after LSV between -0.5 and 1.3 V in 1M KNO_3: (a) full pattern and (b) magnified pattern with a reference pattern of λ-MnO_2.

The XRD patterns of $LiMn_2O_4$, λ-MnO_2, and cycled LiMn100 in 1 M KNO_3 electrodes are compared in Figure 3.37 (a). According to the XRD patterns, shown in Figure 3.37 (b), the LiMn100 electrode in KNO_3 displays diffraction lines shifted to higher 2θ values after the lithium de-intercalation process as expected. The diffraction pattern still originates from the spinel structure but the shifts in diffraction lines are not as much compared to LiMn100 after LSV in the $LiNO_3$ electrolyte. Therefore, the other crystal phases of MnO_2, Mn_3O_4, and Mn_2O_3 were compared using their PDF reference data and found that there is no crystal structure, which fits with this diffraction pattern of LiMn100 after cycling in KNO_3 solution, maybe indicating a partial deintercalation in the KNO_3 solution.

The LiMn100 electrode was cycled 3 times and sweeping was stopped at 0.4 V and -0.3 V on the reverse side of the cycle in 1 M KNO_3 electrolyte. Then, the XPS spectrum was recorded at these potentials to investigate K^+ intercalation into λ-MnO_2 upon negative sweeping. Figure 3.38 displays K 2p and Mn 2p regions of

the XPS survey spectrum. Its analysis provides the atomic percentages of potassium and manganese as 3.5 and 96.5 %, respectively, at both potentials. This proves that partial potassium intercalation takes place in the reduction peak at 0.9 V, see Figure 3.4(c). Thus, the redox couple observed at around 1 V in the KNO_3 electrolyte might be attributed to partial potassium intercalation and de-intercalation process into MnO_2.

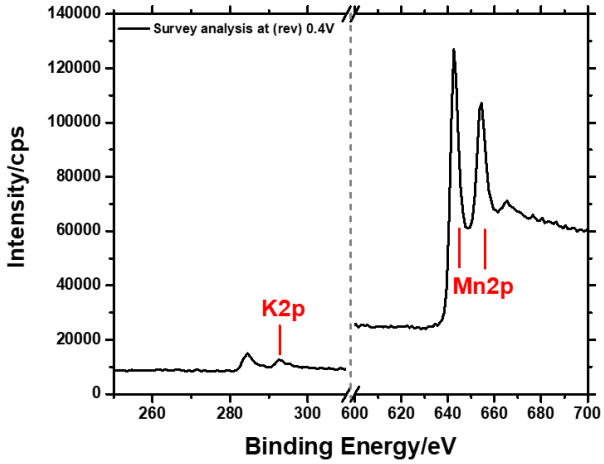

Figure 3.38 XPS survey analysis of LiMn100 electrode after cycling in 1 M KNO_3 and stopped at reverse side 0.4 V.

Furthermore, another acidic electrolyte (HNO_3/KNO_3) was used to investigate the lithium intercalation and MnO_4^- formation in a lithium-poor environment. The electrolyte solution was prepared using the same procedure and its pH was measured to be 3.14. The recorded CVs of the LiMn100 electrode are shown in Figure 3.39.

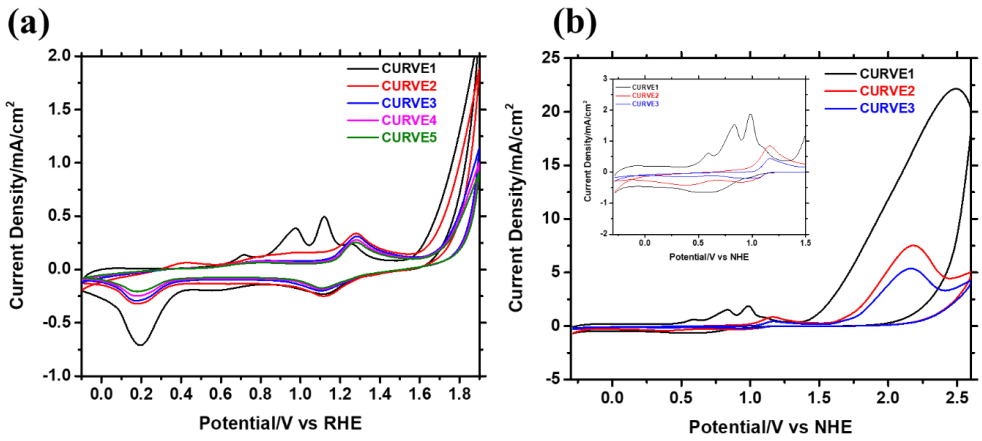

Figure 3.39 Cyclic voltammogram of LiMn100 in electrolyte composed of HNO_3 and KNO_3 (pH 3.14): (a) potential range between -0.3 and 1.7 V vs NHE with a scan rate of 5 mV/s, (b) potential range between -0.3 and 2.6 V with a scan rate of 20 mV/s, inset graph: magnified version of cyclic voltammogram between -0.3V and 1.5 V.

The typical lithium de-intercalation occurs at around 1 V, where the electrode composition becomes MnO_2, see Figure 3.39(a). In the reverse cycle, swept from 1.9 to -0.1 V vs RHE, a single reduction peak appears at 1.1 V. This is clearly not due to a lithium intercalation process since the electrolyte is lithium-poor. Thus, this reduction might be the reduction of MnO_2, which is formed by the de-intercalation of lithium from the LiMn100 electrode. It might be due to the formation of MnOOH, as discussed in the XPS section and further reduction at 0.2 V could be due to the formation of $Mn(OH)_2$. The origin of the reduction peak at 1.1 V might also be due to K^+ intercalation into MnO_2 to form K_xMnO_2. Further analysis using EDX or XPS data are needed to fully understand this oxidation process. Figure 3.39(b) displays CVs in a wide potential window. The CVs display other oxidation peaks starting at 1.5 V and are attributed to MnO_4^- formation. Thus, the electrode behavior is very similar to the acidified $LiNO_3$ electrolyte in the wide potential window.

The CV curves of the LiMn100 electrode in $HNO_3/LiNO_3$ and HNO_3/KNO_3 electrolytes in a -0.3 and 2.6 V potential window are shown in Figure 3.25(b) and Figure 3.39(b), respectively. The Mn (VII) species form in the OER potentials in both electrolytes. The current density of the permanganate peak at around 2.4 V is higher, if the electrode is used in an acidic KNO_3 electrolyte. This may be due to the K^+ ion, which is a more common counter cation for permanganate ion than Li^+ ion. In the reverse direction, the reduction of permanganate ion in acidic KNO_3 solution displays a lower current density than in the acidic $LiNO_3$ electrolyte, indicating that the $[MnO_4]^-$ ions are leached out more from the electrode surface in KNO_3 electrolyte as $KMnO_4$ and dissolved in the electrolyte solution rather than getting reduced back to MnO_2; potassium permanganate leaching is more efficient than lithium permanganate. Previous studies showed that the decomposition mechanism of alkali metal permanganates depends on the counter cation.[123], [124] The permanganate decomposition rates have been investigated using molten alkali-metal nitrates. The highest decomposition rate for the manganates was found in a mixture of molten potassium and lithium nitrates having a higher mole percentage of Li^+. This may be evidence for a more favored decomposition reaction of permanganate with the existence of lithium-ion in the media.[123], [124]

3.1.2.7 Electrochemical Analysis of Mn_3O_4 Electrode

The LiMn100 electrode was further tested by using 1 M KNO_3. The CV of the LiMn100 electrode in the -0.5 to 1.5 V potential range with a scan rate of 5 mV/s is shown in Figure 3.40(a). Also, a Mn_3O_4 electrode was prepared by the MASA method using a 40:1:1 mole ratio of manganese salt: CTAB: P123 and was used in the same potential window in 1 M $LiNO_3$ to collect multiple CVs, see Figure 3.40(b).

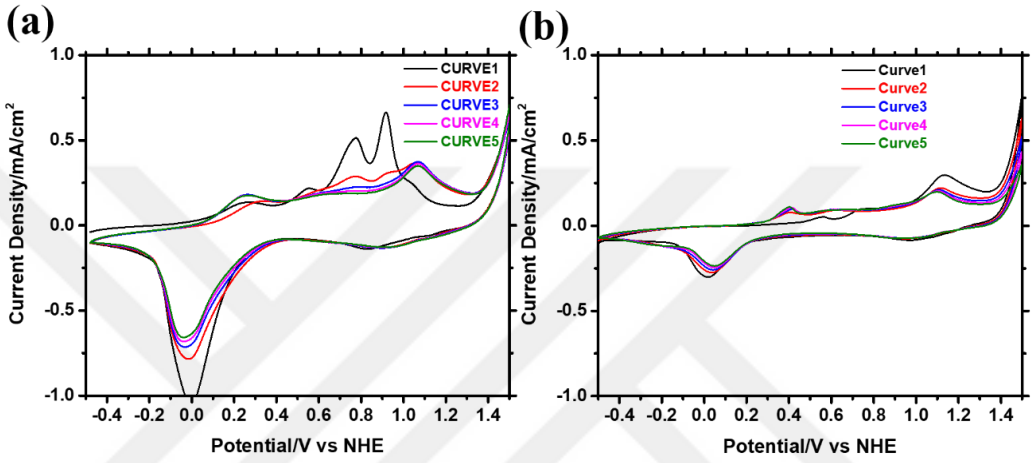

Figure 3.40 CV curves of the electrodes in potential range between -0.5 and 1.5 V with a scan rate of 5 mV/s: (a) LiMn100 in 1 M KNO_3, (b) Mn_3O_4 in 1 M $LiNO_3$.

The LiMn100 electrode in KNO_3 shows similar behavior to the Mn_3O_4 electrode in the $LiNO_3$ electrolyte. According to the CV curves of the LiMn100 electrode in 1 M KNO_3 (Figure 3.40(a)), the 1st CV curve shows a similar deintercalation process between 0.7 and 1.2 V. Also, a sharp oxidation peak appeared at 0.25 V for LiMn100 in 1 M $LiNO_3$ (Figure 3.5 (a)), which is not observed in the KNO_3 electrolyte. In the $LiNO_3$ electrolyte, the peak is due to lithium insertion to form $Li_2Mn_2O_4$. However, the $Li_2Mn_2O_4$ formation is not possible in the KNO_3 electrolyte. On the reverse cycle of the CV, lithium intercalation is not observed in the KNO_3 electrolyte. Rather a new reduction peak at 0.9 V is observed instead of two lithium intercalation peaks, also proving the change in electrode composition. Further cycling of the LiMn100 electrode in KNO_3 causes a gradual decrease of the Li-deintercalation peak currents and the peak at 1.1 V becomes visible at the end of the 5th cycle. These changes may be due to the formation of Mn_3O_4 species, because of the lack of lithium ion in the

KNO_3 solution. To prove this, the Mn_3O_4 electrode was also tested in 1 M $LiNO_3$ electrolyte. The CV curves of the Mn_3O_4 electrode in $LiNO_3$ in the same potential range and scan rate are shown in Figure 3.40 (b). For the comparison of the CV curves of Mn_3O_4 and LiMn100 electrodes, LiMn100 shows a similar curve shape with Mn_3O_4 after the cycling process.

To understand the Mn_3O_4 surface and get information about manganese sites, the Mn_3O_4 electrode was cycled in 1 M $LiNO_3$ in several potential ranges. Firstly, the cycling of Mn_3O_4 was carried between -1.0 and 1.5 V, see Figure 3.41 (a).

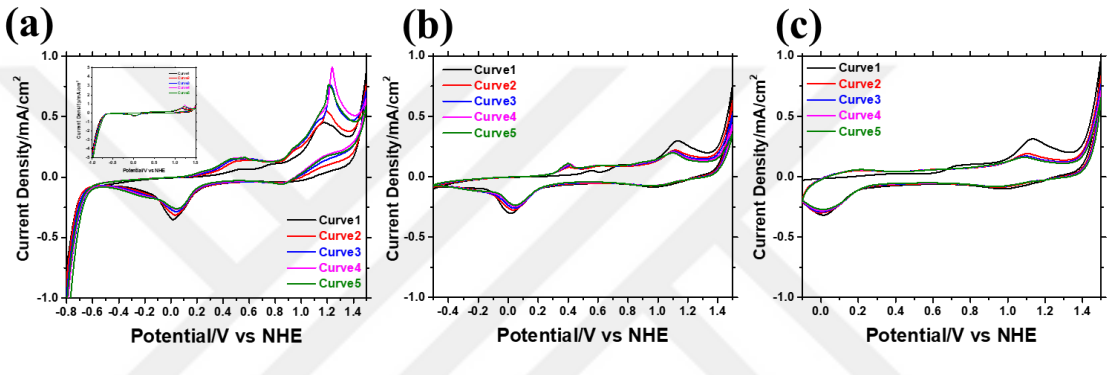

Figure 3.41 Cyclic voltammogram of Mn_3O_4 in 1 M KNO_3 (a) magnified version of potential range between -1.0 and 1.5V with a scan rate of 5 mV/s, inset graph: full version of cyclic voltammogram between -1V and 1.5V, (b) potential range between -0.5 and 1.5 V with a scan rate of 5 mV/s, (c) potential range between -0.1 and 1.5 V with a scan rate of 5 mV/s.

According to the voltammogram, water reduction (HER) is dominant between -1.0 and –0.6 V. This catalytic process is due to OH^-, produced on the electrode surface, and triggers the $Mn(OH)_2$ formation. In the 1st CV, the manganese hydroxide phase is sequentially oxidized to Mn_3O_4 and Mn_2O_3 at more positive potentials, namely a voltage range between 0.2 and 0.7 V. On the more positive potential side, between 0.8 and 1.4 V, the MnO_2 formation is observed by the oxidation of these species at 1.15 V.

Reverse sweeping in the curve to the negative potential side causes MnO_2 reduction to form MnOOH, like $LiMn_2O_4$ discussed in the XPS section. Reduction of MnOOH to $Mn(OH)_2$ occurs at 0 V. In the 2nd CV cycle, the oxidation of $Mn(OH)_2$ to Mn_3O_4 and Mn_2O_3 is more dominant between 0.2 and 0.7 V. Further oxidation produces MnO_2 between 1.0 and 1.4 V, evident as two overlapped peaks in the

CV. The first shoulder peak belongs to Mn_xO_y oxidation to MnO_2 and the second sharp peak is due to oxidation-free Mn^{2+} and deposition on the electrode surface as MnO_2. This is because the electrolyte solution still has free Mn(II) ions from the disproportionation of Mn(III) species. The peak current due to MnO_2 deposition is gradually enhanced because the new MnO_2 layer deposition is triggered by further cycling. We already showed this deposition and peak shape in acidified $LiNO_3$ electrolyte experiments. When the potential window is reduced to -0.5 and 1.5 V range, the surface $Mn(OH)_2$ oxidation could be clearly observed at 0.3 V and it is followed by MnO_2 oxidation at 1.1 V, see Figure 3.41 (b). If the CV measurement is started at -0.1 V, no surface $Mn(OH)_2$ oxidation is observed at 0.3 V in the 1st cycle, the Mn_xO_y species are oxidized to MnO_2 which most likely reduces back to MnOOH in the reverse sweep. The reduction peak at 0 V is a transformation of MnOOH to $Mn(OH)_2$. In the 2nd and further cycles, small broad reversible peaks appear at 0.2 and 0 V in the oxidation-reduction sides, respectively and they are assigned to a reversible $Mn(OH)_2$/Mn(OOH) redox couple.

After potential window-dependent CV measurements of the Mn_3O_4 electrode, the same electrode is used to collect its XPS spectra to sign some light on the oxidation and reduction reaction mechanism of the electrode surface. The LSV was recorded by starting at -0.1 V. Then, the measurement was stopped at 0.95 V (before MnO_2 formation) and 1.3 V (after MnO_2 formation), see Figure 3.41 (c). The spectra of the electrodes at these two potentials were compared with the unused Mn_3O_4 electrode. The O 1s, Mn 2p, and Mn 3s XPS spectra are shown in Figure 3.42.

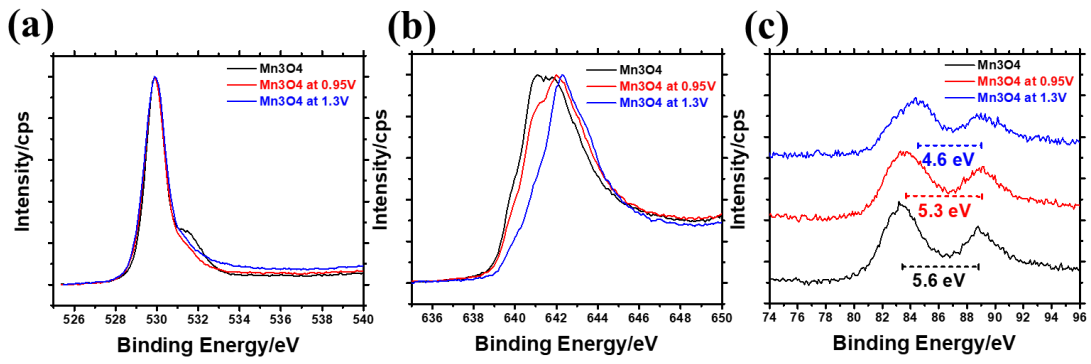

Figure 3.42 XPS spectra of Mn_3O_4 and Mn_3O_4 at 0.95 V and $LiMn_2O_4$ at 1.3 V in the (a) O 1s, (b) Mn 2p ($^2P_{3/2}$), and (c) Mn 3s regions.

According to the XPS O 1s spectra of the Mn_3O_4 electrode, the electrode surface has an enhanced OH^- content and appears as a shoulder at 531.2 eV, see Figure 3.42 (a). Also, similar information is gathered from the Mn 2p region (Figure 3.42 (b)) by observing an amplified peak at around 641 eV due to Mn(II) on the electrode surface. The peak shape in the Mn 2p region is due to the presence of both Mn(II) and Mn(III) species. Also, the Mn 3s displays a splitting of 5.6 eV between the main peak and peak due to multiplet-coupling, corresponding to a manganese oxidation state of Mn(II) and Mn(III), see Figure 3.42 (c).[118] When the electrode is swept from -0.1 to 0.95 V (Figure 3.41 (c)), the OH^- content of the surface is decreased because of oxidation of the surface $Mn(OH)_2$. This is evident by the decay of the shoulder at 531.2 eV in the O 1s spectrum, see Figure 3.42 (a). Additionally, the Mn 2p and 3s XPS spectra change by oxidation of the manganese species and display a diminishing of the peak at 641 eV and decreasing of the Mn 3s peak splitting energy (from 5.6 to 5.3 eV), see Figures 3.42(b) and (c), respectively. Finally, the Mn_3O_4 electrode was swept to 1.3 V to check what happens in the next oxidation peak at 1.1 V, see Figure 3.41(c). Upon oxidation of Mn_3O_4 at 1.3 V, the XPS spectra clearly show that the electrode is completely converted into MnO_2. Notice that the O 1s region, after oxidation at 1.3 V, displays only the lattice oxygen peak, see Figure 3.42(a). The Mn 2p region shows a typical MnO_2 peak shape as discussed in the LiMn100 XPS analysis section (section 3.1.2.1), see Figure 3.42(b). Lastly, the Mn 3s spectrum of the Mn_3O_4 electrode at 1.3 V is recorded and displayed in Figure 3.42 (c). The peak separation between the two peaks in the Mn 3s region is 4.6 eV and is attributed to MnO_2 formation.

The Mn_3O_4 electrode is further characterized electrochemically to elucidate the surface behavior of the lithiated manganese oxides. The surface of the Mn_3O_4 electrode displays some differences compared to the $LiMn_2O_4$ electrode surface after the electrochemical process. However, surface MnO_2 formation was observed for both Mn_3O_4 and LiMn100 electrodes at higher voltages.

3.1.2.8 *Inductively Coupled Plasma Mass Spectrometry (ICP-MS) Analysis of $LiMn_2O_4$ Electrodes in Aqueous Electrolytes*

The ICP-MS technique was used to determine amounts of manganese dispersed into electrolytes due to the manganese disproportionation reaction. The LiMn100 electrodes were electrochemically cycled between 0.3 and 1.3 V, -0.5 and 1.3 V, and, 0.3 and 2.4 V in 20 ml of 1 M $LiNO_3$ and 1 M KNO_3 electrolytes. After 3 cycles in these electrolytes, 7 ml of the electrolyte was drawn with a syringe into a vial and 1 ml of 3 M HNO_3 solution was added to adjust the H_3O^+ concentration of the solution to 0.375 M. Manganese contents in these solutions were determined using ICP-MS technique. Similarly, the Mn_3O_4 electrode was also tested in 1 M KNO_3 electrolyte by cycling between 0.3 and 2.4 V as a control experiment and also to compare the manganese disproportionation amount with $LiMn_2O_4$ disproportionation.

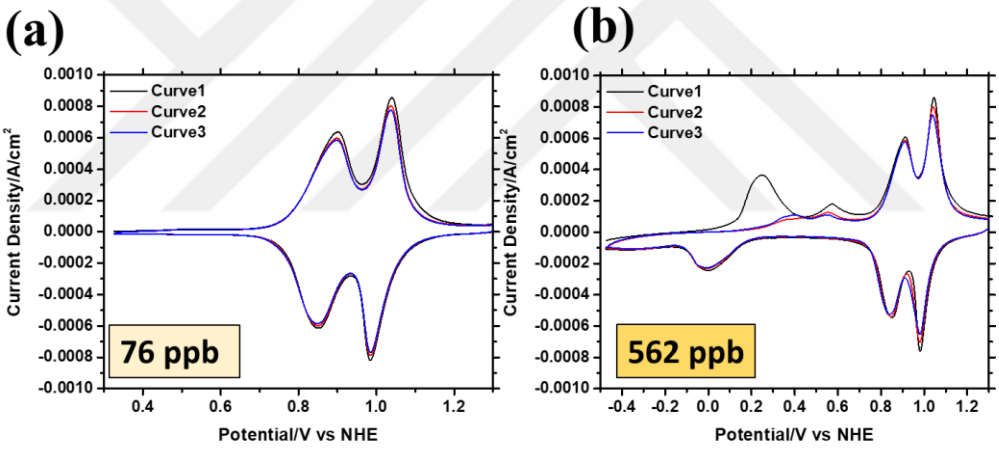

Figure 3.43 CV curves of LiMn100 in 1M $LiNO_3$ with a 5 mV/s scan rate between (a) 0.3 V and 1.3 V, (b) -0.5 V and 1.3 V.

The LiMn100 electrode was cycled between 0.3 and 1.3 V in 1 M $LiNO_3$ electrolyte (Figure 3.43(a)) and the manganese amount in 7 ml of the electrolyte was measured to be 76 ppb. Then, a fresh electrode was cycled 3 times between - 0.5 and 1.3 V to determine the manganese amount in the electrolyte due to Mn(III) disproportionation, see Figure 3.43(b). Manganese dispersed into the electrolyte was determined to be 562 ppb. This might be attributed to small manganese lost in the electrode due to Mn(III) disproportionation at 0.2V.

Then LiMn100 electrode was cycled between 0.3 and 2.4 V in 1 M $LiNO_3$ to determine Mn(VI) disproportionation, see Figure 3.44(a). After cycling the electrode, the ICP-MS results show that the manganese dispersed into 7 mL of electrolyte is about 1163 ppb. A new fresh LiMn100 electrode was cycled in the same potential window in a 1 M KNO_3. The manganese in 7 mL solution was determined as 2738 ppb. CV of LiMn100 electrode in 1 M KNO_3 is shown in Figure 3.44(b). The inset photograph in Figure 3.44(b) also shows the purple permanganate formation on the electrode surface.

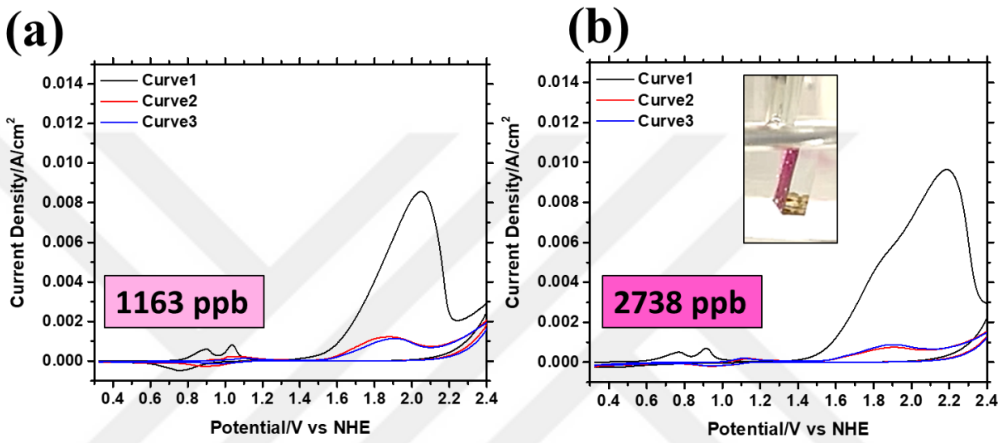

Figure 3.44 CV curves of LiMn100 between 0.3 V and 2.4 V with a 5 mV/s scan rate in (a) 1M $LiNO_3$, (b) in KNO_3, inset photograph: electrode surface at 2.2 V.

According to ICP-MS results, the Mn(VI) disproportionation is significantly enhanced in the presence of K^+ ion in the electrolyte compared to Li^+ ion and visible by the naked eye. This has been attributed to K^+ ions being a more convenient cation for the release of permanganate (MnO_4^-) ions from the electrode surface. This is also evident in the total charge under intense peaks at 2 V, compare Figure 3.44(a) and (b). Also, the pink color of permanganate is more intense in the KNO_3 electrolyte at 2.1 V.

The ICP-MS technique was also employed to determine Mn(VI) disproportionation from the Mn_3O_4 electrode and compared to that of the LiMn100 electrode in 1 M KNO_3 solution. For this analysis, the Mn_3O_4 electrode was cycled between 0.3 and 2.4 V, similar to the LiMn100 electrode. The CV curves of the LiMn100 and Mn_3O_4 electrodes in 1 M KNO_3 electrolytes are shown in Figure 3.45.

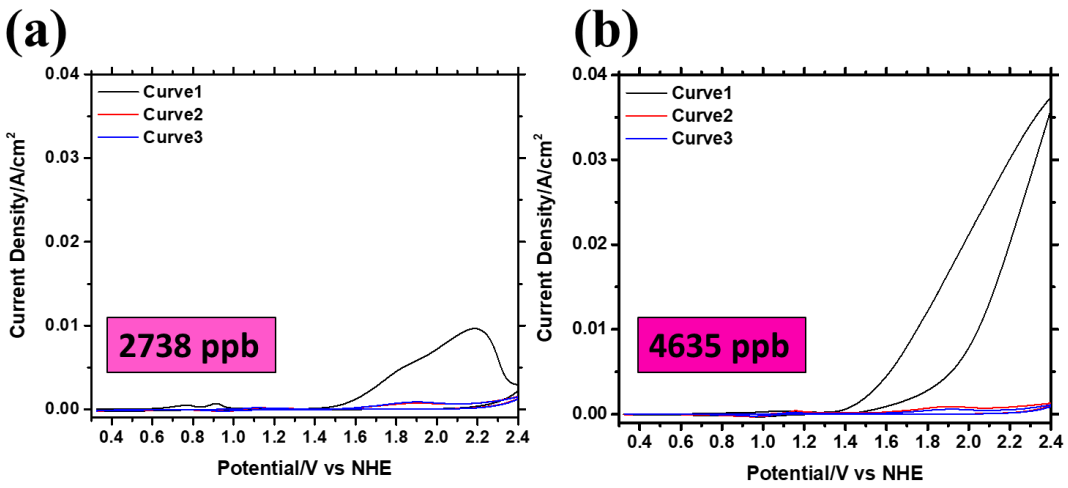

Figure 3.45 CV curves of electrodes between 0.3 V and 2.4 V in 1M KNO_3 with a 5 mV/s scan rate: (a) LiMn100, (b) Mn_3O_4

Using the ICP-MS data, the calculated manganese amount (due to Mn(VI) disproportionation) is almost two times higher (4635 ppb) from the Mn_3O_4 electrode compared to the LiMn100 electrode. This is also evident in the total charge under the peak at 2 V; the Mn_3O_4 electrode has a higher charge density under this peak. Thus, the permanganate formation is elevated with a distinct pink color, visible to the naked eye. Therefore, it is reasonable to conclude that the lithium in the spinel $LiMn_2O_4$ structure limits the Mn(VI) disproportionation reaction, maybe because of the unique structure of the λ-MnO_2 phase.

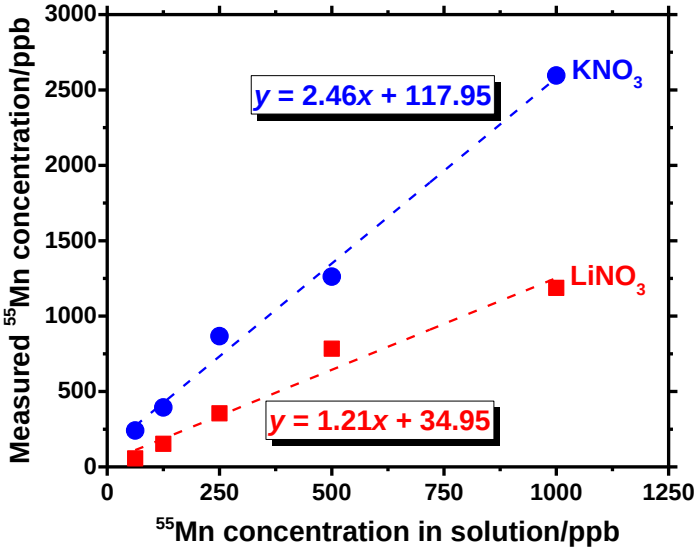

Figure 3.46 Constructed ICP-MS calibration curves of manganese in K^+ and Li^+ rich solutions.

Notice that, the manganese amount is 2738 ppb in 7ml of electrolyte as determined from the ICP-MS data from the $LiMn_2O_4$ electrode, cycled between 0.3 V and 2.4 V in 1M KNO_3. This corresponds to 62.5 µg $LiMn_2O_4$ in 20 ml electrolyte and is not consistent with the catalytic load (54.3 µg) of the LiMn100. This might be interferences in the ICP-MS data. To compensate for this problem, we construct a new calibration curve using 62.5, 125, 250, 500, and 1000 ppb of manganese solutions in a potassium and nitrate-rich environment. For new calibration curves, the theoretical concentrations of manganese were plotted with respect to measured concentrations of manganese. The calibration curves are shown for lithium and potassium-rich solutions of manganese in Figure 3.46.

Based on the new calibration curves in Figure 3.46, the manganese amounts are determined to be much higher (almost 2.5 times) than their actual concentrations in the potassium-rich solutions. In the lithium-rich solutions, there is still some deviation is slightly less, but not as much as the potassium nitrate solutions. The origin of the deviation in the potassium nitrate solution might be due to interference of certain ionic species with a mass of 55 (same as ^{55}Mn). Previous studies have shown that one possible interference is from $^{39}K^{16}O^+$ molecular ion.[125] Since Ar is used as the purging gas, the formation of $ArNH^+$ ion also contributes to total ICP-MS intensity. Therefore, a correction is needed to accurately report the Mn dispersed in the electrolyte solution; the corrected values are tabulated in Table 3.2. The manganese quantity is found to be 41.9 µg from the LiMn100 electrode, cycled between 0.3 and 2.4 V in 1 M KNO_3 and consistent with the catalyst load evaluated from the electrochemical experiments.

Electrode/Electrolyte/Potential Window	Measured Mn (ppb)	Corrected Mn (ppb)	Corrected Mn (µg)
Mn_3O_4/KNO_3/0.3-2.4 V	4635	1836	41.9
LiMn100/KNO_3/0.3-2.4 V	2738	1065	24.3
LiMn100/$LiNO_3$/0.3-2.4 V	1163	932	21.3
LiMn100/$LiNO_3$/0.3-1.3 V	76	34	0.7
LiMn100/ $LiNO_3$/-0.5-1.3 V	562	435	9.9

Table 3.2 ICP-MS results of manganese, dispersed into the electrolyte solutions after cycling.

3.1.3 Electrochemical Characterization of Mesoporous $LiMn_2O_4$ Electrodes in Non-Aqueous Electrolytes

In this section, the LiMn100 electrode behavior in non-aqueous electrolytes was investigated. The main aim of this investigation is to avoid electro-catalytic water oxidation and reduction reactions in a wide potential range and also eliminate the surface formations on the electrode due to hydronium, hydroxide, and H_2O attacks. Thus, acetonitrile (MeCN) solution was used as an electrolyte solution by dissolving $LiClO_4$ and $NaClO_4$ salts in MeCN.

First, CVs of the LiMn100 electrode in 1 M $LiClO_4$/MeCN were recorded using a three electrode cell, in which an Ag wire was used as the reference electrode and Pt wire as the counter electrode. The LiMn100 working electrode was firstly cycled between 0.75 and 1.5 V vs Ag/Ag^+ at a 5 mV/s scan rate, see Figure 3.47 (a).

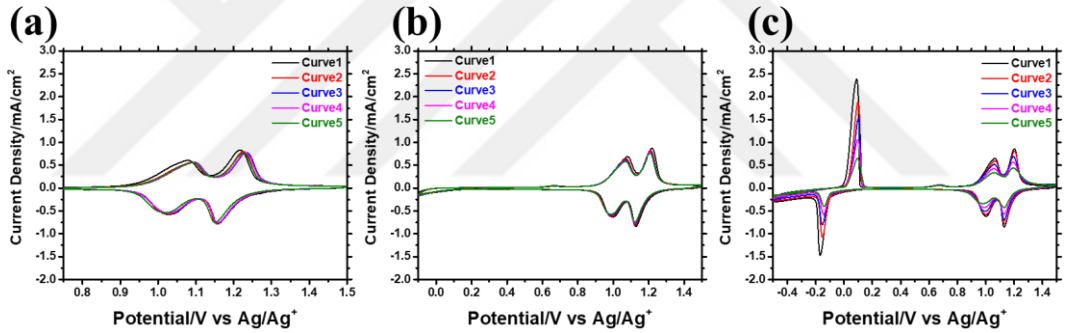

Figure 3.47 Cyclic voltammogram of LiMn100 in 1M $LiClO_4$ in MeCN: (a) potential range between 0.75 and 1.5 V vs Ag/Ag^+ with a scan rate of 5 mV/s, (b) potential range between -0.1 and 1.5 V vs Ag/Ag^+ with a scan rate of 5 mV/s, and (c) potential range between -0.5 and 1.5 V vs Ag/Ag^+ with a scan rate of 5 mV/s.

This potential range includes the lithium intercalation and deintercalation processes of the $LiMn_2O_4$ in this electrolyte and cell configuration. Manganese content remains unchanged by cycling as observed with no redox peak current decrease. Then, a CV was recorded from -0.1 to 1.5 V with a scan rate of 5 mV/s, see Figure 3.47 (b). The Li-intercalation and de-intercalation processes take place between 0.8 V and 1.4 V. Faradaic current density of the total process, decreases slightly by further cycles. Therefore, the Mn(III) disproportionation and Mn(II) dissolving into the electrolyte might occur, which means a loss in manganese content on the electrode. In previous sections, the

peak at 0.55 V vs NHE was assigned to the oxidation of the surface Mn_3O_4 and Mn_2O_3 into MnO_2 in aqueous electrolytes. This peak shifts to 0.65 V vs Ag/Ag^+ in the non-aqueous system.

The LiMn100 electrode was cycled between -0.5 and 1.5 V in 1 M $LiClO_4$ acetonitrile electrolyte, see Figure 3.47 (c). Notice that lithium redox peaks of lithium insertion into $LiMn_2O_4$ are clearly observed between -0.2 and 0.2 V. Thus, the manganese species undergo Mn(III) disproportionation into Mn(II) and MnO_2. The manganese content in the LiMn100 electrode is reduced by disproportionation reaction and results in a decay of the redox peak current densities between 0.8 and 1.4 V. Further cycling also decreases the manganese in the LiMn100 electrode that could be observed in cyclic voltammogram of LiMn100 in Figure 3.47 (c).

Furthermore, the lithium insertion into $LiMn_2O_4$ was analyzed by the XRD technique. Lithium insertion results in the formation of $Li_2Mn_2O_4$. To show this, the XRD pattern was recorded after LSV measurements between -0.5 and -0.2 V, and additionally between -0.5 and 0.1 V (after oxidation peak at 0 V) in $LiClO_4$ electrolyte. Then, the diffraction patterns at these potentials were compared with the reference $LiMnO_2$ in the database to show the lithiated spinel structure formation. The LSV curves and XRD patterns at -0.2 and 0.1 V are shown in Figures 3.48(a) and (b), respectively.

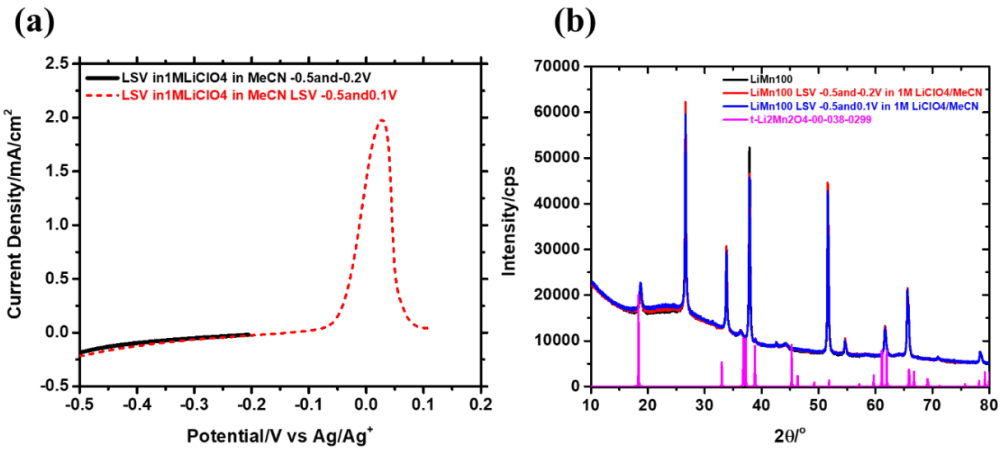

Figure 3.48 (a) LSV curves of LiMn100 in 1 M $LiClO_4$ MeCN solution and (b) XRD patterns of LiMn100 at referring potentials at the end of LSV curves.

No change is observed in the XRD patterns of LiMn100 at -0.2 and 0.1 V, see Figure 3.48 (b). No $Li_2Mn_2O_4$ formation was detected. Thus, as alternative methods might be GCD experiments and in-situ XRD measurements for the identification of $Li_2Mn_2O_4$ experimentally.

The Mn(III) disproportionation reaction was investigated by collecting 15 CV curves between -0.5 and 1.5 V in 1 M $LiClO_4$/MeCN solution at a 10 mV/s scan rate, see Figure 3.49(a).

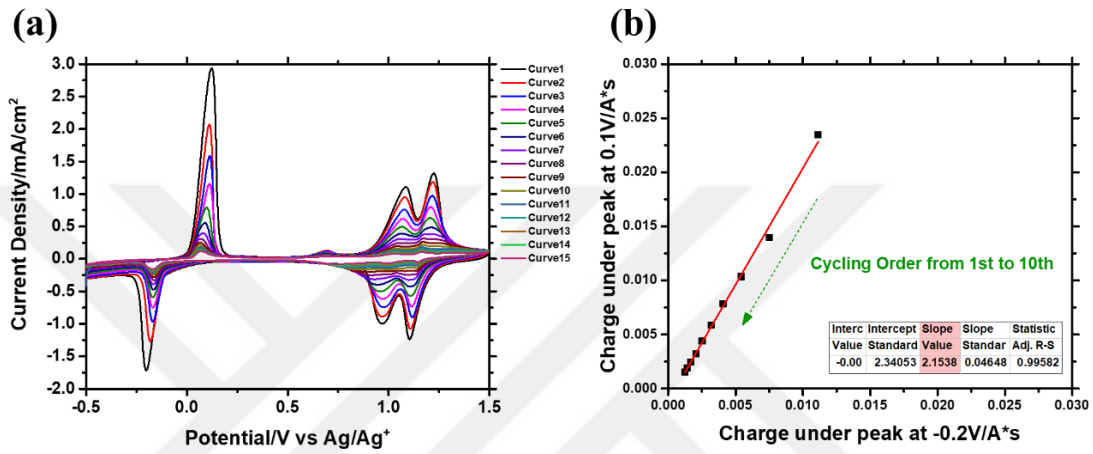

Figure 3.49 (a) CV curves of LiMn100 electrode between -0.5 and 1.5 V with a sweep rate of 10 mV/s in 1M $LiClO_4$/ MeCN, (b) Graph of charge densities under peaks at 0.1 V vs at -0.2 V by cycling process.

According to CVs, the Mn(III) disproportionation, due to lithium insertion into the $LiMn_2O_4$ electrode, is clearly observed by a decrease in current densities of the redox peaks at 0.0 and 1.1 V. The charge density under the oxidation and reduction peaks (between -0.3 and 0.3 V) were plotted to show a change in charge capacity by cycling, see Figure 3.49(b). The charge density linearly drops with cycling with a slope of almost 2.14. Thus, this might be concluded as two Mn(III) sides undergo a disproportionation reaction to produce one Mn(II) and one Mn(IV) side as MnO_2. Therefore, half of the manganese in 1st cycle might be lost by Mn(II) formation. This behavior is also followed by further cycles by cycling the electrode between # V and 0.3 V, where # is -0.6, -0.5, -0.4, and -0.3 V, see Figure 3.50(a-d).

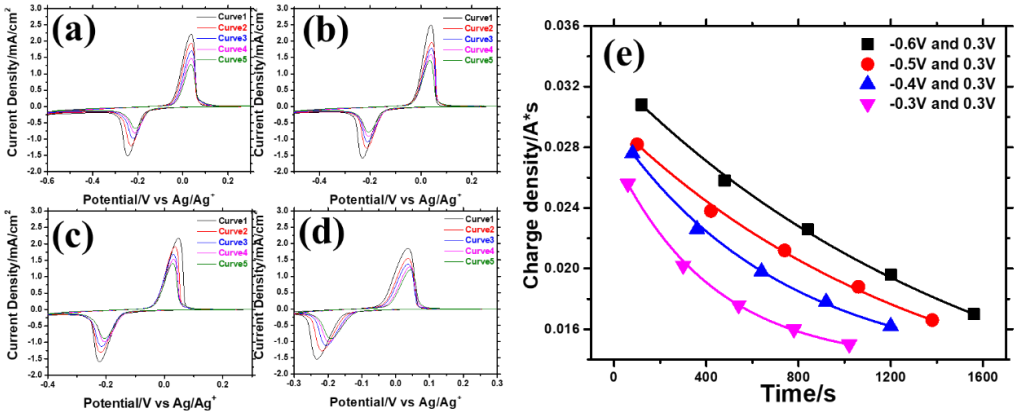

Figure 3.50 The CV curves of the LiMn100 in 1M $LiClO_4$/MeCN with a 5 mV/s scan rate in the potential windows of between # and 0.3 V vs Ag/Ag^+, where # is: (a) -0.6, (b) -0.5, (c) -0.4, and (d) -0.3 V. (e) The plot of charge capacity (oxidation peak at 0 V) vs time.

Then, the total charges under the oxidation peaks at 0 V were plotted with respect to time spent in the cycling process, see Figure 3.50(e). Each plot was fitted to an exponential function. Decay in charge densities showed an almost linear profile when the electrode was cycled between -0.6 and 0.3 V and exponential behavior increased by reducing the potential window to such as -0.3 and 0.3 V. This might be due to spending more time below -0.1 V and more Mn(III) disproportionation reaction. Thus, the 1:2 ratio between the charges of the redox peaks at 0 V is a coincidence as demonstrated in Figure 3.49(a) and (b).

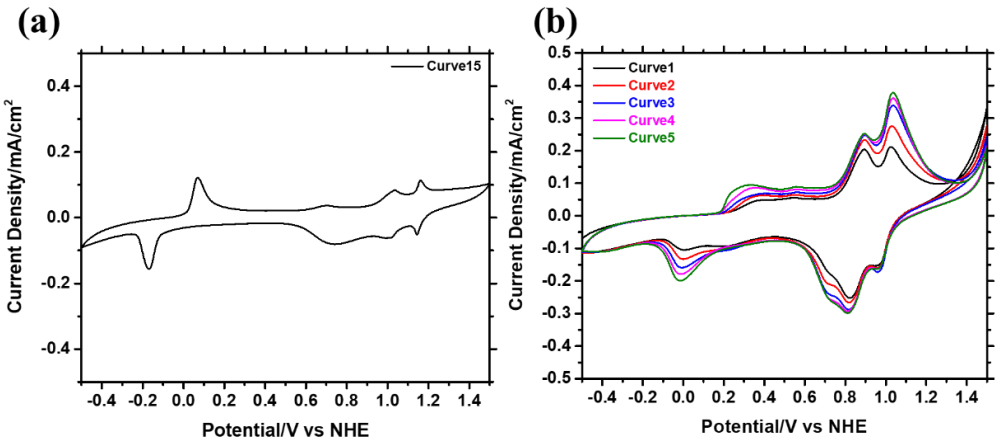

Figure 3.51 (a) CV curve (15th) of LiMn100 electrode between -0.5 and 1.5 V with a sweep rate of 10 mV/s in 1M $LiClO_4$/MeCN, (b) CV curves of LiMn100 electrode between -0.5 and1.5 V with a sweep rate of 10 mV/s in 1M $LiNO_{3(aq)}$ solution after cycling in 1M $LiClO_4$/MeCN.

In addition to the cycling experiment, the same electrode was tested in 1 M $LiNO_3$ electrolyte by collecting a CV curve in to quantify how much manganese is removed by the disproportionation reaction. The electrode material decay is also evident in the final 15th CV curve, which displayed very small faradaic peaks, compared to the 1st curve. The same LiMn100 electrode was washed and dried was used for CV measurements in 1 M $LiNO_3$ aqueous electrolyte. The result was unexpected. The current density of the redox peaks (between 0.6 and 1.2 V) gradually amplifies by cycling in the aqueous electrolyte, see Figure 3.51(b). In conclusion, the lithium intercalation and deintercalation processes are not efficient in a non-aqueous environment, compared to an aqueous environment besides the Mn(III) disproportionation on the electrode surface. For further analysis of the process in aqueous and non-aqueous electrolytes, the CV cyclings in 1 M $LiClO_4$ and 1 M $LiNO_3$ electrolytes (in the lithium intercalation and de-intercalation range) were carried and the charge density under the redox peaks were calculated from each cycle. The CV curves and total charge analysis for the LiMn100 electrodes in 1 M $LiClO_4$ and 1 M $LiNO_3$ are shown in Figure 3.52.

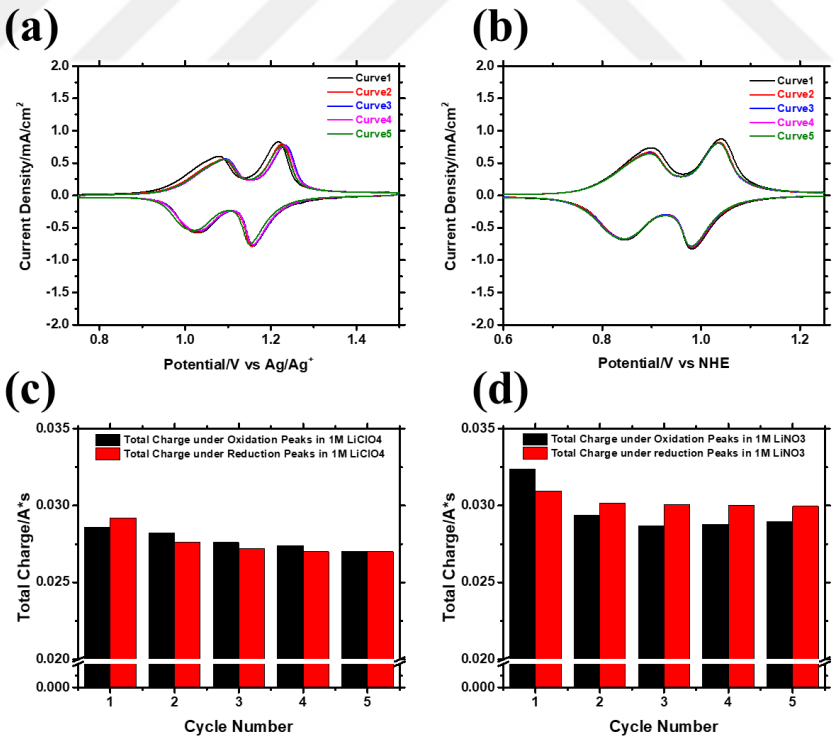

Figure 3.52 (a) CV curves of LiMn100 electrode with a sweep rate of 5 mV/s in 1 M $LiClO_4$/MeCN, (b) CV curves of LiMn100 electrode with a sweep rate of 5 mV/s in 1 M $LiNO_3$, (c) Column graph of charge densities under redox peaks in 1 M $LiClO_4$ and (d) Column graph of charge densities under redox peaks in 1 M $LiNO_3$.

The charge density for the lithium de-intercalation process gradually decreases by cycling in $LiClO_4$/acetonitrile electrolyte, see black columns in Figure 3.52(c). The lithium deintercalation charge amount is mostly higher than lithium intercalation as shown by the red columns in Figure 3.52(c). Thus, it implies that lithium de-intercalation is favored compared to lithium insertion in a non-aqueous environment. This causes a gradual decrease in the charge capacity of the LiMn100 electrode by cycling in non-aqueous media. Moreover, the LiMn100 electrode was cycled in 1 M $LiNO_3$ and the charge densities of the redox peaks are shown in Figure 3.52(d).

According to these results, charge capacity seems relatively higher in 1st cycle during the oxidation (lithium deintercalation) process (see the black column in Figure 3.52(d). However, the lithium intercalation process has a lower capacity, compared to the deintercalation process in the 1st cycle. The LiMn100 electrode in the 2nd cycle shows a lower de-intercalation capacity but the insertion process shows a higher capacity. Further cycling results in stable redox capacities in aqueous electrolytes compared to non-aqueous electrolytes. Therefore, it is reasonable to conclude that the aqueous media has an advantage for the lithium intercalation process and the charge capacity of the LiMn100 electrode is preserved in cycling between the 0.6 and 1.25 V potential window.

The LiMn100 electrode was also tested in a wider potential window in a non-aqueous environment. The CV curves of the LiMn100 electrode between -0.5 and 2.0 V, -0.5 and 2.5 V, and -0.5 and 3 V are shown in Figure 3.53.

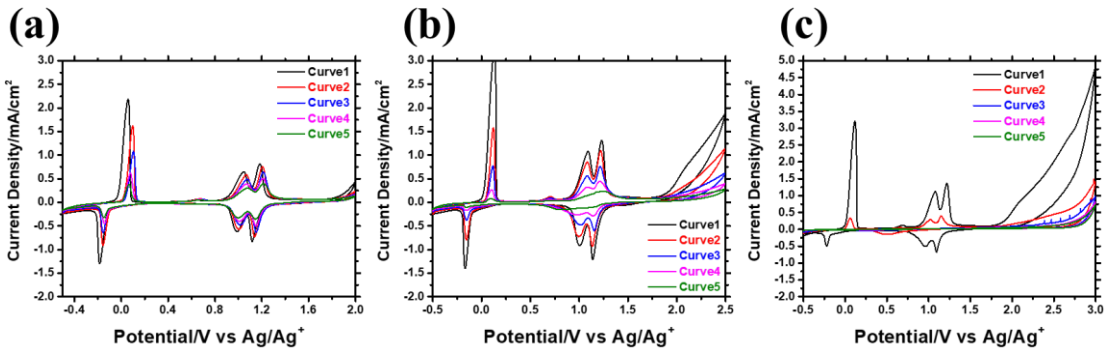

Figure 3.53 CV curves of LiMn100 electrode with a sweep rate of 5 mV/s in 1 M $LiClO_4$/MeCN between: (a)-0.5 and 2.0 V, (b) -0.5 and 2.5 V, and (c)-0.5 and 3.0 V.

If the LiMn100 electrode is cycled between -0.5 and 2.0 V vs Ag/Ag^+ (see Figure 3.53 (a)), there is no significant change, observed compared to the cycles between -0.5 and 1.5 V. There is still manganese lost due to Mn(III) disproportionation reaction. When the potential window is extended up to 2.5 V, an oxidation peak appears at 2.1 V vs Ag/Ag^+. Manganese reduction accelerates by cycling in this potential range. Notice that the redox peaks decrease in intensity, see Figure 3.53 (b). Since at that potential, the manganese oxidation takes place to form manganate (MnO_4^{2-}) ion that undergoes another disproportionation reaction to form MnO_2 and permanganate (MnO_4^-) ion. The freshly formed permanganate ions are dispersed into the non-aqueous electrolyte and are clearly visible by the purple color in the solution. The decay of the manganese species becomes faster through both disproportionation mechanisms in the following cycles. Lastly, the LiMn100 electrode was tested between -0.5 and 3.0 V vs Ag/Ag^+ in a non-aqueous electrolyte, see Figure 3.53 (c). A bare FTO is visible after 2nd CV s due to the fast decomposition of the electrode material over the FTO surface.

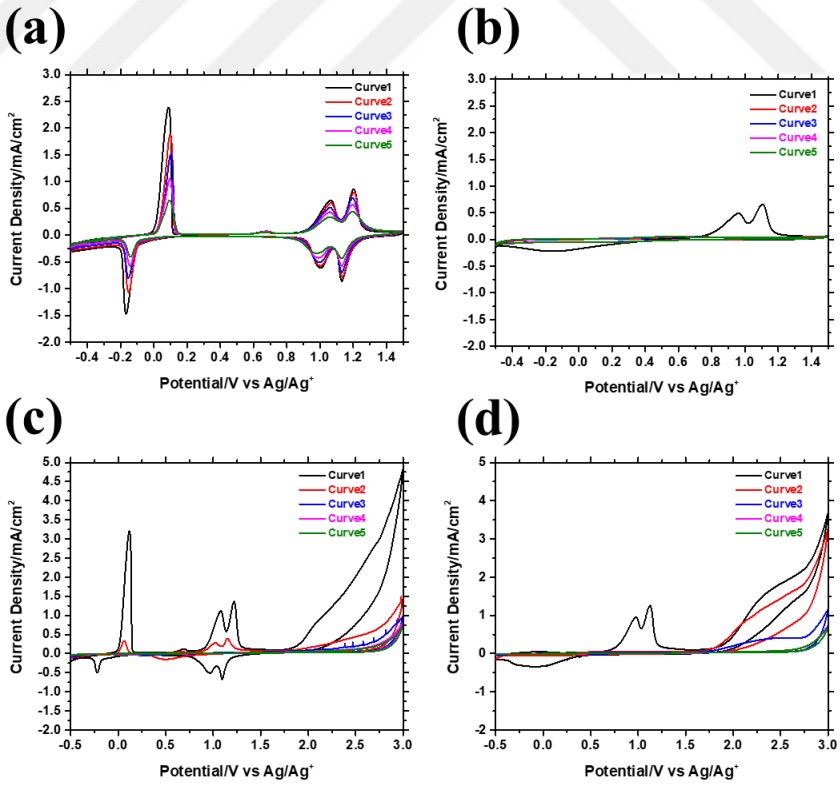

Figure 3.54 CV curves of LiMn100 electrode with a sweep rate of 5 mV/s: (a) in 1 M $LiClO_4$/MeCN between -0.5 and 1.5 V, (b) in 1 M $NaClO_4$/ MeCN between -0.5 and 1.5 V, (c) in 1 M $LiClO_4$/ MeCN between -0.5 and 3 V, (d) in 1 M $NaClO_4$/MeCN between -0.5 and 3 V.

The electrodes were further tested by cyclic voltammetry using another supporting electrolyte. The electrodes were intended to be used in $KClO_4$ solution, but the solubility of $KClO_4$ is limited in acetonitrile. Since sodium and potassium salts have similar behavior in aqueous electrolytes, a 1 M $NaClO_4$/MeCN solution was used to collect the CVs. Figure 3.54 displays the CV curves of the LiMn100 electrode in 1 M $LiClO_4$ and 1 M $NaClO_4$/acetonitrile solutions in various potential windows.

According to voltammograms in Figure 3.54(b), the de-intercalation of lithium takes place between 0.7 and 1.2 V vs Ag/Ag^+ and there is no lithiation into MnO_2 while reverse sweeping from 1.5 to -0.5 V due to lithium poor environment of the electrolyte. Then, LiMn100 electrode was tested in a wider potential window (-0.5 to 3.0 V). There is a significant difference, observed for the peak at 2.1 V between $LiClO_4$ and $NaClO_4$ electrolyte. Notice that, the oxidation peak at 2.1 V has a higher current density in the sodium-rich electrolyte compared to the lithium-rich one, compare Figure 3.54(d) and 3.54(c), respectively. Thus, this might be due to Na^+ being a better counter cation for the manganate ions than Li^+ and favors the manganate formation more in non-aqueous media.

3.1.4 Cycling of Mesoporous $LiMn_2O_4$ Electrodes in Alkaline Electrolytes for the Investigation of Manganese Disproportionation Mechanism

In previous sections, the disproportionation mechanisms of Mn(III) and Mn(VI) were discussed, and found that the manganese disproportionation reactions cause instability in the LiMn100 electrodes. So far, the LiMn100 behavior has been discussed by changing parameters such as pH and potential windows in aqueous and non-aqueous electrolytes. However, an alkaline environment is required for an efficient water oxidation reaction related to the OER mechanism. For this reason, the working electrodes are used in alkaline electrolytes to evaluate the degradation of manganese species by recording multiple CVs. Firstly, analysis was started by cycling the LiMn100 electrode between -0.4 and 1 V with a scan rate of 50 mV/s. Additionally, the Mn_3O_4

electrode was prepared by the MASA method and tested by using the same parameters to compare its properties with LiMn100.

The CV curves of the Mn_3O_4 and LiMn100 electrodes, between -0.4 and 1.0 V in 1 M aqueous KOH solution, are shown in Figures 3.55(a) and (b), respectively. Using these voltammograms, the current density of the electrodes at 1 V for each cycle is plotted, see Figure 3.55 (c).

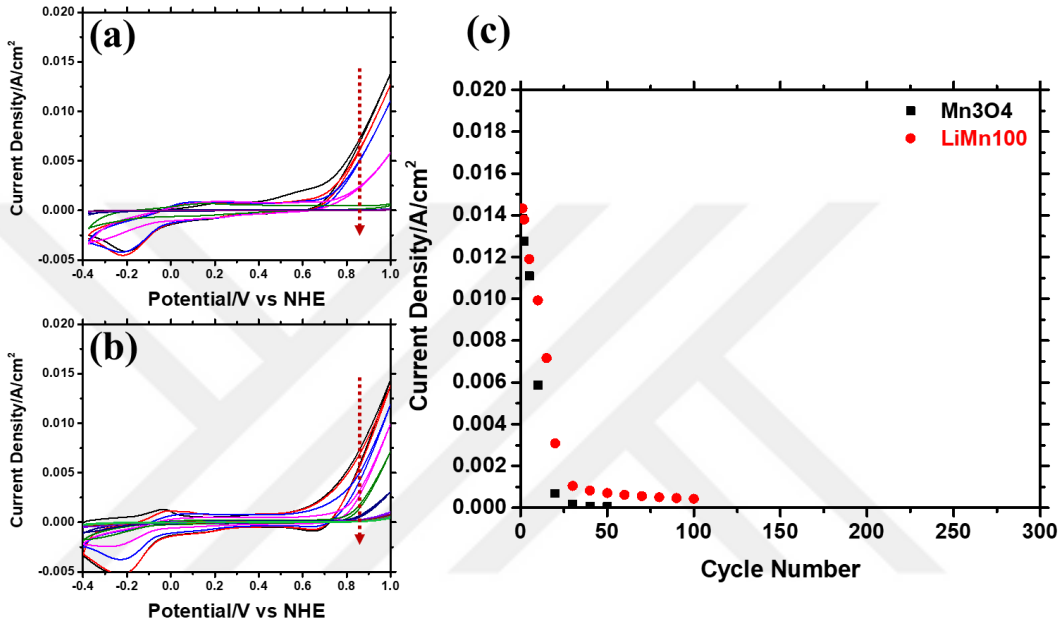

Figure 3.55 (a) CV curves of Mn_3O_4 between -0.4 Vand 1 V with a scan rate of 50 mV/s in 1 M KOH, (b) CV curves of LiMn100 between -0.4 Vand 1 V with a scan rate of 50 mV/s in 1 M KOH, (c) Plot of cycle number vs current density at 1 V for Mn_3O_4 and LiMn100 electrodes.

Note that both Mn(III) and MnO_4^{2-} disproportionation reactions occur in this potential window, see Figure 3.55(c). Both LiMn100 and Mn_3O_4 electrodes show extensive degradation and the Mn_3O_4 electrode shows the bare FTO within the 20th cycle, see Figure 3.55(a). The LiMn100 electrode performance also decays quickly within the 30th cycle, no film is left on the electrode surface. According to the plots in Figure 3.55(c), these two electrodes suffer from the above disproportionation reaction to a similar extent.

To eliminate the Mn(III) disproportionation on the electrode surface, the electrodes are cycled between 0 and 1 V in 1 M KOH solution. The CV curves of

the Mn_3O_4 and LiMn100 electrodes are shown in Figure 3.56(a) and (b), respectively.

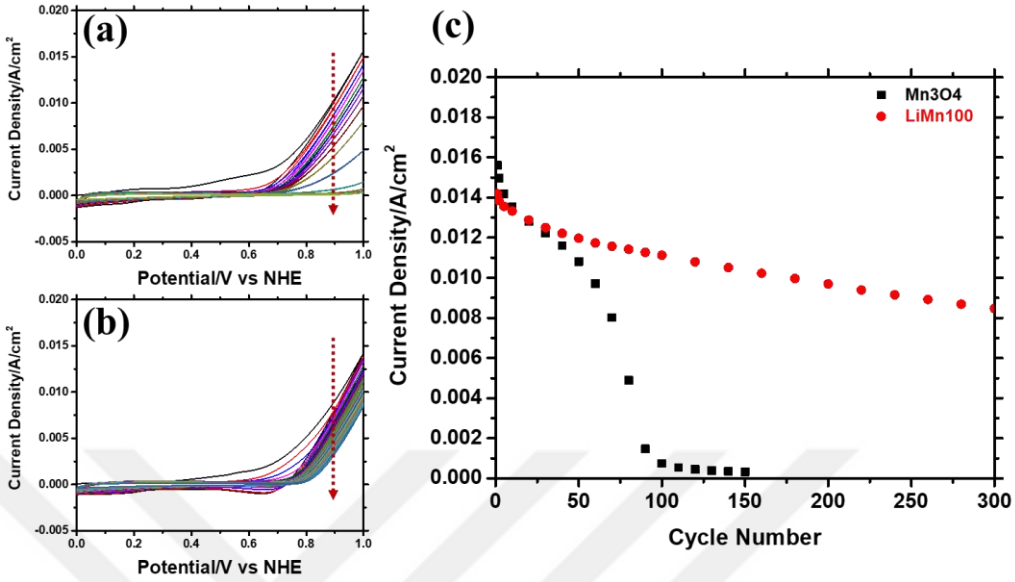

Figure 3.56 (a) CV curves of Mn_3O_4 between 0 V and 1 V with a scan rate of 50 mV/s in 1 M KOH, (b) CV curves of LiMn100 between 0 V and 1 V with a scan rate of 50 mV/s in 1 M KOH, (c)Plot of cycle number vs current density at 1 V for Mn_3O_4 and LiMn100 electrodes.

Both Mn_3O_4 and LiMn100 electrode degradation are reduced by choosing a narrower potential window because, in this potential window, the Mn(III) disproportionation does not occur. The Mn_3O_4 electrode resists up to the 100th cycle over that it shows a bare FTO activity in OER, see Figure 3.56(a). However, the LiMn100 electrode has much higher stability than Mn_3O_4 due to slow degradation since it still shows OER performance in the 300th CV, see Figure 3.56(b). The LiMn100 electrode shows a slower disproportionation than Mn_3O_4, as shown in Figure 3.56(c). To conclude, lithium in the LiMn100 electrode brings stability to the structure, regarding the manganate disproportionation by forming the λ-MnO_2 phase rather than other phases of MnO_2 that form during the electrochemical oxidation of the Mn_3O_4 electrode.

The LiMn100 electrode was also tested by cycling in 3 M KOH to understand the effect of OH^- concentration on manganate disproportionation in the catalytic process. The CV curves of the LiMn100 electrode between 0 and 1 V in 3 M KOH are shown in Figure 3.57(a).

The degradation of LiMn100 in 3 M KOH is very similar to the degradation in 1 M KOH. The electrode still shows some catalytic activity at the 300th cycle. Notice that the current density at 1 V in 3 M KOH solution is higher than that in 1 M KOH. This is due to OH^- dependence of water oxidation reaction. When the hydroxide concentration is increased in the media, the OER efficiency is also enhanced. For this reason, the current density is clearly higher in the 3 M KOH electrolyte. However, the degradation degree of the electrodes is very similar to both solutions.

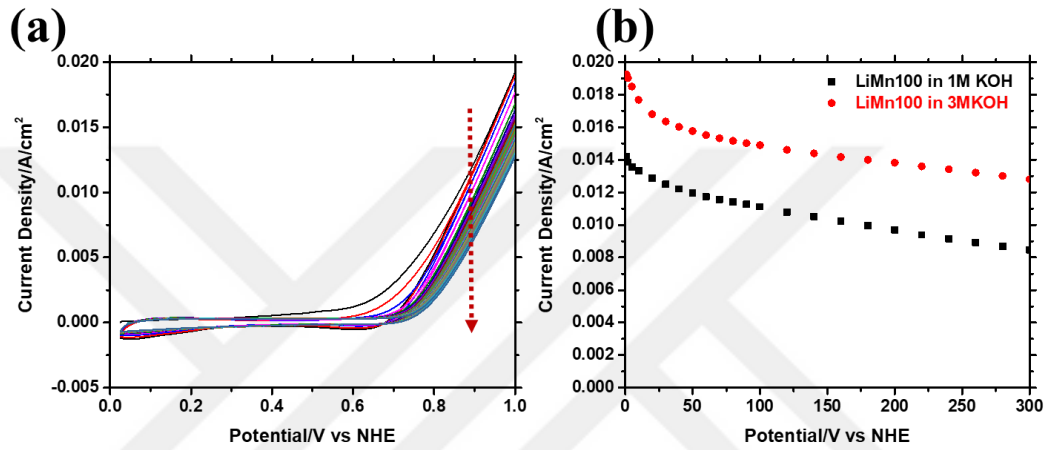

Figure 3.57 (a) CV curves of LiMn100 between 0 V and 1 V with a scan rate of 50 mV/s in 3 M KOH and (b) plot of cycle number vs current density at 1 V for the LiMn100 electrodes in 1M KOH and 3M KOH.

To see the counter cation effect in alkaline electrolytes, the LiMn100 electrode was also cycled between 0 and 1 V in a 1 M LiOH electrolyte. The CV curves of the LiMn100 in 1 M LiOH are shown in Figure 3.58 (a).

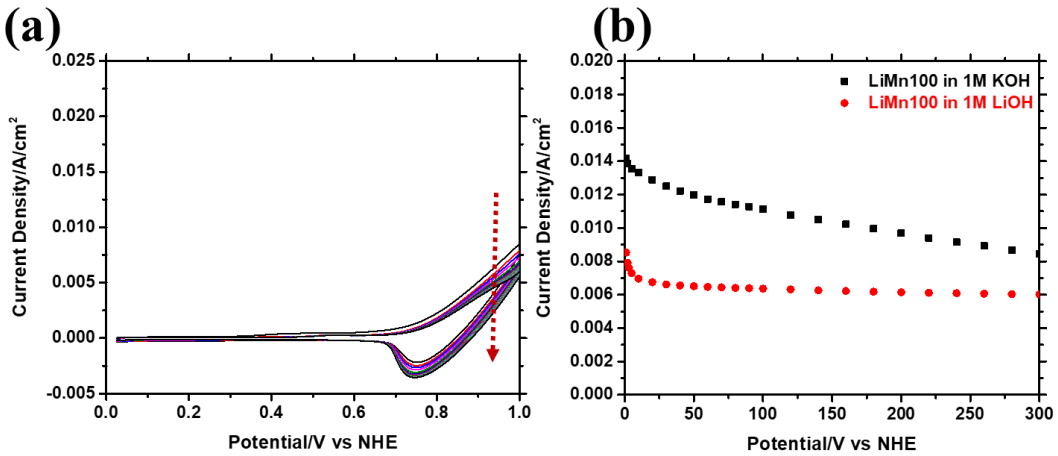

Figure 3.58 (a) CV curves of LiMn100 between 0 V and 1 V with a scan rate of 50 mV/s in 1 M LiOH, (b) Plot of cycle number vs current density at 1 V for LiMn100 electrodes in 1 M KOH and 1 M LiOH.

The reduction peak at 0.75 V in the CVs in 1 M LiOH solution is due to the lithium intercalation process, see Figure 3.58(a). The same peak was also observed in 1 M $LiNO_3$ electrolyte at the same potential. However, the peak at more positive potential and the peaks due to lithium de-intercalation process are not observed in the CVs due to the OER that masks these faradaic peaks. Notice that the current density is 9.3 mA/cm^2 at 1 V and drops to 7.5 mA/cm^2 in the 20th cycle. Then, the current density remains constant at 7.5 mA/cm^2 up to the 300th cycle. The current density is higher in the KOH solution at the beginning of cycling but the degradation is also faster, see plot in Figure 3.58(b). However, the current density is lower at all cycles in the LiOH electrolyte, but after a few cycles, the degradation stops. This is because, after each cycle in the reverse direction, lithium ions are intercalated back to the electrode and may repair the structure. Therefore, degradation due to Mn(VI) disproportionation is prevented in LiOH solutions.

The electrodes were further cycled in a wider potential window, between 0 and 1.5 V to enhance the Mn(VI) disproportionation at higher voltages. The cyclic voltammograms of the LiMn100 electrode in 1 M LiOH and 1 M KOH and the plot of current density at 1 V vs cycle number are shown in Figure 3.59.

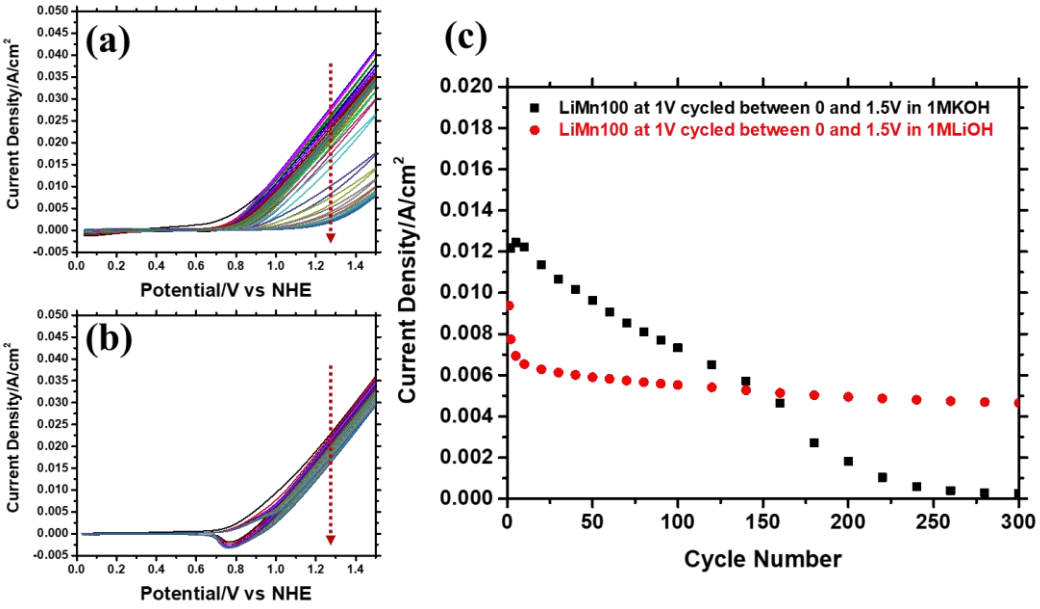

Figure 3.59 CV curves of LiMn100 between 0 V and 1.5 V with a scan rate of 50 mV/s in (a) 1 M KOH, (b) 1 M LiOH, (c) Plot of cycle number vs current density at 1 V for LiMn100 electrodes in 1 M KOH and 1 M LiOH.

The voltammograms in 1 M KOH and 1 M LiOH show that the Mn(VI) disproportionation reaction is faster in 1 M KOH electrolyte, see Figure 3.59(a) and (b). This might be also explained by the presence of K^+ in the electrolyte, it triggers manganese disproportionation and the formation of permanganate. After 300 cycles, the current density at 1 V is almost zero, indicating that all active manganese on the electrode surface is dispersed into the electrolyte solution, see Figure 3.59 (c). In the LiOH case, the disproportionation reaction is very slow. This could be due to the repairing effect of the electrode through lithium intercalation during reverse cycles. Also, the presence of lithium in the electrolyte also hinders the formation of permanganate species even if the potential window is increased to 1.5 V vs NHE.

3.1.5 Oxygen Evolution Reaction (OER) performances of $LiMn_2O_4$ electrodes

The LiMn100 electrode was firstly tested in 1 M KOH electrolyte for a water oxidation reaction. First, 5 curves were recorded by cycling between 0 and 1 V with a scan rate of 50 mV/s. Then, a multistep chronoamperometry (m-CA) was performed for the Tafel slope analysis. After that, the CPs at 1 mA/cm^2 and 10 mA/cm^2 were recorded.

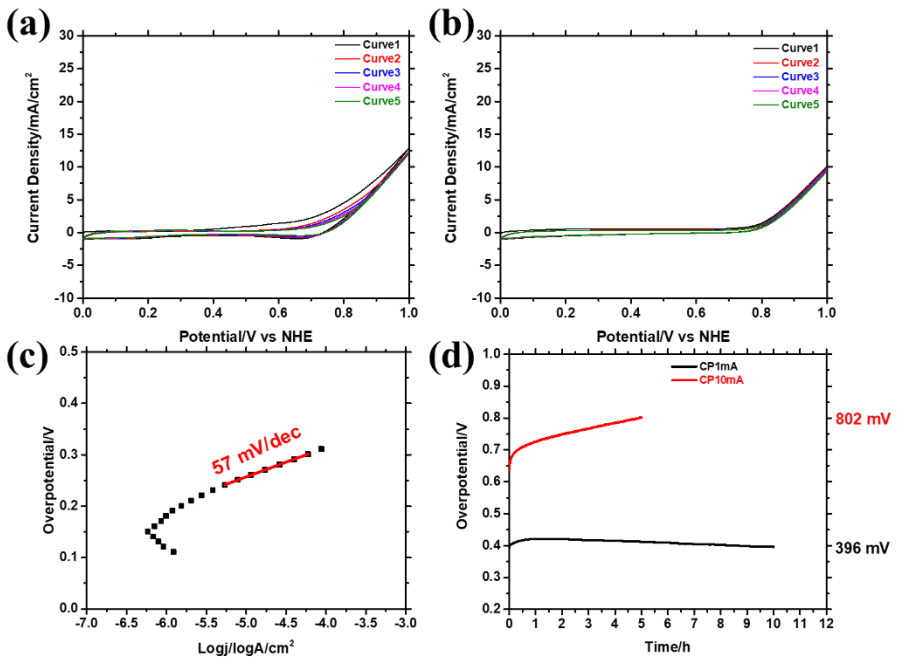

Figure 3.60 (a) CV curves of LiMn100 in 1 M KOH between 0 V and 1 V with a scan rate of 50 mV/s, (b) CV curves after CP at 10 mA/cm^2 , (c) Tafel slope analysis, (d) CP plots at 1 mA/cm^2 and 10 mA/cm^2.

The experiment was terminated by cyclic voltammetry to compare the electrode before and after chronopotentiometry experiments. The CV curves, collected in 1 M KOH are shown in Figure 3.60(a). The water oxidation initiates at 0.6 V vs NHE. The Tafel slope of the electrode was evaluated as 57 mV/dec in 1 M KOH electrolyte from the CA data, see Figure 3.60(c). The overpotential was reported as 396 mV after 10 hours CP at 1mA/cm^2 current density and 802 mV at 10 mA/cm^2 after 5 hours.

Notice that a slight increase is observed in the overpotential value at 10 mA/cm^2 during the CP measurement, see Figure 3.60(d), indicating the electrode degradation during the experiment, due to Mn(VI) disproportionation reaction and also mechanical reasons, such as oxygen bubbles. Lastly, the CV curves, after CP experiments, were collected once more, see Figure 3.60(b), to show the electrode stability after the above electrochemical tests. The current density between 0.8 and 1 V decreases, also showing loss of the active manganese on the electrode surface with CP experiments.

Then LiMn100 electrode was also tested in 1 M LiOH for OER catalysis, using a similar procedure employed to the KOH case. The CV curves, obtained in 1 M LiOH electrolyte are shown in Figure 3.61(a).

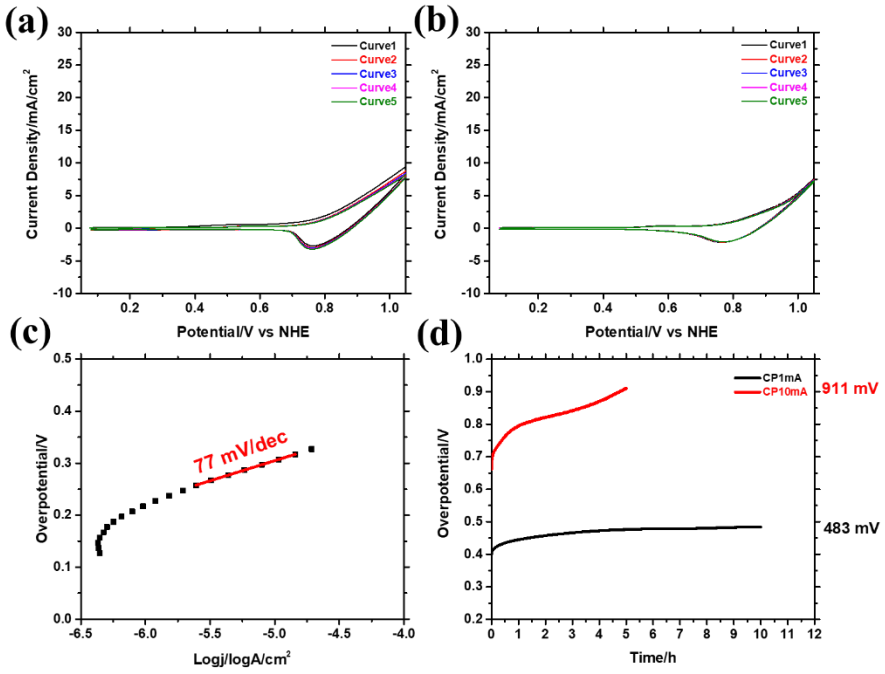

Figure 3.61 (a) CV curves of LiMn100 in 1 M LiOH between 0 V and 1 V with a scan rate of 50 mV/s, (b) CV curves after CP at 10 mA/cm^2, (c) Tafel slope analysis, (d) CP plots at 1 mA/cm^2 and 10 mA/cm^2.

According to CVs in 1 M LiOH solution, the lithium intercalation and deintercalation peaks between 0.8 and 1 V are masked by the water oxidation peak, see Figure 3.61(a). The overlap of these two redox processes may also result in a higher Tafel slope of 77 mV/dec, because the lithium deintercalation process also takes place during the CA experiment, see Figure 3.61(c). Otherwise, the Tafel slope is expected to be the same as the KOH electrolyte, because OH^- concentration and surface morphology are very similar under both conditions. When the electrode was used in CP experiments at 1 and 10 mA/cm^2 current densities for 10 and 5 h, respectively, and the overpotential values were recorded to be 483 and 911 mV. A large increase in the overpotential at 10 mA/cm^2 shows an enhanced Mn(VI) disproportionation reaction from the electrode surface in LiOH electrolyte, see Figure 3.61(d). This is because there is no reverse cycling to repair the electrode through lithium intercalation as discussed before and the current in the CP is only due to the OER process. After the CP experiments, the final CV curves were recorded in 1 M LiOH, and the voltammograms are shown in Figure 3.61(b). OER current density value couldn't be identified clearly in CV curves in Figure 3.61 (b) since lithium de-intercalation takes place in that potential range.

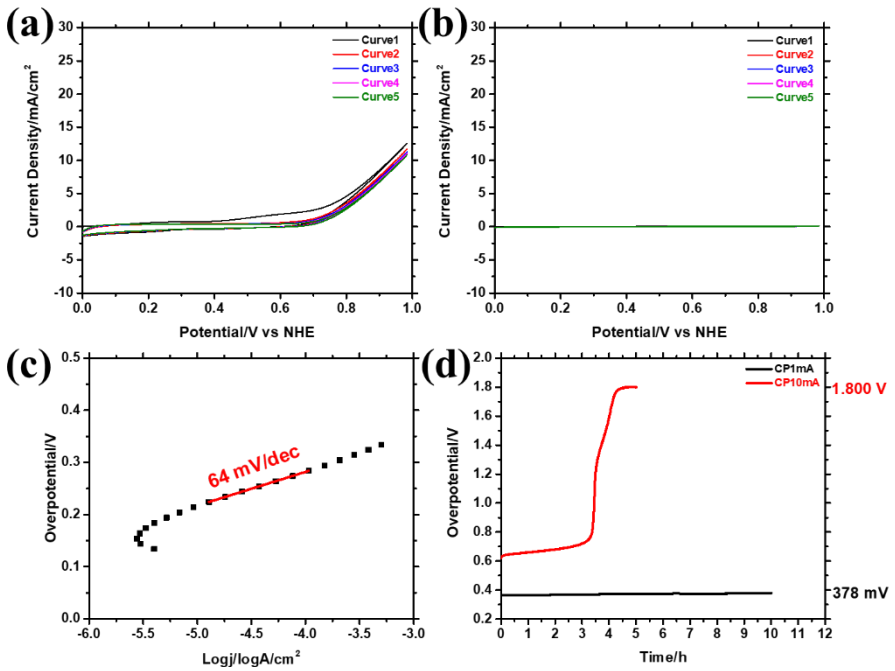

Figure 3.62 (a) CV curves of Mn_3O_4 in 1 M KOH between 0 V and 1 V with a scan rate of 50 mV/s, (b) CV curves after CP at 10 mA/cm^2, (c) Tafel slope analysis, (d) CP plots at 1 mA/cm^2 and 10 mA/cm^2.

As a control experiment, a Mn_3O_4 electrode was also tested in the OER process to compare its catalytic activity with the $LiMn_2O_4$ electrode. The CV curves of the Mn_3O_4 electrode in 1 M KOH electrolyte are shown in Figure 3.62(a).

The CV curves are very similar to the $LiMn_2O_4$ electrode performed in KOH, see Figure 3.60 (a). Similar to CV curves, the Tafel slope of the Mn_3O_4 electrode is 64 mV/dec, very close to the Tafel slope of the $LiMn_2O_4$ electrode. The overpotential versus time plots at 1 and 10 mA/cm^2 are shown in Figure 3.62(d). Notice that the overpotential value at 1 mA/cm^2 is 378 mV after 10 hours of CP measurement. This value is very close to that of the LiMn100 electrode at 1 mA/cm^2 in 1M KOH. This shows that the Mn(VI) disproportionation reaction is very slow at 1 mA/cm^2 current density. However, when the current density is increased to 10 mA/cm^2, the Mn(VI) disproportionation reaction becomes faster in the Mn_3O_4 electrode. This behavior is clearly observed as an increasing overpotential after 2 hours CP, see Figure 3.62(d). The overpotential value at 10 mA/cm^2 reaches to 1.8 V in 5 hours and corresponds to the bare FTO overpotential in 1 M KOH electrolyte. It means there are no manganese species left on the electrode surface. The CVs after CP experiments, shown in Figure 3.62 (b), also correlate with the above observation that the current density is almost zero in the OER region, indicating that there is no active electrode material on the FTO surface.

In conclusion, spinel $LiMn_2O_4$ was found to be a more stable electrode in the OER process compared to spinel Mn_3O_4 electrodes in the KOH electrolyte. This is because the lithium atom in the spinel $LiMn_2O_4$ structure significantly hinders the Mn(VI) disproportionation reaction. In the Mn_3O_4 structure, manganese species easily undergo a Mn(VI) disproportionation reaction to form permanganate species. Therefore, these ionic manganese species are dispersed to the solution and cause a fast degradation of the electrode.

3.1.6 Effect of Thickness and Calcination Temperature on Electrochemical Properties of Mesoporous $LiMn_2O_4$ Thin Films

Until this section, the electrochemical properties (such as the redox processes, Mn(VI) disproportionation reaction rate, electrode stability at OER

potentials, OER efficiencies in various electrolytes, and pH, etc.) of the $LiMn_2O_4$ electrodes have been investigated. In this section, the effect of film thickness and calcination temperature on electrochemical properties will be discussed. Electrodes with different thicknesses and calcined at various temperatures are analyzed to elucidate the effects of electrode thickness and calcination temperature on their stabilities and efficiencies in the OER process.

3.1.6.1 Effect of Thickness on Electrochemical Properties of Mesoporous $LiMn_2O_4$ Thin Films

Thickness analysis of the LiMn100 electrodes starts by coating the lyotropic liquid crystal (LLC) phase of 20Li-40M-1CTAB-1P123 composition from its clear ethanol solution at various spin rates. The solution is coated on microscope slides by the spin coating technique. The spin rates were chosen as 2000, 3000, 5000, 7000, and 10000 rpm to obtain electrodes with 5 different thicknesses. Then, the small-angle XRD patterns of these LLC thin films were recorded. The XRD patterns of the LLC films are shown in Figure 3.63(a).

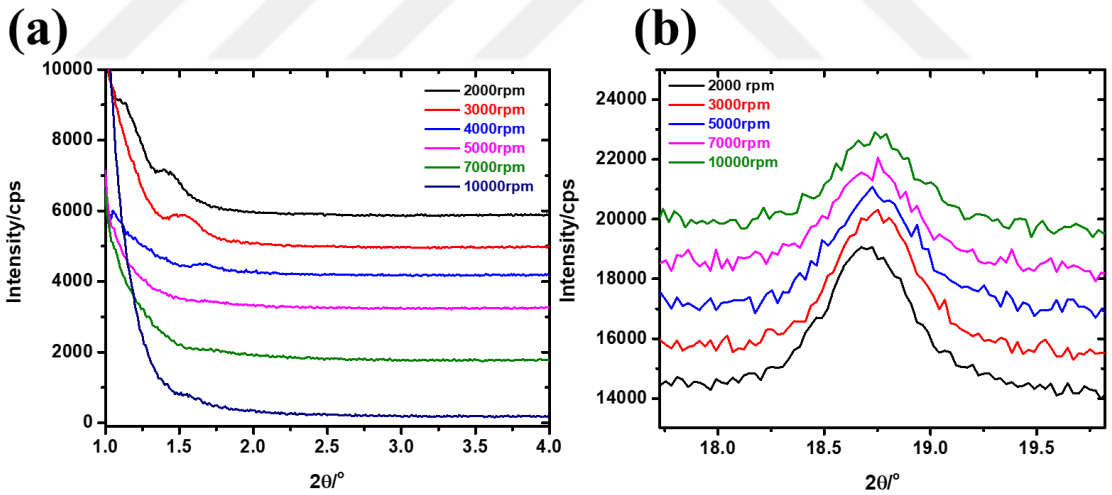

Figure 3.63 (a) Small angle XRD patterns of as prepared LLC of 20Li-40M-1CTAB-1P123 at various spin rates, (b) High angle XRD patterns of thin films fabricated by different spin rates.

The film, spun at 2000 rpm, displays two diffraction lines at 1.13° and 1.41°, 2θ, in its small-angle XRD pattern, proving the mesophase formation. If the solution is spun at 3000 rpm, the diffraction line at 1.41° shifts to a higher angle, meaning that the d-spacing in the LLC phase decreases and the unit cell shrinks. Further increasing the spin rate from 4000 to 7000 rpm, the same diffraction line

is almost unaltered. When the solution is spun at 10000 rpm, the diffraction line slightly shifts to a smaller angle, similar to the film spun at 3000 rpm.

The gel films, prepared over the FTO surface, are calcined at 300 ^{o}C for 1h. Then, the wide- angle XRD patterns of formed LiMn100 electrodes were recorded directly from the FTO surface. In our previous studies, it has been demonstrated that this solution composition forms a spinel $LiMn_2O_4$ crystal structure.[25] The $LiMn_2O_4$ sample displays a sharp diffraction line at 18.54^{o}, 2θ, indexed to (111) plane of the spinel structure and it is used for particle size analysis, see Figure 3.63(b). The Scherrer equation was employed to calculate the particle size or crystalline domain size in thin films. The sizes of the particles are tabulated in Table 3.3. Notice that, the particle size is independent of spin rate and is around 18-19 nm.

Spin rate/rpm	Particle size/nm
2000	19.6
3000	18.3
5000	17.8
7000	18.5
10000	20.6

Table 3.3 Spin-rate dependent particle size in the thin films.

Then, three of the thin films, which are spun at 2000, 5000, and 10000 rpm, were picked for the XPS analysis to investigate the surface composition of the electrodes. O 1s, Mn $2p_{3/2}$, and Mn 3s XPS spectra of the LiMn100 electrodes at various spin rates are shown in Figure 3.64(a), (b), and (c), respectively.

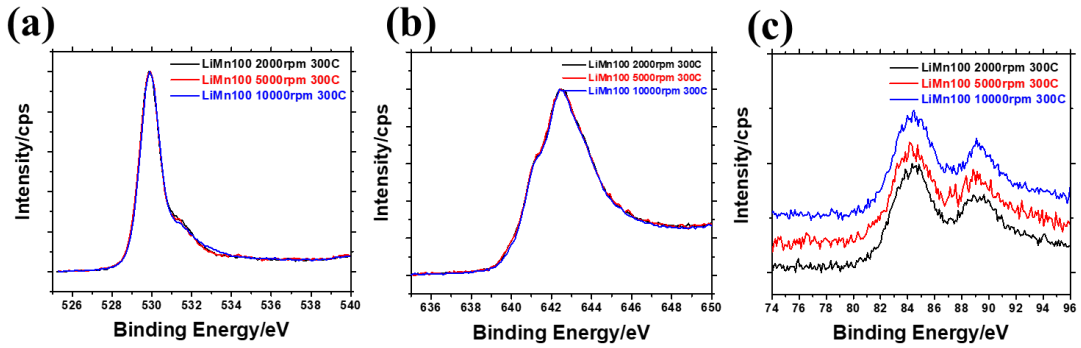

Figure 3.64 XPS spectra of the LiMn100 electrodes at various spin rates: (a) O 1s, (b) Mn 2p ($^2P_{3/2}$) and (c) Mn 3s regions.

There is no difference among the spectra in the O 1s, Mn 2p ($^2P_{3/2}$), and Mn 3s at all spin rates. This means there is no effect of spin rate on the electrode surface composition in terms of manganese and oxygen. The films were further investigated using the SEM technique. Firstly, the thicknesses of the films were measured from the cross-sectional images, see Figure 3.65. For this experiment, each film was coated on a piece of conductive doped-silicon wafer at various spin rates, and then each wafer was smoothly cut and hocked with a carbon type at a 90 angle to an aluminum stub. The images were recorded on the cut edge of the wafers. Figure 3.65 shows the cross-sectional SEM images of the films.

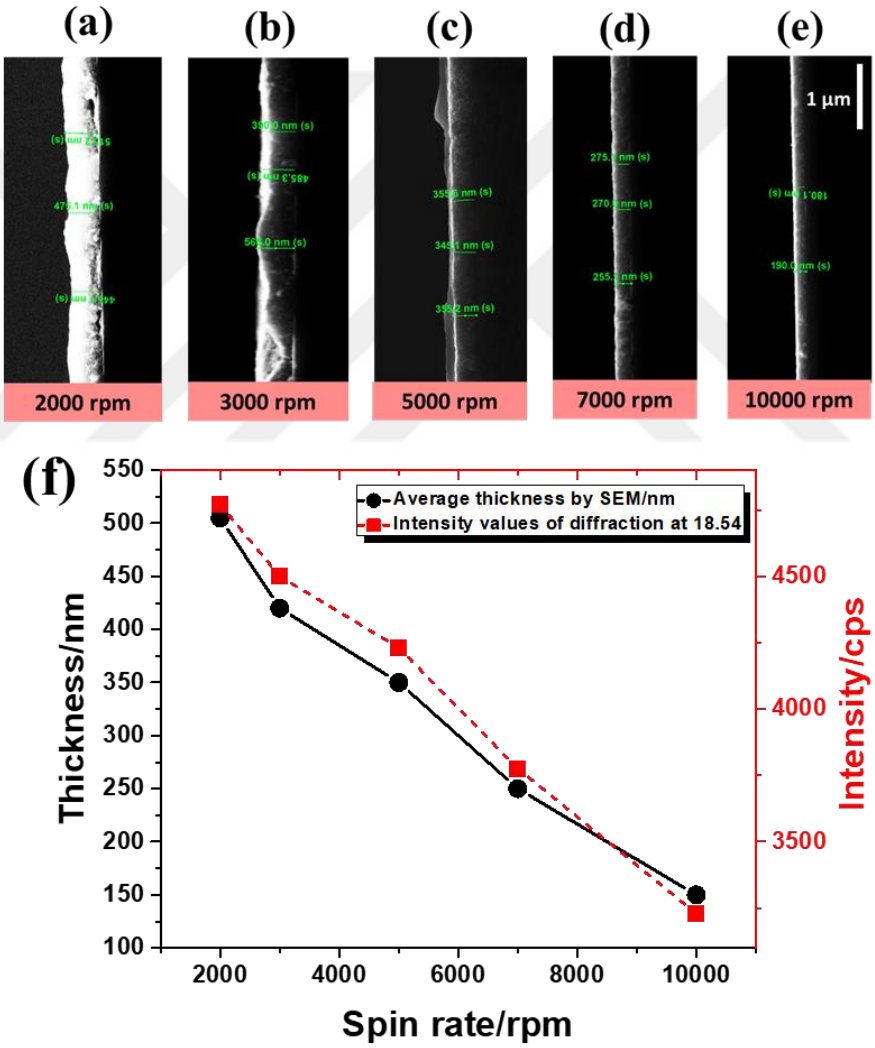

Figure 3.65 SEM images of LiMn100 thin films cross sections: (a) 2000 rpm, (b) 3000 rpm, (c) 5000 rpm, (d) 7000 rpm, (e) 10000 rpm.

The average thicknesses of the films are found to be around 475, 400, 350, 270, and 200 nm for 2000, 3000, 5000, 7000, and 10000 rpm, respectively. Thus,

an increase in spin rate causes a decrease in the thickness of the films as expected. However, the films fabricated at 2000 and 3000 rpm showed rougher film surface with large deviations in the film thickness, see Figure 3.65(a) and (b). When the spin rate is increased to 5000 rpm, a smoother film surface is obtained, see Figure 3.65(c). Further increase in spin rate up to 10000 rpm, smoothness on the surfaces is preserved by decreasing the thicknesses of the films, see Figure 3.65(d) and (e).

The thickness of the LiMn100 films versus diffraction intensities in XRD patterns was also plotted in order to correlate the thickness change observed in SEM images. Figure 3.65(f) shows both plots (spin rate vs thickness and spin rate vs diffraction line intensity). Both plots are almost linear. Here, the average thicknesses of the films were calculated by measuring the thickness of several parts in Figure 3.65(a)-(e) to the XRD intensities using the line at 18.5^{o}, 2θ, originating from all samples (whole depths of the films) because the thickness of all the films used in these measurements are thinner than x-ray depth; one also observes the XRD lines of the FTO underneath the films. The LiMn100 thin films on FTO were also imaged to investigate morphology on top of the electrode surface. The images were directly recorded from the FTO surfaces, see Figure 3.66

The SEM images of the LiMn100 thin films, fabricated at 2000 and 3000 rpm, show larger cracks on the electrode surfaces, see Figure 3.66(a) and (b). This might be also attributed to thicker LLC films that do not retain the perfect film configuration during the calcination process, due to a large amount of gel loading on the substrate. When the electrodes are fabricated at 4000, 5000, and 6000 rpm, the calcined films are smoother and crack-free. Figures 3.66(c), (d), and (e) show the SEM images of LiMn100 films, coated at 4000, 5000, and 6000, respectively. Smoother films are clearly observed in these images at above spin rates.

Figure 3.66(f) displays the SEM image of the LiMn100 film, coated at 7000 rpm. The image displays small crystal-like bumps on the electrode surface. These bumps become more visible in the SEM images of the films, coated by further increasing the spin rate, namely at 8000, 9000, and 10000 rpm, see Figure

3.66(g), (h), and (i), respectively. These features are due to the surface morphology of FTO substrate (crystalline FTO particles, see Figure 3.66(j)) and the LiMn100 coating mimics the FTO surface morphology, when the films get thinner at higher spin rates.

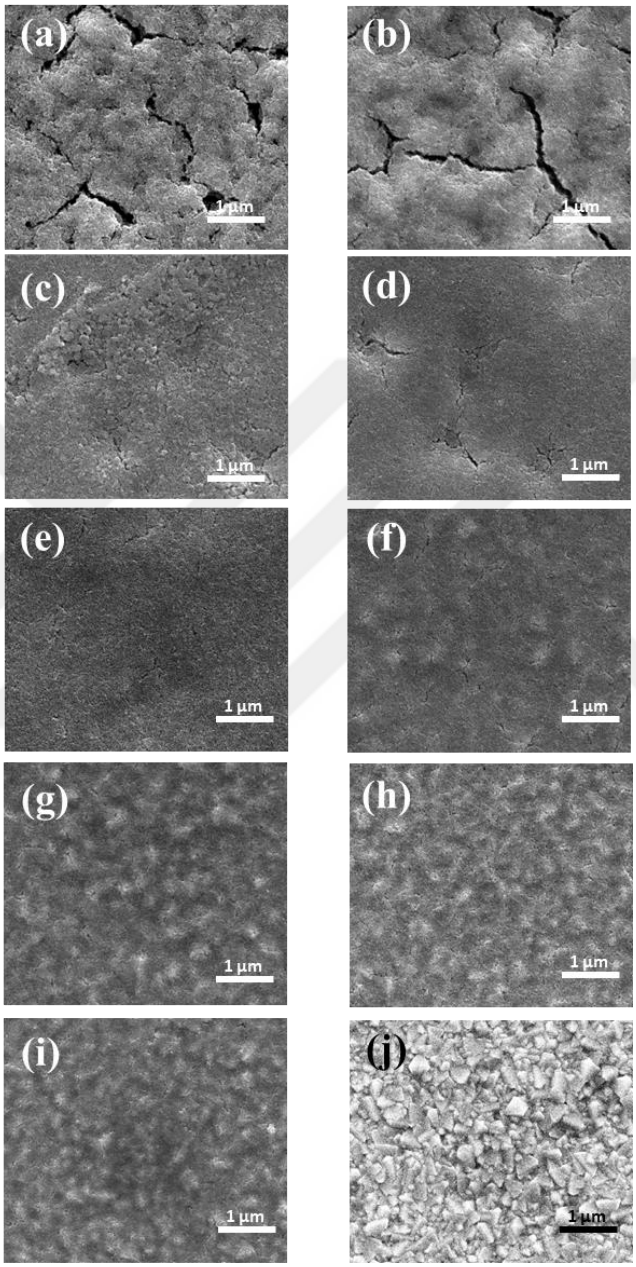

Figure 3.66 SEM images of LiMn100 thin films on top: (a) 2000 rpm, (b) 3000 rpm, (c) 4000 rpm, (d) 5000 rpm, (e) 6000 rpm, (f) 7000 rpm, (g) 8000 rpm, (h) 9000 rpm, (i) 10000 rpm, (j) Bare FTO.

The LiMn100 thin films were also used in electrochemical cells for quantitative analysis. The electrodes were tested electrochemically in 1 M $LiNO_3$ and cycled between 0.3 and 1.3 V at various scan rates, from 2 to 20 mV/s with 2 mV/s increments. Figure 3.67 shows the CV curves of the films in 1 M $LiNO_3$.

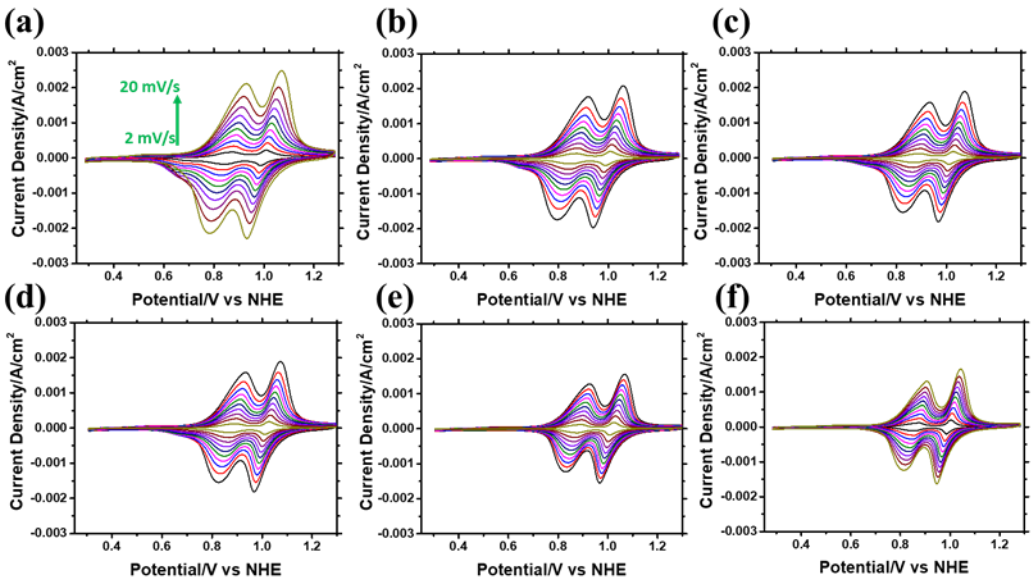

Figure 3.67 CV curves of LiMn100 electrodes fabricated at different spin rates: (a) 2000 rpm, (b) 3000 rpm, (c) 5000 rpm, (d) 5000rpm, (e) 7000 rpm, (f) 10000 rpm.

Firstly, the LiMn100 thin films were analyzed by determining the catalytic load on the FTO substrate using the lithium de-intercalation peaks at 0.9 and 1.1 V in the CVs. Notice that the current density of these peaks decreases by increasing the spin rate, correlating with the thickness measurements from the SEM images and XRD patterns. Therefore, the decrease in the catalytic load is as expected. And, it is due to reduced film thickness by increasing the spin rate. Charge density, under these peaks (see Figure 3.68(a)), was calculated using equation 1.4 from the CVs at 20 mV/s scan rate and converted into catalytic $LiMn_2O_4$ load in mass unit.

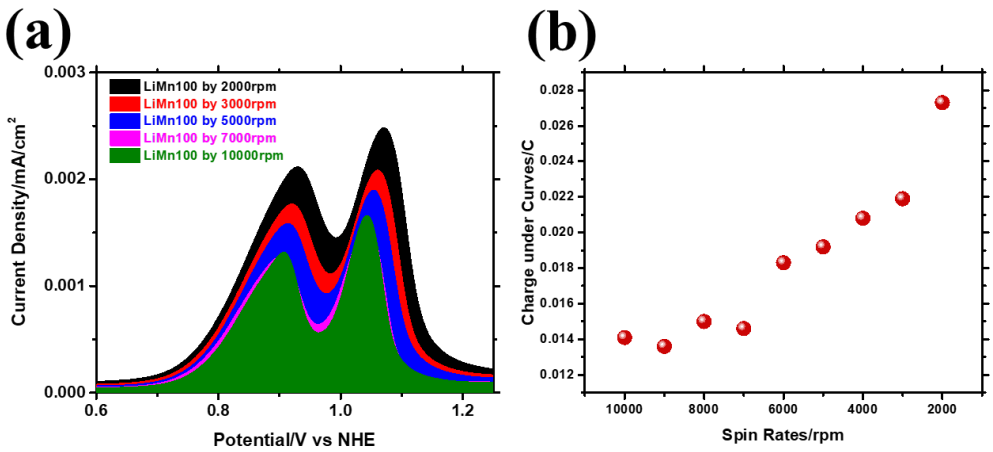

Figure 3.68 (a) Mathematical areas for calculation of charges, (b) Plot of spin rates vs calculated charges.

Electrode spin rate /rpm	Capacity /A*s	Catalytic load on FTO/μg/cm^2
2000	0.0273	61.1
3000	0.0219	49.1
4000	0.0208	46.5
5000	0.0192	42.9
6000	0.0183	40.9
7000	0.0146	32.7
8000	0.0150	33.5
9000	0.0136	30.4
10000	0.0141	31.5

Table 3.4 Table of spin rates and relevant charge densities and catalytic loads.

The charge densities of the LiMn100 electrodes decrease sequentially with increasing spin rate. Accordingly, the catalytic load of the films also inherently decreases by increasing spin rate. The calculated catalytic load decreases from 61.1 to 32.7 μg when the spin rate is increased from 2000 to 7000 rpm (see Table 3.4 for other spin rates). Further increase in spin rate to 10000 rpm causes fluctuation in charge density and catalytic load, but all are about 30-31 μg. This is due to the roughness on the FTO surface and limits the coating by crystalline FTO particles on the surface.

The same electrodes were further used to quantify the amount of active site on the LiMn100 electrode surface. A small faradaic peak at 0.6 V, referred to as MnO_2 formation, was used to calculate active site amounts in nmol/cm^2 by using equation 1.2 (see introduction section). In this calculation, it was assumed that the peaks due to adsorbed species were directly proportional to the scan rate and the surface coverage. Also, number of electrons transferred in this oxidation process is assumed to be one electron. Slopes of current density vs scan rate were extracted for all spin rates and the equations are derived. Using slope "i/ν", and other parameters in the equation, surface coverages of all films were calculated. Scan rate (ν) vs current density (i_p) plots of the films are shown in Figure 3.69(a)

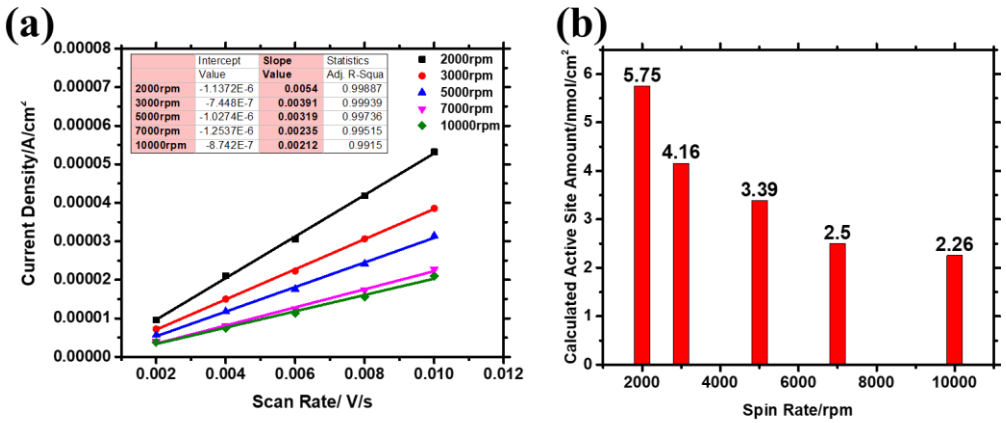

Figure 3.69 (a) Current density vs scan rate plots of the LiMn100 electrodes, (b) calculated surface coverages of the same LiMn100 electrodes at different spin rates.

Active surface coverages of the films were calculated, see Figure 3.69(b). Notice that the highest surface coverage is in the LiMn100, fabricated at 2000 rpm. Notice also that the coverage gradually decreases with increasing spin rate, as expected. The LiMn100 electrode, coated at 2000 rpm is the thickest film and accordingly has the most active sites. Further increase in the coating rate decreases the amount of material and results a less active sites. This behavior might be also explained by the amount of surface coverage, see Figure 3.69 (b).

Same electrodes were further used in CP experiments in 1 M KOH at 1 mA/cm^2 to 50 mA/cm^2 current densities for a duration of 120 or 60 min to investigate the relation between active surface coverages and OER efficiencies. Figure 3.70 displays multistep-CP (the overpotential versus time) plots for all above electrodes.

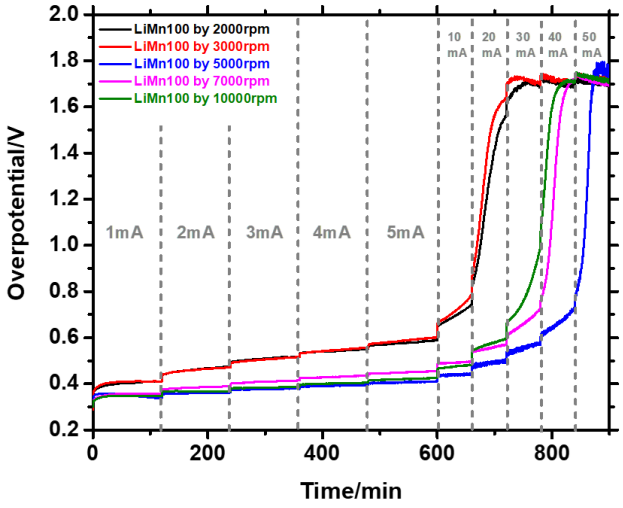

Figure 3.70 Multistep CP results of LiMn100 fabricated at different spin rates.

According to the CPs at 1 mA/cm^2 to 5 mA/cm^2, the LiMn100 films, fabricated at 2000 and 3000 rpm, display higher overpotentials. However, the LiMn100 electrodes, fabricated at 5000 to 10000 rpm have lower and similar overpotentials. This behavior might be attributed to the film quality of the electrodes. The surface morphology has been found to be better and smoother for the LiMn100 electrode, fabricated at 4000 rpm, see SEM section. The CP results also show that the active surface coverage has no effect on the OER catalysis. For instance, an electrode with a highest active surface may displays the lowest OER performance. Electrode quality has a more significant effect on the water oxidation performance. Furthermore, the electrodes were tested at higher current densities from 10 to 50 mA/cm^2 to investigate the electrode stability under harsh catalytic conditions. Notice that the overpotentials of the electrodes, coated at 2000 and 3000 rpm, increase very fast at 10 mA/cm^2. At 20 mA/cm^2 current density, the degradation completes very fast and a bare FTO overpotential is observed in the CP. When the electrodes are fabricated at 5000 rpm, it shows the lowest overpotential values among other spin rates. No overpotential increase is observed at 10 mA/cm^2 current density. An increase in the overpotential is observed at 20 to 40 mA/cm^2 current densities, but increase of the overpotential is not as fast as the other electrodes. It reaches to a bare FTO overpotential value at 50 mA/cm^2 current density. Also, the electrodes fabricated at 7000 and 10000 rpm show a faster degradation at higher current densities compared to the LiMn100 electrode, coated at 5000 rpm. This might be due to FTO roughness, related to pointy crystalline FTO particles on the electrode surface at higher spin rates. These pointy sides may trigger more degradation.

To understand the degradation mechanism of the films, the electrodes, fabricated at 2000 and 5000 rpm were cycled in 1 M KOH solution between 0 and 1 V for 300 times with a 50 mV/s scan rate. Then, the current densities at 1 V are plotted against the cycle number to show the degradation by cycling. Figures 3.71(a) and (b) show the CV curves of the electrodes, coated at 2000 and 5000 rpm, respectively.

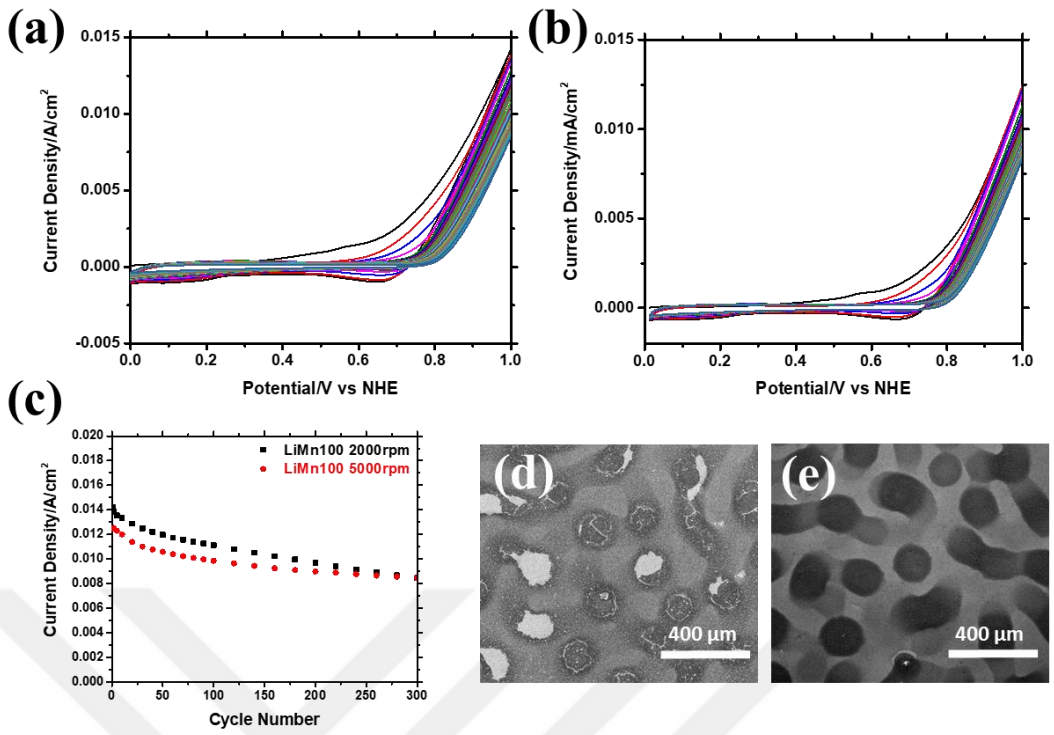

Figure 3.71 (a) CV curves of LiMn100 by 2000 rpm, (b) CV curves of LiMn100 by 5000 rpm, (c) Cycle number vs current densities at 1 V, (d)SEM image of LiMn100 by 2000 rpm after cycling, (e) SEM image of LiMn100 by 5000 rpm after cycling.

The current density changes by cycling process, as shown in Figure 3.71(c). Notice that the current density decay, at 1 V, is faster in the electrode fabricated at 2000 rpm than 5000 rpm. It means that the degradation is faster in the 2000 rpm electrode.

SEM images of the electrodes were also recorded after using in above cycling experiment. Figure 3.71(d) and (e) show the SEM images of the 2000 and 5000 rpm electrodes, respectively. According to SEM images after cycling, the damage on the electrode surface, generated by oxygen bubbles, is clearly observed in the 2000 rpm electrode. It has been already shown that the LiMn100 electrode, fabricated at 2000 rpm spin rate, has more cracks. These cracks may make the electrode surface more fragile for oxygen evolution. On the other hand, no damage is observed in the electrode, fabricated at 5000 rpm. Degradation in the 2000 rpm electrode might be also correlated with the damage due to the loss of the film particles on the electrode surface in addition to the Mn(VI) disproportionation. As a conclusion, the $LiMn_2O_4$ electrode, fabricated by 5000

rpm spin rate, is found to be efficient and stable for further electrochemical characterization.

3.1.6.2 Effect of Calcination Temperature on Electrochemical Properties of Mesoporous $LiMn_2O_4$ Thin Films

The electrodes, fabricated at 5000 rpm, are used to determine the effect of calcination temperature on the electrochemical properties of the electrodes. Firstly, the crystalline particle size of LiMn100 has been analyzed using the XRD data. Electrodes are firstly fabricated by calcining at 300 °C for 1 h and then further annealed at 350, 400, 450, and 500 °C for another hour. It has been previously shown that annealing above 550 °C results in the formation of Mn_2O_3 crystallites.[25] XRD patterns are recorded between 17.5 and 20.0°, 2θ, to focus on the diffraction line at 18.5°, see Figure 3.72.

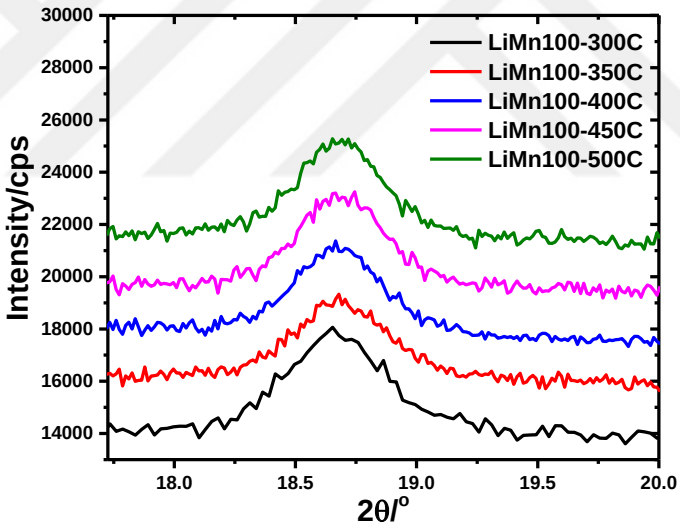

Figure 3.72 Wide-angle XRD patterns of the LiMn100 thin films, fabricated at 5000 rpm and annealed at various temperatures.

All annealed electrodes display a similar FHWM value, indicating that the crystalline particles on the electrodes are almost the same size. This behavior of the annealed $LiMn_2O_4$ electrodes is also correlated by BET surface area and BJH pore size calculations from the N2 adsorption-desorption isotherms. The BET surface area of the $LiMn_2O_4$ powders has been previously reported as 98, 90, and 69 m^2/g at 300, 400, and 500 °C, respectively. The BJH average pore size has also been previously reported as around 11 nm at each annealing temperature.[25]

This is also strong evidence for the thermal stability of the LiMn100 films and attributed to the thermal stability of the manganese oxides.[126]

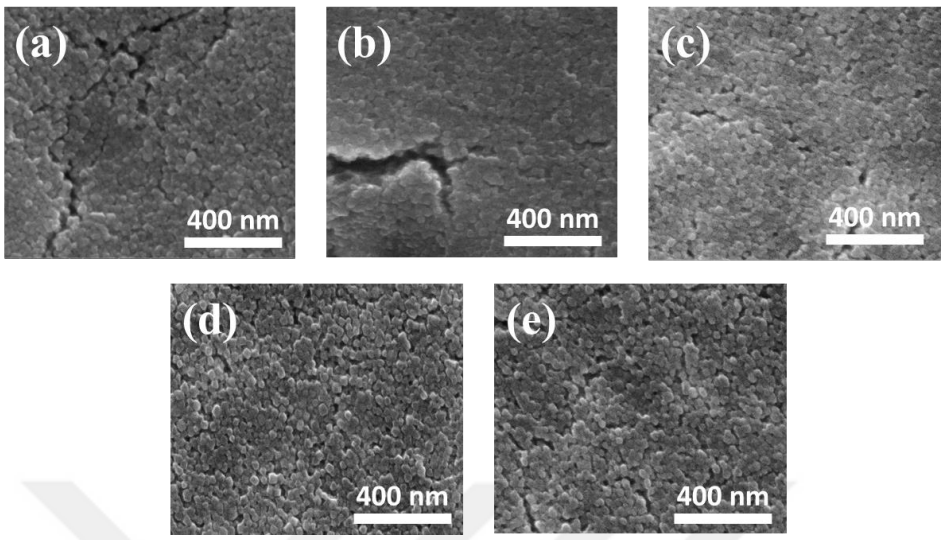

Figure 3.73 SEM images of LiMn100 thin films at 5000 rpm on top: (a) 300 °C, (b) 350 °C, (c) 400 °C, (d) 450 °C, (e) 500 °C.

Furthermore, SEM images of the thin films, annealed at various temperatures were also collected to investigate the temperature dependent changes in the morphology and particle size and found that both does not alter within the above temperature range, see Figure 3.73.

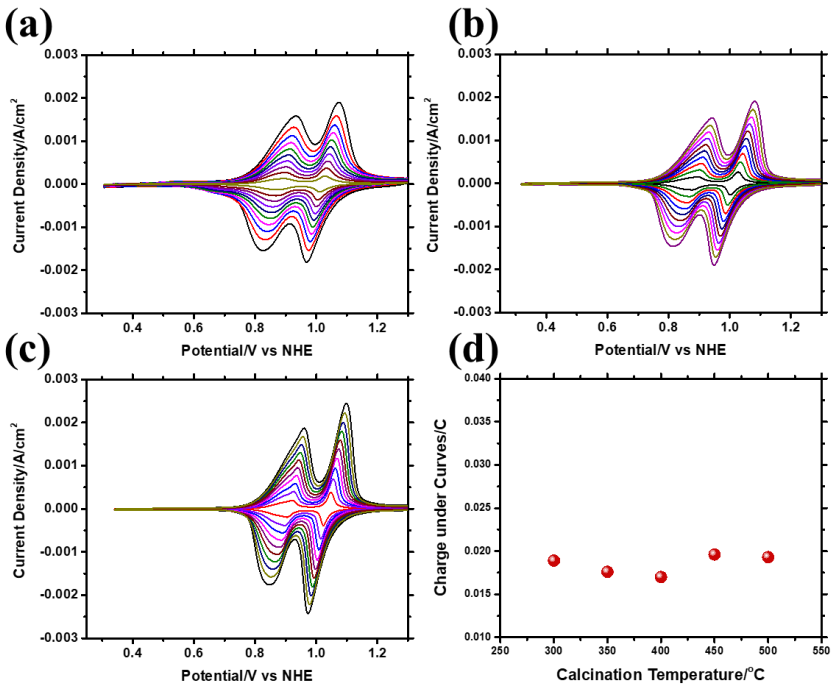

Figure 3.74 CV curves of LiMn100 (5000 rpm) electrodes in 1 M $LiNO_3$ fabricated at various annealing temperatures. (a) 300 °C, (b) 400 °C, (c) 500 °C. (d) Plot of annealing temperature versus calculated charges.

The LiMn100 electrodes were further used to investigate the electrochemical properties. Initially, these electrodes were cycled in 1 M $LiNO_3$ electrolyte at various scan rates between 0.3 and 1.3 V. The CV curves are shown in Figure 3.74(a), (b), and (c) for the electrodes, annealed at 300, 400, and 500 ^oC, respectively.

Notice that current densities of the redox peaks between 0.7 and 1.2 V are similar to each other for all annealed electrodes. This means that the $LiMn_2O_4$ load is preserved during annealing process. Amounts of total charge, under the oxidation peaks, are calculated by dividing the area under the curves to scan rate, 20 mV/s. Figure 3.74(d) shows the plot of the capacity of the electrodes with respect to the calcination/annealing temperatures. According to the plot, the total charge values fluctuate, but are approximately the same. These charge values and calculated catalytic (using equation 3.1) masses are tabulated in Table 3.5. There are no significant changes in the charge densities and catalytic masses by increasing the annealing temperature; the electrodes have similar behaviors

Electrode annealing temperature/ ^oC	Capacity /A*s	Catalytic load on FTO/μg/cm^2
300	0.0189	42.2
350	0.0176	39.4
400	0.0170	38.1
450	0.0196	43.8
500	0.0193	43.1

Table 3.5 Electrode calcination temperatures and relevant charge densities and catalytic loads.

The current density as a function of scan rate graphs for each oxidation and reduction peaks are obtained to quantify the lithium intercalation and de-intercalation process using Equation 1.2. Figure 3.75 (a), (b) and (c) represents the current density versus ν^x graphs for the LiMn100 electrode, calcined at 300, 400 and 500 ^oC, respectively.

A diffusion controlled redox displays a direct relationship between the square root of scan rate versus current density. If the redox process is from the surface adsorbed species, then the scan rate is directly proportional to the

current density and x is equal to 1. However, all plots failed to be linear for x equal to 1. To eliminate this deviation, various values of x between 0.5 and 1 as the exponent of ν, are tested to obtain a best fit. The fitted graphs with suitable exponentials are shown in Figure 3.75 for all the redox peaks. The current density versus ν^x fits the best with x being 0.85, 0.8 and 0.75 for the electrodes, calcined at 300, 400 and 500 ^oC, respectively. These values are almost in the middle of 0.5 and 1. Thus, the lithium intercalation de-intercalation processes show both freely diffusive (x = ½) redox (bulk of the material) and adsorptive (x = 1) redox (surface of the electrode, maybe including pore surfaces) property by these values. It is reasonable to suggest that the redox process occurs at the electrode surface and drives the lithium de-intercalation/intercalation through diffusion of Li^+ ions from the bulk of the electrodes.

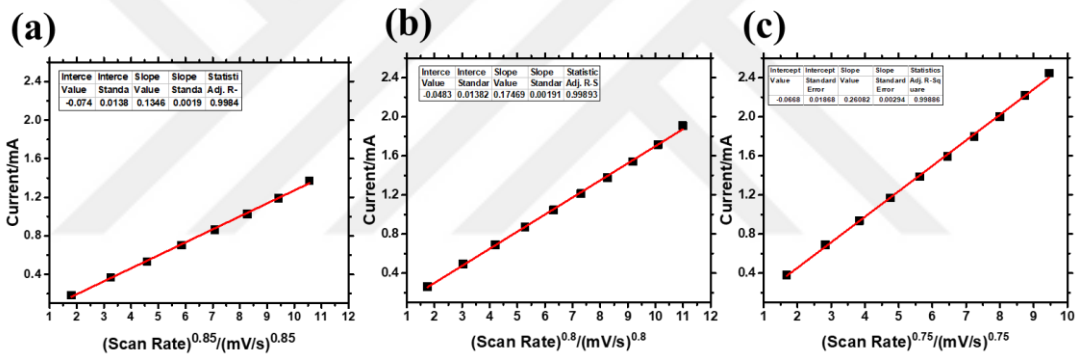

Figure 3.75 Graphs of ν^x vs i_p (at 1.05V) of LiMn100 electrodes, annealed at (a) 300 ^oC, (b) 400 ^oC, (c) 500 ^oC.

Notice that, LiMn100 at 300 ^oC has higher surface area of 98 m^2/g and smaller particles. Thus, adsorptive contribution is higher (x=0.85 and closer to 1), see Figure 3.75(a). When the annealing temperature increases to 500 ^oC, x becomes 0.75, which is closer to 0.5, see Figure 3.75(c). It means diffusive contribution is higher for the lithium de-intercalation since the surface area decreases to 69 m^2/g and the particles become larger.

Lastly, the annealed LiMn100 electrodes were tested in the OER potentials by recoding their multi-step CP data at 1 to 50 mA/cm^2 current densities. Figure 3.76 shows the CP plots, overpotentials versus time.

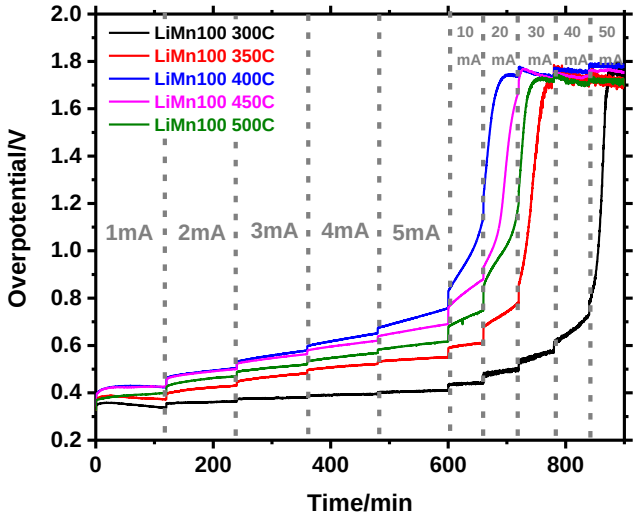

Figure 3.76 Multistep CPs of the LiMn100 electrodes, prepared at various calcination temperatures.

Higher annealing temperatures did not improve the OER performance and electrode stability, compare the plots in Figure 3.76. The electrode, calcined at 300 ^{o}C, displays the best performance and stability among the electrodes, annealed within 300 and 500 ^{o}C range. Anonymously, all FTO coated electrodes undergo degradation and this could be due to FTO itself. Because FTO is coated over glass and glass is not stable in basic solutions. To test this, similar electrodes were also fabricated on graphite rods and used for electrochemical tests.

3.1.6.3 Effect of the Electrode Substrate on Electrochemical Properties of Mesoporous $LiMn_2O_4$ Thin films

In this section, the substrate effect on the electrochemical properties of thin films is investigated. Graphite rods are used as a conductive substrate that are coated and calcined as usual. However, for coating instead of spin-coating, a dip coating method was employed. Stability tests were performed by long-term cycling experiments in 1 M KOH and the graphite results are compared with the results of FTO coated electrodes.

The clear precursor solutions were diluted 5, 10, 20, 50, and 100 times by volume using absolute ethanol and used for dip-coating. First, the graphite rods are cleaned and dried as described in the experimental section. Then, the

graphite rods are immersed into the diluted solutions and pulled out with a speed of 10 cm/min. Finally, the coated graphite rods are calcined at 300 ^{o}C for 1 h.

SEM technique was employed to check the film formation on the graphite surface, see Figure 3.77.

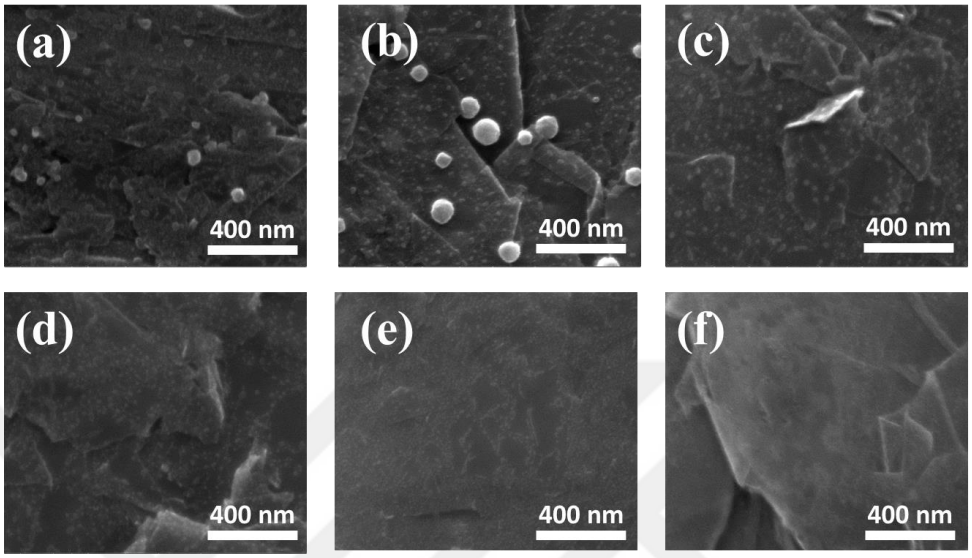

Figure 3.77 SEM images of LiMn100 films fabricated on graphite electrodes using diluted solutions with dilution factor of: (a) 5x, (b) 10x, (c) 20x, (d) 50x, (e) 100x, (f) bare graphite.

According to the SEM images, the electrodes, fabricated using 5- and 10-times diluted precursor solutions, have large spherical particles on their surface, in addition to smaller particles on the graphite surface with film-like structure, see Figure 3.77(a) and (b). The SEM image of the electrode, prepared from 20-times diluted solution, displays no large particles, but the smaller particles are more obvious in the image, see Figure 3.77 (c). In electrodes of further diluted solutions (50- and 100-times), the accumulation of smaller particles is still visible in the images, see Figure 3.77(d) and (e). Note also that the bare graphite surface does not show any particles, see image in Figure 3.77(f).

The graphite-electrodes were also used to investigate their electrochemical properties in 1M $LiNO_3$ electrolyte and also to quantify total charge. CVs of the electrodes are recorded at 5 mV/s scan rate between 0.3 and 1.3 V vs NHE potential window. Figure 3.78(a) shows the CV curves of the graphite electrodes. The CVs display typical lithiation and de-lithiation peaks,

similar to FTO-based electrodes. Also, increasing the dilution factor results in a decrease in charge densities under the curves, see Figure 3.78.

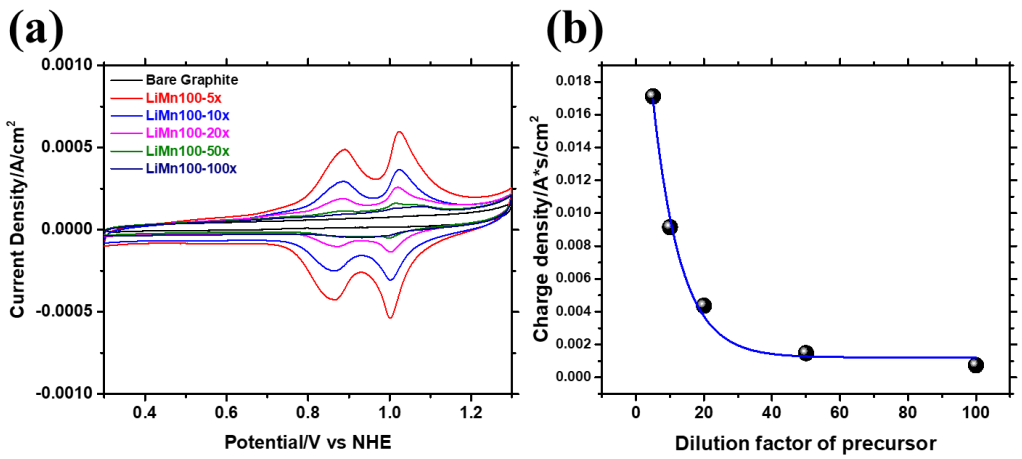

Figure 3.78 (a) CV curves of $LiMn_2O_4$ thin films on graphite substrates, (b) plot of precursor dilution factor versus charge densities.

Charge densities under the curves were calculated utilizing the area under the peaks and plotted with respect to dilution factors, see Figure 3.78(b). The total charge is 17.1, 9.1, 4.3, 1.4 and 0.7 mC in the electrodes, obtained from 5-, 10-, 20-, 50- and 100-times diluted solutions, respectively. Notice that the charge density decreases exponentially with dilution up to 50-times dilution and becomes almost flat above 50. The decrease is as expected since diluted solution produces thinner coating and therefore thinner electrodes.

For a fair comparison of electrode substrates, LiMn100 electrodes, fabricated over FTO at 5000 rpm and graphite rod, coated using 5-times diluted solution were chosen. The LiMn100 electrode, fabricated at 5000 rpm on FTO, is preferred due to its stability. For the graphite-based electrodes, the LiMn100 electrode, coated using 5-times diluted solution is preferred, because the charge density (accordingly catalytic load) on graphite surface is almost identical to the FTO electrode, coated at 5000 rpm. Then, a series of CVs were recorded in 1 M KOH electrolyte and the current density changes at 1 V are monitored. Figure 3.79 shows the 1st and 300th CV curves of both electrodes.

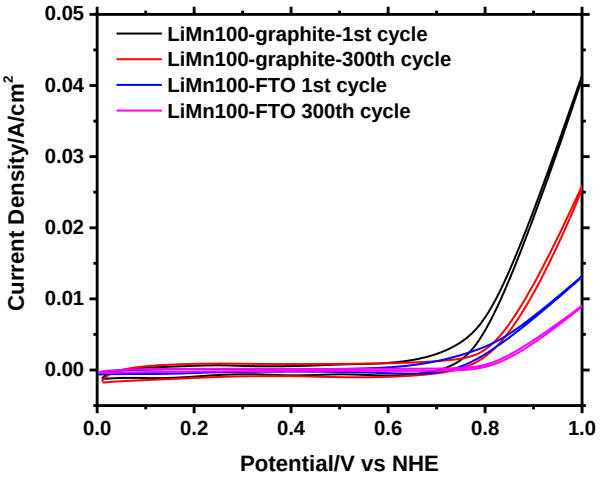

Figure 3.79 CV curves (1M KOH with a 50 mV/s scan rate) of LiMn100 electrodes fabricated on FTO and graphite electrodes.

Similar to the FTO electrode, the LiMn100 on graphite also shows a decrease in current density at 1 V. This means that the Mn(VI) disproportionation reaction also occurs in the graphite electrodes. Current density after 300 cycles is around 65 % of the 1st cycle in both electrodes. Therefore, it is reasonable to conclude that the graphite substrate does not improve the stabilities of the LiMn100 electrodes and main source of electrode degradation is the Mn(VI) disproportionation reaction.

3.1.7 Mn(VI) Disproportionation Reaction Mechanism

Permanganate ($[MnO_4]^-$) formation was observed on the LiMn100 electrode surface and the amount of manganese dispersed into the electrolyte was quantified using the ICP-MS technique (section 3.1.2.8). Also, the electrochemical experiments in KNO_3 and $LiNO_3$ electrolytes showed that the manganese amount decays when the LiMn100 electrodes are swept to OER potentials. It is commonly known that the Mn(VI) disproportionation reaction (see equation 1.10) takes place at high voltages and produces solid MnO_2 and soluble $[MnO_4]^-$ species that disperse into electrolyte and loss in manganese content on the electrode surface. We have also observed this type of manganese loss in our electrochemical experiments. Based on this information, we suggested a Mn(VI) disproportionation reaction mechanism on the electrode surface.[52] In Figure 3.80, a schematic representation of the Mn(VI) disproportionation reaction mechanism is demonstrated.

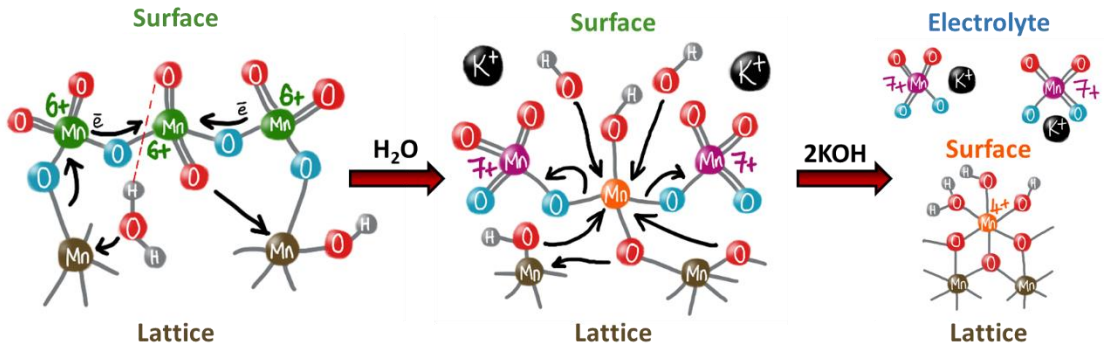

Figure 3.80 Schematic representation of Mn(VI) disproportionation on LiMn100 electrode surface.

In the mechanism, three adjacent manganese sides on the electrode surface undergo a degradation. The Mn(IV) dominates the electrode surface after the de-lithiation process at specific potentials. When the electrode is used at a higher potential, the manganese oxidizes to Mn(VI). Notice that the 3 Mn are connected to each other by bridging oxygens; see Figure 3.63. Two manganese in the terminal sides are less electronegative compared to the middle manganese since they are connected to the lattice Mn(IV) sites by bridging oxygens. Thus, the Mn(IV) sides in the lattice are less electronegative and directly affect or decrease the electronegativity of the terminal Mn(VI) species. The middle Mn(VI) side is surrounded by two Mn=O oxo-oxygens and two bridging oxygens that are attached to the terminal Mn(VI) sides. This connectivity makes the middle manganese side oxygen-rich and more electronegative. This electronegativity variance on the manganese sides leads to electron transfer from less electronegative sides to more electronegative side. Therefore, 2 electrons are transferred from the terminal Mn(VI) to the middle Mn(VI). The middle manganese side is reduced to Mn(IV) and the terminal ones oxidize Mn (VII). The Mn(VII) species on the electrode surface are quite unstable and disperse into the electrolyte solution in the presence of proper cation species in the electrolyte solution. Also, it is likely that the formation H_3O^+ ion, due to water oxidation (water self-dissociation), enhances the permanganate release into the electrolyte solution. Thus, two manganese sides are lost by this disproportionation reaction and middle one is left as Mn(IV) on the electrode surface.

The presence of K^+ ions in the electrolyte solution enhances the dispersion of Mn(VII) species. In the LiOH electrolytes, the dispersion of permanganate ions

from the electrode surface is relatively less, compared to the KOH electrolytes. We have already shown this behavior from ICP-MS analysis and electrochemical cycling experiments in the $LiNO_3$, KNO_3, LiOH, and KOH electrolytes. Also, the structure of the electrode material affects the disproportionation reaction rate. For instance, layered $Mn(OH)_2$ structure undergoes a fast degradation compared to the Mn_3O_4 and $LiMn_2O_4$ structures. Also, note that $LiMn_2O_4$ is converted to λ-MnO_2 after de-lithiation and brings a unique crystal structure to resist manganate disproportionation reaction. Thus, the Mn_3O_4 electrode degrades much faster compared to the $LiMn_2O_4$ electrode.[52]

In conclusion, the Mn(VI) disproportion reaction is one of the significant problems since it causes degradation of the manganese-based electrodes in short or long-term electrochemical applications. Adjusting crystal structures, film thicknesses or increasing particle size might be a temporary solution for the short-term stability. However, prolonged and harsh conditions result in fast degradation of the manganese-based electrodes. In this case, the integration of a different 1st row transition metal ion into the manganese oxide matrix or surface might prevent the Mn(VI) disproportionation reaction. The middle manganese between the two Mn(VI) sides might be changed by another metal ion to prevent electron transfer from the terminal Mn(VI) sides. Thus, the Mn(VII) formation might be blocked on the electrode surface.

3.2 Electrochemical Properties of Mesoporous $LiMn_{2-x}M_xO_4$ Thin Films

Until this section, mesoporous spinel $LiMn_2O_4$ thin films were electrochemically investigated according to electrolyte types, surface species, OER efficiencies and stabilities to explain manganese disproportionation reaction. Moreover, various film morphologies of $LiMn_2O_4$ were also analyzed to find optimized synthesis parameters to produce electrodes with better resistance to the Mn(VI) disproportionation reaction and physical degradation in electrochemical OER electro-catalysis. Moreover, the spinel $LiMn_{2-x}M_xO_4$ electrodes were also prepared to search for right composition towards an

enhance OER efficiency and electrode stability. In addition to stability, addition of another transition metal into the structure may provide a synergistic effect for a more efficient OER electro-catalysis.

Transition metals, which were incorporated into the $LiMn_{2-x}M_xO_4$ structure are Fe, Co, Ni and Cu. Total 40 mole ratio of both transition metal per surfactant was used to prepare the electrodes and the atomic percentage of the compositions are used to denote the electrodes. The notations are given and explained in the experimental section. Here, LiMn100, LiMn95-M5, LiMn85-M15 and LiMn75-M25 compositions were investigated by fabricating electrodes at 5000 rpm. Additionally, the LiMn66-M33 electrodes were prepared. Because this composition was chosen as a unique ratio to prevent Mn(VI) disproportionation reaction in OER process. In this section, all electrodes were fabricated at 5000 rpm and calcined at 300 ^oC for an hour.

3.2.1 Synthesis and Characterization of $LiMn_{2-x}M_xO_4$ Thin Films

The $LiMn_{2-x}M_xO_4$ thin films were prepared using the MASA approach as described in the previous sections and characterized by utilizing XRD, XPS, and SEM techniques before electrochemical analysis. In the synthesis, the LLC film formation of various 20Li-40M-1C-1P compositions is ensured first by coating their solutions at 5000 rpm over microscope slides and abbreviated as LiMn%-M%. Small-angle XRD patterns of the LLC films were recorded between 1 and 5^o, 2θ. For the comparisons, the LiMn100, LiMn66-Fe33, LiMn66-Co33, LiMn66-Ni33 and LiMn66-Cu33 mesophases have been analyzed.

Figure 3.81 shows the XRD patterns of all compositions in the wide- and small-angles. According to the small-angle XRD patterns of the spin-coated LLC films, all compositions displayed diffraction lines. Notice that LiMn100 composition diffraction line(s) appears at a higher angle, namely at 1.45^o,2θ, compared to other compositions, see Figure 3.81(a).

The LiMn66-M33 sample diffracts at 1.89^o, 2θ. This might be due to difference in the structure of the LLC mesophase of the LiMn100 and LiMn66-M33 compositions. The d-spacing of the small-angle diffraction line is higher in

pure manganese nitrate mesophase and it decreases with the addition of another transition metal salt to the LLC mesophase.

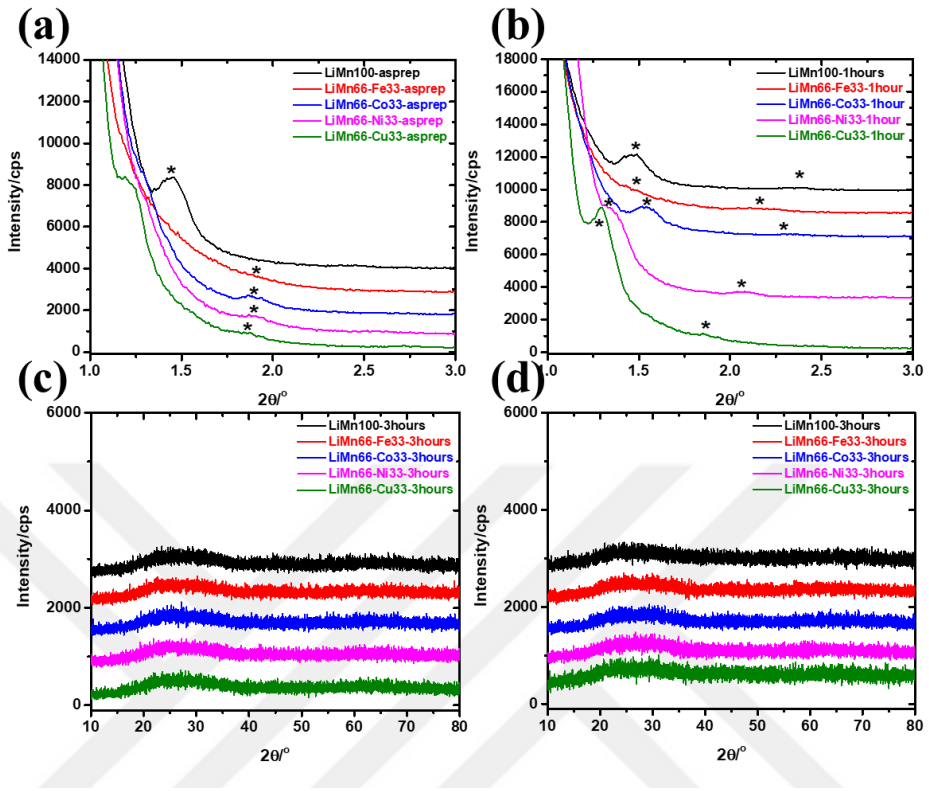

Figure 3.81 XRD patterns of LiMn66-M33 LLC systems: (a) Small angle patterns of as prepared LLC films at 5000 rpm, (b) Small-angle patterns of an hour aged drop-cast LLC films, (c) Wide-angle patterns of 3 hours aged LLC films at 5000 rpm, (d) Wide-angle patterns of 3 hours aged drop-cast LLC films.

The drop-casted LLC films also diffract at similar angles, see Figure 3.81(b). The drop-casted film displays more diffraction lines. The smallest angle diffraction line is observed at 1.29 to 1.55°, 2θ, range with a small shift in the drop-casted LiMn66-M33 mesophase, where M is a second metal salt, namely Fe(III), Co(II), Ni(II), and Cu(II) nitrate salts, respectively. Also, a 2nd diffraction line is observed between 1.83 and 2.38°, 2θ. Moreover, stability of the LLC mesophase was also investigated by recording wide-angle XRD patterns to check if there is any salt crystallization from the LLC mesophases. No diffraction line(s) is observed due to salt crystals in wide-angle XRD patterns of both drop-casted and spin-coated LLC films for at least 3 hours, see Figure 3.81(c) and (d).

The mesophases are calcined at 300 °C for 1-3 h depending on the film thickness. Spin-coated LLCs were instantly calcined upon spin coating at 2000 or 5000 rpm. Drop-casted LLCs were aged for an hour at RT, then calcined at 300 °C.

Then, the films were scraped from the microscope slides to collect their wide-angle powder XRD patterns.

Firstly, the XRD pattern of the mesoporous spinel $LiMn_{2-x}Fe_xO_4$ powders was collected. Figure 3.82 shows the XRD patterns of the $LiMn_{2-x}Fe_xO_4$ samples.

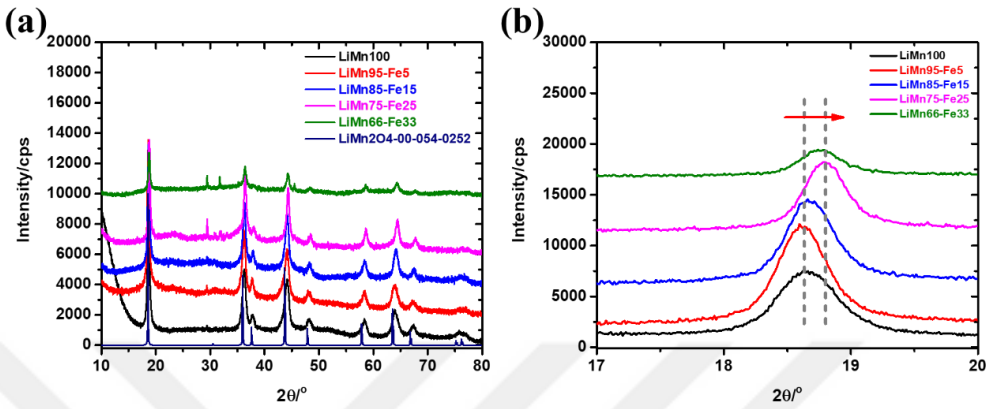

Figure 3.82 XRD patterns of the $LiMn_{2-x}Fe_xO_4$ thin films in the (a) 10 to 80° and (b) 17 to 20°, 2θ.

The films were prepared by spin coating of the relevant solution over microscope slides at 2000 rpm and calcined at 300 °C for 2 hours. Then, the thin films on microscope slides are scraped and collected as powders and their XRD patterns were recorded. The patterns of the $LiMn_{2-x}Fe_xO_4$ films are very similar to the spinel $LiMn_2O_4$ structure and all the diffraction lines are indexed to cubic spinel $LiMn_2O_4$ using the reference data (JCPDS no. 00-054-0252). There are also weak diffraction lines at 29.5 and 31.7°, 2θ, due to some impurities. These diffraction lines will be discussed later. Also, integration of Fe into the $LiMn_2O_4$ structure is evident from the gradual shift of diffraction lines to higher angles, due to slight difference between the size of the manganese and iron ions in the lattice.

The mesoporous $LiMn_{2-x}Fe_xO_4$ samples, fabricated by 5000 rpm spin rate, were also analyzed using XPS technique. The C 1s and O 1s spectra are shown in Figure 3.83.

In C 1s spectra shown in Figure 3.83(a), the peak at 284.8 eV is attributed to the signal of C-C species on the electrode surface. Notice that an extra peak appears and amplifies at 288.5 eV by increasing the iron content in the $LiMn_{2-x}Fe_xO_4$ samples. This peak is due to O-C=O species and strong evidence for the formation of carbonate species on the electrode surface. Thus, $FeCO_3$ formation

on the surface might be favored in the $LiMn_{2-x}Fe_xO_4$ samples. In the O 1s spectra, the lattice oxygen peak is observed at 529.8 eV. A shoulder at 531.4 eV might be attributed to carbonate species that amplifies with increasing iron amount in the structure, see Figure 3.83(b).

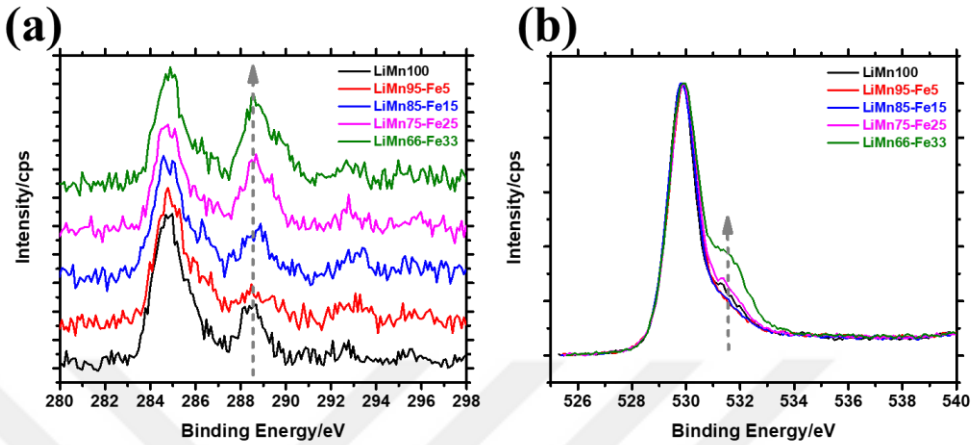

Figure 3.83 XPS spectra of $LiMn_{2-x}Fe_xO_4$ electrodes: (a) C 1s, (b) O 1s.

Then, the Mn 2p, Mn 3s and Fe 2p regions were also recorded and analyzed to elucidate structural detail of the surface species. Figure 3.84(a), (b), and (c) show the XPS spectra in the Mn 2p, Mn 3s and Fe 2p regions, respectively.

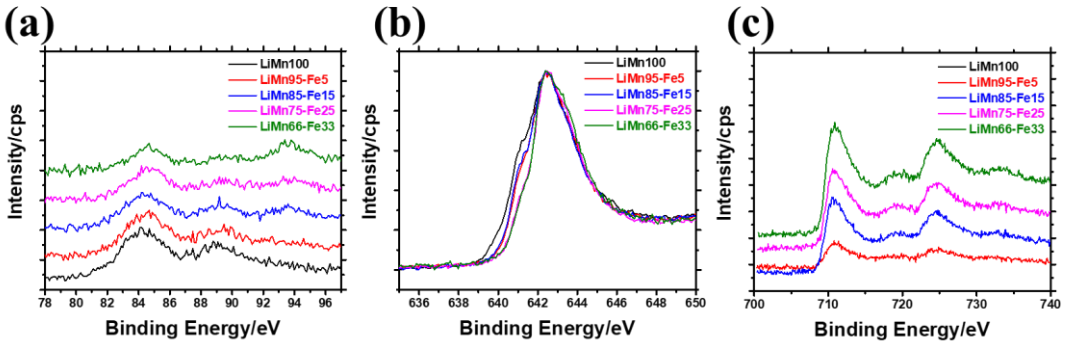

Figure 3.84 XPS spectra of $LiMn_{2-x}Fe_xO_4$ in the (a) Mn 3s, (b) Mn 2p ($^2P_{3/2}$), and (c) Fe 2p regions.

The Mn 3s XPS spectrum (Figure 3.84(a)) of the LiMn100 electrode displays two peaks in the Mn 3s region due to core and valance electrons coupling with a separation of 4.7 eV. This splitting is due to the presence of both Mn(III) and Mn(IV) species. The peak at 84.5 eV slightly shifts to higher energy by a gradual increase of iron and results in a decrease in the splitting energy of the two peaks. It also means that the manganese oxidation state increases slightly in the $LiMn_{2-x}Fe_xO_4$ samples. Also, Mn 2p spectra (in the $^2P_{3/2}$ region, in Figure

3.84(b)) display a shoulder at 641 eV due to Mn(II) that loses intensity with the integration of iron into the structure together with an enhancement of the manganese 3+ and 4+ peaks. These observations are consistent with the observed changes in the Mn 3s region. Finally, the Fe 2p region was investigated and the spectra of the $LiMn_{2-x}Fe_xO_4$ electrodes are shown in Figure 3.84(c). The peak at 710.8 eV and a broad satellite peak at 719.3 eV in the Fe 2p ($^2P_{3/2}$) region are strong evidence for the presence of Fe(III) species in the electrode structure. Notice also that the only change in the spectra with increasing Fe content is the intensity of Fe 2p peaks. Thus, the oxidation state of iron should be 3+ in all $LiMn_{2-x}Fe_xO_4$ compositions.[127]

The top-view SEM images of the $LiMn_{2-x}Fe_xO_4$ electrodes were also recorded. Figure 3.85 shows the SEM images of electrodes.

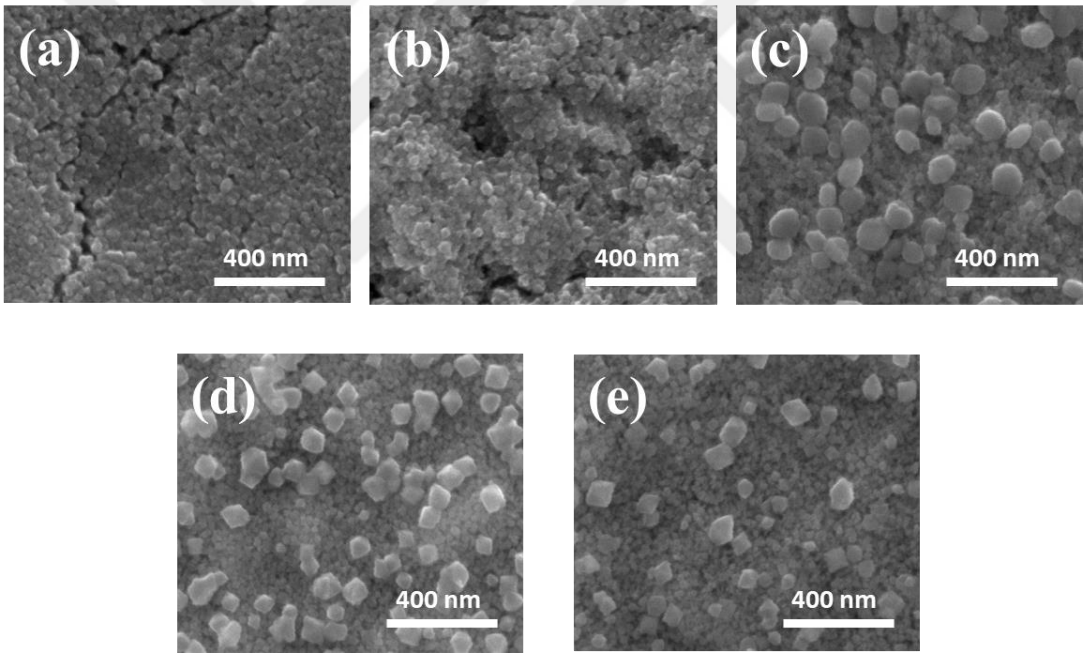

Figure 3.85 SEM images of $LiMn_{2-x}Fe_xO_4$: (a) LiMn100, (b) LiMn95-Fe5, (c) LiMn85-Fe15, (d) LiMn75-Fe25, and (e) LiMn66-Fe33.

SEM image of the LiMn100 composition display mesoporous features constructed by ultra-small $LiMn_2O_4$ nanoparticles and the electrode surface is smooth, see Figure 3.85(a). By the addition of 5 % iron into the $LiMn_{2-x}Fe_xO_4$ (LiMn95-Fe5) structure, the film becomes rougher but still shows porous structure, see Figure 3.85(b). Notice that other compositions of $LiMn_{2-x}Fe_xO_4$ show a porous structure with some large particles, see Figure 3.85(c), (d), and

(e). These particles could be $FeCO_3$ particles that accumulate on the electrode surface. However, the number large particles are less in the LiMn66-Fe33 and do not follow the iron content in the structure.

The $LiMn_{2-x}Co_xO_4$ samples were prepared using the same method and characterized using the same techniques. Materials fabricated by 2000 rpm were used to record powder XRD patterns. Their powder XRD patterns are shown in Figure 3.86(a).

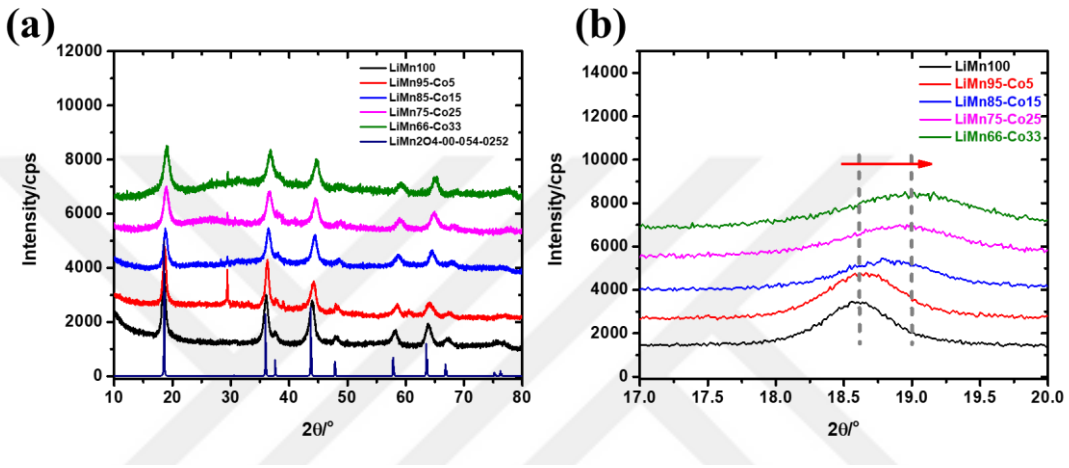

Figure 3.86 (a) XRD films of $LiMn_{2-x}Co_xO_4$ thin films, (b)Magnified version of pattern between 17° and 20°, 2θ.

Similar to $LiMn_{2-x}Fe_xO_4$, all the $LiMn_{2-x}Co_xO_4$ samples have a very similar diffraction pattern of the cubic spinel structure, as confirmed by comparing with the reference data of $LiMn_2O_4$. Diffraction line at 29.5°, 2θ, appears in the powder patterns of the samples, containing cobalt. The origin of this line will be discussed later. However, the diffraction line, observed from the $LiMn_{2-x}Fe_xO_4$ sample, at 31.7°, 2θ, disappears in cobalt containing samples. Thus, it may be attributed to no metal carbonate formation in these films. Shifts of diffraction lines to higher angles also prove that cobalt is successfully integrated into the $LiMn_{2-x}Co_xO_4$ structure without phase separation, see Figure 3.86 (b).

Then, XPS analysis of the $LiMn_{2-x}Co_xO_4$ thin films, fabricated at 5000 rpm on FTO substrate was carried out. A sharp carbonate signal is observed in the C 1s region of the $LiMn_{2-x}Fe_xO_4$ sample but this signal is not observed in the C 1s region of the $LiMn_{2-x}Co_xO_4$ spectrum, as also confirmed by the XRD data. The O

1s, Mn 3s, Mn2p ($^2P_{3/2}$), and Co 2p ($^2P_{3/2}$) spectra were also recorded and displayed in Figure 3.87.

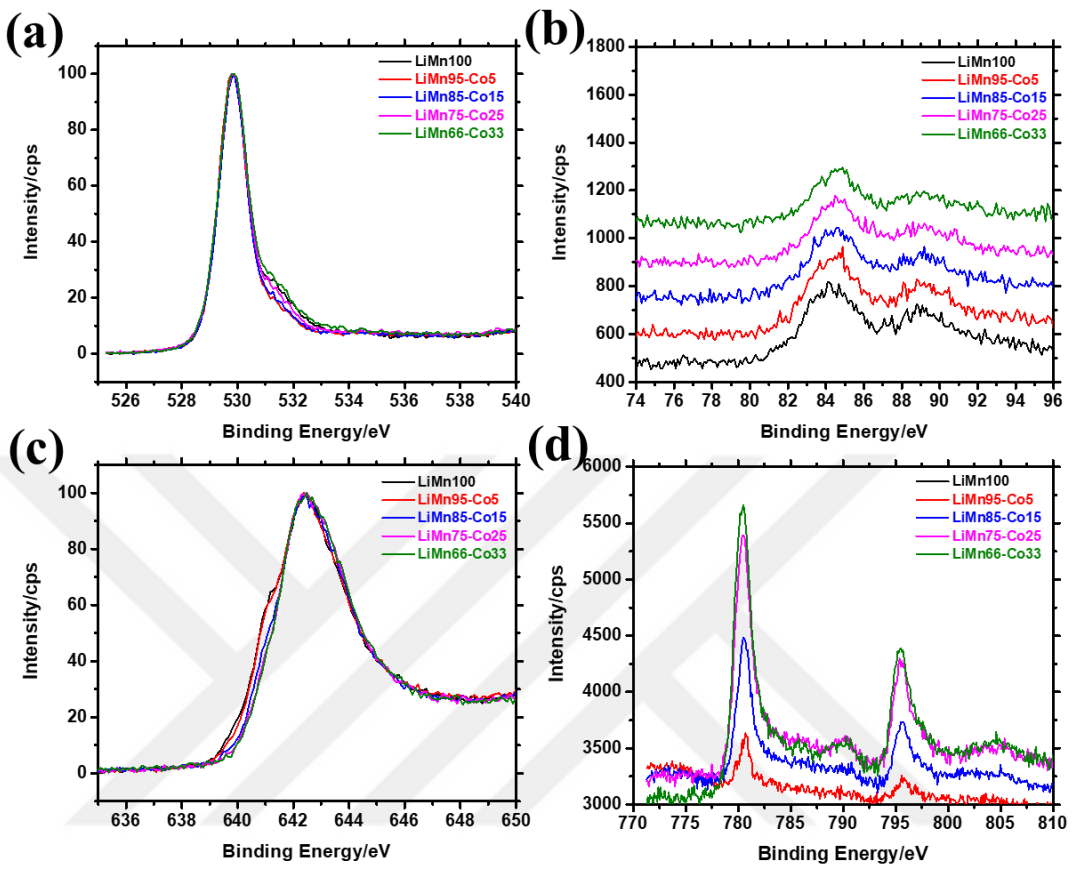

Figure 3.87 XPS spectra of $LiMn_{2-x}Co_xO_4$ electrodes: (a) O 1s, (b)Mn 3s, (c) Mn 2p ($^2P_{3/2}$), and (d) Co 2p.

Lattice oxygen peaks at 529.8 eV are normalized for the $LiMn_{2-x}Co_xO_4$ electrodes to compare the amount of other oxygen species on electrode surfaces in the O 1s spectra. The shoulder peak due to the hydroxyl feature at 531.2 eV is quite weak in all compositions with approximately the same intensities, see Figure 3.87(a). According to this peak intensity, the hydroxide species, accumulated on the electrode surface is a small amount. The Mn 3s spectra of the $LiMn_{2-x}Co_xO_4$ samples are shown in Figure 3.87(b). The splitting of peaks in the Mn 3s region decreases from 4.7 to 4.4 eV when the composition reaches LiMn66-Co33 from LiMn100. This is strong evidence of the manganese oxidation state that is predominantly 4+. This observation might be also correlated with the Mn 2p ($^2P_{3/2}$) spectra, see Figure 3.87(c). The shoulder peak at 641 eV (due to Mn(II) species) gradually diminishes by adding cobalt into the structure. Also, the Co

satellite peak in the Co 2p region at 790.3 eV is strong evidence for the Co(III) formation on the electrode surface.[127]

Film morphology of the $LiMn_{2-x}Co_xO_4$ samples is also investigated by collecting a series of SEM images, see Figure 3.88.

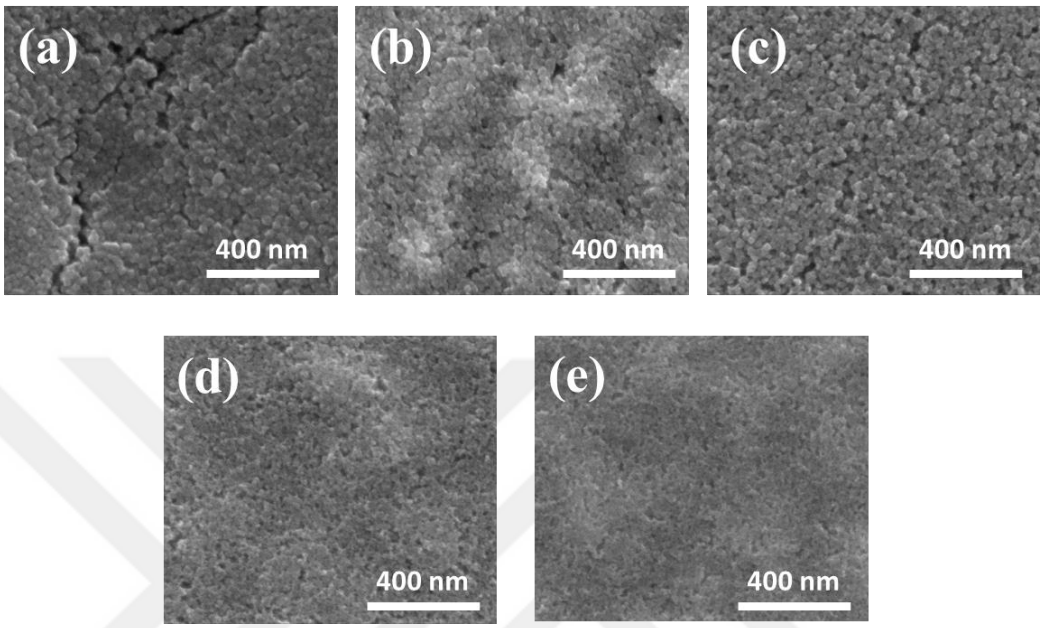

Figure 3.88 SEM images of $LiMn_{2-x}Co_xO_4$ electrodes: (a) LiMn100, (b) LiMn95-Co, (c) LiMn85-Co15, (d) LiMn75-Co25, (e) LiMn66-Co33.

Notice that film formations at all compositions are better compared to the $LiMn_{2-x}Fe_xO_4$ samples, see images in Figure 3.88. Also notice that the particle size decreases with the addition of more cobalt. This might also lead to a higher surface area for the Co containing electrodes.

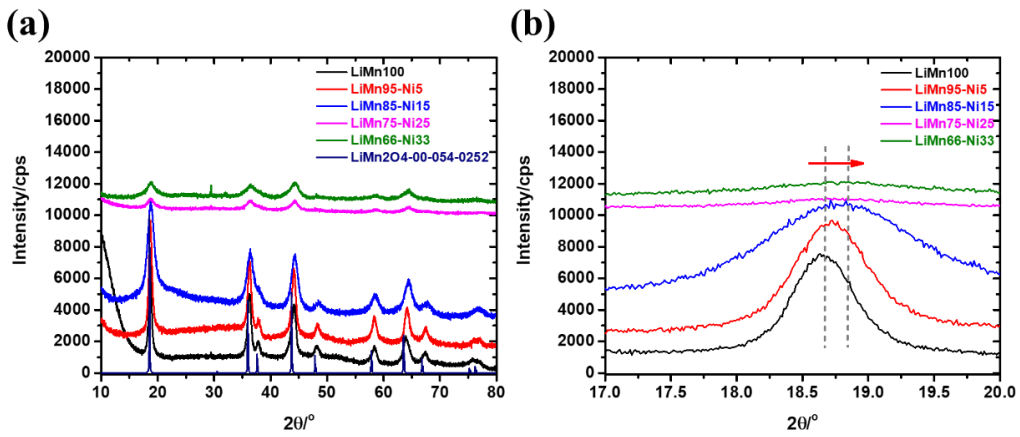

Figure 3.89 (a) XRD films of $LiMn_{2-x}Ni_xO_4$ thin films, (b) Magnified version of pattern between 17° and 20°, 2θ.

$LiMn_{2-x}Ni_xO_4$ thin films are also prepared using the same method and the electrodes are characterized using the same analytical techniques. Figure 3.89(a) displays a series of XRD patterns of the $LiMn_{2-x}Ni_xO_4$ powder samples, which are collected from a large number of samples, coated on microscope slides.

All XRD patterns of the $LiMn_{2-x}Ni_xO_4$ thin films display diffraction lines that can be indexed to cubic spinel $LiMn_2O_4$ structure by using the reference data of $LiMn_2O_4$ (from ICDD database, JCPDS no. 54-0252). Compositions with LiMn100 to LiMn85-Ni15 display similar diffraction patterns. However, films enriched by nickel at higher percentages than 15, show broader diffraction lines attributed to much smaller particle size for these compositions. Figure 3.89(b) displays the XRD patterns from 17° and 20°, 2θ. The shift of the line to a higher angle by a gradually increasing of the nickel content also shows the incorporation of nickel ions to the $LiMn_2O_4$ structure.

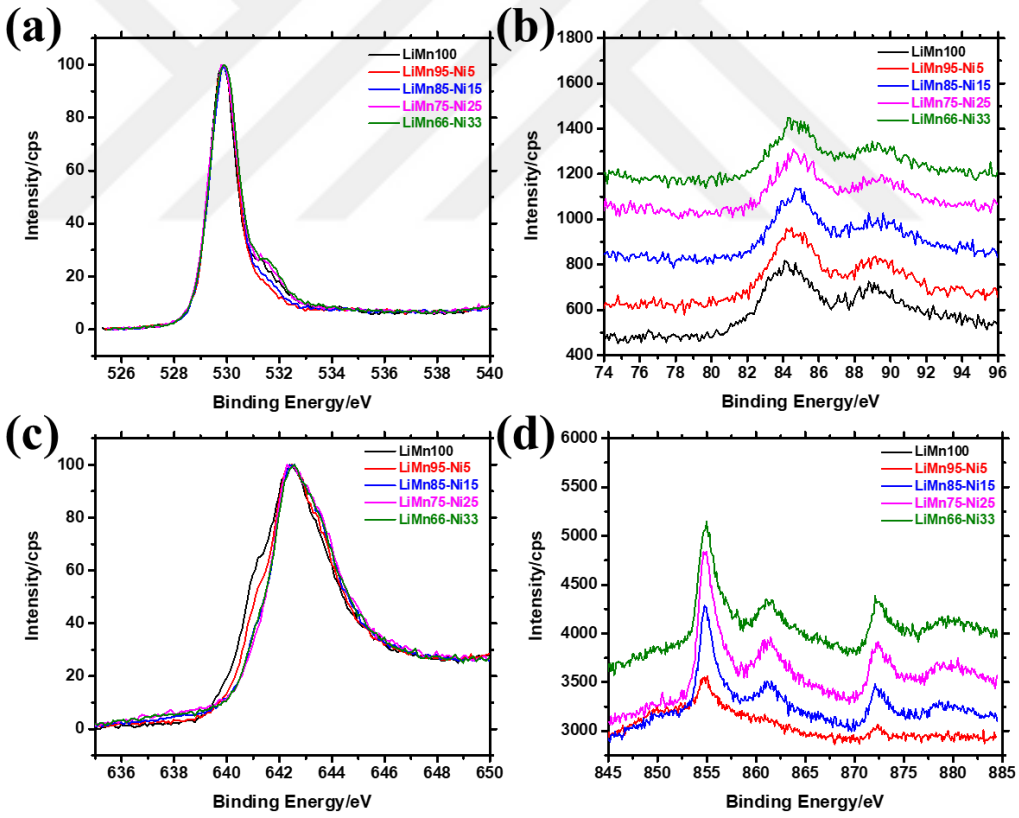

Figure 3.90 XPS spectra of $LiMn_{2-x}Ni_xO_4$ electrodes in the (a) O 1s, (b) Mn 3s, (c) Mn 2p ($^2P_{3/2}$), and (d) Ni 2p regions.

XPS analysis has been carried out using the $LiMn_{2-x}Ni_xO_4$ electrodes. O 1s spectra of the $LiMn_{2-x}Ni_xO_4$ samples are shown in Figure 3.90(a). According to the spectra, shoulder peaks due to the hydroxyl groups at 531.2 eV is weakly

observed in the nickel samples, similar to $LiMn_{2-x}Co_xO_4$. Then, the Mn 3s spectra of the same electrodes were recorded and the spectra are displayed in Figure 3.90(b). The splitting of the peaks in the Mn 3s region decreases from 4.7 eV to 4.4 eV when the composition changes from LiMn100 to LiMn66-Ni3. This is strong evidence that the Mn(IV) species are dominant in structures. The Mn 2p ($^2P_{3/2}$) spectra, in Figure 3.90 (c), also show that the shoulder of Mn(II) at 641 eV gradually decreases when the nickel amount is increased in the $LiMn_{2-x}Ni_xO_4$ structures. Thus, the manganese oxidation state increases with the addition of nickel. Discussion about the Ni 2p spectrum is complicated because satellite peaks and their binding energies are very similar in both Ni(II) and Ni(III) in their oxide and hydroxide derivatives.[128]

SEM images of the $LiMn_{2-x}Ni_xO_4$ samples (top-view) were also recorded to show the morphological features of the films, see Figure 3.91.

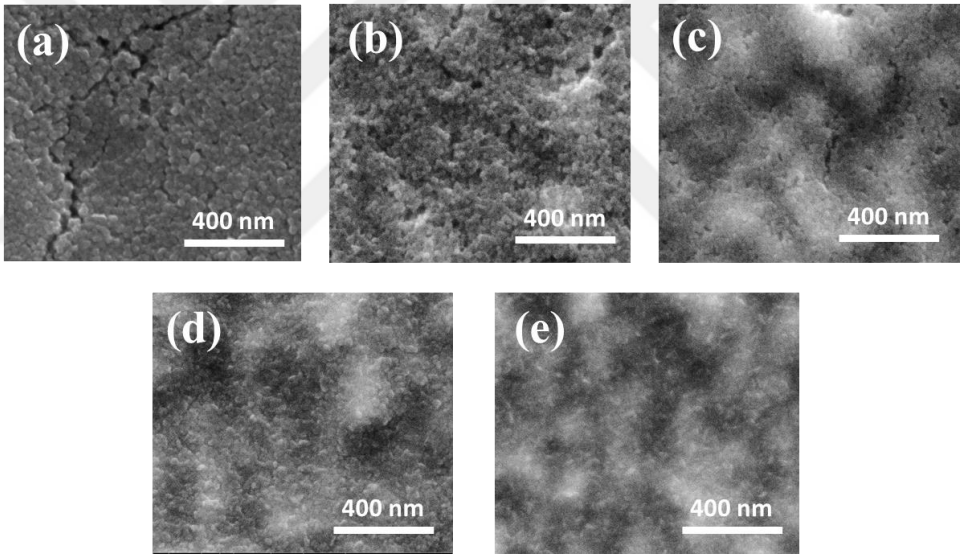

Figure 3.91 SEM images of $LiMn_{2-x}Ni_xO_4$ electrodes: (a) LiMn100, (b) LiMn95-Ni5, (c) LiMn85-Ni15, (d) LiMn75-Ni25, (e) LiMn66-Ni33.

Comparing the SEM images of the LiMn100 and LiMn95-Ni5 films, the morphology and particle size are similar to each other, see Figure 3.91(a) and (b). With further addition of nickel into the $LiMn_2O_4$ structure, the particle size decreased. Thus, LiMn85-Ni15, LiMn75-Ni25 and LiMn66-Ni33 compositions have smaller particle sizes as shown in Figures 3.91(c), (d), and (e), respectively. This might be also correlated by the XRD line-widths, observed from these films. The FWHM of the diffraction lines increases with increasing nickel content, indicating a decrease in the particle size, see Figure 3.89.

Finally, LiMn%-Cu% thin films are also prepared and investigated utilizing XRD, XPS and SEM techniques. The XRD patterns were recorded between 10° and 80°, 2θ, using powder samples, calcined at 300 °C and displayed in Figure 3.92(a).

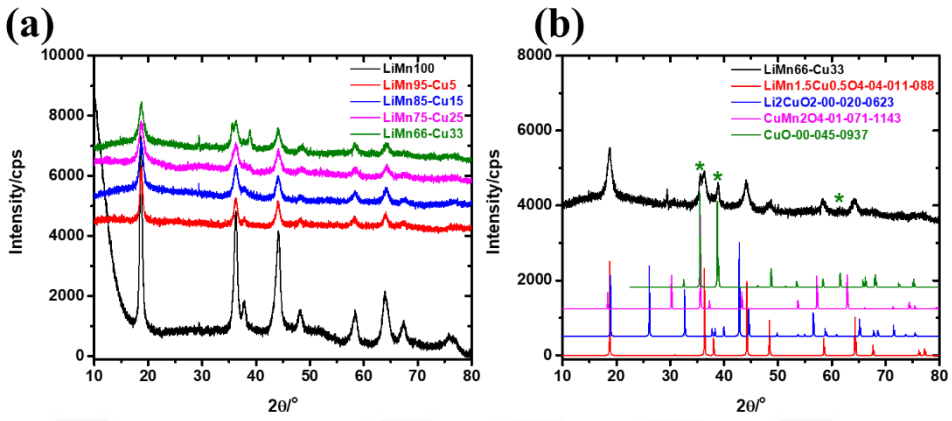

Figure 3.92 (a) XRD films of $LiMn_{2-x}Cu_xO_4$ thin films, (b) XRD pattern of LiMn66-Cu33 thin film and reference patterns of various copper-based oxides.

The XRD patterns of LiMn100, LiMn95-Cu5 and LiMn85-Cu15 films are indexed to cubic spinel $LiMn_2O_4$ as previously discussed in other metal systems. However, further addition of copper (higher than 25%), a phase separation becomes more obvious and the XRD pattern displays new extra diffraction lines at 35.58, 38.84, and 61.53, 2θ. These diffraction lines of LiMn66-Cu33 are indexed to CuO (all extra lines match with the CuO PDF card, JCPDS card no. 00-045-0937), see Figure 3.92(b) This is not surprising, because M in $LiMn_{2-x}M_xO_4$ structure should be at least in 3+ oxidation state, however, the stable highest oxidation state of copper is 2+. Thus, for higher compositions, copper prefers to form its own oxide phase, namely CuO.

The XPS spectra were also collected for further characterization of the $LiMn_{2-x}Cu_xO_4$ electrodes. Figure 3.93(a) shows the O 1s spectra of the LiMn100, LiMn85-Cu15 and LiMn66-Cu33 samples.

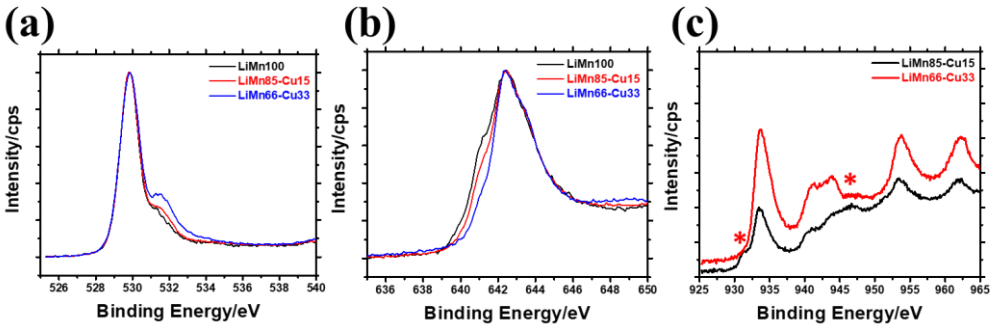

Figure 3.93 XPS spectra of $LiMn_{2-x}Cu_xO_4$ electrodes: (a) O 1s, (b) Mn 2p ($^2P_{3/2}$), and (c) Cu 2p.

According to O 1s spectra, the shoulder at 531.2 eV amplifies with increasing copper in $LiMn_{2-x}Cu_xO_4$ electrodes and originates from the hydroxyl sides on electrode surfaces. Figure 3.93 (b) shows the Mn 2p ($^2P_{3/2}$) region of the XPS spectra of the same electrodes. Similar to other metal systems, the shoulder at 641 eV belonged to Mn(II) which gradually decreases with the addition of copper since copper prefers the lower oxidation states, such as Cu(II). Therefore, the Mn(IV) content in the structure increases with increasing copper in the samples as evident in the Mn 2p region; the spectrum is typical with a MnO_2 peak shape in the LiMn66-Cu33 sample.

For further investigation, the Cu 2p region was also recorded. Notice that in the LiMn66-Cu33 spectrum, the satellite peaks appear at 941 and 943.5 eV. They are characteristic of CuO formation.[129] This formation is also correlated with the XRD measurements. The XRD pattern of the LiMn66-Cu33 composition displays CuO related diffraction lines. Additionally, Cu 2p peaks overlap with other manganese $L_2M_{23}M_{23}$ and $L_3M_{23}M_{23}$ peaks. Small peaks that appeared at 931 and 946 eV (assigned with asterisks) were attributed to $L_2M_{23}M_{23}$ and $L_3M_{23}M_{23}$, respectively.[130]

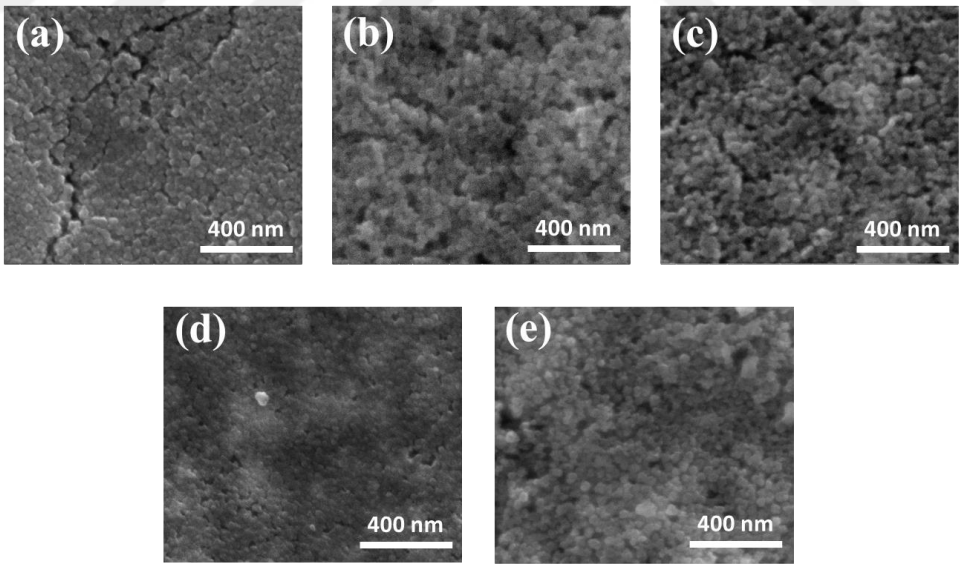

Figure 3.94 SEM images of $LiMn_{2-x}Cu_xO_4$ electrodes: (a) LiMn100, (b) LiMn95-Cu5, (c)LiMn85-Cu15, (d) LiMn75-Cu25, (e) LiMn66-Cu33.

For morphological characterization, the $LiMn_{2-x}Cu_xO_4$ electrodes are further investigated under SEM. The SEM images show similar spherical particles with approximately the same size. In the cobalt and nickel systems, addition of another metal into the structure caused a decrease in particle size. However, the

$LiMn_{2-x}Cu_xO_4$ electrodes are very similar to the $LiMn_{2-x}Fe_xO_4$ electrodes that are affected by the addition of more iron, see Figure 3.94.

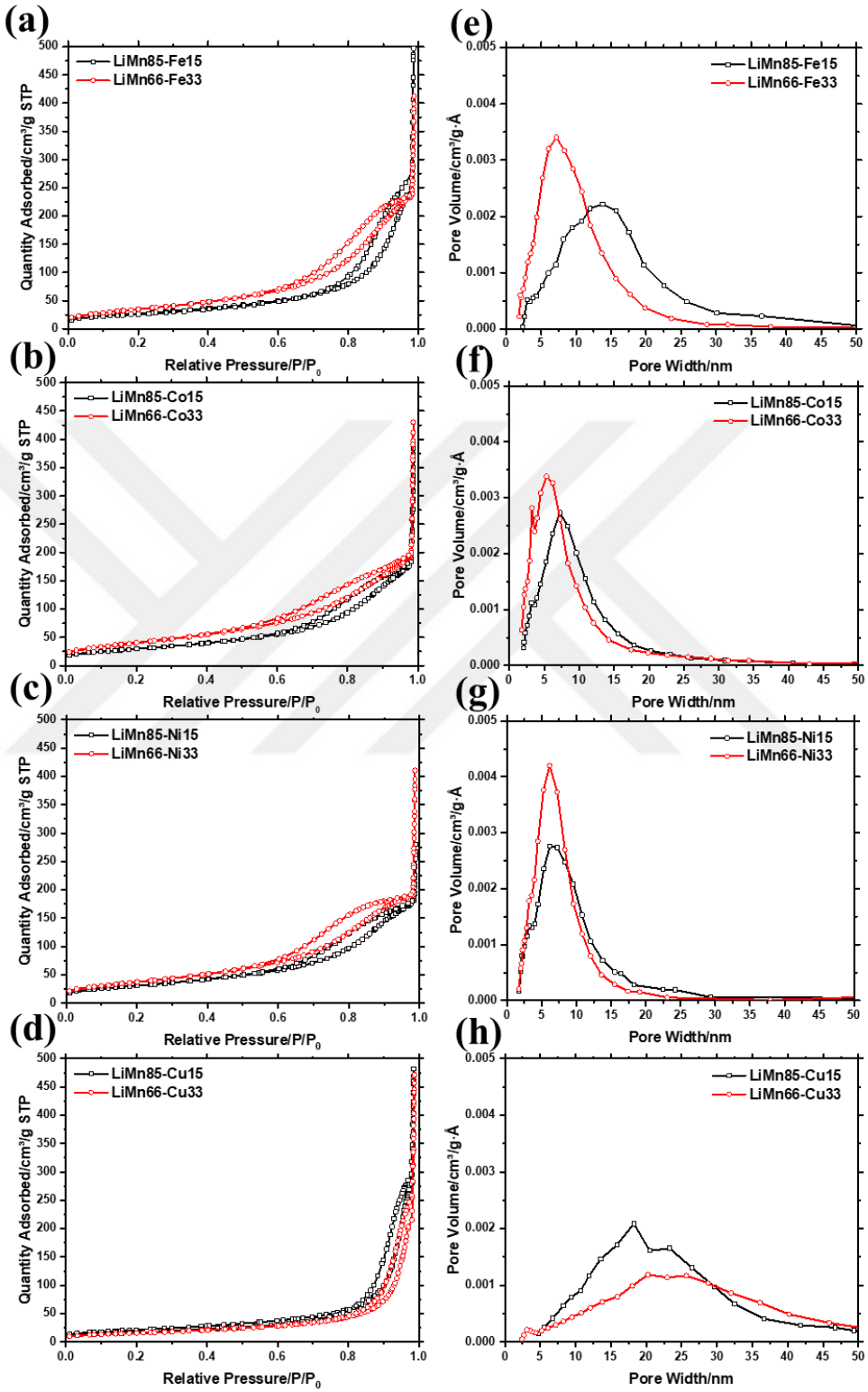

Figure 3.95 N_2 adsorption-desorption isotherms: (a) LiMn%-Fe%, (b) LiMn%-Co%, (c) LiMn%-Ni%, (d) LiMn%-Cu%. BJH pore size distribution: (e) LiMn%-Fe%, (f) LiMn%-Co%, (g) LiMn%-Ni%, (h) LiMn%-Cu%.

N_2 adsorption-desorption isotherms are also recorded from mesoporous $LiMn_{2-x}M_xO_4$ films and BET surface area and BJH pore size distribution values are evaluated. The powder samples are collected from the $LiMn_{2-x}M_xO_4$ thick films, fabricated by drop-casting and calcined at 300 ^oC for 3 hours. Figure 3.95 displays the isotherms and BJH pore-size distribution plots. The BET surface area values, average pore sizes and pore volumes are tabulated in Table 3.6.

$LiMn_{2-x}M_xO_4$	BET Surface Area /m^2/g	BJH Pore Size /nm	Pore Volume /cm^3/g
LiMn100	98	11.5	0.26
LiMn85-Fe15	99	12.9	0.62
LiMn66-Fe33	126	7.2	0.42
LiMn85-Co33	116	7.2	0.42
LiMn66-Co33	146	5.3	0.35
LiMn85-Ni15	112	7.2	0.29
LiMn66-Ni33	136	6.1	0.37
LiMn85-Cu15	75	19.6	0.56
LiMn66-Cu33	57	22.9	0.62

Table 3.6 N_2 adsorption-desorption data of the $LiMn_{2-x}M_xO_4$ thick films.

All linear isotherms of the $LiMn_{2-x}M_xO_2$ samples (Figure 3.95 (a), (b), (c), and (d)) have type IV hysteresis, which is unique for the mesoporous materials. Also, pore size distributions are narrower in the $LiMn_{2-x}Fe_xO_4$, $LiMn_{2-x}Co_xO_4$, and $LiMn_{2-x}Ni_xO_4$ samples; see Figure 3.95 (e), (f) and (g). However, the $LiMn_{2-x}Cu_xO_4$ sample has a broader pore size distribution plot. The LiMn100 and LiMn85-Fe15 films have similar BET surface area value (around 100 m^2/g) as tabulated in Table 3.6. Increasing iron content in the films increases the BET surface area which becomes 126 m^2/g in the LiMn66-Fe33 composition. Therefore, the average pore size also decreases from 12.9 to 7.2 nm with increasing surface area. In cobalt samples, further addition of cobalt into the $LiMn_{2-x}Co_xO_4$ sample leads to a gradual increase in the surface area, compare the BET surface areas of the LiMn85-Co15 and LiMn66-Co33 samples. Their average pore size becomes 7.2 and 5.3 nm, respectively. It is consistent with the SEM image since smaller pores are also observed in the SEM image of the LiMn66-Co33 electrodes, see Figure 3.88. Similar to the $LiMn_{2-x}Co_xO_4$, the $LiMn_{2-x}Ni_xO_4$ films also show a gradual increase in BET surface with the addition of nickel into the system. Remember also the XRD patterns of the $LiMn_{2-x}Ni_xO_4$ films (Figure 3.89) show that the

diffraction lines become broader, which is attributed to a decrease in particle size by increasing the amount of nickel. This also correlates with a shrink in pore size. Thus, a 6.1 nm average pore size is obtained for the LiMn66-Ni33 films. The copper system has an odder behavior, compared to the other metal systems, since BET surface area gradually decreases with increasing copper in the $LiMn_{2-x}Cu_xO_4$ samples. Notice that excess copper causes phase separation in the samples. CuO diffraction lines are also visible in the XRD pattern of LiMn66-Cu33, see Figure 3.92. This might be attributed to the formation of bulk CuO particles. Therefore, they have lower surface areas that reduce the cumulative surface areas of the $LiMn_{2-x}Cu_xO_4$ films. Also, the average pore size becomes bigger with the addition of copper into the LiMn100 system. Pores become as large as 20-22 nm due to this phase separation.

For the general comparison of the XRD patterns of $LiMn_{2-x}M_xO_4$ powders, the patterns of the all LiMn66-M33 samples are demonstrated in Figure 3.96.

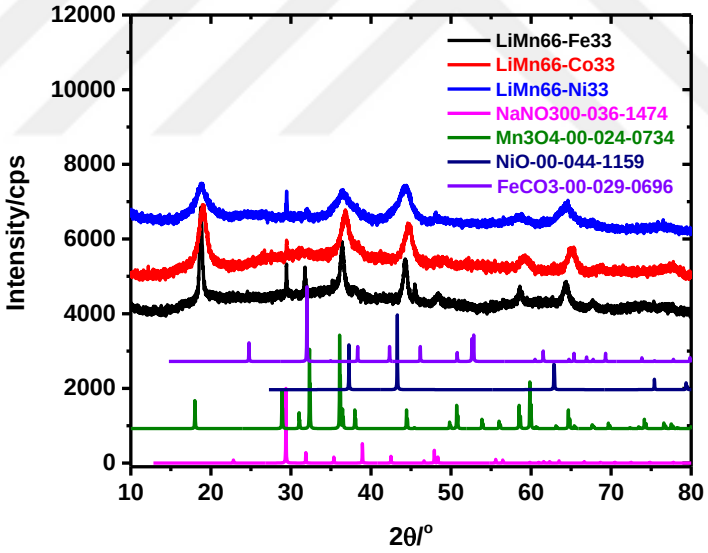

Figure 3.96 XRD patterns of LiMn66-M33 powders at 300 °C for 1hour.

A sharp diffraction at 29.4, 2θ° appears and does not shift by changing the metal type, namely iron, cobalt, or nickel. Thus, this diffraction is likely not related to these metals. The diffraction patterns of several manganese oxides were compared to identify this diffraction line, but there is no exact match from all likely manganese oxide species. However, the extra sharp diffraction line(s) matches perfectly with the pattern of $NaNO_3$ crystals. Note that these samples are calcined at 300 °C over glass microscope slides that contain about 23 % Na(I). It

is likely the NO_3^- ions of the precursors (namely $LiNO_3$) and Na(I) of glass form the $NaNO_3$ crystals in the samples. Also, note that the $NaNO_3$ crystals are stable at 300 °C, but decompose at around 350 °C.[131] The diffraction lines of LiMn66-Ni33 powders are quite broad either due to smaller crystalline domains or overlapping of these lines with the diffraction lines NiO and Mn_3O_4 due to phase separation. Moreover, the diffraction line at 31.9°, 2θ, has been attributed to Mn_3O_4 formation in the powder. Lastly, the sharp diffraction line at 31.7°, 2θ, in LiMn66-Fe33 composition may originate due to the formation of $FeCO_3$ particles in the sample, evaluated using $FeCO_3$ reference data from the database. The formation of these species on the $LiMn_{2-x}M_xO_4$ electrode has been previously discussed in the XPS characterization section. To further characterize, the XPS survey spectra were recorded to quantify the $NaNO_3$ content in the powders. The LiMn75-Co25 composition was chosen and a thin film of LiMn75-Co25 was synthesized at 2000 rpm followed by calcination at 300 °C for 2 hours. The XPS survey spectra of the powders, collected from two different thicknesses and two different substrates (namely, the sample coated on a glass slide at 2000 and the sample coated on FTO at 5000 rpm) are shown in Figure 3.96. Then, the sodium and nitrogen quantities were extracted in the whole spectrum and tabulated in the inset table of Figure 3.97.

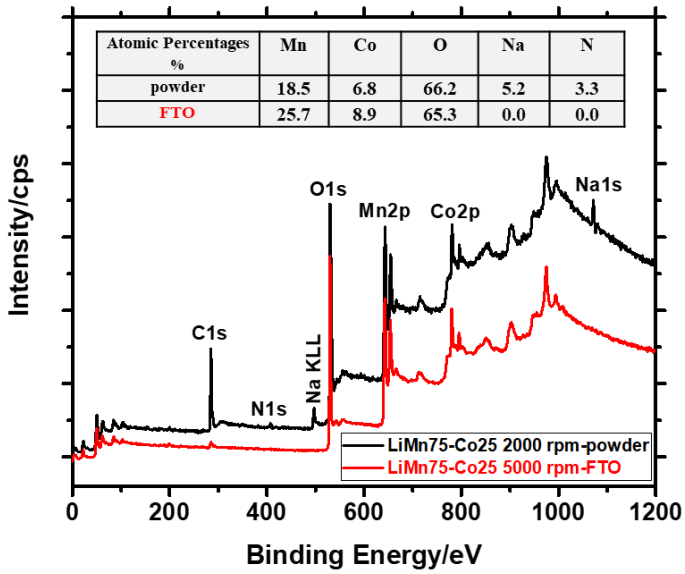

Figure 3.97 XPS survey spectra of LiMn75-Co25 fabricated on glass slide and FTO substrates. Atomic contributions were tabulated in the inserted table.

Notice that the LiMn75-Co25 fabricated on a glass slide contains 5.2% sodium and 3.3% nitrogen. This is consistent with the diffraction pattern of this sample that display of $NaNO_3$ diffraction line(s), see Figure 3.96. Moreover, the same composition was also used to produce LiMn75-Co25 thin film on the FTO substrate and its XPS survey spectrum was recorded, see red spectrum in Figure 3.97. The spectrum does not show any peak in the Na and N 1s regions. This behavior of the thin films might be attributed to the effect of substrates. Since the FTO layer coated on a glass slide prevents the diffusion of sodium ion into the film, using FTO prevents the issue of $NaNO_3$ formation and sodium-free LiMn75-Co25 films might be fabricated. The survey spectrum also shows that the thinner films are calcined more efficiently and displays much weaker C 1s peak(s); the C 1s region is much stronger in the sample coated at 2000 rpm, see Figure 3.97.

$LiMn_{2-x}M_xO_4$ thin films and electrodes have been characterized utilizing several techniques towards crystal structures, phase separations, oxidation states of the transition metals and morphologies. Unique chemical features have been demonstrated for the lithiated manganese oxides upon integration of another 1st row transition metal ion. In the next section, the electrochemical properties of these systems will be investigated.

3.2.2 Electrochemical Properties of Mesoporous $LiMn_{2-x}Fe_xO_4$ Thin Films

Electrochemical properties of the $LiMn_{2-x}Fe_xO_4$ thin films are investigated by first CV measurements in a $LiNO_3$ electrolyte to investigate lithium intercalation and de-intercalation faradaic reaction. The electrodes were fabricated by coating the relevant solutions over the FTO substrate at 5000 rpm. Because the quality films, coated 5000 rpm is the best, as shown in the $LiMn_2O_4$ electrodes. CVs of the $LiMn_{2-x}Fe_xO_4$ electrodes were recorded between 0.3 and 1.3 V with a scan rate of from 20 to 2 mV/s in 1 M $LiNO_3$ electrolyte. The CV curves of the $LiMn_{2-x}Fe_xO_4$ with various compositions are shown in Figure 3.98.

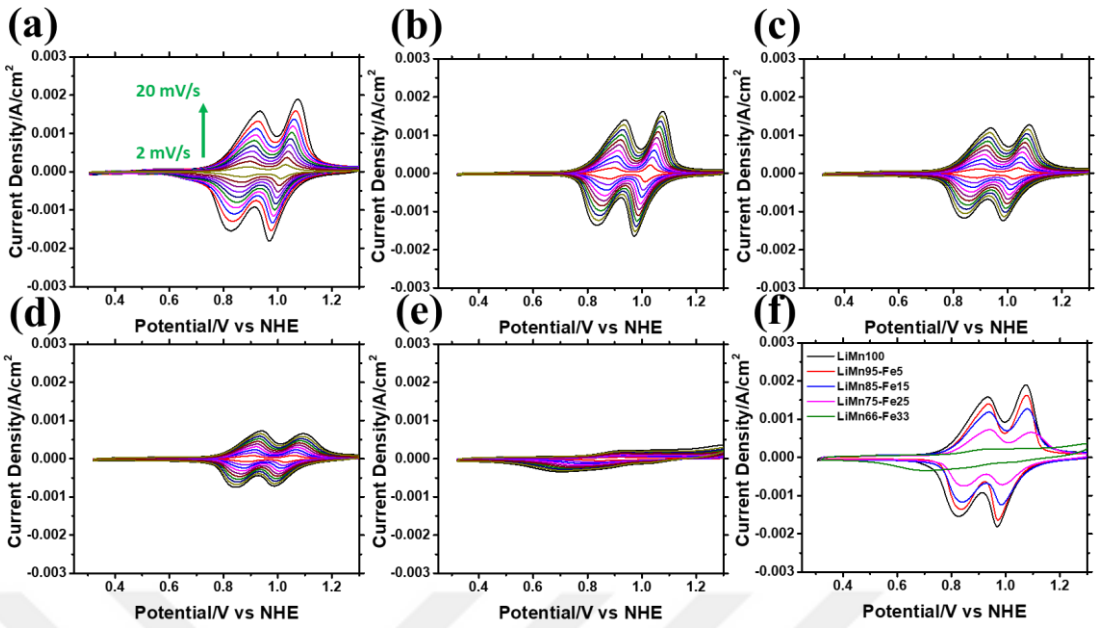

Figure 3.98 CV curves of $LiMn_{2-x}Fe_xO_4$ in 1 M $LiNO_3$: (a) LiMn100, (b) LiMn95-Fe5, (c) LiMn85-Fe15, (d) LiMn75-Fe25, (e) LiMn66-Fe33 and (f) CV curves of all composition at 20 mV/s.

According to the CV curves, the LiMn100 composition shows the highest charge density under the curves for lithium intercalation and de-intercalation reactions, see Figure 3.98(a). The charge density decreases gradually when more iron is incorporated into the structure, see Figure 3.98(b), (c), and (d). Notice that CV curves of the LiMn66-Fe33 electrode have very weak lithium intercalation and de-intercalation peaks. Figure 3.98(f) shows the CV curves of all compositions at 20 mV/s scan rate. Lithium de-intercalation process occurs in two steps. In the first oxidation peak at 0.9 V, half of the lithium content in $LiMn_2O_4$ is de-intercalated to form $Li_{0.5}Mn_2O_4$. The other half is de-intercalated at 1.1 V to form λ-MnO_2. Notice that this process requires Mn(III) site for the extraction of lithium ion. The Mn(III) content decreases with the addition of iron into the structure that causes a decrease in lithium de-intercalation. It is likely that the Fe(III) oxidation takes place at higher potentials to fully de-intercalate all lithium ions from the structure. This behavior of the electrodes will be discussed in the next part towards quantitative analysis of the $LiMn_{2-x}Fe_xO_4$ electrodes. However, one should note that the relative charges under these two peaks change by increasing iron in the electrodes.

Current densities of the 1st and 2nd peaks of the lithium de-lithiation are plotted with respect to scan rate to provide a clear picture for the changes in current densities in $LiMn_{2-x}Fe_xO_4$ electrodes. Plots are shown in Figure 3.99 (a) and (b) for 1st and 2nd peaks, respectively.

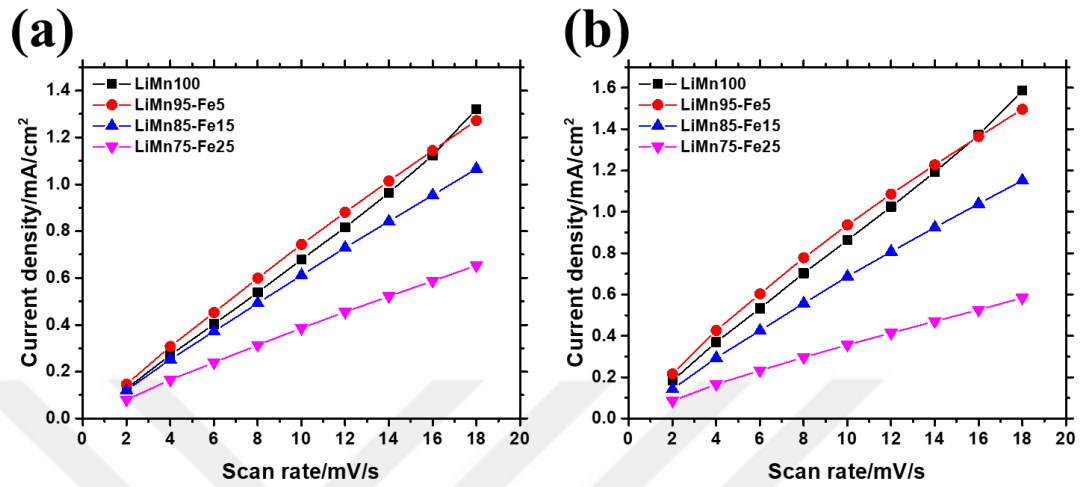

Figure 3.99 Current density versus scan rate plots of the de-lithiation peaks for the $LiMn_{2-x}Fe_xO_4$ electrode at (a) 0.9 V (1st peak) and (b) 1.1 V (2nd peak).

According to plots of the LiMn100 and LiMn95-Fe5 electrodes, these electrodes have similar current density variations in the 1st and 2nd peaks. However, the addition of 5% iron into the spinel structure causes a more deviation from the linearity compared to the LiMn100 plot. It means that these peaks show a diffusion-dependent oxidation rather than adsorption. This behavior has already been discussed in section 3.1.6.2. Furthermore, when the iron content is increased to 15 and 25% in the electrodes, deviation from linearity is still observable but decreases with further addition of iron. In that case, the surface area of the electrodes might enhance in iron rich electrodes and surface dominates the redox process.

From the LiMn100 electrode, the first peak has a higher charge density than the second peak. When the iron is incorporated into the electrode structure, the relative charge density under the second peak decreases gradually compared to the 1st peak. This might be due to the fact that half of the lithium ions near the Mn(III) sites are de-intercalated in the 1st oxidation peak and the manganese sides are already oxidized. The other portion of the Mn(III) sites are connected to more electronegative iron(III) ions. This is clear from the shift of the oxidation to

higher positive potentials with increasing iron in the structure. Also, the lithium ions in close vicinity to iron sides may be de-intercalated by oxidation of the Fe(III) sites and occur at more positive potentials. An increase of Fe(III) in this environment might increase above the electronic effect. This is because the lithium amount, de-intercalated in 2nd peak, is relatively lower than the 1st peak in the $LiMn_{2-x}Fe_xO_4$ electrodes. In addition to the electronic effect, the total charge under the peaks also decreases with the addition of iron into the structure. As discussed above, this might be due to Mn(III) content a decrease in $LiMn_{2-x}M_xO_4$ electrodes. When iron, cobalt, nickel, or copper is added to the spinel $LiMn_2O_4$ structure, these ions will be in a 3+ oxidation state (creating M(III) sites) and reduce the Mn(III) concentration in the structure. The Mn(III) sites are responsible for the observed delithiation and lithiation processes in the shown potential window. The result of the oxidation of Mn(III) to Mn(IV) is the de-lithiation process for the charge balance in the structure. Fe (III), Co(III), and Ni(III) could also be oxidized to (IV) state, but at relatively more positive potentials due to higher electronegativities of these metal ions. Electronegativity increases from left to right in a row in the periodic table (such as Ni > Co > Fe > Mn). Mulliken electronegativities of the metals and their ions are tabulated in Table 3.7.[132], [133] Thus, the Ni(III) requires higher potential to get oxidized compared to Mn(III). Thus, the de-lithiation by Fe(III), Co(III), and Ni(III) oxidation requires a higher voltage.

	Mn	Fe	Co	Ni
X(eV)	5.23	6.06	6.21	6.30

Table 3.7 Mulliken electronegativities (X) of manganese, iron, cobalt and nickel in eV.

For the quantitative analysis of $LiMn_{2-x}Fe_xO_4$ electrodes, the LSV, between 0.6 and 1.2 V, is recorded by a 5 mV/s scan rate and the charge density is calculated by using the mathematical area under the curves, see Figure 3.100(a).

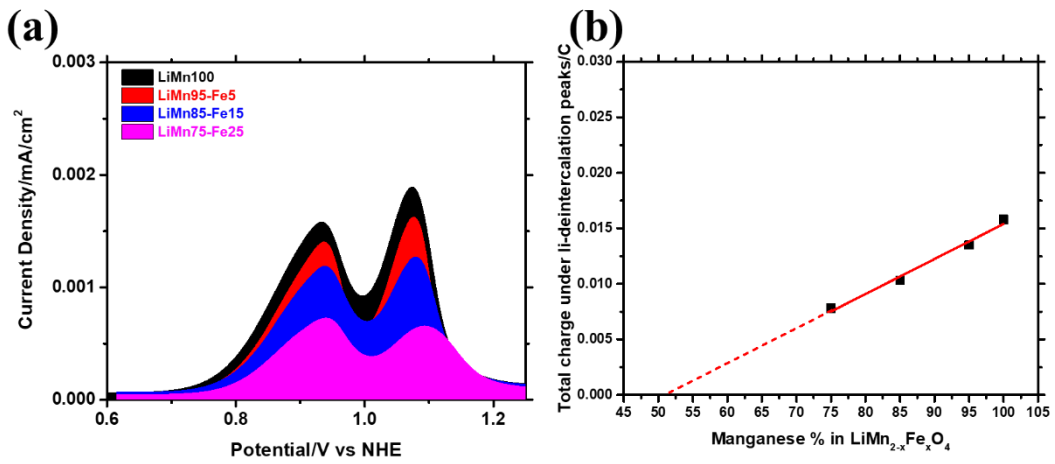

Figure 3.100 (a) Mathematical area under the LSV curve for calculation of charge density and (b) plot of charge density vs manganese % in the $LiMn_{2-x}Fe_xO_4$ electrodes.

The LiMn66-Fe33 composition was not swept because its lithium de-intercalation peaks are very weak, as shown in Figure 3.98(e). Then, these values are plotted with respect to manganese percentage in the $LiMn_{2-x}Fe_xO_4$ electrodes., see Figure 3.100(b). The plot gives an almost linear fit with an intercept of 50 %. This means lithium de-intercalation process might take place electrochemically until the material composition reaches LiMn50-Fe50. This makes sense because Mn(III) species exist in the electrodes up to 50 % iron. This does not mean, it is possible to prepare a LiMn50-Fe50 electrode, but it means that while the iron species is in 3+ oxidation state, all the manganese in the structure will be 4+ oxidation state to balance the charge in the lithiated spinel structure.

The $LiMn_{2-x}Fe_xO_4$ electrodes were further used to investigate the Mn(VI) disproportionation reaction to show the effect of iron on the disproportionation reaction and electrode degradation. The electrodes, fabricated at 5000 rpm, are used in CV cycling experiments between 0 and 1 V with a 50 mV/s scan rate. Each electrode was exposed to 300 cycles in 1 M KOH solution. The CV curves of the $LiMn_{2-x}Fe_xO_4$ electrodes are shown in Figure 3.101.

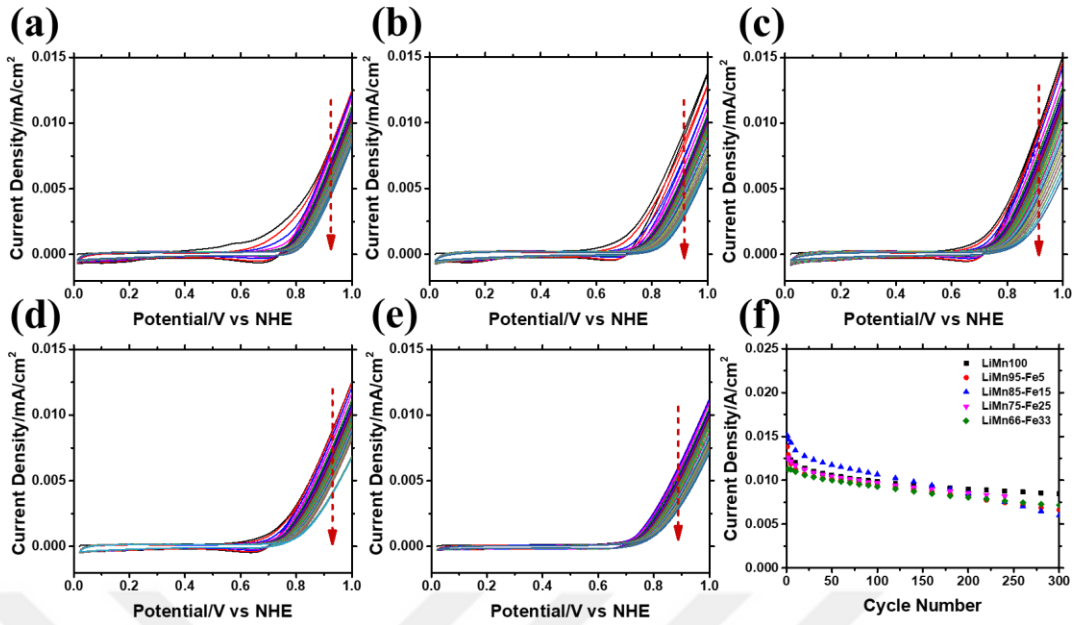

Figure 3.101 CV curves of $LiMn_{2-x}Fe_xO_4$ electrodes in 1 M KOH solution: (a) LiMn100, (b) LiMn95-Fe5, (c) LiMn85-Fe15, (d) LiMn75-Fe25, (e) LiMn66-Fe33 and (f) cycle number vs current density plot by 300 cycles.

According to the voltammograms of $LiMn_{2-x}Fe_xO_4$, all of the electrodes show efficiency decrease by cycling and observed as current density decrease in the OER region between 0.7 and 1 V. This decay means that the Mn(VI) disproportionation reaction is taking place in all compositions during CV measurements. To analyze the behavior of Mn(VI) disproportionation reaction, the current density at 1 V versus CV cycle number (300 cycles) is plotted. The plot is shown in Figure 3.101(f). Notice that there is no $LiMn_{2-x}Fe_xO_4$ composition that provides a stable current density by cycling. They all show a decrease in current density in first 300 cycles. Thus, iron doesn't improve the stability issues of the $LiMn_2O_4$ electrodes and has no effect on preventing disproportionation reaction. Moreover, iron might have its own electrochemical disproportionation reaction and may not be good candidate. Iron species are also known to undergo a degradation since it forms $[FeO_4]^{2-}$ species at higher potentials, see Frost and Pourbaix diagrams of iron in Figure 1.5(a) and Figure 1.7(a).

$LiMn_{2-x}Fe_xO_4$ electrodes were further analyzed after the cycling process using XPS technique. The O 1s spectra of the cycled electrodes are shown in Figure 3.102(a).

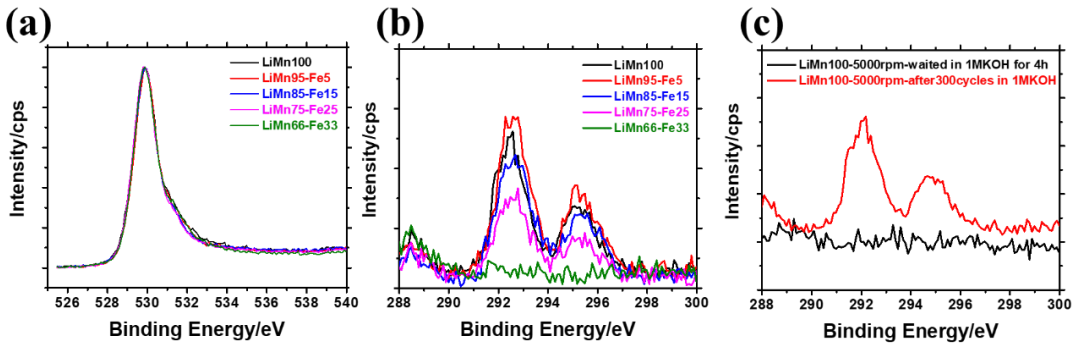

Figure 3.102 XPS spectra of $LiMn_{2-x}Fe_xO_4$ electrodes after 300 cycles in the (a) O 1s, (b) K 2p, and (c) K 2p region of LiMn100 cycled and aged in 1 M KOH solution for 4 hours.

Notice that the shoulder at 531.2 eV due to the carbonate feature disappeared after cycling the electrodes in 1 M KOH solution. C 1s region of the $LiMn_{2-x}Fe_xO_4$ electrodes also show that the shoulder at 288.8 eV completely disappears after cycling. This is not surprising because in the cycling process, the electrodes are used in the water oxidation region between 0.7 and 1 V. The catalytic process produces H_3O^+ rich environment on the electrode surface. Therefore, an acidic environment might dissolve carbonates.

XPS spectra in K 2p region was also analyzed upon cycling process. The K 2p spectra of the $LiMn_{2-x}Fe_xO_4$ electrodes after cycling are shown in Figure 3.102(b). Cycling in 1 M KOH causes K^+ intercalation to the structure. Intensity of K 2p peak enhances by increasing manganese amount in the $LiMn_{2-x}Fe_xO_4$ electrodes and no potassium signal is observed in the LiMn66-Fe33 composition. To be sure about the washing and drying procedure of the electrodes after cycling experiments, a control experiment has been done. Total time of the cycling experiment was calculated as 4 hours and a fresh LiMn100 electrode was also kept in 1 M KOH solution for 4 hours. Then, this electrode was washed using the same procedure and the XPS spectrum of the electrode was recorded to observe the potassium residual, but the spectrum displays no signal in the K 2p region, see Figure 3.102(c). As a conclusion, the washing procedure used in this experiment is a successful process to eliminate all electrolytic residuals.

The electrodes were further investigated by checking the Mn 3s, Mn 2p, and Fe 2p region using the cycled $LiMn_{2-x}Fe_xO_4$ electrodes. The Mn 3s spectra are shown in Figure 3.103(a).

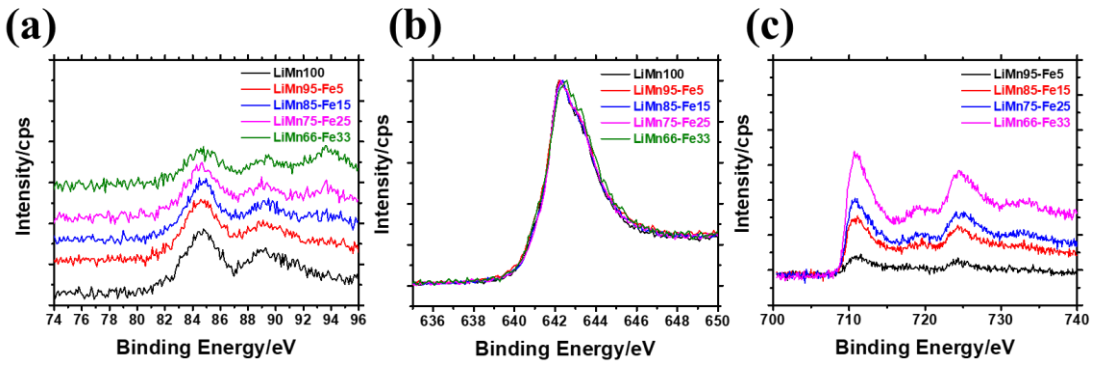

Figure 3.103 XPS spectra of $LiMn_{2-x}Fe_xO_4$ electrodes after 300 cycles: (a) Mn 3s, (b) Mn 2p ($^2P_{3/2}$), (c) Fe 2p.

The differences in the binding energy of split peaks are 4.4 eV for all compositions and it means that the manganese species are in a 4+ oxidation state on the electrode surface. This was also confirmed by the Mn 2p spectra, which displays the typical peak shapes of MnO_2 see Figure 3.103(b). Further support comes from the Fe 2p spectra that display predominately Fe(III) signals, as evidenced by the position of the satellite peak at 719.3 eV.[127] Thus, Fe (III) is the highest oxidation state, observed on the electrode surface as a stable species. There are two ways to oxidize iron to higher oxidation states. The first one is electrochemical oxidation of surface iron species that react with water and reduced quickly back to Fe(III). The second one is the oxidation of Fe(III) to Fe(VI) which undergoes a dispersion reaction and dissociates into the electrolyte.

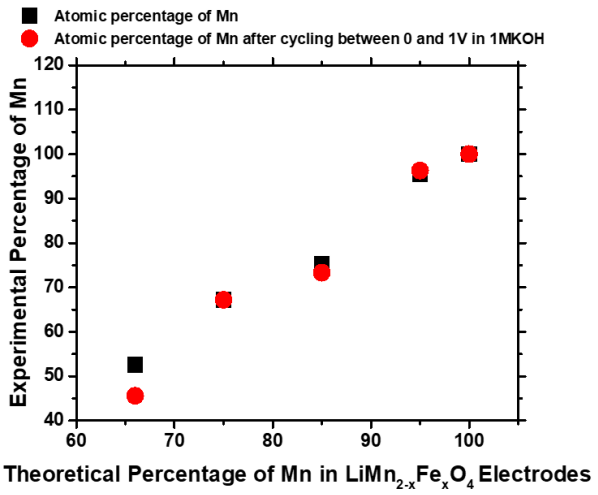

Figure 3.104 XPS survey analysis results of $LiMn_{2-x}Fe_xO_4$ electrodes before and after cycling in 1 M KOH solution.

The disproportionation reaction of the electrodes was investigated by the XPS measurement. Theoretical manganese percentages of $LiMn_{2-x}Fe_xO_4$ are plotted against experimental manganese percentage, obtained from the XPS survey analysis, see Figure 3.104.

The plots show that the Mn content gets low at electrode surface with increasing Fe content of the electrodes. The drop is enhanced with usage of the electrode indicating that the Mn disproportionation reaction is more extended than that of iron in the most iron-rich electrode. However, the other electrodes before and after the cycling process follow a linear trend and a similar atomic percentage of manganese. It means both manganese and iron are dispersed into electrolytes through their disproportionation reactions with CV cycling. The electrode composition is preserved in terms of their percentage. One should also mention that the experimental manganese percentages for both cases were found to be smaller than the theoretical percentages. This may be evidence for the accumulation of $FeCO_3$ on the electrode surface.

3.2.3 Electrochemical Properties of Mesoporous $LiMn_{2-x}Co_xO_4$ Thin Films

A series of $LiMn_{2-x}Co_xO_4$ electrodes were prepared and investigated by electrochemical methods. First, the FTO coated electrodes were used to collect a series of scan rate dependent CVs between 0.3 and 1.3 V in 1 M $LiNO_3$ electrolyte solution with a scan rate of 20 to 2 mV/s and a decrement of 2 mV/s. These CV curves of the $LiMn_{2-x}Co_xO_4$ electrodes are shown in Figure 3.105.

Similar to the iron system, lithium intercalation and deintercalation amounts under oxidation curves decrease with the addition of cobalt into the spinel structure. This might be attributed to a decrease in Mn(III) amount by increasing cobalt content. Therefore, these manganese species could only be oxidized to leave lithium ions from the structure and total charges decreased gradually with the addition of cobalt.

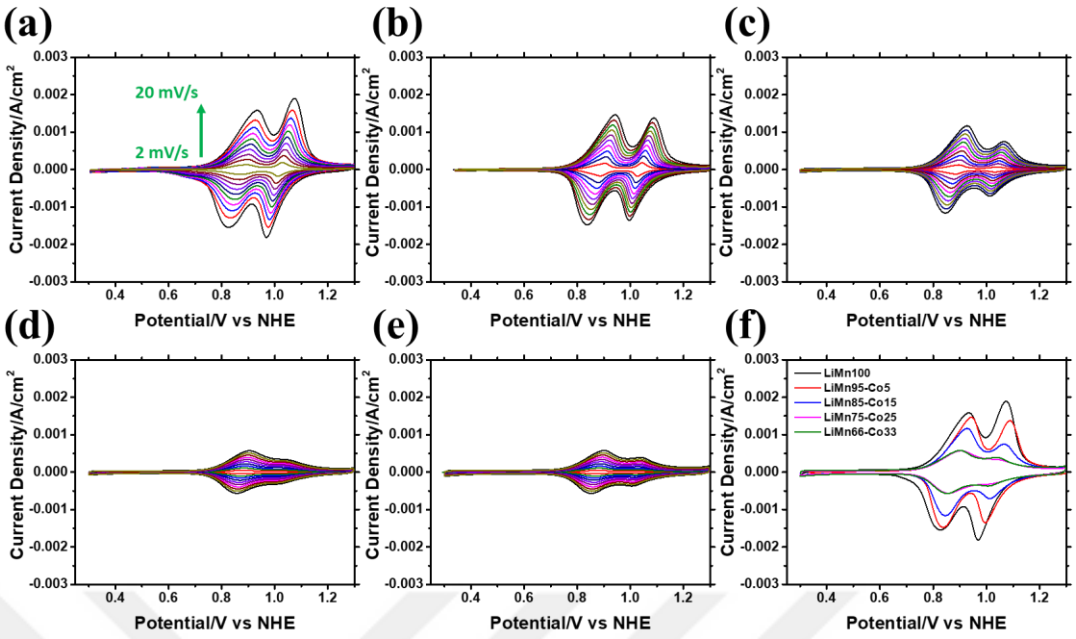

Figure 3.105 CV curves of $LiMn_{2-x}Co_xO_4$ in 1 M $LiNO_3$: (a) LiMn100, (b) LiMn95-Co5, (c) LiMn85-Co15, (d) LiMn75-Co25, and (e) LiMn66-Co33 (f) CV curves of $LiMn_{2-x}Co_xO_4$ at 20 mV/s.

The CVs of all compositions, collected at 20 mV/s scan rate, are shown in Figure 3.105(f). Relative current densities at 0.9 and 1.1 V show the same trend as $LiMn_{2-x}Fe_xO_4$ electrodes, which have been discussed in the previous section. Adding more cobalt ion into the spinel structure might cause some change in the current densities and peak shapes of lithium de-intercalation/intercalation region.

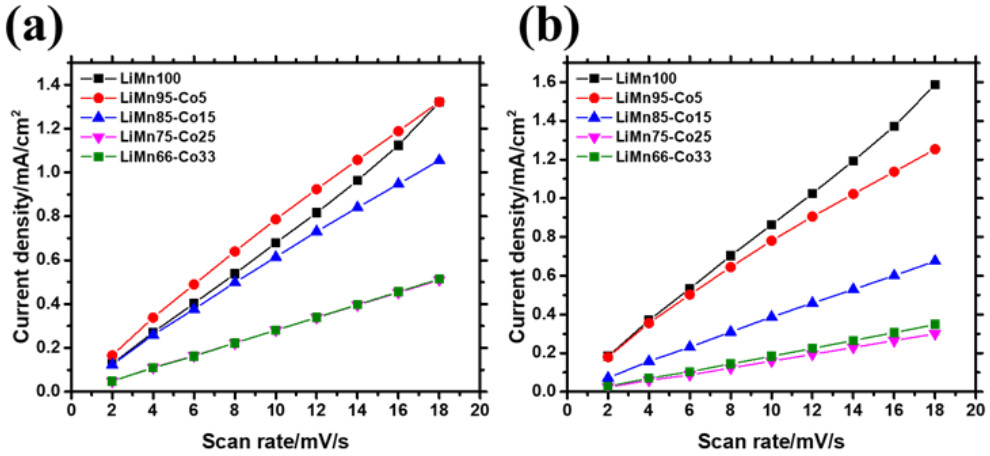

Figure 3.106 Current density versus scan rate plots of the de-lithiation peaks for the $LiMn_{2-x}Co_xO_4$ electrodes from (a) 1st peak (at 0.9 V) and (b) 2nd peak (at 1.1 V).

Current densities of the 1st and 2nd peaks of the lithium de-lithiation are plotted with respect to scan rate to provide a clear picture on the process in the $LiMn_{2-x}Co_xO_4$ electrodes. Plots are shown in Figure 3.106 (a) and (b) for the 1st and 2nd peaks, respectively.

According to the 1st and 2nd peaks of the LiMn95-Co5 electrode, the plots show deviation linearity compared to the LiMn100 plot. It means that these peaks show a diffusion limited oxidation (de-lithiation) rather than adsorption limited. This behavior has also been discussed in the $LiMn_{2-x}Fe_xO_4$ case. Furthermore, when the cobalt content is increased to 15% and higher, the deviation from the linearity is still visible, but the current density drastically decreases in the 2nd peak.

Notice that the charge density under the lithium de-intercalation/intercalation curves of the LiMn75-Co25 and LiMn66-Co33 electrodes are very similar to each other. This behavior might be attributed to the higher electronegativity of Co(III) that makes lithium de-intercalation harder and prevents the Mn(III) oxidation after reaching a significant Co composition in the $LiMn_{2-x}Co_xO_4$ electrode. To understand this behavior of the cobalt system, the total charge density under each curve was calculated by sweeping between 0.6 and 1.2 V with a 5 mV/s scan rate. The mathematical areas used for charge calculation are shown in Figure 3.107(a).

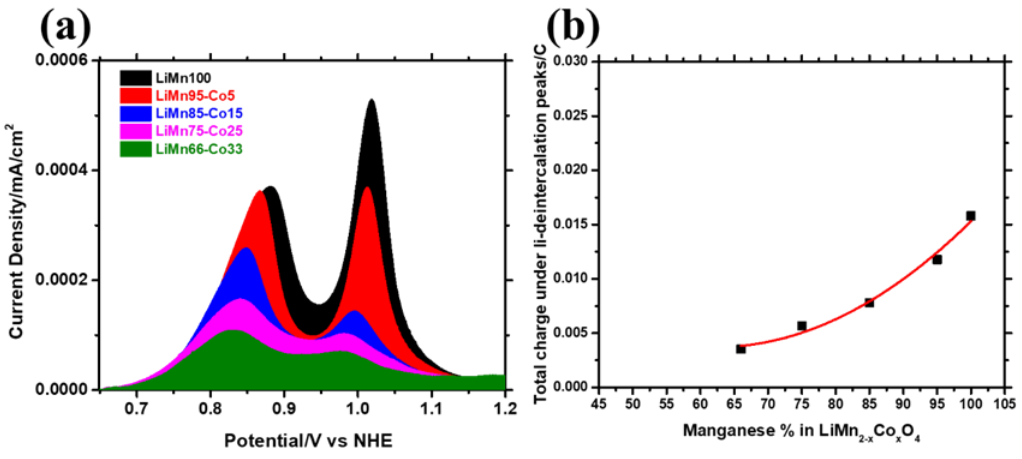

Figure 3.107 (a) Mathematical area for calculation of the charge densities and (b) Charge density vs manganese % plot of the $LiMn_{2-x}Co_xO_4$ electrodes.

According to the calculations, the decrease in charge density didn't show a linear trend with the percent manganese in the $LiMn_{2-x}Co_xO_4$ electrode, see Figure 3.107(b). The fit becomes polynomial in $LiMn_{2-x}Co_xO_4$ system. All Mn(III) couldn't be oxidized to Mn(VI) to remove equivalent lithium ions due to the electronegative cobalt sides. This electronic effect might cause a deviation in the plot or catalytic load might be different in $LiMn_{2-x}Co_xO_4$ compared to $LiMn_{2-x}Fe_xO_4$ system. Lithium de-intercalation could be identified by sweeping the LiMn50-Co50 composition in the same potential window for further charge density analysis.

After quantitative analysis of the electrodes, they were used in CV cycling experiments to understand Mn(VI) disproportionation reaction in these compositions. Figure 3.108 shows 300 cyclic voltammograms. The experiment was performed at a 50 mV/s scan rate in 1 M KOH solution using the 5000 rpm electrodes. Notice that, the current density at 1 V in the first cycles is higher for compositions containing more cobalt, see Figure 3.108 (c), (d) and (e).

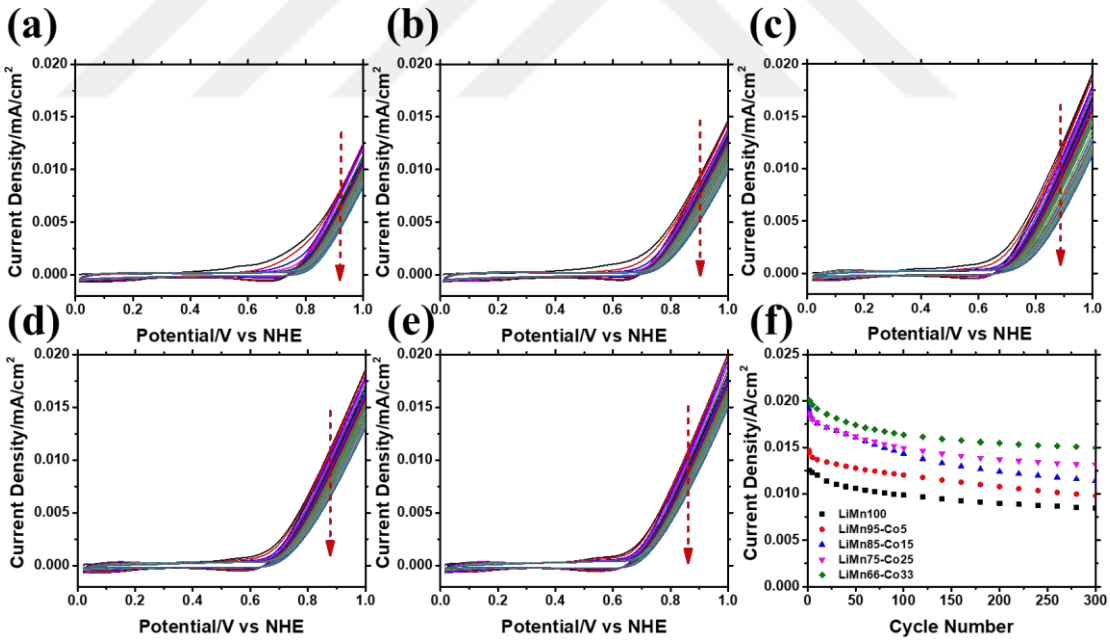

Figure 3.108 CV curves of the $LiMn_{2-x}Co_xO_4$ electrodes in 1M KOH solution: (a) LiMn100, (b) LiMn95-Co5, (c) LiMn85-Co15, (d) LiMn75-Co25, (e) LiMn66-Co33, and (f) cycle number vs current density plot by 300 cycles.

This is due to the electronic effect of cobalt on manganese sites (electronegativity difference of two transition metals) to enhance OER performance. OER efficiency is found to be low for the LiMn100 and LiMn95-Co5

compositions by analyzing current densities at 1 V, see Figure 3.108 (a) and (b). These compositions lack of cobalt content on the electrode surface. The current density at 1 V is plotted with respect to cycle number to investigate the Mn(VI) disproportionation mechanism, see Figure 3.108(f).

Two compositions, LiMn100 and LiMn95-Co5, show lower current densities by cycling with a gradual continuous decrease. Other compositions, containing cobalt of more than 15%, have fast decrease current density in the first 100 cycles, attributed to electrochemical surface alteration due to the disproportionation of Mn(VI) sides. However, this behavior of the compositions stops after 200 cycles and the electrodes became more stable to Mn(VI) disproportionation. In particular, LiMn66-Co33 composition shows excellent stability in the cycling process with alteration in the current density.

The electrodes were further analyzed by recording their XPS spectra. Figure 3.109(a) shows O1s spectra of the cycled electrodes.

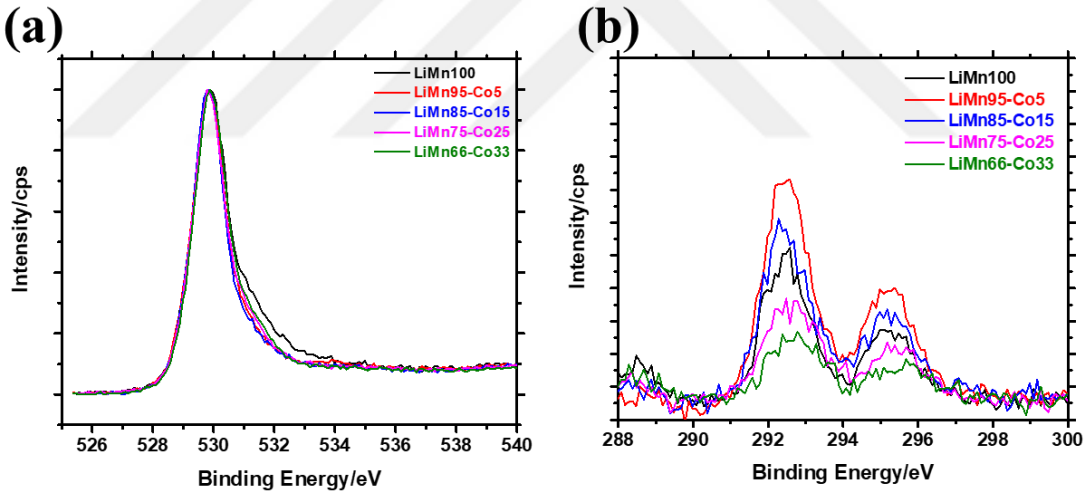

Figure 3.109 XPS spectra of the $LiMn_{2-x}Co_xO_4$ electrodes after 300 cycles: (a) O 1s and (b) K 2p regions.

The shoulder peak at 531.2 eV belongs to hydroxyl feature that disappears after cycling as expected, because the cycling process is stopped at 1 V at which electrode surface becomes MnO_2 and there is no reason to observe any other species other than lattice oxygen. Also, potassium de-intercalation in these $LiMn_{2-x}Co_xO_4$ electrodes was analyzed by recording the K 2p spectra, see Figure 3.109(b). Notice that all compositions contain potassium after the cycling process

even cycling was finished at very positive potentials. Thus, intercalated K^+ couldn't be de-intercalated completely at the end of the experiment.

Then, the Mn 3s, Mn 2p and Co 2p spectra were recorded to investigate oxidation states of surface species.

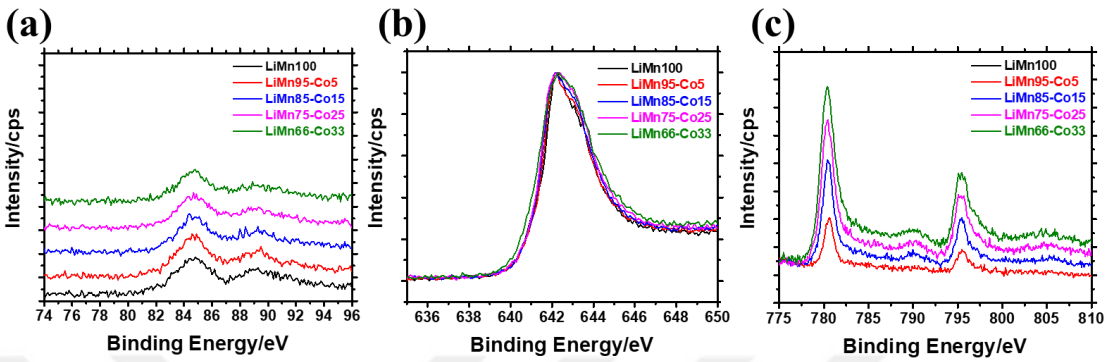

Figure 3.110 XPS spectra of the $LiMn_{2-x}Co_xO_4$ electrodes after 300 cycles: (a) Mn 3s, (b)Mn 2p ($^2P_{3/2}$), and (c) Co 2p regions.

According to Mn 3s spectra shown in Figure 3.110 (a), the energy difference between split peaks is 4.4 eV for each composition, due to Mn(VI) domination on the electrode surface. This is also supported by the Mn 2p ($^2P_{3/2}$) spectra; the peak shape is similar to MnO_2 features, see Figure 3.110(b). The Co 2p spectra are shown in Figure 3.110(c). The satellite peak at 790 eV due to Co(III) species is well resolved after CV cycling. Notice that the cycling process has been stopped at 1 V and the electrodes were washed and dried and immediately used for the XPS analysis. Cobalt may stay stable as Co(IV) because there are investigations on the formation of CoO_2.[134], [135] However, cobalt species in $LiMn_{2-x}Co_xO_4$ may not be oxidized to Co(IV) at 1 V. Higher voltage might be required to form Co(IV) species.

XPS survey spectra was also recorded to analyze the atomic percentages of manganese and cobalt before and after 300 CVs. Atomic percentages of $LiMn_{2-x}Co_xO_4$ electrodes are shown by black squares in Figure 3.111. As shown in the plot, the experimental manganese percentage of the electrodes is found to be higher by survey analysis. This might be attributed to the accumulation of manganese species on electrode surfaces. After cycling the electrodes in 1 M KOH, the experimental manganese percentages diminish, see red dots in Figure 3.111.

It might result from the dissolving of these manganese species by cycling. Thus, it provides cobalt rich electrode surface after electrochemical process.

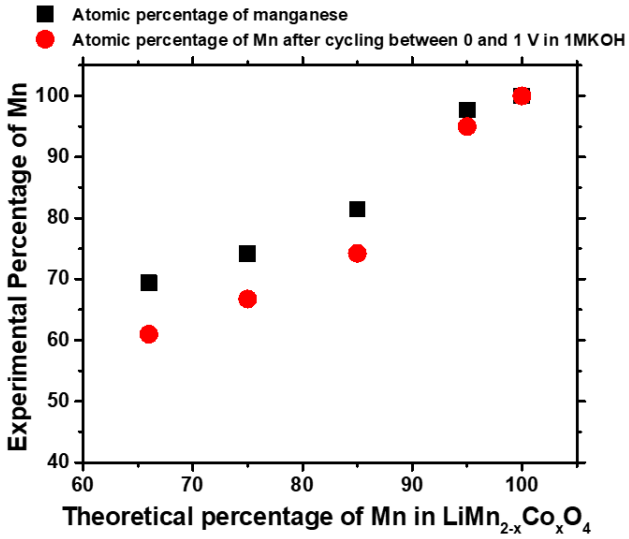

Figure 3.111 XPS survey analysis results of the $LiMn_{2-x}Co_xO_4$ electrodes before and after cycling in 1M KOH solution.

3.2.4 Electrochemical Properties of Mesoporous $LiMn_{2-x}Ni_xO_4$ Thin Films

Electrochemical analysis of $LiMn_{2-x}Ni_xO_4$ thin films was started with scan rate dependent cyclic voltammograms in 1 M $LiNO_3$ electrolyte solution. Figure 3.112 shows the CV curves of the electrodes.

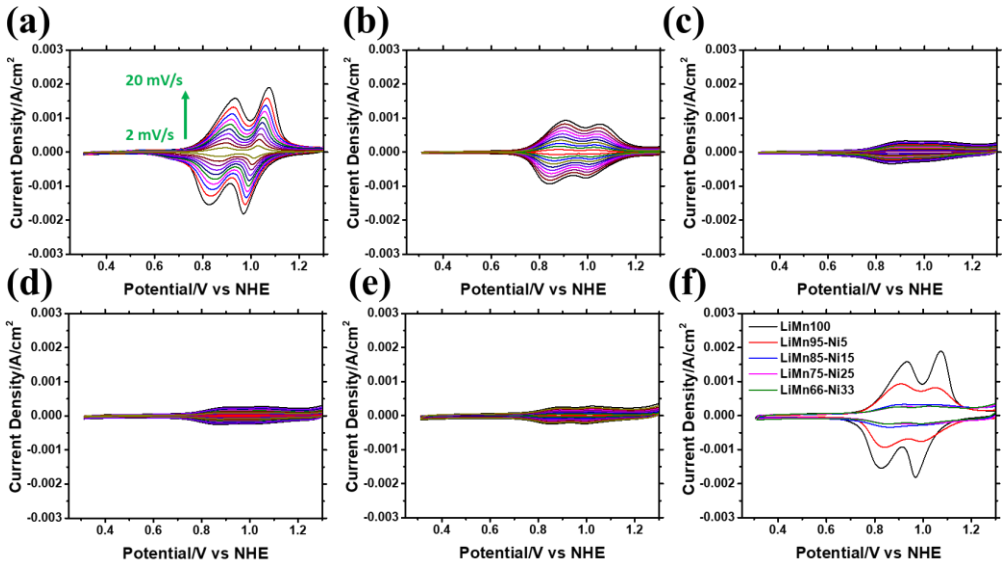

Figure 3.112 CV curves of the $LiMn_{2-x}Ni_xO_4$ electrodes in 1 M $LiNO_3$: (a) LiMn100, (b) LiMn95-Ni5, (c) LiMn85-Ni15, (d) LiMn75-Ni25, and (e) LiMn66-Ni33 and (f) CV curves of the $LiMn_{2-x}Ni_xO_4$ electrodes at 20 mV/s.

According to the CV curves of the $LiMn_{2-x}Ni_xO_4$ electrodes, the lithium de-intercalation and intercalation process in the electrodes decrease by increasing nickel content. The oxidation/reduction peaks are clearly visible for the LiMn100 and LiMn95-Ni5 compositions, see Figure 3.112(a) and (b). However, electrodes with higher nickel content displayed a very similar CV curve. CV of the LiMn75-Ni15 electrode displayed a highly diminished lithium de-intercalation peak between 0.8 and 1.1 V, see Figure 3.112(c). Notice that the other compositions having nickel more than 25% have almost the same voltammograms. CV curves at 20 mV/s scan rate are shown in Figure 3.112(f) for the comparison of current densities and charge densities.

Current densities of the 1st and 2nd peaks of the lithium de-lithiation are plotted with respect to scan rate to provide a clear observation of the relative changes in current densities in $LiMn_{2-x}Ni_xO_4$ electrodes. Plots are shown in Figure 3.113 (a) and (b) for the 1st and 2nd peaks, respectively.

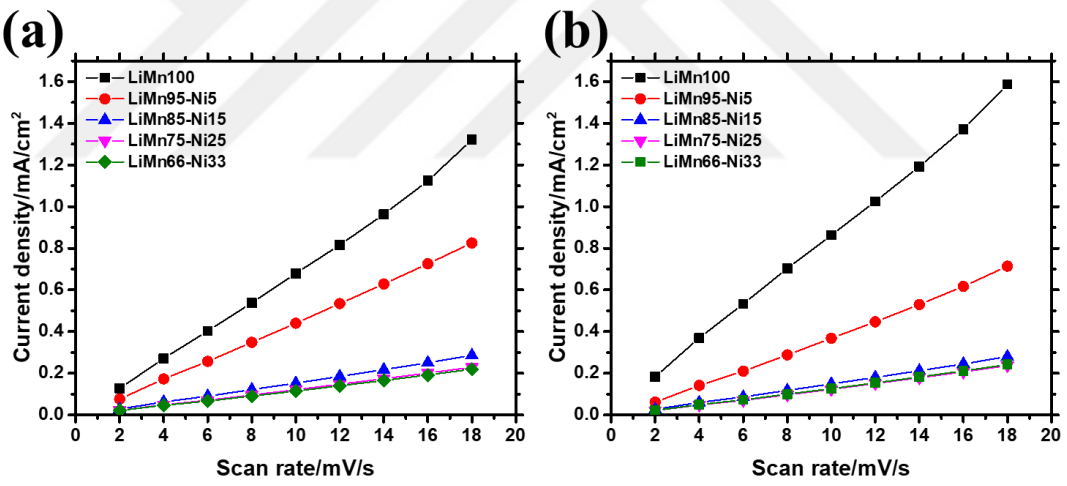

Figure 3.113 Current density versus scan rate plots of the de-lithiation peaks for the $LiMn_{2-x}Ni_xO_4$ electrodes of the (a) 1st peak (at 0.9 V) and (b) 2nd peak (at 1.1 V).

According to the plots of the 1st and 2nd peaks of all the electrodes containing nickel, the current densities decrease in the 2nd peaks compared to the 1st peak, very similar to the other metal systems. However, current density versus scan rate plots of the $LiMn_{2-x}Ni_xO_4$ electrodes don't show any deviation and are linear. It might be attributed to adsorption-limited redox process in the de-lithiation for these films. Since we showed that thin films containing nickel result

in higher surface areas. Thus, surface domination becomes significant in electrochemical redox processes.

For quantitative analysis, the electrodes were swept from 0.6 to 1.2 V with a scan rate of 5 mV/s. Charge densities under the curves are calculated by mathematical areas and plotted according to theoretical manganese percentages in $LiMn_{2-x}Ni_xO_4$ electrodes, see Figure 3.114(a) and (b), respectively.

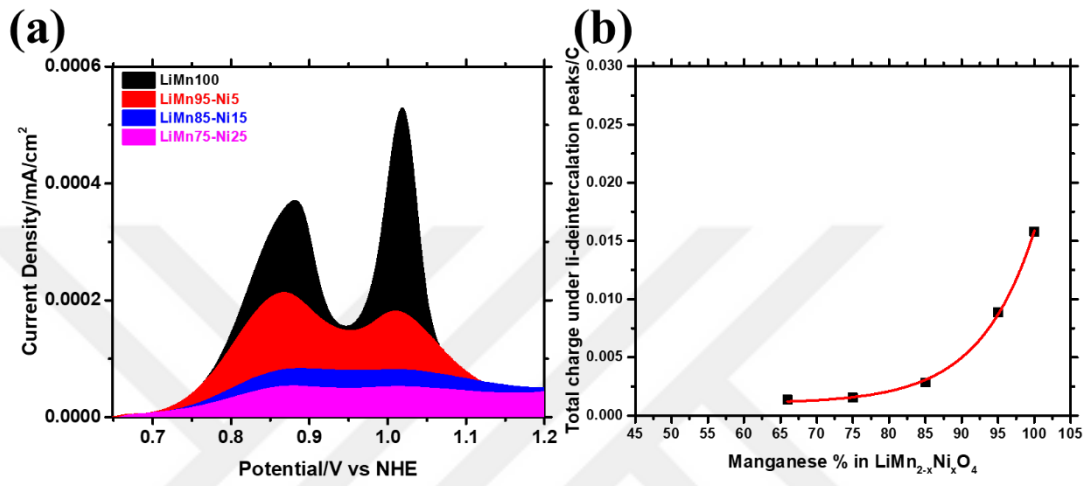

Figure 3.114 (a) Mathematical area for calculation of charge densities and (b) charge density vs manganese % in $LiMn_{2-x}Ni_xO_4$.

Notice that, when 5% nickel was integrated into the spinel structure, the lithium de-intercalation efficiency decreased more than other metal systems. As explained before, electronegativities of these metals have effects on the oxidation of Mn(III) species and indirectly lithium de-intercalation process. Further increase of nickel in the system, decreases the charge densities more, as represented in Figure 3.114(b). It seems that the lithium de-intercalation stops when it reaches to LiMn75-Ni25 composition, even though 25% manganese is still in 3+ oxidation state.

$LiMn_{2-x}Ni_xO_4$ electrodes were further investigated in order to understand the effect of nickel on the Mn(VI) disproportionation reaction. The same procedure in previous systems was employed for the cycling in 1 M KOH electrolyte solution. According to cyclic voltammograms, catalytic efficiency of the $LiMn_{2-x}Ni_xO_4$ electrodes are enhanced by the increase of nickel in the electrodes by analyzing current density amplification in the water oxidation potentials, see Figure 3.115.

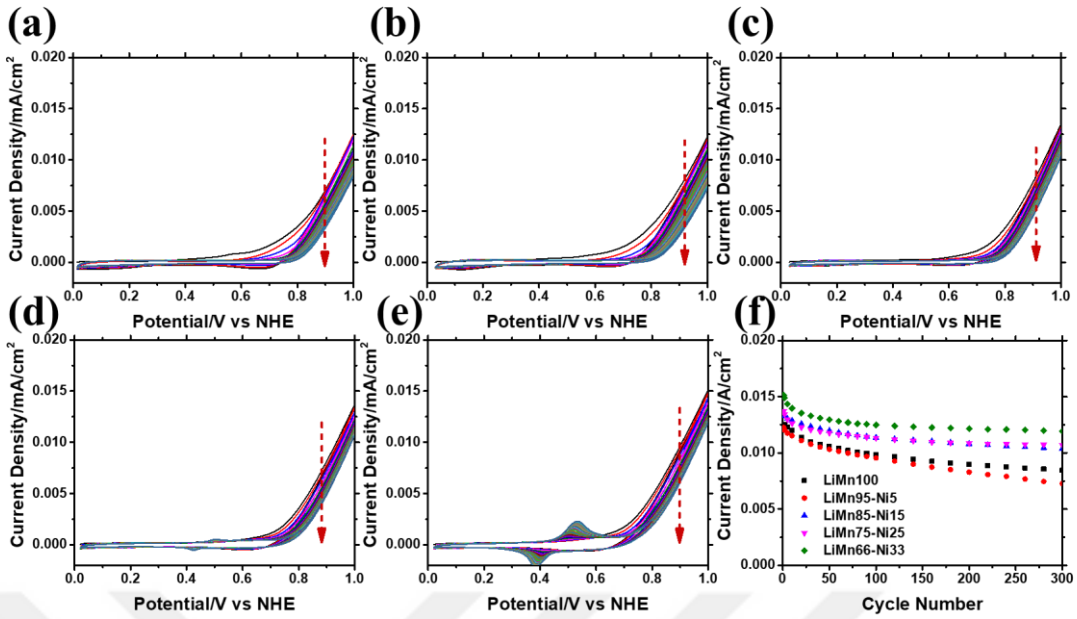

Figure 3.115 CV curves of the $LiMn_{2-x}Ni_xO_4$ electrodes in 1 M KOH solution: (a) LiMn100, (b) LiMn95-Ni5, (c) LiMn85-Ni15, (d) LiMn75-Ni25, (e) LiMn66-Ni33, and (f) cycle number vs current density plot by 300 cycles.

This is due to the synergetic electronic effect of nickel on manganese sites in the water oxidation process. The LiMn66-Ni33 electrode shows the highest catalytic efficiency among all electrodes. Notice that compositions including nickel more than 25% show redox couple at 0.45 V. These redox peaks are gradually enhanced by cycling and become more visible in the LiMn66-Ni33 composition. Therefore, the reason for the peaks might be attributed to nickel species.

Current density variation by cycling of the electrodes is shown in Figure 3.115(f). Notice that the current density drops, at 1 V, are observed for all $LiMn_{2-x}Ni_xO_4$ electrodes in the first 100 cycles. Distinct current density drops occurs in the LiMn95-Ni5 composition. When the nickel content is increased to 15% and 25%, the drops in current density become smaller between 200 and 300 cycles. This drops might be due to Mn(VI) disproportion reaction that still takes place in low nickel contents. For the electrode that has a significant Ni composition such as LiMn66-Ni33, it shows high stability in current density after 200 cycles. In these cycles, the Mn(VI) disproportionation reaction is prevented somehow.

The origin of the peaks between 0.3 and 0.6 V in the CVs of LiMn66-Ni33 was investigated. It was previously reported that nickel oxide forms NiOOH on the electrode surface at positive potentials. Then, sweeping the electrode to the

reverse side produces the $Ni(OH)_2$ species in an alkaline environment. Thus, electrode surface couldn't be converted to its initial form by the cycling process.[26] Here, nickel ions are integrated into the spinel structure, but upon cycling, the CVs have similar features to that of $Ni(OH)_2$. For comprehensive investigation, LiMn66-Ni33 composition was cycled between 0 and 0.7 V to prevent OER catalysis on the electrode surface to a huge extent. Then, redox peaks were analyzed to understand the effect of water oxidation on these peaks. Figure 3.116(a), (b), and (c) show the CV curves of the LiMn66-Ni33 electrodes up to 1, 0.7, and 0.55 V, respectively.

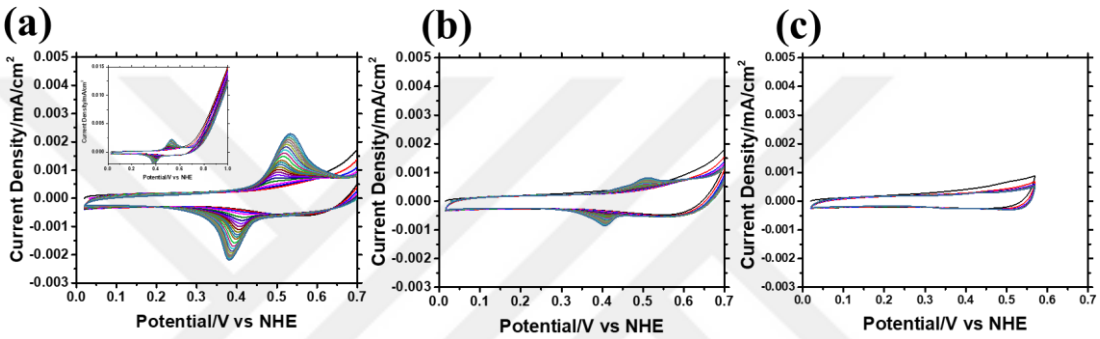

Figure 3.116 The CV curves of the LiMn66-Ni33 electrode in 1 M KOH solution between (a) 0 and 1 V (magnified between 0 and 0.7 V), (b) 0 and 0.7 V, and (c) 0 and 0.55V.

Based on CV curves, shown in Figure 3.116(a) and (b), the current density enhancement in redox peaks at 0.45 V is related to the water oxidation reaction. This is because the current density increase in the peaks is faster by cycling when the electrode is exposed to OER potentials, see Figure 3.116 (a). It might be correlated to acidity on the electrode surface. Note that for the water oxidation reaction, H_3O^+ concentration on the electrode surface is drastically amplified. Thus, pH of the interface decreases. According to the Pourbaix diagram of nickel in Figure 1.7(c), the ionic Ni(II) is favored. It causes the dissolution of the Ni(II) into the electrolyte solution, likely as $Ni(OH)_2$. Then, sweeping in CV to negative potential causes re-deposition of these free ions on the electrode surface as $Ni(OH)_2$ in spinel $LiMn_{2-x}Ni_xO_4$ structures. When the potential range of CV was set between 0 and 0.55 V, no OER process took place, see Figure 3.116(c). Thus, the redox peaks at 0.45 disappear and the curve shows non-faradaic feature (capacitive feature).

After suspecting the nickel hydroxide formation, the XPS spectra of the used $LiMn_{2-x}Ni_xO_4$ electrodes (cycled between 0 and 1 V) were recorded in the O 1s, K 2p, Mn (3s and 2p), and Ni 2p regions. Figure 3.117(a) and (b), show the O 1s and K 2p spectra, respectively.

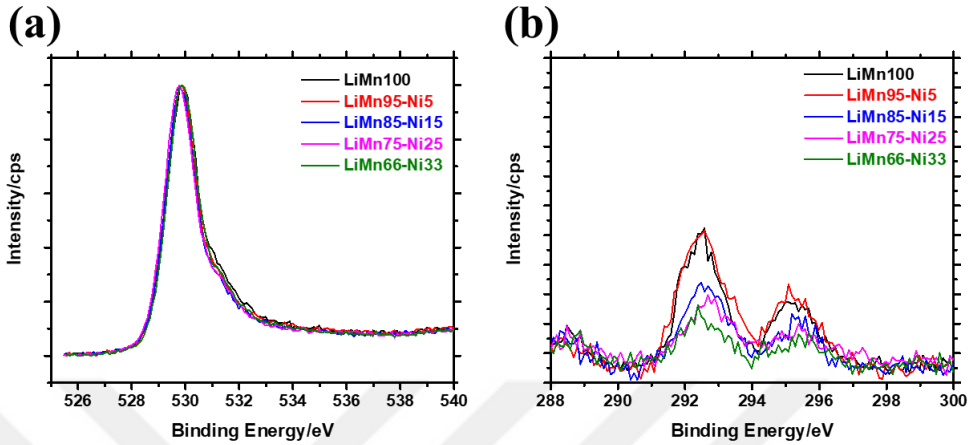

Figure 3.117 XPS spectra of the $LiMn_{2-x}Ni_xO_4$ electrodes after 300 cycles in the (a) O 1s and (b) K 2p regions.

The O 1s spectra display a weak shoulder at 531.2 eV similar to the other $LiMn_{2-x}M_xO_4$ samples due to lattice oxygens, see Figure 3.117(a). Then K 2p region was analyzed and found that the K^+ intercalation occurs for these electrodes, see Figure 3.117(b). The spectra also show that the potassium intercalation is enhanced by an increase in manganese content in the $LiMn_{2-x}Ni_xO_4$ structure. Notice that a small reduction peak at 0.1 V might be attributed to K^+ intercalation due to the reduction of Mn or Ni sites. The small peak due to de-intercalation is most likely masked by the OER process. The Mn 3s, Mn 2p, and Ni 2p XPS spectra were also recorded after cycling the electrodes.

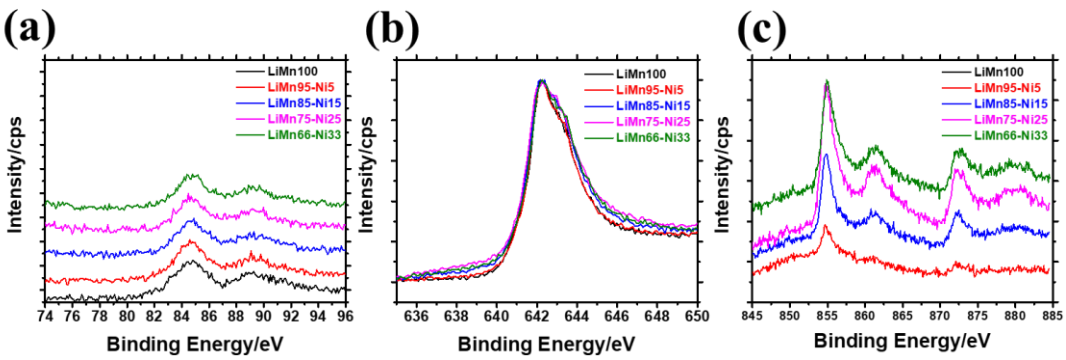

Figure 3.118 XPS spectra of $LiMn_{2-x}Ni_xO_4$ electrodes after 300 cycles (a) Mn 3s, (b) Mn 2p ($^2P_{3/2}$), (c) Ni 2p.

In the Mn 3s spectra, shown in Figure 3.118(a), the splitting of the peaks is 4.4 eV for all compositions, which means Mn(IV) species are dominant on electrode surfaces. Typical MnO_2, peak shapes were observed in the Mn 2p ($^2P_{3/2}$) region in the XPS spectra, which is strong evidence for the Mn(IV) formation on the electrode surface, see Figure 3.118(b). Lastly, the Ni 2p spectra were recorded and analyzed. The Ni 2p ($^2P_{3/2}$) region shows that there is no difference in the spectra in terms of peak shape and satellite binding energies after the cycling experiment, see Figure 3.118(c). It means, nickel species are mostly Ni(III).

The XPS survey spectra were also recorded and analyzed to determine electrode surface compositions before and after cycling. Figure 3.119 shows the plots of the theoretical versus experimental manganese percentages.

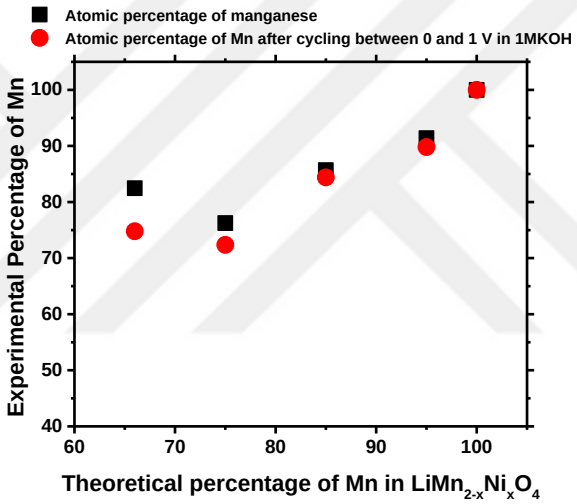

Figure 3.119 XPS survey analysis results of the $LiMn_{2-x}Ni_xO_4$ electrodes before and after cycling in 1 M KOH solution.

Notice that the compositions from LiMn100 to LiMn85-Ni15 show an interesting trend, but similar to the $LiMn_{2-x}Co_xO_4$ electrodes. Moreover, the experimental Mn content is increasing with increasing Ni content more than that of the theoretical amounts, indicating Mn rich surface. When the nickel content is increased further to 25%, the experimental nickel contribution on the surface is also 25% and lightly higher after electrochemical usage of the electrode, indicating some Mn disproportionation. The LiMn66-Ni33 electrode has 80% manganese on the electrode surface due to more manganese accumulation on the electrode surface. After cycling the electrodes in 1 M KOH solution, the manganese content decreases for all compositions, as indicated by red dots in Figure 3.119. However, the LiMn75-Ni75 and LiMn66-Ni33 compositions show

that the manganese decrease is much more than the other electrodes after cycling. The extra manganese species easily undergo a disproportionation reaction and makes the electrode surface nickel-rich. This is evident from the redox peaks (at 0.45 V) that appeared by cycling due to formation of $Ni(OH)_2$ on electrode surface.

3.2.5 Electrochemical Properties of Mesoporous $LiMn_{2-x}Cu_xO_4$ Thin Films

Electrochemical properties of the $LiMn_{2-x}Cu_xO_4$ electrodes were first characterized by recording CVs of the electrodes in 1 M $LiNO_3$ with a 5 mV/s scan rate. The CV curves of all compositions are shown in Figure 3.120 (a).

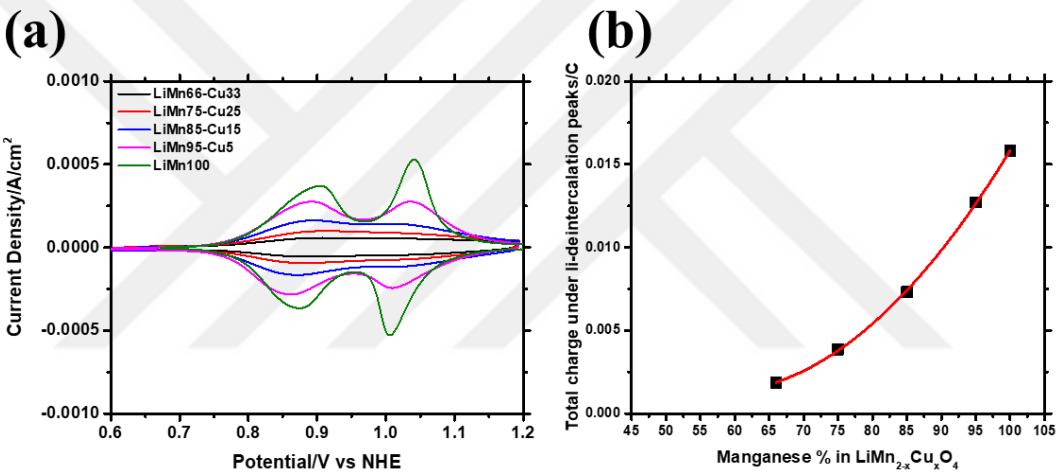

Figure 3.120 (a) CV curves of $LiMn_{2-x}Cu_xO_4$ in 1 M $LiNO_3$ at 5 mV/s, (b) charge density vs manganese % in $LiMn_{2-x}Cu_xO_4$.

According to the CV curves, a similar trend is observed for the $LiMn_{2-x}Cu_xO_4$ electrodes, in terms of peak intensities, when they were compared with other metal systems. This might be due to Cu(II) presence in the electrodes. Inherently, charge capacity decreases since the Mn(III) content decreases with the addition of copper into the structure, see Figure 3.120(b). Then, the electrodes were tested for OER stability in 1 M KOH electrolyte by recording 300 CVs between 0 and 1 V. The CV curves for each composition are shown in Figure 3.121(a-e).

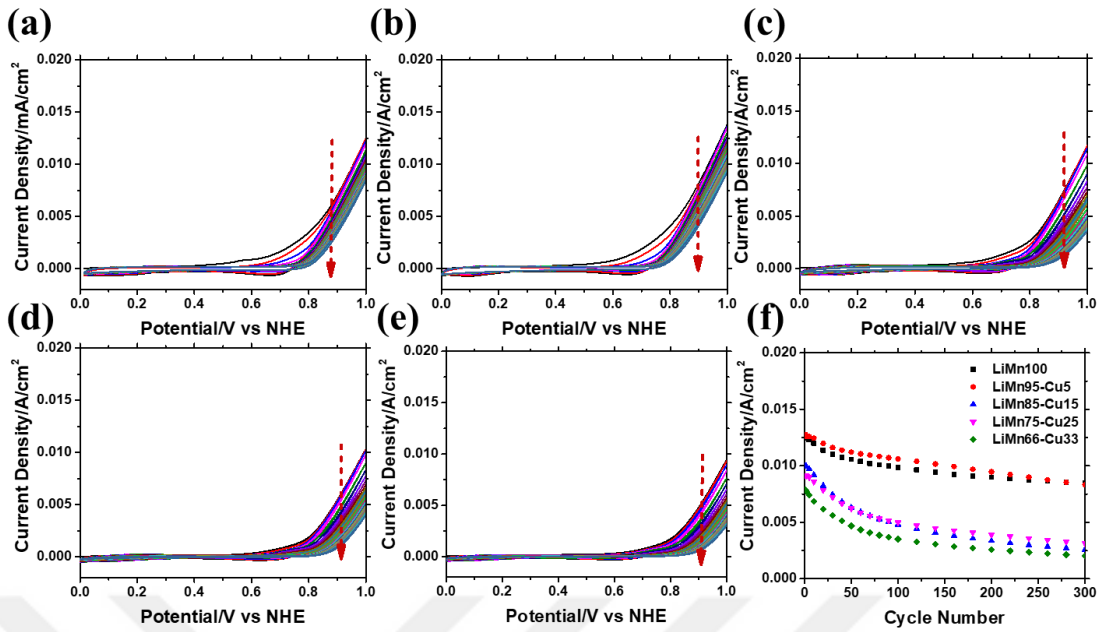

Figure 3.121 CV curves of the $LiMn_{2-x}Cu_xO_4$ electrodes in 1 M KOH solution: (a) LiMn100, (b) LiMn95-Cu5, (c) LiMn85-Cu15, (d) LiMn75-Cu25, (e) LiMn66-Cu33, and (f) cycle number vs current density plot by 300 cycles.

Notice that the LiMn100 and LiMn95-Cu5 electrodes show similar behavior during the cycling process in 1 M KOH, compare Figures 3.121(a) and (b). When the copper content reaches to 15% and higher, decay in current densities becomes faster by cycling, see Figure 3.121(c), (d), and (e). This might be attributed to phase separation of Mn_3O_4 and CuO in these compositions, which have been previously demonstrated in the XRD patterns. When the current density at 1 V is plotted with respect to cycle number, the decay rates could be clearly observed, see Figure 3.121(f). Notice that the LiMn100 and LiMn95-Cu5 electrodes showed higher current densities at first cycles. For the other electrodes, namely LiMn85-Cu15, LiMn75-Cu25 and LiMn66-Cu33, the current density is below 10 mA/cm^2. It might be due to the lower electrocatalytic OER activity of CuO-based materials, because the Cu(II) species are difficult to further oxidize to higher oxidation state that is necessary for an efficient OER.

After cycling the electrodes in 1 M KOH, the XPS spectra of the electrodes were also recorded in the O 1s and K 2p regions, see Figure 3.122(a) and (b).

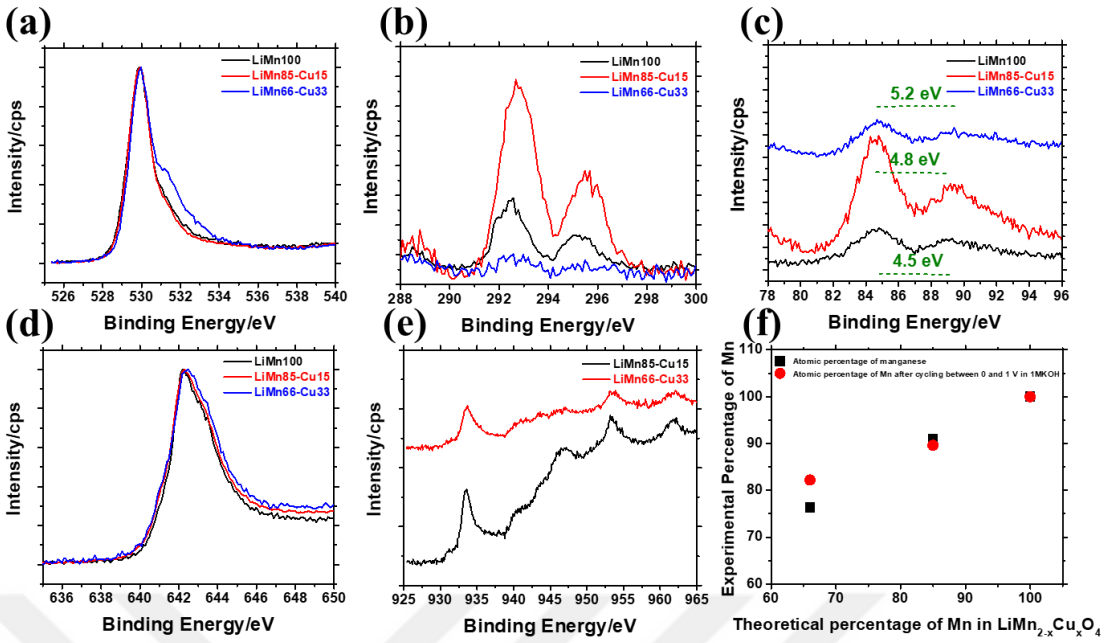

Figure 3.122 XPS spectra of the $LiMn_{2-x}Cu_xO_4$ electrodes after 300 CVs: (a) O 1s, (b) K 2p, (c) Mn 3s, (d) Mn 2p ($^2P_{3/2}$), and (e) Cu 2p regions. (f) the XPS survey analysis results of the $LiMn_{2-x}Cu_xO_4$ electrodes before and after cycling in 1 M KOH solution (black dots: before, red dots: after cycling).

According to the O 1s XPS spectrum after cycling in 1 M KOH, the LiMn66-Cu33 composition showed a hydroxyl feature at 531.2 eV due to surface $Cu(OH)_2$, see Figure 3.122(a). The K 2p spectra are shown in Figure 3.122(b). The origin of K 2p peaks is the potassium intercalation into the structure favored in the LiMn85-Cu15 composition and diminishes in the LiMn66-Cu33 composition. The splitting between the Mn 3s peaks gets increased with an increase in copper content, see Figure 3.122(c). This might be due to the phase separation of CuO and Mn_3O_4 with Mn(II) dominant surface as $Mn(OH)_2$.[118] However, the Mn 2p ($^2P_{3/2}$) region is very similar to the peak shape of a typical MnO_2 for three compositions, see Figure 3.122(d). In Cu 2p XPS spectra, the Cu(II) specie is dominant after the cycling experiment on the surface of both LiMn85-Cu15 and LiMn66-Cu33 electrodes, see Figure 3.122(e). [129] Furthermore, XPS survey analysis showed that surface accumulation of manganese is enhanced and gives higher manganese percent, compared to the theoretical value, see Figure 3.122(f). The manganese oxide accumulation on the electrode surface might be favored in the copper-integrated samples. After the cycling process, the manganese contribution becomes even higher in the LiMn66-Cu33 electrode, compared to the not cycled electrode, see Figure 3.122(f).

3.2.6 Basic Interpretation on OER Efficiencies of $LiMn_{2-x}M_xO_4$ Thin Films

To compare the catalytic activities of all electrodes, mass activities of the electrodes have been evaluated and reported in this section. For this purpose, catalytic loads of the thin films are calculated using the charge capacity obtained from the $LiNO_3$ cycling experiments. Catalytic load calculation is not as simple as the $LiMn_2O_4$ electrode. In the $LiMn_2O_4$ electrode, 2 moles of total manganese include 1 mol of Mn (III) and 1 mol of Mn (IV). Thus, the charge amount in the CV curve is responsible for the oxidation of 1 mol Mn(III) to Mn(IV). It is directly correlated to 1 mol of $LiMn_2O_4$. However, with the addition of another metal, the Mn(III) content decreases since the new metal prefers to stay in its M(III) (or even M(II)) oxidation state because of its higher electronegativity. Thus, it reduces the Mn(III) content. For instance, the LiMn85-M15 ($LiMn_{1.7}M_{0.3}O_4$), contains 1 mole of Mn(IV), 0.7 mole of Mn(III) and 0.3 mole of M(III). The capacity value obtained from CV in $LiNO_3$ resulted from the oxidation of 0.7 moles of Mn(III) to Mn(IV). Thus, CF could be regarded as 1/(1-x) where x is the mole contribution of M(III) in the $LiMn_{2-x}M_xO_4$ structure. Therefore, a correction factor should be inserted into equation 3.1 to accurately determine electrode weight (or catalytic load). A derived formula and correction factors (CF) for each composition are given in Equation 3.2 and Table 3.8, respectively.

$$\text{Electrode mass}\left(\frac{g}{cm^2}\right) = \frac{\text{q}\left(\frac{A\cdot s}{cm^2}\right) \times MW_{LiMn2-xMxO4}\left(\frac{g}{mol}\right) \times 100 \times CF}{1.6\times10^{-19}\left(\frac{A\cdot s}{e}\right) \times 6.022\times10^{23}\left(\frac{e}{mol}\right) \times 83.7} \qquad \textbf{Equation 3.2}$$

Percentage notation	Chemical Formula	Correction Factor (CF)
LiMn100	$LiMn_2O_4$	1
LiMn95-M5	$LiMn_{1.9}M_{0.1}O_4$	1/0.9
LiMn85-M15	$LiMn_{1.7}M_{0.3}O_4$	1/0.7
LiMn75-M25	$LiMn_{1.5}M_{0.5}O_4$	1/0.5
LiMn66-M33	$LiMn_{1.33}M_{0.66}O_4$	1/0.33

Table 3.8 Table of electrode notations and corresponding correction factor for the calculation of catalytic loads.

In the $LiMn_{2-x}M_xO_4$ system, iron and cobalt are identified as dominantly Fe(III) and Co(III) by XPS, see section 3.2.1. Thus, the correction factor mentioned above might be practically to calculate the electrode mass using the lithium deintercalation process. Table 3.9 tabulates charge amounts, masses before correction, correction factors and masses after correction for the $LiMn_{2-x}Fe_xO_4$ and $LiMn_{2-x}Co_xO_4$ electrodes.

Percentage notation	Total charge/mC	Electrode mass(NC*) µg/cm²	Correction Factor (CF)	Electrode mass(C*) µg/cm²	Mass activity/A/g
LiMn100	15.80	35.46	1	35.46	50.29
LiMn95-Fe5	13.51	30.27	1.11	33.59	58.93
LiMn85-Fe15	10.32	23.09	1.42	32.78	57.28
LiMn75-Fe25	7.81	17.49	2	34.98	41.16
LiMn66-Fe33	-	-	3	-	--
LiMn95-Co5	11.78	26.70	1.11	29.63	96.11
LiMn85-Co15	7.77	17.61	1.42	25.00	155.58
LiMn75-Co25	5.67	12.85	2	25.70	155.57
LiMn66-Co33	3.63	8.23	3	24.93	177.99

Table 3.9 Table of total charge, electrode masses and mass activities of the LiMn%-M% electrodes at η = 350 mV where NC*: not corrected, C*:corrected.

Based on this calculation method, the catalytic loads of the LiMn%-M% electrodes at 5000 rpm are calculated utilizing the charge amount obtained by cycling experiments in 1 M $LiNO_3$. After that, current density values of the electrodes are obtained using CV curves of the cycling experiments between 0 and 1 V in 1 M KOH solution, the 2nd cycles of the curves are analyzed and current density values at 0.75 V vs NHE (1.575 vs RHE) are collected This voltage approximately refers to overpotential value, η = 0.35 V. Then, each current density value was divided by the catalytic load and calculated for each electrode.[136] Thus, the catalytic masses and mass activities of all electrodes are tabulated in Table 3.9. According to Table 3.9, the mass activities of the $LiMn_{2-x}Fe_xO_4$ electrodes are approximately 50 A/g at 350 mV overpotential. Thus, the addition of iron into the LiMn100 system has no significant effect on OER electrocatalysis. After the addition of 5 % Co into the LiMn100 electrode, the mass activity increases from 50.3 to 96.1 A/g. It represents a synergetic electronic effect between manganese and cobalt during the water oxidation process.

Further increase in cobalt content amplifies the mass activity up to 155 A/g. For the unique percentage, namely the LiMn66-Co33 electrode, the highest activity is recorded to be as high as 177.9 A/g.

In $LiMn_{2-x}Ni_xO_4$, it has been shown by XPS that both Ni(II) and Ni(III) species exist in the spinel structure and CuO formation is favored for the $LiMn_{2-x}Cu_xO_4$ system, see section 3.2.1. Thus, using the correction factor discussed above might cause deceptive results for the electrode masses of these electrodes. Therefore, these electrodes have a $LiMn(IV)Mn(III)_{1-x}M(III)_xO_4$ or $LiMn(IV)_{1+x}Mn(III)_{1-2x}M(II)_xO_4$ composition. The charge capacities are obtained by the oxidation of either (1-x) or (1-2x) Mn(III) species in the electrodes. By this assumption, we have constructed a CF value for each electrode. Therefore, the CF values are tabulated as 1, 1.11, 1.43, 2, and 3 for the LiMn100 ($LiMn_2O_4$), LiMn95-M5 ($LiMn_{1.9}M_{0.1}O_4$), LiMn85-M15 ($LiMn_{1.7}M_{0.3}O_4$), LiMn75-M25 ($LiMn_{1.5}M_{0.5}O_4$), and LiMn66-M33 ($LiMn_{1.33}M_{0.67}O_4$) electrodes, respectively. This approximation is valid for the Fe(III) and Co(III) electrodes. However, when M bears M(II) state, the CF should be 1/(1-2x) and it is 1, 1.25, and 2.5 for the LiMn100, LiMn95-M5, and LiMn85-M15 electrodes, respectively. Thus, nickels are either Ni(II) or Ni(III) and which means that CF is between 1/(1-x) and 1/(1-2x). Copper bears Cu(II) state (shown by XPS), and CF should be 1/(1-2x) for this system. Therefore, electrode masses are similar in both LiMn100 and LiMn%-Fe% electrodes. A slight decrease in the electrode mass is observed in the cobalt electrodes. This means that these electrodes are getting thinner with increasing cobalt in the LiMn%-Co% electrodes.

In the $LiMn_{2-x}Cu_xO_4$ system, we assume all of the copper is Cu(II) and CF is 1/(1-2x). Here, we made an assumption based on the LiMn95-Cu5 electrode, which is 5% Cu(II) could integrate the $LiMn_{2-x}Cu_xO_4$ spinel system completely. Therefore, CF in LiMn95-Cu5 becomes 1.25 using 1/(1-2x) where x is 0.1. By multiplying CF with 29.08 μg (non-corrected mass), we found 36.35 μg (corrected mass). This value was used to construction a new CF for the electrodes. Charge amounts in the delithiation process were obtained by cyclic voltammetry and used for the calculation of non-corrected electrode masses for other

compositions. 36.35 µg was divided into non-corrected mass values to find new CF. Charge amounts, corresponding masses, and CFs are tabulated in Table 3.10

Percentage notation	Total charge/mC	Electrode mass(NC*) µg/cm²	New CF	Electrode mass(C*) µg/cm²	Mass activity/A/g
LiMn95-Cu5	12.69	29.08	1.25	36.35	58.32
LiMn85-Cu15	7.32	16.77	2.16	39.03	37.40
LiMn75-Cu25	3.86	8.84	4.11	41.83	24.61
LiMn66-Cu33	1.86	4.26	8.53	43.26	22.19
LiMn95-Ni5	8.87	20.11	1.76	-	-
LiMn85-Ni15	2.84	6.43	5.51	-	-
LiMn75-Ni25	1.54	3.49	10.16	-	-
LiMn66-Ni33	1.36	3.08	11.51	-	-

Table 3.10 Table of total charge, electrode masses, constructed CFs and mass activities of the LiMn%-M% electrodes at η = 350 mV where NC*: not corrected, C*: corrected.

The new CF values were 1.25, 2.16, 4.11, and 8.53 for the LiMn%-Cu% ($LiMn_{2-x}Cu_xO_4$) electrodes, where theoretical x values are 0.1, 0.3, 0.5, and 0.67, respectively, and also means using 1/(1-2x) formula, experimental x values are found as 0.10, 0.26, 0.37, and 0.44, respectively. These might be considered as Cu(II) species participating in spinel $LiMn_{2-x}Cu_xO_4$ structure. Thus, the moles of the CuO phase are found to be 0.00, 0.04, 0.13, and 0.22, respectively, in the above electrodes. Notice that the CuO formation is observed in XRD patterns, see section 3.2.1. $LiMn_{2-x}Cu_xO_4$ spinel part masses were assumed to be around 36.35 µg/cm² for all of the compositions. Additionally, CuO masses on these electrodes were calculated regarding 0.00, 0.04, 0.13, and 0.22 CuO mole contributions for LiMn95-Cu5, LiMn85-Cu15, LiMn75-Cu25, and LiMn66-Cu33, respectively. Then, these CuO mass values were added to 36.35 µg. These new corrected electrode masses were tabulated in Table 3.10. The $LiMn_{2-x}Cu_xO_4$ electrodes show lower mass activity than the $LiMn_2O_4$ and $LiMn_{2-x}Fe_xO_4$ electrodes, likely due to CuO formation in the electrodes. Mass activity gradually decreases with the addition of copper in the electrodes.

However, the nickel electrodes show different behavior. It seems that the $LiMn_{2-x}Ni_xO_4$ electrodes are much thinner than other metal systems and they

have lower masses. This behavior might be understood by evaluating the correction factors. However, these factors are even higher than copper electrodes. If the structure contains only Ni(II), it would give CF values similar to copper electrodes. Since these electrodes also have Ni(III) sites, the CFs must be much smaller than copper values. Therefore, this behavior may be related to the Ni(II) LLC mesophase system that holds more water in the mesophase [31] as a result the LLC phase of the nickel samples is firstly thicker due to excess water and films become much more thinner after calcination. Another reason for this might be a phase separation of NiO. It was not clear in the XRD patterns; the diffraction line broadening makes the investigation harder. This broadening might be due to NiO formation on the structure. Therefore, we couldn't take the average electrode mass as 35 μg/cm^2 here and couldn't extract mass activity values for these electrodes.

3.2.7 Mesoporous $LiMn_{1.33}M_{0.66}O_4$ and $LiMn_{1.7}M_{0.3}O_4$ Thin Films for Efficient OER Catalysis

Mesoporous lithiated manganese metal oxides were investigated according to OER performances and stabilities. All compositions of spinel $LiMn_{2-x}M_xO_4$ electrodes were analyzed in terms of disproportionation reaction by cycling in 1 M KOH electrolyte and optimized composition has been found as LiMn66-M33. Notice that this specific composition is suggested as a unique ratio for preventing Mn(VI) disproportionation reaction by adding one Fe, Co, Ni or Cu between every two Mn atoms on the electrode surface.

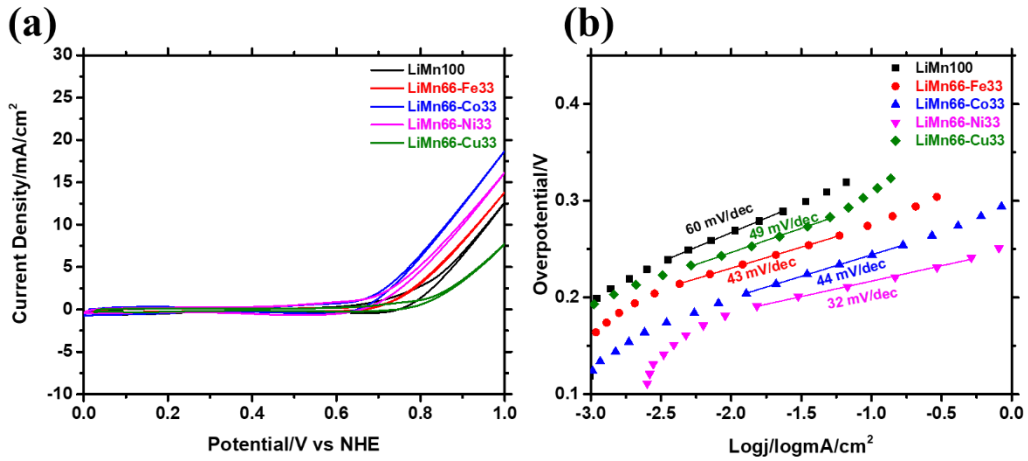

Figure 3.123 (a) CV curves of LiMn66-M33 electrodes in 1M KOH with 50 mV/s scan rate and (b) Tafel slope analysis of LiMn66-M33 electrodes.

OER analysis was started with the CV measurements (Figure 3.123(a)) and has been already discussed in the electrochemical properties of $LiMn_{2-x}M_xO_4$ sections. Electrodes have been fabricated at 5000 rpm spin rate over the FTO substrates and calcined at 300 ^oC for 1 hour. All catalytic characterizations have been carried in 1 M KOH solution and then the same electrodes have been used for stepwise electrochemical experiments such as CVs, multistep CAs, CPs at 1 mA/cm^2 to 50 mA/cm^2. Finally, the cyclic voltammograms were recorded to check electrodes at the end of these experiments.

Tafel slopes of the electrodes are obtained after multistep CA experiments and their graphs are shown in Figure 3.123(b). Notice that the LiMn100 electrode displays the highest Tafel slope value compared to the other compositions. Tafel slope decreases when 33 % copper is added to the crystal structure. When iron and cobalt ware used in the LiMn100-M33 electrodes, the Tafel slope decreased to 43 and 44 mV/dec, respectively. This is strong evidence for the role of electronegativity of the transition metal ion into the spinel structure except the copper case. Notice that the LiMn66-Cu33 composition has yielded phase separation of CuO and deviation in the cubic spinel structure. In the other metal systems, presence of a more electronegative metal amplifies the OER performance of the manganese sites by synergetic interactions of manganese and the second metal. When nickel is integrated into the LiMn66-M33 structure, a huge drop is observed in the Tafel slope, namely 30 mV/dec. This could be due to nickel being more electronegative than iron and cobalt. It improves the OER efficiency of the structure. Also, $Ni(OH)_2$ formation/deposition on the electrode surface might also enhance the OER efficiency of the nickel electrodes.

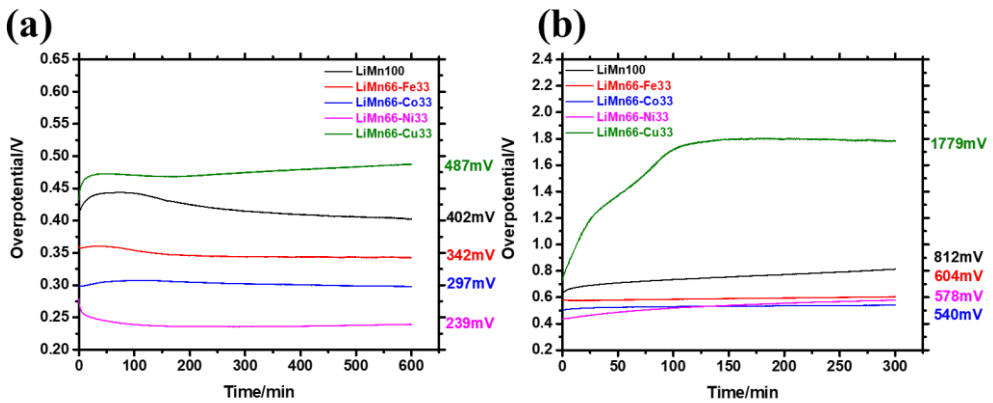

Figure 3.124 CP results of LiMn66-M33 electrodes (a) at 1mA/cm^2 and (b) at 10 mA/cm^2 current densities.

Then, the chronopotentiometry (CP) experiments were carried out for each composition. Firstly, the electrodes have been used at 1 mA/cm^2 current density for 10 hours. Figure 3.124(a) shows the CP plots of the LiMn100-M33 electrodes for the 1 mA/cm^2 current density.

The CP at 1 mA/cm^2 current density of the LiMn66-Cu33 electrode gives the highest overpotential value, likely due to phase separation in the crystal structure. Notice that the overpotential increases up to 50 minutes. It might be attributed to K^+ de-intercalation in the LiMn100 electrode. Then, a slow decrease in overpotential is observed. This improvement could be due to the cleaning of the surface manganese species, which are not part of λ-MnO_2. Therefore, these species are removed from the electrode surface through the Mn(VI) disproportionation reaction, making the electrode more efficient in OER. Then, all the LiMn66-M33 electrodes were used in CP experiments at 1mA/cm^2 current density. Notice that the overpotential values decrease gradually by the incorporation of 33% Fe, Co, and Ni. This improvement might be attributed to the synergetic electronic effect of the secondary metal ions due to their electronegativity. At low current density, we believe that the nickel is kept in the spinel $LiMn_xM_xO_4$ structure that has already been proven by cycling the LiMn66-Ni33 electrode in different potential windows in 1 M KOH solution. All the electrodes have also been used for CP experiments by adjusting the current density to 10 mA/cm^2. First 50 minutes, the electrodes show a similar trend as of the 1 mA/cm^2 current density. The overpotential value decreases by incorporating iron, cobalt, or nickel into the spinel structure. The LiMn100 electrode undergoes to a fast disproportionation reaction, evidenced by a fast increase of the overpotential over time. Notice that the LiMn66-Ni33 composition also shows an overpotential increase at 10 mA/cm^2 current density, see Figure 3.123(b). The LiMn66-Cu33 electrode has the highest overpotential value and undergoes to a complete degradation at 10 mA/cm^2 in 100 minutes.

Then, all the electrodes are used for the CP experiments from 20 to 50 mA/cm^2 current densities. Figure 3.125(a) shows the CP plots.

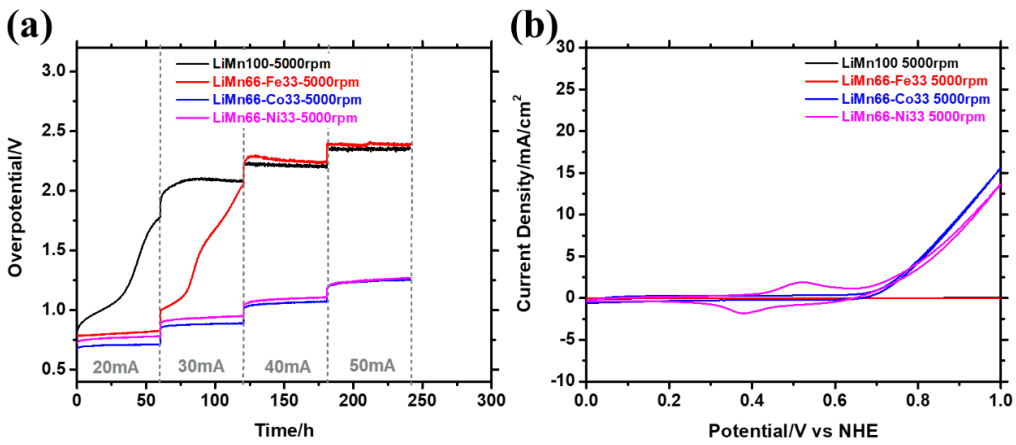

Figure 3.125 (a) Multistep-CP results of LiMn66-M33 electrodes and (b) CV curves of LiMn66-M33 electrodes after CP experiments.

The CP plot of the LiMn100 electrode at 20 mA/cm^2 current density shows that the Mn(VI) disproportionation reaction takes place in a very short time. In 60 minutes, the overpotential value reaches to the bare FTO value. This behavior is attributed to that; all the active manganese is dispersed into the electrolyte. The LiMn66-Fe33 electrode resists to the disproportionation reaction at 20 mA/cm^2 current density. As previously discussed, iron has also degraded at higher potentials by the formation of FeO_4^{2-} species. This behavior is observed in its CP at 30 mA/cm^2 current density by a drastic overpotential increase with time, see Figure 3.125(a). It also reaches to the bare FTO overpotential value. However, the iron system is a bit more stable in the OER process than the LiMn100 system. The LiMn66-Co33 and LiMn66-Ni33 electrodes can be used at harsh conditions. They show similar overpotentials at 20 to 50 mA/cm^2 current densities. It is expected that the nickel system exhibits a higher efficiency than cobalt because of the electronic effect. However, at higher current densities, the resistance of the working electrode becomes highly important and affects the overpotential values. Investigation of the electronic effect becomes more difficult at high current densities. One should note that the LiMn66-Co33 and LiMn66-Ni33 electrodes are very stable at high current densities as shown in the overpotential values. Stable overpotential may mean that the Mn(VI) disproportionation reaction has been prevented at these compositions in OER potentials. The LiMn66-Cu33 electrode was not tested electrochemically at higher current densities since full degradation of the electrode occurred at 10 mA/cm^2, see

Figure 3.124(b). Finally, the electrodes were cycled between 0 and 1 V in the same electrolytes without removing the used electrodes. These CV curves are shown in Figure 3.125(b). Notice that the LiMn100 and LiMn66-Fe33 electrodes don't show any faradaic peaks in the voltammograms and proves that the surface of the FTO has no active species. The LiMn66-Co33 electrode has almost the same voltammogram as the first CV of the unused electrode and might be attributed to that the cobalt ions integrate into the spinel structure and work with the manganese coherently in OER catalysis, improving the efficiency of manganese sites. In the LiMn66-Ni33 system, even if the electrode is stable and efficient, the nickel integration into spinel structure is still doubtful since redox peaks are similar to that of $Ni(OH)_2$/NiOOH couple, see Figure 3.125 (b). Maybe the NiOOH formation on the surface causes an efficient water oxidation and there is no clear proof of the role of $LiMn_{2-x}Ni_xO_4$ on efficient OER catalysis.

Due to $Ni(OH)_2$ formation on the electrode surface, another composition of the LMOs was investigated in order to analyze the OER performance of the spinel structures. A LiMn85-M15 composition has been chosen as an optimized composition since iron, cobalt or nickel content is relatively small with respect to manganese. This composition also preserves the spinel structure without any phase separation such as $Ni(OH)_2$ formation during OER. For the cycling experiments in 1 M KOH, the LiMn85-M15 electrodes have been used as an intermediate composition that is stable after 300 cycles.

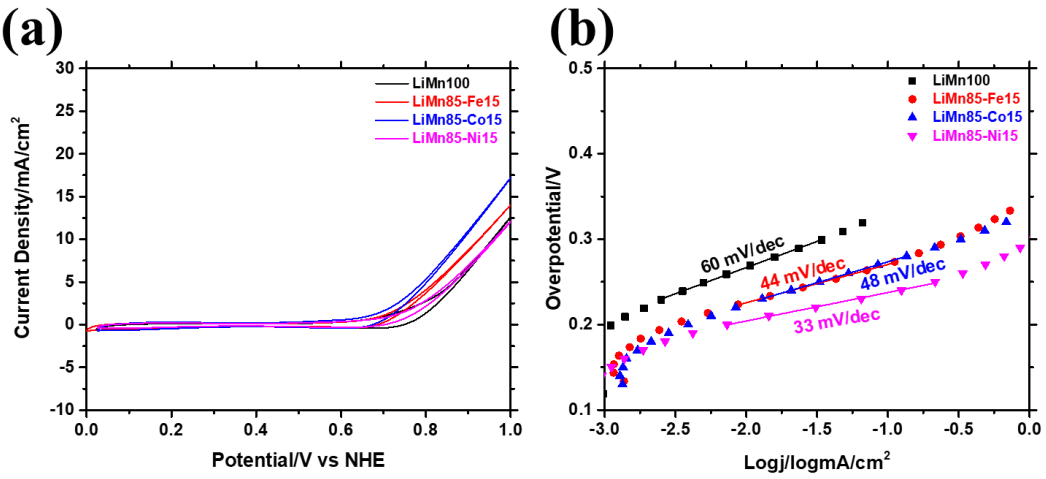

Figure 3.126 (a) CV curves of the LiMn85-M15 electrodes in 1 M KOH, recorded at a 50 mV/s scan rate and (b) Tafel slope analysis of the LiMn85-M15 electrodes.

The LiMn85-Mn15 compositions were firstly analyzed by CV measurements in 1 M KOH between 0 and 1 V at 50 mV/s. The voltammograms of the electrodes are shown in Figure 3.126(a).

There is no dominant redox peak(s), observed in the non-faradaic region between 0 and 0.7 V. In the OER region, the LiMn85-Fe15 and LiMn85-Co15 electrodes display higher current values, which are attributed increasing of the catalytic efficiency due to iron and cobalt and their electronic effect to the manganese sites. However, the LiMn85-Ni15 electrode displays almost the same current density as of the LiMn100 electrode. In this case, the accumulation of less reactive manganese oxide species on the electrode surface might be responsible for this behavior. Thus, the electrode could behave similarly to the LiMn100 electrode in the first cycles and need to be activated by further cycling or CA, CP experiments. Then, the electrodes were tested in chronoamperometry experiments to extract Tafel slope values. From Figure 3.126(b), Tafel slope of the LiMn100, LiMn85-Fe15, LiMn85-Co15, and LiMn85-Ni15 electrodes are obtained using the log(j) versus overpotential plots and reported as 60, 44, 48 and 33 mV/dec, respectively. This also proved that the addition of iron, cobalt, and nickel into the LiMn100 structure decreased the Tafel slope values.

Furthermore, the electrodes were used in long-term CP experiments at 1 and 10 mA/cm^2 current densities and the results are shown in Figure 3.127(a) and (b), respectively.

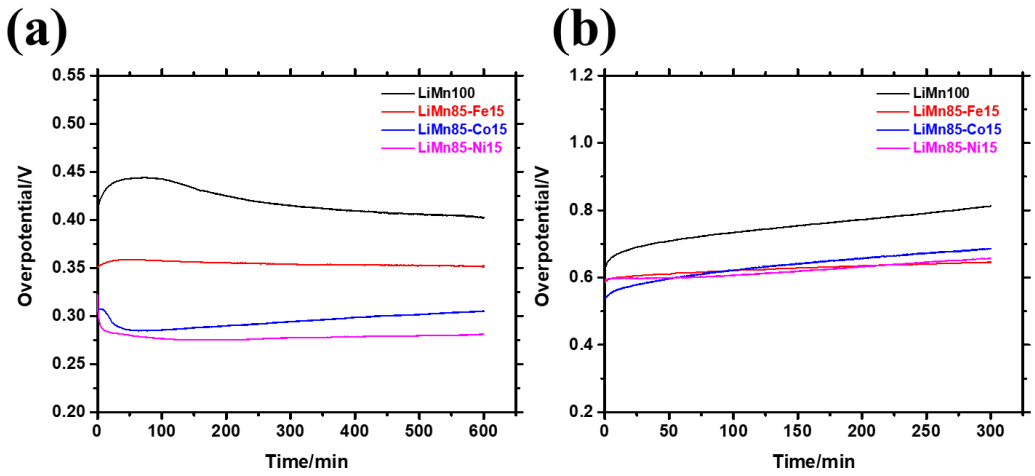

Figure 3.127 CP results of the LiMn85-M15 electrodes (a) at 1 mA/cm^2 and (b) at 10 mA/cm^2 current densities.

According to the CP at 1 mA/cm^2 current density, the overpotential values decrease by the addition of 15% of another transition metal into the spinel structure, see Figure 3.127(a). This behavior has already been discussed in the LiMn66-M33 systems. Also, the CP results at 10 mA/cm^2 current density show similar behavior, see Figure 3.127(b). Notice that, the overpotential values of the LiMn85-M15 electrodes are slightly higher than the LiMn66-M33 electrodes. This is expected since less iron, cobalt, or nickel in the $LiMn_{2-x}M_xO_4$ electrode cause a decrease in the OER efficiencies. However, the overpotential values are still reasonable for these manganese rich $LiMn_{2-x}M_xO_4$ electrodes.

Mainly, the LiMn85-M15 electrodes were tested in harsh OER conditions at high current densities to understand their degradations. The electrodes have been used for the CP experiments at 20, 30, 40 and 50 mA/cm^2 current densities, see Figure 3.128(a).

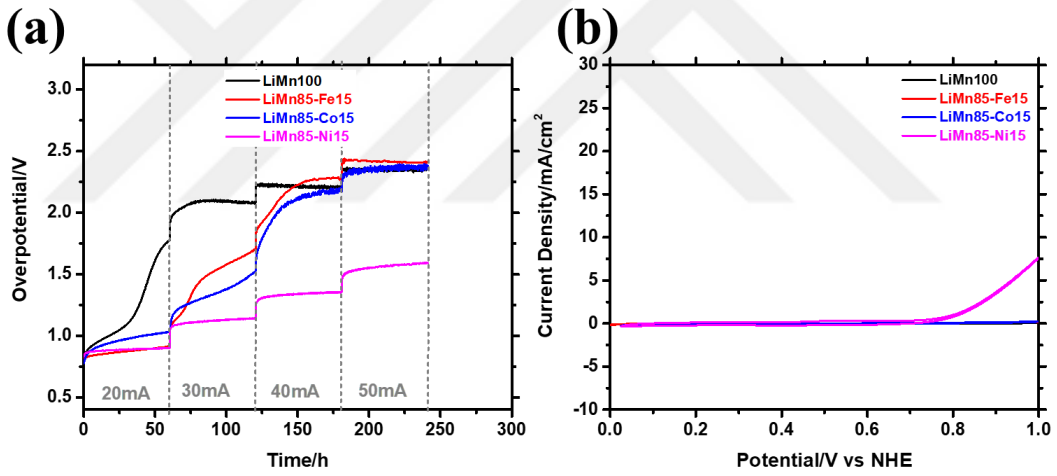

Figure 3.128 (a) Multistep-CP results of the LiMn85-M15 electrodes and (b) CV curves of the LiMn85-M15 electrodes after CP experiments.

According to multi-step CP experiments, the LiMn85-Fe15 and LiMn85-Co15 degradation rates are similar and occur at between 20 and 50 mA/cm^2 current densities. This is as expected for the iron case, since it has already been demonstrated by the LiMn66-Fe33 electrode. However, decreasing of cobalt content in the electrodes from 33 to 15% enhanced the degradation rate of the LiMn85-Co15 electrode since its overpotential gradually increases at 20 mA/cm^2 current density over time. For the LiMn85-Ni15 case, the electrode didn't show a sharp degradation during the experiment even at 50 mA/cm^2 current density, see

Figure 3.128(a). Also, the CV of the electrode, after multi-step CP experiments, shows that the electrode is still active and robust in the OER region without showing any $Ni(OH)_2$ formation on the electrode surface, see Figure 3.128(b).

To conclude, the LiMn66-Co33 and LiMn85-Ni15 electrodes have a good OER performance. At higher current densities, the overpotentials are relatively constant and can be considered as robust electrodes for harsh electrocatalytic OER conditions. Due to IR drop by FTO substrate, the overpotential values are reported to be higher for these thin film electrodes. This issue might be eliminated by using more conductive substrates such as graphite and several metal foams. Mesoporous LiMn85-M15 films are also fabricated on conductive graphite rods by dip coating method depicted lower overpotentials as mentioned in the experimental section. After dip coating of the relevant solutions, the rods are calcined at 300 ^{o}C for an hour. Electrochemical analysis is started by recording the CV curves of these electrodes in 1 M KOH with a 50 mV/s scan rate, see Figure 3.129.

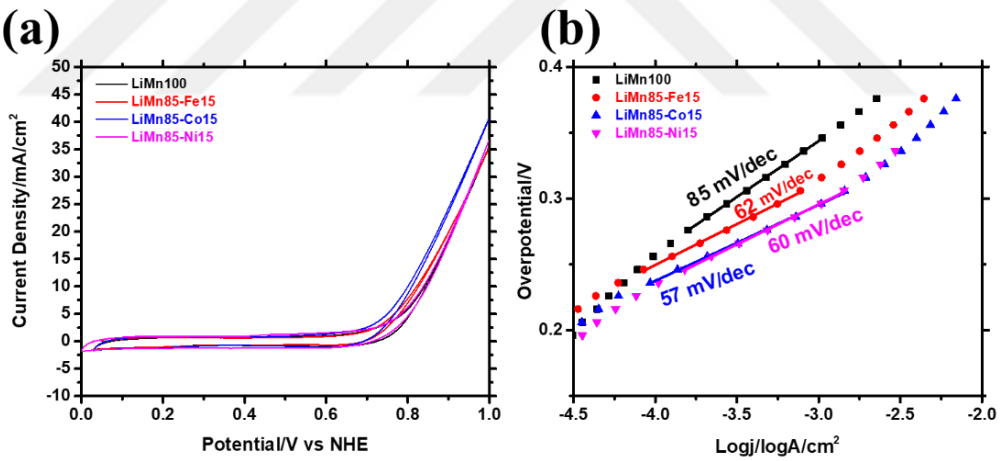

Figure 3.129 (a) CV curves of the LiMn85-M15 electrodes on graphite rods in 1 M KOH, recorded at a 50 mV/s scan rate and (b) Tafel slope analysis of the LiMn85-M15 electrodes.

As shown in Figure 3.129(a), all the LiMn85-M15 electrodes display higher current density values (around 40 mA/cm^2) at 1.0 V compared to the LiMn85-M15 films on FTO surfaces. This behavior is strongly related to conductive nature of graphite substrate. The LiMn85-Co15 electrode has the highest efficiency among the LiMn85-M15 electrodes, see Figure 3.129(a). Furthermore, Tafel slope analysis of the electrodes are carried by CA experiments and log(j) versus

overpotential plots of each LiMn85-M15 electrode are shown in Figure 3.129(b). Notice that, all the electrodes on graphite give higher Tafel slope values, compared to the electrodes on FTO surface. Film quality on the graphite surface might increase the Tafel slope values. In section 3.1.6.3, the LiMn100 film has been investigated on the graphite rods that have accumulated LiMn100 on certain parts of the surface. Thus, films became poor in quality on graphite when it was compared with the films on FTO. The LiMn85-M15 on FTO might give lower Tafel slope values at lower potentials due to smoother film formation.

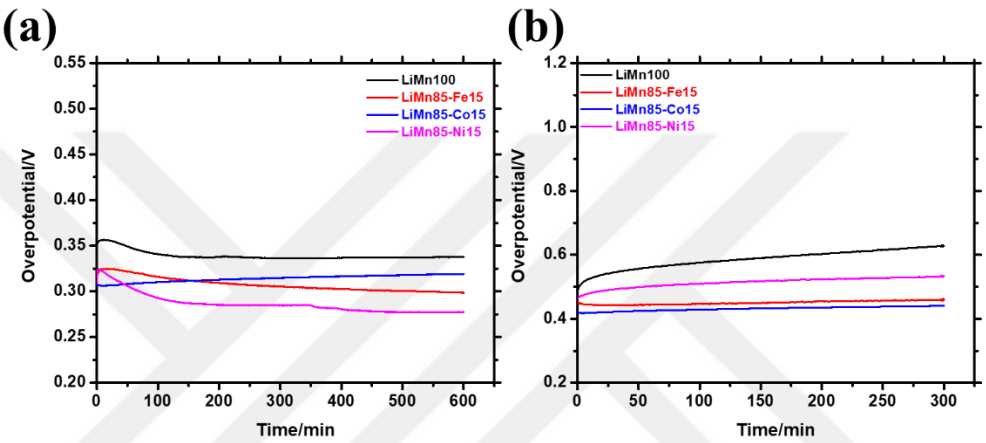

Figure 3.130 CP results of the LiMn85-M15 on graphite (a) at 1 mA/cm^2 and (b) at 10 mA/cm^2 current densities.

The LiMn85-M15 films on graphite are also tested in CP experiments at 1 and 10 mA/cm^2 and the CP graphs are shown in Figure 3.130 (a) and (b), respectively. Notice that effect of using conductive substrate may not be important since the overpotential values of the electrodes are smaller compared to FTO case. This is due to IR compensation, when the substrate is switched to graphite (4-5 ohms) from FTO (14-17 ohms). Especially at 10 mA/cm^2, overpotential values of the LiMn85-Co15 and LiMn85-Ni15 electrodes are decreased to around 0.4 V in the graphite case, where the FTO overpotential values at the same current density are around 0.6 V, compare Figures 3.127 (b) and 3.130(b). More CP experiments are also performed to check the efficiency and stability of these electrodes at 20-50 mA/cm^2 current densities, see Figure 3.131(a).

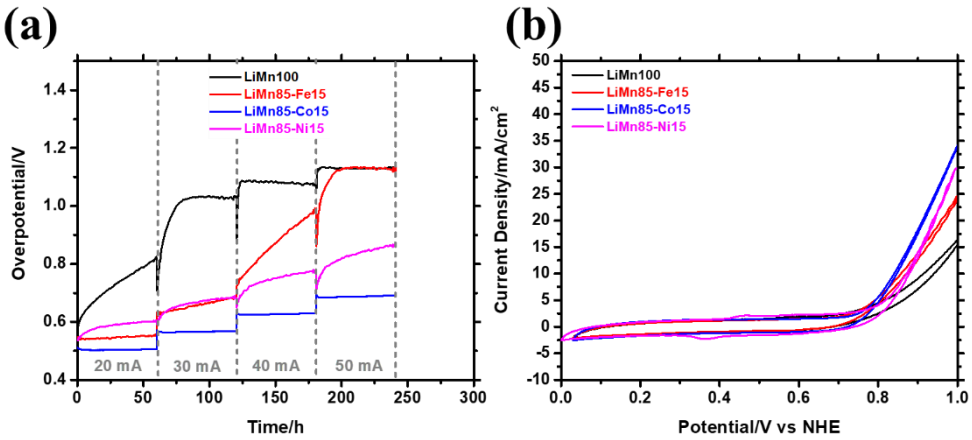

Figure 3.131 (a) Multistep-CP results of the LiMn85-M15 electrodes on graphite and (b) CV curves of the LiMn85-M15 electrodes after CP experiments.

According to CP graphs in Figure 3.131 (a), the LiMn100 shows fast degradation at 20 mA/cm^2, which is similar to LiMn100 on FTO. Manganese disproportionation reaction still dominates the degradation of the LiMn100 film on the graphite surface. Overpotential value reaches to bare graphite overpotential value at 30 mA/cm^2 current density. However, the LiMn85-Fe15 electrode shows an improvement in the overpotential values and stability. In the graphite coated electrodes, the fast degradation starts at 40 mA/cm^2 current density on graphite surface. This fast degradation is observed at 30 mA/cm^2 current density on the FTO surface. The LiMn85-Co15 on graphite is robust even at 50 mA/cm^2 which is a distinct improvement when it is compared with the FTO substrate, see Figure 3.131 (a). Notice that the overpotential values at each current density are quite small among in metal systems. The LiMn85-Ni15 has a relatively slower degradation at much higher current densities. However, the overpotential values are still higher compared to the LiMn85-Co15 graphite case. The CV curves are also recorded using the electrodes after the CP at 50 mA/cm^2 current density, see Figure 3.130(b). Among the CV curves, the LiMn85-Co15 and LiMn85-Ni15 electrodes show the highest current densities in the OER region, and might be attributed to graphite surfaces still bearing films. The LiMn100 CV shows bare graphite behavior due to the complete degradation of the film on graphite. However, the LiMn85-Fe15 electrode shows OER activity in the OER region (between 0.7 V and 1.0 V) in the voltammogram, see Figure 3.131(b). In the CP test, the overpotential value of the LiMn85-Fe15 electrode reaches to

overpotential value of the bare graphite. In this case, cycling might cause redeposition of the iron species in the electrolyte and the formation of Fe_xO_y, $Fe(OH)_3$, or FeOOH species on the electrode surface. These species might perform OER electrocatalysis at relatively lower potentials and cause a current density increase in the OER region, see Figure 3.131(b).

In conclusion, the graphite substrate is one of the ways to decrease the overpotential values. Highly resistive substrates cause an increase in the overpotential values. Potential required to flow the current through the substrate is added up to our experimental overpotential value. Thus, the conductive substrates are needed to compensate this extra potential.

Chapter 4

4 Conclusion

In this study, mesoporous spinel $LiMn_{2-x}M_xO_4$ thin films have been synthesized by the MASA method and characterized in terms of crystal structures, manganese oxidation states, and electrochemical behavior under acidic, alkaline, and neutral conditions.

The surface Mn disproportionation reaction mechanism of the mesoporous LiMn100 electrodes has been analyzed by CV and LSV and post-characterization methods such as XPS, and XRD. At negative potentials, the Mn(III) undergoes a disproportionation reaction to form Mn(II) and Mn(IV) species and at positive potentials the Mn(VI) disproportionation reaction takes place. These two processes cause a stability problem for the LiMn100 electrodes. Lithium ions in the LiMn100 electrodes can be almost completely removed to form the λ-MnO_2 phase as evidenced by XRD analysis and this phase is considered to be the active catalyst due to its unique structure. In the non-aqueous environment, the lithium intercalation-deintercalation process is irreversible as shown by the charge density decrease in related redox peaks. It has been shown that the problem is related to a non-aqueous environment since the lithium intercalation process is more efficient in the aqueous $LiNO_3$ media. Electrochemical properties of the LiMn100 electrodes with various thicknesses have been investigated and the charge capacity of the films have been determined by CV experiments in $LiNO_3$ environment as of between 0.0136 and 0.273 coulombs for these films. Using these capacities, approximate catalytic loads on the electrodes are estimated between 30 and 60 $\mu g/cm^2$.

Mesoporous LiMn100 electrodes have also been tested in 1 M KOH and 1 M LiOH electrolytes by cycling between 0 and 1 V to investigate the Mn(VI) disproportionation reactions. The LiMn100 electrodes, used in LiOH electrolyte, are more stable and the disproportionation reaction can be slowed down by using LiOH due to lithium intercalation that partially repairs the electrode. The mesoporous Mn_3O_4 electrode was also fabricated by the MASA method and used in CV cycling experiments for comparison with the mesoporous LiMn100 electrode. The results show that the spinel lithiated manganese oxide electrodes are much more stable than the mesoporous Mn_3O_4 electrodes. The thickness of the film has been optimized by considering the OER durability during chemical and physical degradations. Fabrication parameters, such as spin coating rate and calcination temperature are optimized for an effective catalytic reaction. The LiMn100 electrode, fabricated at 5000 rpm spin rate and calcined at 300 ^oC, is found to be the most efficient electrode for the OER. The same optimization parameters have been used for the fabrication of the $LiMn_{2-x}M_xO_4$ thin film electrodes.

The $LiMn_{2-x}M_xO_4$ electrodes, fabricated at 5000 rpm spin rate and 300 ^oC calcination temperature, have been investigated for lithium intercalation/de-intercalation properties and electrochemical Mn(VI) disproportionation reaction. The lithium-ion intercalation and de-intercalation processes are more efficient in the $LiMn_2O_4$ and $LiMn_{2-x}Fe_xO_4$ electrodes compared to the $LiMn_{2-x}Co_xO_4$ and $LiMn_{2-x}Ni_xO_4$ electrodes. The Mn(VI) disproportionation reaction in mesoporous $LiMn_{2-x}M_xO_4$ electrodes has been investigated by CV cycling experiments in 1 M KOH. The $LiMn_{2-x}Fe_xO_4$ electrodes are found to be unstable due to fast electrode degradation at 1 V; both manganese and iron undergo disproportionation reactions in all compositions. The $LiMn_{2-x}Cu_xO_4$ electrodes are also unstable due to phase separation; CuO formation is observed in the Cu rich samples. Spinel $LiMn_{2-x}Fe_xO_4$, $LiMn_{2-x}Co_xO_4$ and $LiMn_{2-x}Ni_xO_4$ electrodes are relatively more stable and stability increases with increasing the secondary metal ion in the structure. The LiMn66-Co33 and LiMn66-Ni33 electrodes are the most stable ones, because of preventing the manganese disproportionation reaction by unique cobalt and nickel to manganese ratio on the electrodes surface. Considering the suggested Mn(VI) disproportionation reaction mechanism, the

permanganate formation can be slowed and eliminated by incorporating relatively more electronegative metal ions, such as the ions Co and Ni in the surface or structure of the $LiMn_{2-x}M_xO_4$ electrodes.

In 1 M KOH electrolyte solution, the LiMn66-M33 electrodes have also been tested for efficient OER. Tafel slopes of the LiMn100 and LiMn66-Fe33, LiMn66-Co33, LiMn66-Ni33, and LiMn66-Cu33 electrodes are found to be 60, 44, 43, 32, and 49 mV/dec, respectively. Copper-based electrodes readily degrade even at lower current densities. The LiMn100 and LiMn66-Fe33 electrodes are also unstable under harsh OER experimental conditions. However, the LiMn66-Co33 and LiMn66-Ni33 electrodes are very efficient and stable in chronopotentiometry experiments at high current densities. The LiMn66-Co33 composition preserves its spinel structure during and after OER. However, the LiMn66-Ni33 composition undergoes to a transformation to form $Ni(OH)_2$ on the electrode surface upon catalytic reactions. Due to $Ni(OH)_2$ formation in the LiMn66-Ni33, the LiMn85-M15 compositions are also tested to get rid of phase separation on the electrode surface. The LiMn85-Ni15 electrode is found to be much more stable in OER, compared to the LiMn85-Co15 electrode, maybe due to an enhanced synergetic effect between manganese and nickel species. Lastly, graphite substrate was tested in harsh OER experiments. Thus, overpotential values were decreased by using of more conductive substrate. LiMn85-Co15 on graphite were found most efficient and stable electrode among LiMn85-M15 films on graphite surfaces. It resulted 0.692 V overpotential value at 50 mA/cm^2 without any degradation problem.

Chapter 5

5 Future Recommendation

So far, lithiated manganese metal oxide electrodes have been fabricated from certain solutions of all metal salt ingredients and characterized. Then, their OER stabilities have been improved by incorporating another transition metal ion (such as cobalt and nickel) to the spinel structure. Incorporated transition metal species are homogeneously dispersed into the $LiMn_2O_4$ matrix to form $LiMn_{2-x}M_xO_4$ compounds. For a robust electrode, these active metal sites must be located on the electrode surface. However, this is almost impossible by calcination of the precursor gel-phases. If only the electrode surface is enriched by these active metal species, a synergetic electronic effect may also be effective for an improved efficiencies and this surface may also be much more resistive to a Mn(VI) disproportionation reaction during the OER process.

Nicolau *et al.* focused on a unique and simple technique used for surface modification by reaction between adsorbed ions and solid solution interface. The process is known as the successive ionic layer adsorption and reaction (SILAR) method. In the SILAR method, the process starts by immersing the film material into a concentrated solution of the target cations. The cations are adsorbed on the surface of the film material that will be modified. Then, the film is rinsed with a certain solvent followed by immersing it into a second solution with anions that will react with the adsorbed cations. Finally, the film is washed to clean its surface from unreacted ions.[137]

Karakaya *et al*. in 2020, modified a mesoporous $LiMn_{2-x}Co_xO_4$ thin film surface by employing the SILAR method.[34] The films were dipped into a 1 M $Co(NO_3)_2$ solution, followed by a washing procedure, and finally calcined at various temperatures to form one or two monolayers of cobalt oxide to improve

the catalytic performance and stability of the $LiMn_2O_4$ electrodes. The surface of the electrodes is enriched in terms of cobalt content and the OER efficiency has been increased by this modification. However, the accumulation of cobalt sites on the electrode surface is not controllable. The calcination causes diffusion of the cobalt ions into the $LiMn_2O_4$ to form $LiMn_{2-x}Co_xO_4$. The surface contains both manganese and cobalt species.

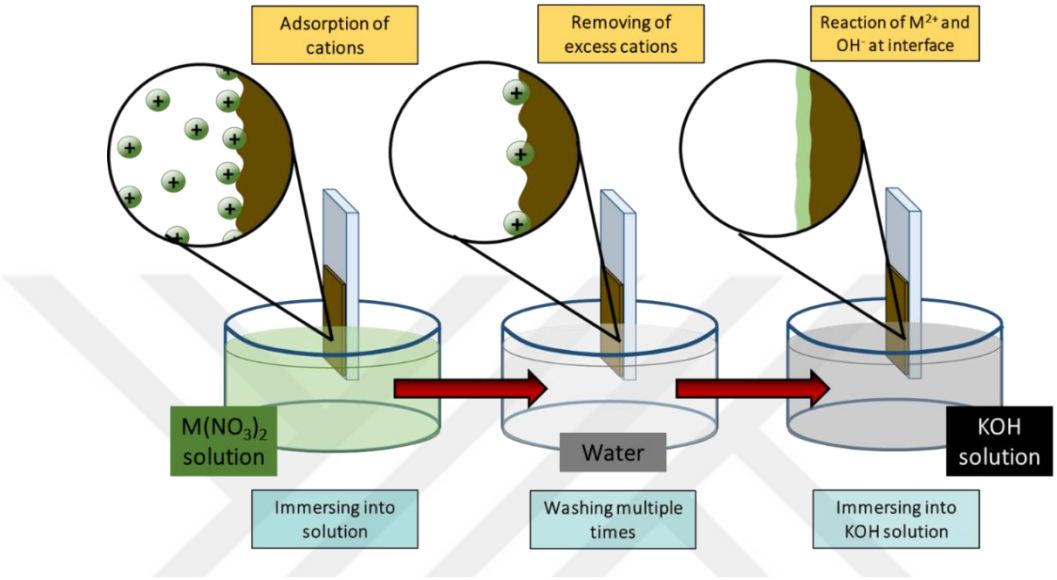

Figure 5.1 Schematic representation of SILAR method.

For a higher yield of the active metal ions on the surface, the SILAR method may be employed by eliminating the calcination step. For this reason, the films might be immersed in iron, cobalt, nickel or copper solutions. Typical washing procedure is applied and the trace amounts of metal cations are adsorbed on the electrode surface. These electrodes are immersed into an alkaline solution. Thus, one or two layers of $M(OH)_2$ formation might be aimed at the electrode surface. We believe that this solid thin layer protects the electrode in terms of Mn(III) and Mn(VI) disproportionation reactions. Also, the electronic synergetic effect between the electrode and layer might enhance the catalytic efficiencies at the interface. Also, low temperature calcination could be applied after SILAR such as at 50, 100, 150 and 200 ^oC. The concentration of the metal salt solutions, and repeating times of the washing procedure might be also parametrized to find effective coating on film surfaces. Nickel-based SILAR modification is regarded as the main part of this project. $Ni(OH)_2$ species are easy to identify by the simple electrochemical techniques and may help to quantify the effectiveness of the SILAR method. Upon optimization of the nickel system, the other metals might be

employed to diminish manganese loss on the electrode surface. A schematic representation of the SILAR method is shown in Figure 5.1.

We employed the SILAR method for the modification to cover the electrode surface by a very thin layer of $Ni(OH)_2$. Some preliminary experiments have been carried to optimize the modification parameters. First parameter is times of washing procedure by deionized water (DI) after dipping the LiMn100 electrode into a concentrated $Ni(NO_3)_2$ solution. The LiMn100 electrode, fabricated at 5000 rpm, is dipped into a 1 M $Ni(NO_3)_2$ solution as the first step. In 2nd step, the electrode is removed from nickel nitrate solution and dipped into a fresh DI water for several times using a fresh DI water in each time. Then, the

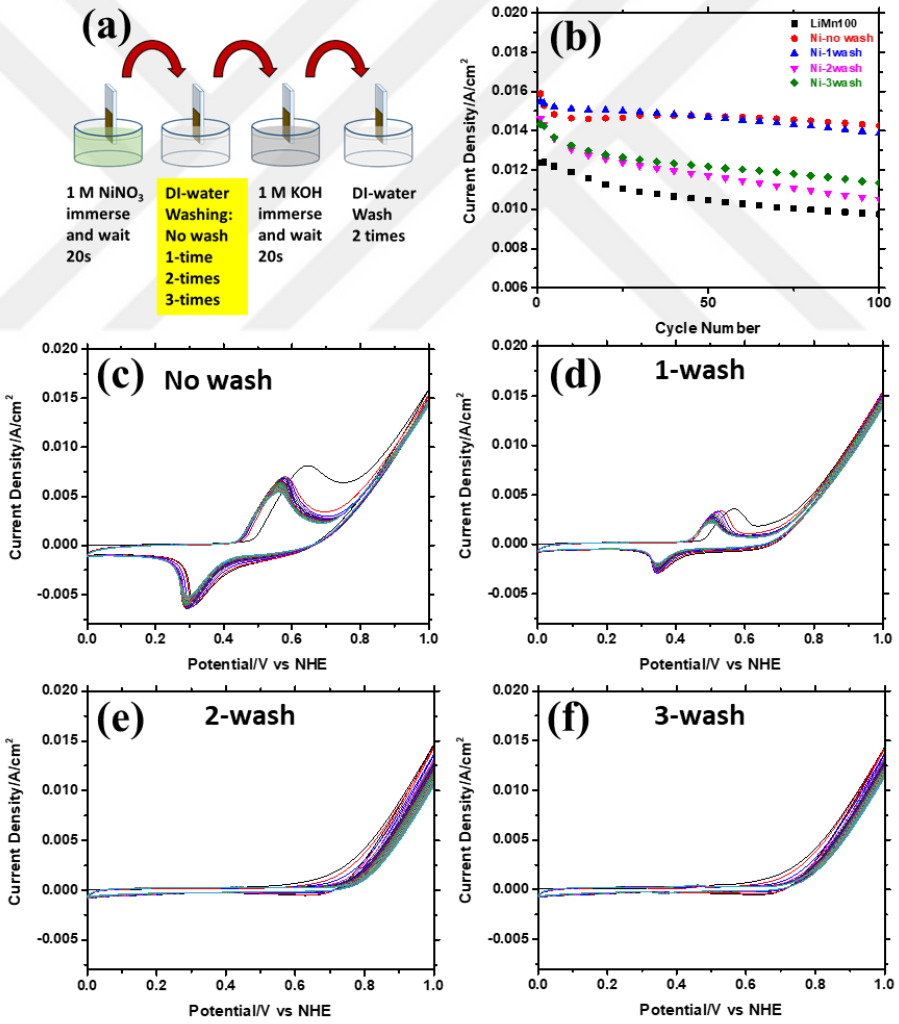

Figure 5.2 (a) Schematic representation of SILAR modification on LiMn100, (b) Current density of LiMn100 at 1 V in CV curves by cycling, CV curves (50 cycles) of modified LiMn100 electrodes in 1 M KOH with a 50 mV/s scan rate: (c) non-washed, (d) 1-time washed, (e) 2-times washed, (f) 3-times washed.

electrode is immersed into 1 M KOH solution followed by a final washing of the electrode with DI water to remove excess KOH content on the surface. Schematic representation of the experiment is shown in Figure 5.2(a).

Then the modified LiMn100 electrode is used to record its CV curves, unwashed and 1-time washed electrodes display distinct redox peaks of the $Ni(OH)_2$/NiOOH couple. It means excess $Ni(OH)_2$ formation occurs on the LiMn100 electrode surface, see Figure 5.2(c) and (d). However, we aimed to create one or few monolayer of $Ni(OH)_2$ formation on the electrode surface. Thus, further washing of the electrode such as 2 or 3 times, may be needed to establish a more effective method for a thinner modification. The 2 and 3 times washed electrodes do not display the $Ni(OH)_2$/NiOOH redox peaks in the CVs, see Figure 5.2(e) and (f). The current density values of the electrodes at 1 V are plotted with respect to cycle number in Figure 5.2(b). The unwashed and 1-time washed electrodes shows stable behavior up to 300 cycles due to $Ni(OH)_2$ feature on the electrode surface. 2 and 3 times washed electrodes show decay in current densities but they showed higher current density values compared to unmodified LiMn100 electrode.

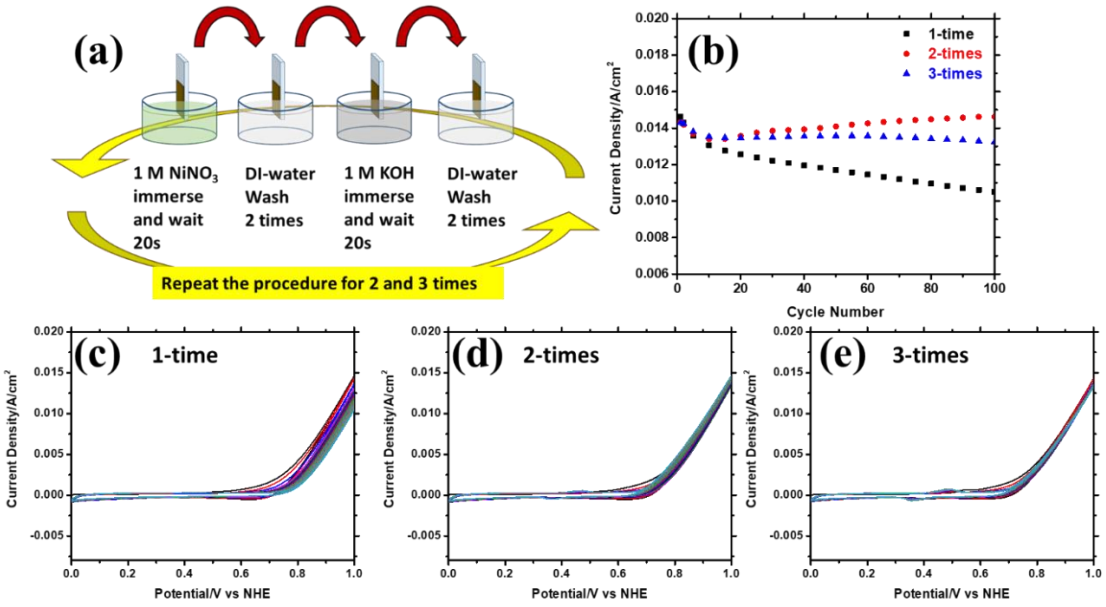

Figure 5.3 (a) Schematic representation of SILAR modification on LiMn100 (b) Current density of LiMn100 at 1 V in CV curves by cycling, CV curves (50 cycles) of modified LiMn100 electrodes in 1 M KOH with 50 mV/s scan rate: (c) 1-repeat, (d) 2-repeat (e) 3-repeat.

Afterwards, 2-times washed electrode is used for further modifications. Thus, the whole step is repeated multiple times to make the modification in a controlled manner. In other words, step-by-step $Ni(OH)_2$ deposition on the electrode surface is aimed to modify the electrode surface. Whole step is repeated for 1, 2 and 3 times. A schematic representation of the modification is demonstrated in Figure 5.3(a).

Controlled $Ni(OH)_2$ formation on the LiMn100 electrode surface is achieved by employing this type of modification. Thus, no distinct $Ni(OH)_2$/NiOOH redox peaks are observed in all voltammograms, see Figure 5.3(c), (d) and (e). An electrode modified 3-times displays a weak oxidation reduction peaks in Figure 5.3(e), meaning a $Ni(OH)_2$ formation on the electrode surface, but in a small amount. Furthermore, the current density values of the modified LiMn100 electrode at 1 V are plotted against the cycle number. Surprisingly, 2 and 3-times repeated modification amplified the current density by cycling process, which might be attributed to activation of the electrode surface somehow since OER performances of these electrodes are improved.

In conclusion, the SILAR method is a promising method to modify an unstable LiMn100 electrode for further investigation ion. The new process enhances electrocatalytic activities, stabilities by integrating a small amount of nickel species on the LiMn100 electrode surface. As future work, other parameters such as repeating, annealing, electrodeposition etc. might be variated or added to modify the surface for much more controlled deposition of $Ni(OH)_2$. Effect of each parameter on OER performance needs to be investigated. Even, the lithium intercalation/deintercalation process might be investigated by GCD experiments since we believe that the $Ni(OH)_2$ covers only the surface. Interior of the electrode is still $LiMn_2O_4$ and this may allow an efficient lithium de-intercalation reaction. It makes the electrodes multi-functional materials that can be used for both OER electrocatalysis and energy storage. Besides the electrochemical characterization, XRD, SEM, XPS and other relevant techniques should be employed for characterization of the modified electrodes to obtain information about nickel hydroxide distribution and quantification on the electrode surface before and after electrochemical processes.

6 References

[1] A. Walcarius, "Mesoporous materials and electrochemistry," *Chem. Soc. Rev.*, vol. 42, no. 9, pp. 4098–4140, 2013.

[2] M. S. Park, J. Kim, K. J. Kim, J. W. Lee, J. H. Kim, and Y. Yamauchi, "Porous nanoarchitectures of spinel-type transition metal oxides for electrochemical energy storage systems," *Phys. Chem. Chem. Phys.*, vol. 17, pp. 30963–30977, 2015.

[3] P. Yang, D. Zhao, D. I. Margolese, B. F. Chmelka, and G. D. Stucky, "Generalized syntheses of large-pore mesoporous metal oxides with semicrystalline frameworks," *Nature*, vol. 396, pp. 152–155, 1998.

[4] Q. Huo *et al.*, "Generalized synthesis of periodic surfactant/inorganic composite materials," *Nature*, vol. 368, no. 6469, pp. 317–321, 1994.

[5] P. Behrens, "Voids in Variable Chemical Surroundings: Mesoporous Metal Oxides," *Angew. Chemie (International Ed. English)*, vol. 35, no. 5, pp. 515–518, 1996.

[6] R. Ryoo, S. H. Joo, and S. Jun, "Synthesis of highly ordered carbon molecular sieves via template-mediated structural transformation," *J. Phys. Chem. B*, vol. 103, pp. 7743–7746, 1999.

[7] F. Jiao, A. Harrison, J. Jumas, A. V Chadwick, W. Kockelmann, and P. G. Bruce, "Ordered mesoporous Fe $_2$ O $_3$ with crystalline walls," *J. Am. Chem Soc.* vol. 128, no. 16, pp. 5468-5474, 2006.

[8] Y. Wang, C. M. Yang, W. Schmidt, B. Spliethoff, E. Bill, and F. Schüth, "Weakly ferromagnetic ordered mesoporous Co_3O_4 synthesized by nanocasting from vinyl-functionalized cubic Ia3d mesoporous silica," *Adv. Mater.*, vol. 17, no. 1, pp. 53–56, 2005.

[9] X. J. Wu and D. Xu, "Soft template synthesis of yolk/silica shell particles," *Adv. Mater.*, vol. 22, no. 13, pp. 1516–1520, 2010.

[10] A. H. Lu, W. C. Li, W. Schmidt, and F. Schüth, "Template synthesis of large pore ordered mesoporous carbon," *Microporous Mesoporous Mater.*, vol. 80, no. 1–3, pp. 117–128, 2005.

[11] W. C. Li, A. H. Lu, C. Weidenthaler, and F. Schüth, "Hard-templating pathway to create mesoporous magnesium oxide," *Chem. Mater.*, vol. 16, no. 26, pp. 5676–5681, 2004.

[12] H. Kim and J. Cho, "Hard templating synthesis of mesoporous and nanowire SnO_2 lithium battery anode materials," *J. Mater. Chem.*, vol. 18, pp. 771–775, 2008.

[13] Z. Zhang, F. Zuo, and P. Feng, "Hard template synthesis of crystalline mesoporous anatase TiO_2 for photocatalytic hydrogen evolution," *J. Mater. Chem.*, vol. 20, pp. 2206-2212, 2010.

[14] X. Gu, W. Zhu, C. Jia, R. Zhao, W. Schmidt, and Y. Wang, “Synthesis and microwave absorbing properties of highly ordered mesoporous crystalline $NiFe_2O_4$,” *Chem. Commun.*, vol. 47, no. 18, pp. 5337–5339, 2011.

[15] Y. Ren, Z. Ma, and P. G. Bruce, “Ordered mesoporous $NiCoMnO_4$: Synthesis and application in energy storage and catalytic decomposition of N_2O,” *J. Mater. Chem.*, vol. 22, no. 30, pp. 15121–15127, 2012.

[16] Y. Lv *et al.*, “A comprehensive study on KOH activation of ordered mesoporous carbons and their supercapacitor application,” *J. Mater. Chem.*, vol. 22, no. 1, pp. 93–99, 2012.

[17] N. Dahal, I. A. Ibarra, and S. M. Humphrey, “High surface area mesoporous Co_3O_4 from a direct soft template route,” *J. Mater. Chem.*, vol. 22, no. 25, pp. 12675–12681, 2012.

[18] H. Qutaish *et al.*, “Soft-templated synthesis of mesoporous nickel oxide using poly(styrene-block-acrylic acid-block-ethylene glycol) block copolymers,” *Microporous Mesoporous Mater.*, vol. 271, pp. 16–22, 2018.

[19] M. Y. Yaman, A. S. Han, J. Bandara, C. Karakaya, and Ö. Dag, “Modifying titania using the molten-salt-assisted self-assembly process for cadmium selenide-quantum dot-sensitized photoanodes,” *ACS Omega*, vol. 2, no. 8, pp. 4982–4990, 2017.

[20] I. Ulu, B. Ulgut, and Ö. Dag, “Nanoarchitectonics of Mesoporous $M_2P_2O_7$ (M = Mn(II), Co(II), and Ni(II)) and $M_{2-x}Co_xP_2O_7$ and Transformation to Their Metal Hydroxides with Decent Charge Capacity in Alkali Media,” *Inorg. Chem.*, vol. 62, no. 41, pp. 16994–17011, 2023.

[21] I. Uzunok *et al.*, “Lyotropic Liquid Crystalline Mesophases Made of Salt-Acid-Surfactant Systems for the Synthesis of Novel Mesoporous Lithium Metal Phosphates,” *Chempluschem*, vol. 84, no. 10, pp. 1544–1553, 2019.

[22] C. Karakaya, Y. Türker, and Ö. Dag, “Molten-salt-assisted self-assembly (MASA)-synthesis of mesoporous metal titanate-titania, metal sulfide-titania, and metal selenide-titania thin films,” *Adv. Funct. Mater.*, vol. 23, no. 32, pp. 4002–4010, 2013.

[23] H. A. Raza, I. Karakaya, and Ö. Dag, “Nanoarchitectonics of Mesoporous $CaFe_2O_4$ Thin-Film Electrodes from Salt-Surfactant Lyotropic Liquid Crystalline Mesophases and Their OER Performance,” *ACS Appl. Energy Mater.*, vol. 6, no. 18, pp. 9681–9697, 2023.

[24] A. Amirzhanova, N. Akmanşen, I. Karakaya, and Ö. Dag, “Mesoporous $MnCo_2O_4$, $NiCo_2O_4$, and $ZnCo_2O_4$Thin-Film Electrodes as Electrocatalysts for the Oxygen Evolution Reaction in Alkaline Solutions,” *ACS Appl. Energy Mater.*, vol. 4, no. 3, pp. 2769–2785, 2021.

[25] F. M. Balci *et al.*, “Synthesis of mesoporous $LiMn_2O_4$ and $LiMn_{2-x}Co_xO_4$ thin films using the MASA approach as efficient water oxidation electrocatalysts,” *J. Mater. Chem. A*, vol. 6, no. 28, pp. 13925–13933, 2018.

[26] A. Amirzhanova *et al.*, “Synthesis and water oxidation electrocatalytic and

electrochromic behaviours of mesoporous nickel oxide thin film electrodes," *J. Mater. Chem. A*, vol. 7, no. 38, pp. 22012–22020, 2019.

[27] C. Karakaya, Y. Türker, C. Albayrak, and Ö. Dag, "Assembly of molten transition metal salt-surfactant in a confined space for the synthesis of mesoporous metal oxide-rich metal oxide-silica thin films," *Chem. Mater.*, vol. 23, no. 12, pp. 3062–3071, 2011.

[28] G. Saat, F. M. Balci, E. P. Alsaç, F. Karadas, and Ö. Dag, "Molten salt assisted self-assembly: Synthesis of mesoporous $LiCoO_2$ and $LiMn_2O_4$ thin films and investigation of electrocatalytic water oxidation performance of lithium cobaltate," *Small*, vol. 14, p. 1701913, 2018.

[29] D. Andrienko, "Introduction to liquid crystals," *J. Mol. Liq.*, vol. 267, pp. 520-541, 2018.

[30] G. J. T. Tiddy, "Surfactant-water liquid crystal phases," *Phys. Rep.*, vol. 57, pp. 1–46, 1980.

[31] Ö. Çelik and Ö. Dag, "A new lyotropic liquid-crystalline phase is formed from oligo- (ethylene oxide) surfactants and M(H_2O)," *Angew. Chem. Int. Ed.*, vol. 40, no. 20, pp. 3799–3803, 2001.

[32] G. Barm, C. Albayrak, E. Ylmaz, and Ö. Dag, "Highly conducting lyotropic liquid crystalline mesophases of pluronics (P65, P85, P103, and P123) and hydrated lithium salts (LiCl and $LiNO_3$)," *Langmuir*, vol. 30, no. 23, pp. 6938–6945, 2014.

[33] K. Goossens, K. Lava, C. W. Bielawski, and K. Binnemans, "Ionic Liquid Crystals: Versatile Materials," *Chem. Rev.*, vol. 116, no. 8, pp. 4643–4807, 2016.

[34] I. Karakaya, F. Karadas, B. Ulgut, and Ö. Dag, "Modification of Mesoporous $LiMn_2O_4$ and $LiMn_{2-x}Co_xO_4$ by SILAR Method for Highly Efficient Water Oxidation Electrocatalysis," *Adv. Mater. Technol.*, vol. 5, no. 8, pp. 1–12, 2020.

[35] C. Avcı *et al.*, "Molten Salt Assisted Self Assembly (MASA): Synthesis of Mesoporous Metal Titanate ($CoTiO_3$, $MnTiO_3$, and $Li_4Ti_5O_{12}$) Thin Films and Monoliths," *Chem. Mater.*, vol. 26, no. 20, pp. 6050–6057, 2014.

[36] A. J. Bard and L. R. Faulkner, *Electrochemical methods: Fundamentals and applications*, 2nd ed. John Wiley & Sons, Inc., 2001.

[37] N. Elgrishi, K. J. Rountree, B. D. McCarthy, E. S. Rountree, T. T. Eisenhart, and J. L. Dempsey, "A Practical Beginner's Guide to Cyclic Voltammetry," *J. Chem. Educ.*, vol. 95, no. 2, pp. 197–206, 2018.

[38] X. Pu *et al.*, "Understanding and Calibration of Charge Storage Mechanism in Cyclic Voltammetry Curves," *Angew. Chemie - Int. Ed.*, vol. 60, no. 39, pp. 21310–21318, 2021.

[39] A. Allagui, T. J. Freeborn, A. S. Elwakil, and B. J. Maundy, "Reevaluation of Performance of Electric Double-layer Capacitors from Constant-current Charge/Discharge and Cyclic Voltammetry," *Sci. Rep.*, vol. 6, 2016.

[40] J. Xie, P. Yang, Y. Wang, T. Qi, Y. Lei, and C. M. Li, “Puzzles and confusions in supercapacitor and battery: Theory and solutions,” *J. Power Sources*, vol. 401, pp. 213–223, 2018.

[41] B. M. Hunter, H. B. Gray, and A. M. Müller, “Earth-abundant heterogeneous water oxidation catalysts,” *Chem. Rev.*, vol. 116, pp. 14120–14136, 2016.

[42] M. Tahir *et al.*, “Electrocatalytic oxygen evolution reaction for energy conversion and storage: A comprehensive review,” *Nano Energy*, vol. 37, no. May, pp. 136–157, 2017.

[43] T. Shinagawa, A. T. Garcia-Esparza, and K. Takanabe, “Insight on Tafel slopes from a microkinetic analysis of aqueous electrocatalysis for energy conversion,” *Sci. Rep.*, vol. 5, p. 13801, 2015.

[44] D. Shriver and P. Atkins, *Inorganic Chemistry*, 5th ed. Oxford University Press, 2010.

[45] M. Bajdich, M. García-Mota, A. Vojvodic, J. K. Nørskov, and A. T. Bell, “Theoretical investigation of the activity of cobalt oxides for the electrochemical oxidation of water,” *J. Am. Chem. Soc.*, vol. 135, no. 36, pp. 13521–13530, 2013.

[46] L. F. Huang, M. J. Hutchison, R. J. Santucci, J. R. Scully, and J. M. Rondinelli, “Improved Electrochemical Phase Diagrams from Theory and Experiment: The Ni-Water System and Its Complex Compounds,” *J. Phys. Chem. C*, vol. 121, no. 18, pp. 9782–9789, 2017.

[47] B. Beverskog and I. Puigdomenech, “Revised Pourbaix Diagrams for Copper at 25 to 300°C,” *J. Electrochem. Soc.*, vol. 144, no. 10, pp. 3476–3483, 1997.

[48] T. Takashima, K. Hashimoto, and R. Nakamura, “Mechanisms of pH-dependent activity for water oxidation to molecular oxygen by MnO_2 electrocatalysts,” *J. Am. Chem. Soc.*, vol. 134, pp. 1519–1527, 2012.

[49] D. Reynard, S. Maye, P. Peljo, V. Chanda, H. H. Girault, and S. Gentil, “Vanadium–Manganese Redox Flow Battery: Study of MnIII Disproportionation in the Presence of Other Metallic Ions,” *Chem. - A Eur. J.*, vol. 26, no. 32, pp. 7250–7257, 2020.

[50] E. Zahoyni-Budo and L. I. Simandi, “Oxidations with unstable manganese(VI) in acidic solution,” *Inorganica Chim. Acta*, vol. 237, pp. 173–175, 1995.

[51] F. R. Duke, “The disproportionation of manganate ion. Manganese dioxide as heterogeneous catalyst,” *J. Phys. Chem.*, vol. 56, no. 7, pp. 882–884, 1952.

[52] I. K. Durukan, I. Ulu, and Ö. Dag, “Manganese oxide-based mesoporous thin-film electrodes: manganese disproportionation reaction in alkaline media,” *J. Mater. Chem. A*, vol. 12, no. 11, pp. 6359–6375, 2024.

[53] K. Jin *et al.*, “Mechanistic Investigation of Water Oxidation Catalyzed by Uniform, Assembled MnO Nanoparticles,” *J. Am. Chem. Soc.*, vol. 139, no. 6, pp. 2277–2285, 2017.

[54] A. Li *et al.*, "Stable Potential Windows for Long-Term Electrocatalysis by Manganese Oxides Under Acidic Conditions," *Angew. Chemie - Int. Ed.*, vol. 58, no. 15, pp. 5054–5058, 2019.

[55] B. Zhang, Q. Daniel, L. Fan, T. Liu, Q. Meng, and L. Sun, "Identifying MnVII-oxo Species during Electrochemical Water Oxidation by Manganese Oxide," *iScience*, vol. 4, pp. 144–152, 2018.

[56] S. Rana, J. P. Biswas, S. Paul, A. Paik, and D. Maiti, "Organic synthesis with the most abundant transition metal-iron: From rust to multitasking catalysts," *Chem. Soc. Rev.*, vol. 50, no. 1, pp. 243–472, 2021.

[57] T. Xue, C. L. Xu, D. D. Zhao, X. H. Li, and H. L. Li, "Electrodeposition of mesoporous manganese dioxide supercapacitor electrodes through self-assembled triblock copolymer templates," *J. Power Sources*, vol. 164, no. 2, pp. 953–958, 2007.

[58] Y. T. Wang, A. H. Lu, H. L. Zhang, and W. C. Li, "Synthesis of Nanostructured mesoporous manganese oxides with three-dimensional frameworks and their application in supercapacitors," *J. Phys. Chem. C*, vol. 115, no. 13, pp. 5413–5421, 2011.

[59] L. Chen, N. Gu, R. Ding, L. Qi, and H. Wang, "Facile fabrication of mesoporous manganese oxides as advanced electrode materials for supercapacitors," *J. Solid State Electrochem.*, vol. 17, no. 10, pp. 2579–2588, 2013.

[60] A. Pal, T. Das, S. Ghosh, and M. Nandi, "Supercapacitor behaviour of manganese dioxide decorated mesoporous silica synthesized by a rapid sol-gel inverse micelle method," *Dalt. Trans.*, vol. 49, no. 36, pp. 12716–12730, 2020.

[61] P. M. Ette, K. Selvakumar, S. M. Senthil Kumar, and K. Ramesha, "Silica template assisted synthesis of ordered mesoporous β–MnO_2 nanostructures and their performance evaluation as negative electrode in Li-ion batteries," *Electrochim. Acta*, vol. 292, pp. 532–539, 2018.

[62] J. Yoon *et al.*, "Reaction mechanism and additional lithium storage of mesoporous MnO_2 anode in Li batteries," *J. Energy Chem.*, vol. 53, pp. 276–284, 2020.

[63] C. H. Kuo *et al.*, "Robust mesoporous manganese oxide catalysts for water oxidation," *ACS Catal.*, vol. 5, no. 3, pp. 1693–1699, 2015.

[64] S. Lian *et al.*, "Template-free synthesis of mesoporous manganese oxides with catalytic activity in the oxygen evolution reaction," *Sustain. Energy Fuels*, vol. 1, no. 4, pp. 780–788, 2017.

[65] K. Selvakumar, S. M. S. Kumar, R. Thangamuthu, P. Rajput, D. Bhattacharyya, and S. N. Jha, "2D and 3D Silica-Template-Derived MnO_2 Electrocatalysts towards Enhanced Oxygen Evolution and Oxygen Reduction Activity," *ChemElectroChem*, vol. 5, no. 24, pp. 3980–3990, 2018.

[66] S. Chen, Z. Chen, and C. Cao, "Mesoporous Spinel LiMn2O4 Cathode Material by a Soft-templating Route," *Electrochim. Acta*, vol. 199, pp. 51–58, 2016.

[67] J. Y. Luo, Y. G. Wang, H. M. Xiong, and Y. Y. Xia, "Ordered mesoporous spinel $LiMn_2O_4$ by a soft-chemical process as a cathode material for lithium-ion batteries," *Chem. Mater.*, vol. 19, no. 19, pp. 4791–4795, 2007.

[68] F. Jiao, J. Bao, A. H. Hill, and P. G. Bruce, "Synthesis of Ordered Mesoporous Li–Mn–O Spinel as a Positive Electrode for Rechargeable Lithium Batteries," *Angew. Chemie*, vol. 120, no. 50, pp. 9857–9862, 2008.

[69] D. M. Robinson *et al.*, "Photochemical water oxidation by crystalline polymorphs of manganese oxides: Structural requirements for catalysis," *J. Am. Chem. Soc.*, vol. 135, no. 9, pp. 3494–3501, 2013.

[70] D. Tavar *et al.*, "Investigation of Li-rich manganese oxide spinel structures for electrochemical water oxidation catalysis," *Dalt. Trans.*, vol. 51, no. 33, pp. 12558–12568, 2022.

[71] O. Y. Bisen, M. Baumung, M. Tatzel, C. A. Volkert, and M. Risch, "Manganese dissolution in alkaline medium with and without concurrent oxygen evolution in LiMn2O4," *Energy Adv.*, vol. 21, pp. 504–514, 2024.

[72] F. Ataherian, K. T. Lee, and N. L. Wu, "Long-term electrochemical behaviors of manganese oxide aqueous electrochemical capacitor under reducing potentials," *Electrochim. Acta*, vol. 55, no. 25, pp. 7429–7435, 2010.

[73] S. Sun, J. Li, C. Xu, T. Zhai, and H. Xia, "Manganese-based layered oxides for electrochemical energy storage: a review of degradation mechanisms and engineering strategies at the atomic level," *J. Mater. Chem. A*, vol. 10, no. 37, pp. 19231–19253, 2022.

[74] A. Banerjee *et al.*, "On the oxidation state of manganese ions in li-ion battery electrolyte solutions," *J. Am. Chem. Soc.*, vol. 139, no. 5, pp. 1738–1741, 2017.

[75] U. Siamionau *et al.*, "Rechargeable zinc-ion batteries with manganese dioxide cathode: How critical is choice of manganese dioxide polymorphs in aqueous solutions?," *J. Power Sources*, vol. 523, p. 231023, 2022.

[76] D. Tang, Y. Sun, Z. Yang, L. Ben, L. Gu, and X. Huang, "Surface structure evolution of $LiMn_2O_4$ cathode material upon charge/discharge," *Chem. Mater.*, vol. 26, no. 11, pp. 3535–3543, 2014.

[77] M. Y. Song, D. S. Ahn, and H. R. Park, "Capacity fading of spinel phase $LiMn_2O_4$ with cycling," *J. Power Sources*, vol. 83, no. 1–2, pp. 57–60, 1999.

[78] C. Zhan *et al.*, "Mn(II) deposition on anodes and its effects on capacity fade in spinel lithium manganate-carbon systems," *Nat. Commun.*, vol. 4, p. 2437, 2013.

[79] Y. G. Cho *et al.*, "A metal-ion-chelating organogel electrolyte for le Chatelier depression of Mn^{3+} disproportionation of lithium manganese oxide spinel," *J. Mater. Chem. A*, vol. 6, no. 45, pp. 22483–22488, 2018.

[80] H. Lv *et al.*, "Disproportionation enabling reversible MnO_2/Mn^{2+} transformation in a mild aqueous Zn-MnO2 hybrid battery," *Chem. Eng. J.*, vol. 430, 2022.

[81] K. Xiao, S. L. Zhao, M. Cao, L. Zhang, N. Li, and Z. Q. Liu, "Electron affinity regulation on ultrathin manganese oxide nanosheets toward ultra-stable pseudocapacitance," *J. Mater. Chem. A*, vol. 8, no. 44, pp. 23257–23264, 2020.

[82] J. Ji *et al.*, "$Co^{2+/3+/4+}$-Regulated Electron State of Mn-O for Superb Aqueous Zinc-Manganese Oxide Batteries," *Adv. Energy Mater.*, vol. 11, no. 6, p. 2003203, 2021.

[83] S. Deng, Z. Tie, F. Yue, H. Cao, M. Yao, and Z. Niu, " Rational Design of $ZnMn_2O_4$ Quantum Dots in a Carbon Framework for Durable Aqueous Zinc-Ion Batteries ," *Angew. Chemie*, vol. 134, no. 12, pp. 1–6, 2022.

[84] M. Huynh, C. Shi, S. J. L. Billinge, and D. G. Nocera, "Nature of Activated Manganese Oxide for Oxygen Evolution," *J. Am. Chem. Soc.*, vol. 137, no. 47, pp. 14887–14904, 2015.

[85] A. Li *et al.*, "Stable Potential Windows for Long-Term Electrocatalysis by Manganese Oxides Under Acidic Conditions," *Angew. Chemie*, vol. 131, no. 15, pp. 5108–5112, 2019.

[86] Y. Yang *et al.*, "In Situ X-ray Absorption Spectroscopy of a Synergistic Co-Mn Oxide Catalyst for the Oxygen Reduction Reaction," *J. Am. Chem. Soc.*, vol. 141, no. 4, pp. 1463–1466, 2019.

[87] C. Qi, Q. Liu, Y. Dong, G. Zhang, X. Jiang, and D. Gao, "Fe^{3+} in a tetrahedral position determined the electrocatalytic properties in FeMn2O4," *RSC Adv.*, vol. 12, no. 42, pp. 27206–27211, 2022.

[88] C. Qi, Q. Liu, Y. Dong, G. Zhang, X. Jiang, and D. Gao, "Quenching-induced surface reconstruction of $FeMn_2O_4$ for promoted oxygen evolution reaction," *J. Alloys Compd.*, vol. 967, p. 171754, 2023.

[89] Y. Yuan, Z. Jiang, M. Li, and K. Peng, "Magnetic Field Enhancing the Electrocatalytic Oxygen Evolution Reaction of FeMn-Based Spinel Oxides," *ACS Appl. Energy Mater.*, vol. 6, no. 15, pp. 7865–7876, 2023.

[90] P. W. Menezes, A. Indra, N. R. Sahraie, A. Bergmann, P. Strasser, and M. Driess, "Cobalt-manganese-based spinels as multifunctional materials that unify catalytic water oxidation and oxygen reduction reactions," *ChemSusChem*, vol. 8, no. 1, pp. 164–167, 2015.

[91] J. Du, C. Chen, F. Cheng, and J. Chen, "Rapid synthesis and efficient electrocatalytic oxygen reduction/evolution reaction of $CoMn_2O_4$ nanodots supported on graphene," *Inorg. Chem.*, vol. 54, no. 11, pp. 5467–5474, 2015.

[92] H. Zhu *et al.*, "Morphology and Structure Engineering in Nanofiber Reactor: Tubular Hierarchical Integrated Networks Composed of Dual Phase Octahedral $CoMn_2O_4$/Carbon Nanofibers for Water Oxidation," *Small*, vol. 13, no. 26, p. 1700468, 2017.

[93] Y. Zhang *et al.*, "Manganese-Cobalt Spinel Nanoparticles Anchored on Carbon Nanotubes as Bi-Functional Catalysts for Oxygen Reduction and Oxygen Evolution Reactions," *Appl. Sci.*, vol. 13, no. 23, p. 12702, 2023.

[94] M. Zhang *et al.*, "Preparation of $NiMn_2O_4$ with large specific surface area from an epoxide-driven sol-gel process and its capacitance," *Electrochim. Acta*, vol. 87, pp. 546–553, 2013.

[95] A. Ray *et al.*, "Study on charge storage mechanism in working electrodes fabricated by sol-gel derived spinel $NiMn_2O_4$ nanoparticles for supercapacitor application," *Appl. Surf. Sci.*, vol. 463, pp. 513–525, 2019.

[96] S. Saha *et al.*, "Effect of particle morphology on the electrochemical performance of hydrothermally synthesized $NiMn_2O_4$," *Electrochim. Acta*, vol. 353, p. 136515, 2020.

[97] C. Busacca *et al.*, "Electrospun $NiMn_2O_4$ and $NiCo_2O_4$ spinel oxides supported on carbon nanofibers as electrocatalysts for the oxygen evolution reaction in an anion exchange membrane-based electrolysis cell," *Int. J. Hydrogen Energy*, vol. 44, no. 38, pp. 20987–20996, 2019.

[98] P. C. Nagajyothi, K. Pavani, R. Ramaraghavulu, and J. Shim, "Microwave synthesis of $NiMn_2O_4$/Ni-foam: Efficient bifunctional electrocatalysts for overall water splitting," *Int. J. Hydrogen Energy*, vol. 54, pp. 691–699, 2024.

[99] C. Zhang *et al.*, "$CuMn_2O_4$ spinel anchored on graphene nanosheets as a novel electrode material for supercapacitor," *J. Energy Storage*, vol. 34, no. November 2020, p. 102181, 2021.

[100] M. Zhou *et al.*, "Facet Impact of $CuMn_2O_4$ Spinel Nanocatalysts on Enhancement of the Oxygen Reduction Reaction in Alkaline Media," *ACS Catal.*, vol. 12, no. 21, pp. 13663–13670, 2022.

[101] B. J. Rani, A. Sivanantham, T. S. Shridharan, T. Runfa, and I. S. Cho, "Faceted and defect-rich $CuMn_2O_4$ nanoparticles for efficient electrochemical water splitting," *J. Mater. Chem. A*, vol. 4, pp. 17710–17720, 2022.

[102] J. Jiang, X. L. Zhou, H. G. Lv, H. Q. Yu, and Y. Yu, "Bimetallic-Based Electrocatalysts for Oxygen Evolution Reaction," *Adv. Funct. Mater.*, vol. 33, no. 10, p. 2212160, 2023.

[103] Z. Chen *et al.*, "Activity of pure and transition metal-modified CoOOH for the oxygen evolution reaction in an alkaline medium," *J. Mater. Chem. A*, vol. 5, no. 2, pp. 842–850, 2017.

[104] L. Wen *et al.*, "Cr-Dopant Induced Breaking of Scaling Relations in CoFe Layered Double Hydroxides for Improvement of Oxygen Evolution Reaction," *Small*, vol. 15, no. 35, p. 1902373, 2019.

[105] X. Liu *et al.*, "Nanoporous Zn-doped Co_3O_4 sheets with single-unit-cell-wide lateral surfaces for efficient oxygen evolution and water splitting," *Nano Energy*, vol. 44, pp. 371–377, 2018.

[106] W. Cheng, Z. Wu, D. Luan, S. Zang, and X. W. (David) Lou, "Synergetic Cobalt-Copper-Based Bimetal–Organic Framework Nanoboxes toward Efficient Electrochemical Oxygen Evolution," *Angew. Chemie*, vol. 133, no. 50, pp. 26601–26606, 2021.

[107] Z. P. Wu, X. F. Lu, S. Q. Zang, and X. W. Lou, "Non-Noble-Metal-Based

Electrocatalysts toward the Oxygen Evolution Reaction," *Adv. Funct. Mater.*, vol. 30, no. 15, p. 1910274, 2020.

[108] Y. Sun, X. Ren, S. Sun, Z. Liu, S. Xi, and Z. J. Xu, "Engineering High-Spin State Cobalt Cations in Spinel Zinc Cobalt Oxide for Spin Channel Propagation and Active Site Enhancement in Water Oxidation," *Angew. Chemie - Int. Ed.*, vol. 60, no. 26, pp. 14536–14544, 2021.

[109] X. Zhou *et al.*, "Theoretically Revealed and Experimentally Demonstrated Synergistic Electronic Interaction of CoFe Dual-Metal Sites on N-doped Carbon for Boosting Both Oxygen Reduction and Evolution Reactions," *Nano Lett.*, vol. 22, no. 8, pp. 3392–3399, 2022.

[110] Y. Ying, X. Luo, J. Qiao, and H. Huang, "'More is Different:' Synergistic Effect and Structural Engineering in Double-Atom Catalysts," *Adv. Funct. Mater.*, vol. 31, no. 3, p. 2007423, 2021.

[111] A. Pedersen *et al.*, "Dual-Metal Atom Electrocatalysts: Theory, Synthesis, Characterization, and Applications," *Adv. Energy Mater.*, vol. 12, no. 3, p. 2101715, 2022.

[112] Z. Li *et al.*, "Geometric and Electronic Engineering of Atomically Dispersed Copper-Cobalt Diatomic Sites for Synergistic Promotion of Bifunctional Oxygen Electrocatalysis in Zinc–Air Batteries," *Adv. Mater.*, vol. 35, no. 25, p. 2300905, 2023.

[113] T. Cui *et al.*, "Engineering Dual Single-Atom Sites on 2D Ultrathin N-doped Carbon Nanosheets Attaining Ultra-Low-Temperature Zinc-Air Battery," *Angew. Chemie - Int. Ed.*, vol. 61, no. 12, p. 202115219, 2022.

[114] H. Chen, W. Fu, Z. Geng, J. Zeng, and B. Yang, "Inductive effect as a universal concept to design efficient catalysts for CO_2 electrochemical reduction: electronegativity difference makes a difference," *J. Mater. Chem. A*, vol. 9, no. 8, pp. 4626–4647, 2021.

[115] M. M. Thackeray, W. I. F. David, P. G. Bruce, and J. B. Goodenough, "Lithium insertion into manganese spinels," *Mater. Res. Bull.*, vol. 18, no. 4, pp. 461–472, 1983.

[116] D. K. Kim *et al.*, "Spinel $LiMn_2O_4$ nanorods as lithium ion battery cathodes," *Nano Lett.*, vol. 8, no. 11, pp. 3948–3952, 2008.

[117] D. Skoog, D. West, J. Holler, and S. Crouch, *Fundamentals of Analytical Chemistry*, 9th ed. Belmont: Cengage Learning, 2014.

[118] E. S. Ilton, J. E. Post, P. J. Heaney, F. T. Ling, and S. N. Kerisit, "XPS determination of Mn oxidation states in Mn (hydr)oxides," *Appl. Surf. Sci.*, vol. 366, pp. 475–485, 2016.

[119] R. J. Gummow and M. M. Thackeray, "An Investigation of Spinel-Related and Orthorhombic $LiMnO_2$ Cathodes for Rechargeable Lithium Batteries," *J. Electrochem. Soc.*, vol. 141, no. 5, pp. 1178–1182, 1994.

[120] A. B. Haruna *et al.*, "Microwave irradiation suppresses the Jahn-Teller distortion in Spinel $LiMn_2O_4$ cathode material for lithium-ion batteries,"

Electrochim. Acta, vol. 426, p. 140786, 2022.

[121] C. E. Housecroft and A. G. Sharpe, *Inorganic Chemistry*, 4th ed. London: Pearson Education, 2012.

[122] A. I. Mizev, A. V. Shmyrov, and E. A. Mosheva, "Concentration-dependent diffusion of lithium, sodium, potassium, and cesium hydroxides in water," *J. Phys. Conf. Ser.*, vol. 1809, no. 1, 2021.

[123] L. Kotai, I. Gacs, I. E. Sajo, P. K. Sharma, and K. K. Banerji, "Beliefs and Facts in Permanganate Chemistry - An Overview on the Synthesis and the Reactivity of Simple and Complex Permanganates," *ChemInform*, vol. 42, no. 13, pp. 26-104, 2011.

[124] R. B. Temple and G. W. Thickett, "The decomposition of permanganate in molten alkali-metal nitrates," *Aust. J. Chem.*, vol. 27, no. 5, pp. 943–953, 1974.

[125] T. W. May *et al.*, "A Table of Polyatomic Interferences in ICP-MS," *At. Spectrosc.*, vol. 19, pp. 150–155, 1998.

[126] M. M. Thackeray, M. F. Mansuetto, D. W. Dees, and D. R. Vissers, "The thermal stability of lithium-manganese-oxide spinel phases," *Mater. Res. Bull.*, vol. 31, no. 2, pp. 133–140, 1996.

[127] M. C. Biesinger, B. P. Payne, A. P. Grosvenor, L. W. M. Lau, A. R. Gerson, and R. S. C. Smart, "Resolving surface chemical states in XPS analysis of first row transition metals, oxides and hydroxides: Cr, Mn, Fe, Co and Ni," *Appl. Surf. Sci.*, vol. 257, no. 7, pp. 2717–2730, 2011.

[128] A. P. Grosvenor, M. C. Biesinger, R. S. C. Smart, and N. S. McIntyre, "New interpretations of XPS spectra of nickel metal and oxides," *Surf. Sci.*, vol. 600, no. 9, pp. 1771–1779, 2006.

[129] M. C. Biesinger, L. W. M. Lau, A. R. Gerson, and R. S. C. Smart, "Resolving surface chemical states in XPS analysis of first row transition metals, oxides and hydroxides: Sc, Ti, V, Cu and Zn," *Appl. Surf. Sci.*, vol. 257, no. 3, pp. 887–898, 2010.

[130] V. Fournée *et al.*, "Electronic structure of quasicrystalline surfaces: Effects of surface preparation and bulk structure," *Phys. Rev. B - Condens. Matter Mater. Phys.*, vol. 62, no. 21, pp. 14049–14060, 2000.

[131] E. S. Freeman, "The kinetics of the thermal decomposition of sodium nitrate and of the reaction between sodium nitrite and oxygen," *J. Phys. Chem.*, vol. 60, no. 13, pp. 1487–1493, 1956.

[132] J. Hinze and H. H. Jaffé, "Electronegativity. I. Orbital Electronegativity of Neutral Atoms," *J. Am. Chem. Soc.*, vol. 84, no. 4, pp. 540–546, 1962.

[133] J. Hinze and H. H. Jaffé, "Electronegativity III. Orbital Electronegativities and Electron Affinities of Transition Metals," *Can. J. Chem.*, vol. 41, no. 5, pp. 1315–1328, 1963.

[134] G. G. Amatucci, J. M. Tarascon, and L. C. Klein, "CoO_2, The End Member of

the Li $_x$ CoO_2 Solid Solution," *J. Electrochem. Soc.*, vol. 143, no. 3, pp. 1114–1123, 1996.

[135] L. Dahéron *et al.*, "Electron transfer mechanisms upon lithium deintercalation from LiCoO 2 to CoO_2 investigated by XPS," *Chem. Mater.*, vol. 20, no. 2, pp. 583–590, 2008.

[136] M. Gao *et al.*, "Efficient water oxidation using nanostructured α-nickel-hydroxide as an electrocatalyst," *J. Am. Chem. Soc.*, vol. 136, no. 19, pp. 7077–7084, 2014.

[137] Y. F. Nicolau, "Solution deposition of thin solid compound films by a successive ionic-layer adsorption and reaction process," *Appl. Surf. Sci.*, vol. 22–23, no. PART 2, pp. 1061–1074, 1985.